Methods and application of deep-time thermochronology: Insights from slowly-cooled terranes of Mongolia and the North American craton

by

Kalin Trevor McDannell

A Dissertation

Presented to the Graduate and Research Committee

of Lehigh University

in Candidacy for the Degree of

Doctor of Philosophy

in

Earth and Environmental Sciences

Lehigh University

21 May 2017

© 2017 Copyright
Kalin Trevor McDannell

Approved and recommended for acceptance as a dissertation in partial fulfillment of the requirements for the degree of Doctor of Philosophy

Kalin Trevor McDannell

Methods and application of deep-time thermochronology: Insights from slowly-cooled terranes of Mongolia and the North American craton

May 01, 2017

Defense Date

Dissertation Director
Dr. Peter K. Zeitler

Approved Date

Committee Members

Dr. Kenneth P. Kodama

Dr. Anne S. Meltzer

Dr. Rebecca M. Flowers (external)

ACKNOWLEDGMENTS

There are far too many people to recognize and in the spirit of brevity, I wish to thank my committee, Dr. Anne Meltzer, Dr. Ken Kodama, and Dr. Rebecca Flowers for their guidance throughout my time at Lehigh. I would especially like to thank my advisor, Dr. Peter Zeitler for his dedication and mentorship – and for helping me to become a better scientist through countless hours of discussion, emails, and reflections about the concepts presented in this document. Thanks to David Schneider, Sam Bowring, and Becky Flowers for providing rocks and mineral separates from various remote locations, also Ryan Morelli at the Saskatchewan Geologic Survey for sharing rock cores. Bruce Idleman for laboratory support and discussions of $^{40}Ar/^{39}Ar$ and U-Th/He dating. Thanks to David Whipp, Matthew Fox, Frédéric Herman, Jean Braun, and Malcolm Sambridge for their assistance with inverse thermal modeling and Fortran code, and Alex Pacheco in Lehigh Computing for his assistance and patience. I would like to especially thank my parents, Monty and Dawn, for their many sacrifices and for instilling in me the importance of pursuing education. Thanks to my sweet Siberian Husky, Juneau, who has always been a comfort – whether she is aware of it or not. Finally, this work would not have been possible over the last few years without the support of my lovely wife, Jennifer.

"The stability of the solid earth is instability itself."
Alexander Winchell

TABLE OF CONTENTS

List of Figures x

List of Tables xii

Abstract 1

Preface 4

Chapter 1 – RELICT TOPOGRAPHY WITHIN THE HANGAY MOUNTAINS IN CENTRAL MONGOLIA: QUANTIFYING LONG-TERM EXHUMATION AND RELIEF CHANGE IN AN OLD LANDSCAPE 17

Chapter abstract 18

1. Introduction 19

2. Tectonic Setting 21

2.1 Regional Thermochronology 24

2.2 Long and short-term erosion rates 25

2.3 Hangay geomorphology 26

3. (U-Th)/He methods (abridged) 27

4. (U-Th)/He results

4.1 Bedrock (U-Th)/He data 28

4.2 Detrital data 31

5. Modeling

5.1 Detrital apatite (U-Th)/He modeling 31

5.2 Thermo-kinematic modeling 39

6. Discussion and interpretation 42

7. Conclusions 51

Acknowledgements 53

References 54

Appendix A

A1: Methodology – (U-Th)/He thermochronology 58

A2: Coupled Pecube-Neighborhood Algorithm modeling 60

A3: Pecube-NA Inversion resolution tests 63

Appendix B – Supplementary figures and tables 66

Chapter 2 – SCREENING APATITES FOR (U-Th)/He THERMOCHRONOMETRY VIA CONTINUOUS RAMPED HEATING: HELIUM AGE COMPONENTS AND IMPLICATIONS FOR AGE DISPERSION 79

Chapter abstract 80

1. Introduction 81

2. Continuous Ramped Heating (CRH) method

2.1 Analytical Procedures 83

2.2 Data reduction 85

2.3 Expected behavior 87

2.4 Peak fitting 90

2.5 Sample characterization 92

3. Results 96

3.1 Mongolia CRH results 99

3.2 Namche Barwa CRH results 104

3.3 Sierra Nevada CRH results 107

3.4 Appalachian CRH results 109

3.5 Mt. Dromedary CRH results 111

4. Discussion

4.1 General Observations 113

4.2 Gas Spikes 114

4.3 High-temperature release 114

4.4 Evidence for kinetic variability 115

4.5 Evidence for the role of deformation/microstructures 115

4.6 Support for the re-extract protocol 116

4.7 Future directions 117

5. Conclusions 118

Acknowledgements 118

References 120

Appendix A: Full CRH (U-Th)/He dataset 124

Chapter 3 – INSTABILITY OF THE CANADIAN SHIELD DURING THE LATE PROTEROZOIC 126

Chapter abstract 127

1. Introduction

1.1 The nature of cratons and stabilization 130

1.2 Stability: record or lack thereof? 134

2. K-feldspar MDD $^{40}Ar/^{39}Ar$ thermochronology

2.1 Linking high and low-T thermochronometers 136

2.2 $^{40}Ar/^{39}Ar$ MDD thermochronology results 139

2.3 Thermal history data and modeling 141

2.3.1 Superior Province, Ontario 142

2.3.2 Trans-Hudson, Saskatchewan 144

2.3.3 Trans-Hudson, Baffin Island 145

2.3.4 Grenville Province 146

2.4 Summary of results 147

3. Discussion 150

3.1 Erosional exhumation via isostasy 150

3.2 Burial heating and geotherm variability 152

3.3 Magmatic underplating 156

3.3.1 Underplating at the Mid-Continental Rift 157

3.3.2 Archean versus Proterozoic crust 158

3.3.3 Underplating in the Superior Province 159

3.3.4 Summary of mechanisms to explain histories 164

4. Conclusions 165

Acknowledgements 167

References 168

Appendix A: Sample characterization and other geochronology 178

Appendix B: $^{40}Ar/^{39}Ar$ thermochronology analytical methods 189

Appendix C: Age spectra and thermal history models 194

Dissertation Conclusions 237

*Supplementary data files available ($^{40}Ar/^{39}Ar$ & CRH *f*-loss data)

Vita 242

LIST OF FIGURES

Chapter 1

Figure 1: Mongolia regional topographic map 22

Figure 2: Granitic bedrock mean apatite (U-Th)/He age map 30

Figure 3: Selenga and Orkhon River detrital age populations 31

Figure 4: Hypsometry, SPDFs, and CSPDFs for Selenga River detrital age data 33

Figure 5: Apatite age-elevation relationships for western Hangay and region 38

Figure 6: Pecube-NA inversion results for Run 1-TSW 45

Figure 7: Observed vs. predicted cooling ages for W. Hangay 48

Figure 8: Pecube forward model age predictions using 1-TSW best-fit parameters at the regional scale 50

Figure B1: Regional elevations and adjoining high topography 66

Figure B2: Elevation and He age transect 67

Figure B3: Pecube-NA resolution test 68

Figure B4: Pecube-NA run 1-C for 9504 models 69

Figure B5: Scatter plot matrix of 5-D parameter space 70

Chapter 2

Figure 1: Schematic plot of sigmoidal ^{4}He release 86

Figure 2: Cumulative fractional loss curves from modeling 88

Figure 3: Mean cumulative *f* and *df*-curves for Durango apatite 97

Figure 4: Summary of CRH (U-Th)/He results 98

Chapter 2 (*continued)*

Figure 5: Behavior comparison for expected, Durango and fitting examples 103

Figure 6: Summary of *f* and *df*-curves from Mongolia 104

Figure 7: Namche Barwa CRH *f* and *df*-curves 107

Figure 8: Sierra Nevada CRH *f* and *df*-curves 109

Figure 9: Appalachian CRH *f* and *df*-curves 111

Figure 10: Mount Dromedary CRH *f* and *df*-curves 113

Chapter 3

Figure 1: Map of Canadian Shield with geology and sample locations 138

Figure 2: K-feldspar $^{40}Ar/^{39}Ar$ MDD age spectra for craton 140

Figure 3: K-feldspar $^{40}Ar/^{39}Ar$ thermal history summary 149

Figure 4: Reheating thermal history examples 154

Figure 5: Map of Canadian Shield with erosion depths, terranes, and underplated area 161

Appendix: Summary $^{40}Ar/^{39}Ar$ MDD age spectra plots 192

Appendix: Arvert thermal history models and domains info. 194-231

LIST OF TABLES

Chapter 1

Table 1: Pecube-NA inversion results for sensitivity test and full inversions 44

Table S1: Mongolian bedrock apatite (U-Th)/He data 71

Table S2: Mongolian detrital apatite (U-Th)/He data 74

Table S3: Bedrock sample locations 76

Table S4: Pecube fixed thermal model parameters 78

Chapter 2

Table 1: Samples characterized by the CRH method 92

Table 2: Mongolian samples - CRH age correction 102

Table 3: Namche Barwa samples - CRH age correction 106

Table 4: Sierra Nevada samples - CRH age correction 108

Table 5: Appalachian samples - CRH age correction 110

Table 6: Mount Dromedary samples - CRH age correction 112

Table S1: Full CRH (U-Th)/He dataset 124

Chapter 3

Table 1: Uplift and denudation amounts for underplating 164

Table S1: Craton sample locations and rock types 178

Table S2: W. Superior Province (U-Th)/He data 179

ABSTRACT

Continental interiors are an underappreciated facet of plate tectonics due to the perception that they are often static over long timescales. Salient tectonic margins receive more attention, owing to their comparatively dynamic state during the creation and destruction of continents and ocean basins. I utilize low-temperature (U-Th)/He and $^{40}Ar/^{39}Ar$ thermochronology to address questions regarding the spatial and temporal thermal evolution, and by proxy, the exhumation and burial histories of these slowly-cooled terranes through deep time. Chapter One is focused on the topographic evolution of the Hangay Mountains of central Mongolia, where apatite (U-Th)/He data and thermal models suggest that the post-orogenic landscape experienced rapid relief loss of a few hundred meters in the mid-Mesozoic. The Hangay are now characterized by a relict landscape that has undergone slow exhumation on the order of ~10 m/Ma since the Cretaceous (~100 Ma), analogous to other old landscapes such as the Appalachians. The central Mongolian landscape remains in a state of topographic disequilibrium, while modest surface uplift since the Oligocene and recent glaciation have had little effect on erosion rates due to the fact that there has been minor tectonism and a very dry climate during the Cenozoic.

Chapter Two confronts the problem of dispersed apatite (U-Th)/He cooling ages that often afflict slowly-cooled terranes, such as the Hangay Mountains. Conventional total-gas analysis offers little explanation or remedy for He age scatter that has been typically attributed to many factors, such as isotopic zonation, crystal lattice defects, and radiation damage. Unlike conventional analysis, the continuous ramped heating (CRH) technique

exploits incremental ^{4}He release during a continuous, controlled heating rate under static extraction line conditions. This approach allows the measurement of the cumulative gas released from apatite grains and assessment of the characteristic sigmoidal release curve shape as a means to distinguish between expected (radiogenic) and anomalous volume-diffusion behavior. Screening results for multiple apatite suites show that the CRH method can discriminate between the simple, smooth release of apatites exhibiting expected behavior and well-replicated ages, and grains that do not replicate well with more complicated ^{4}He release patterns – and offers a means to correct these ages.

Chapter Three is focused on understanding the assumed long-term stability of the southern Canadian Shield. Craton stability over billion-year timescales is often inferred due to the lack of geologic records to suggest otherwise. For the Proterozoic (2.5-0.54 Ga) there is little or no intermediate temperature thermal-history information for many locations, however K-feldspar ^{40}Ar/^{39}Ar MDD data and modeled thermal histories linked to published high- and low-temperature data from the Canadian Shield suggest the southern craton experienced unroofing delayed until ~1 Ga, coeval with the formation of the supercontinent Rodinia. K-feldspar data suggest a prolonged period of near-isothermal cooling of <0.5°C/Ma in the late Proterozoic where rocks were positioned at cratonic depths in the middle crust for up to ~500 million years at temperatures of ~150-200°C and subsequently exhumed to the surface in the Neoproterozoic. Thermal history solutions and geophysical evidence of underplating and crustal thickening at the Mid-Continental Rift and adjacent regions suggest uplift and a previously unrecognized phase

of cratonic unroofing that began in the Neoproterozoic, which ultimately contributed to the development of the Great Unconformity of North America.

PREFACE

The thermal histories of slowly-cooled terranes are inherently important for understanding continental evolution through deep time. Deciphering the temporal and thermal evolution of continental interiors is unequivocally tied to their unusually long record of continental dynamics that have endured without the severe overprint of marginal tectonics. Plate tectonic theory adequately explains many features of collisional settings, including orogenic processes, but has less obvious implications in relatively stable interiors. The degree to which plate margin and interior phenomena are connected in time and space is less clear. Examples of such processes include epeirogenesis and the apparent resistance of much cratonic lithosphere to deformation or significant vertical motions for great lengths of time, reaching billion-year timescales. The distribution and degree of vertical motions within interiors is enigmatic. Some work has shown that the record of erosion and sedimentation in continental interiors provides important information about how deep Earth processes operate and in turn how these processes influence the surface record, e.g. (Allen, 2011; Braun et al., 2014; Braun et al., 2013). Other areas show significant uplift, e.g. the Colorado and Tibetan Plateaus, while in most cratonic settings evidence has accrued for remarkably small degrees of vertical motion (Ault et al., 2009; Blackburn et al., 2012; Flowers et al., 2006b). This variability alone is inherently interesting, but one could argue that it is the tails of the hypsometric curve that have received disproportionate attention with modern techniques for quantifying timing, magnitude, and rates, although on a planetary scale most lower elevation, tectonically inactive regions dominate the hypsometry. The work presented here examines two settings that capture some of this variability, the post-Mesozoic exhumation history of the

high-elevation Mongolian interior and the secular thermal record of cratonic North America.

The Hangay Mountains of central Mongolia are far from active plate boundaries and lie between two cratons, the Siberian craton to the north, and the Sino-Korean to the south. This seemingly epeirogenic region is characterized by anomalous, thin lithosphere and thick crust that is expressed at the surface as high-elevation, low-relief topography. How this rugged mountain landscape has been elevated within the Mongolian Plateau is a current geodynamic question involving the interplay of northward-propagated deformation from the India-Asia collision and lithosphere-asthenosphere interactions bounding a thick craton. The Hangay landscape is characterized by minimal fault deformation relative to other areas of Mongolia, limited mass transport, Quaternary alpine glaciation, Cenozoic volcanism, and an increasingly arid climate since the latest Mesozoic. Chapter 1 addresses questions regarding the spatial and temporal exhumation history of the Hangay Mountains and outlying central Mongolia over long timescales. How has the topographic relief evolved through time? How has exhumation progressed in a setting that is characterized by minor tectonic activity and an arid climate? How are crustal (lithospheric) and surface processes linked in Mongolia, and to what degree through time? The tools used to assess the topographic evolution of relief and exhumation of the Mongolian landscape are low-temperature (U-Th-Sm)/He thermochronology of apatite in granitic bedrock and detrital river sediments and thermo-kinematic modeling. Thermochronology can be used to assess the topographic signal and

provide estimates of the erosional history of the crust, which is an important boundary condition for models of lithospheric evolution.

Clues to the exhumation and relief history of a landscape are held in the thermochronologic record of surface rocks across both short and long topographic wavelengths (Braun, 2002a, b). The employed chronometer gives an estimate of the time since a mineral has passed through its closure temperature (Dodson, 1973), or the range of temperature when adequate retention of the daughter product is realized within a mineral. For steady-state topography, vertical elevation transects take advantage of the closure temperature concept and the inherent age progression with depth, where older apparent cooling ages are nearer to the surface and approach zero age with greater depth (Brown et al., 1994; Wagner et al., 1977). Topography affects the upper crustal thermal structure, with the severity of the thermal disturbance decreasing with depth and proportionally with the topographic wavelength (Braun, 2002b, 2005; Mancktelow and Grasemann, 1997; Stüwe et al., 1994). At deep crustal levels, higher temperature isotherms are unaffected by the surface topography, but are disturbed closer to the surface. Isotherm perturbation is modulated by the wavelength and amplitude of topography. At long topographic wavelengths (10s-100s km), isotherms conform to the broad shape of the topography and cooling ages become independent of elevation, whereas at very short wavelengths (≤10 km) low-temperature isotherms directly mimic the topographic surface. Rocks that are exposed at peaks have traveled a greater distance after crossing the closure isotherms and therefore a cooling age increase with elevation is expected and provides a direct estimate of the exhumation rate (Braun, 2002a, b;

Mancktelow and Grasemann, 1997). In the case of high erosion rates, the advection of heat towards the surface causes isotherm compression, which further enhances the thermal disturbances felt by higher-temperature thermochronometers. These effects are less severe in the case of slow erosion. Low-temperature thermochronometers overestimate the exhumation rate in actively uplifting and eroding regions due to the perturbations to the upper crustal thermal structure (Braun, 2002b; Stüwe et al., 1994). The valley-scale, short wavelengths can be used to directly estimate the mean exhumation rate when higher temperature systems are used or in regions characterized by slow exhumation. An observed positive slope age-elevation relationship (AER) becomes flattened if there has been relief growth or steepened and even inverted if topographic relief has been reduced (Braun, 2002b). Therefore, short wavelength AERs are suitable for exhumation rate estimation, while long topographic wavelengths can be used to estimate relief change (Braun, 2002a; Braun and Robert, 2005). These fundamental characteristics of surface deformation coupled with the upper crustal thermal field are applied in this chapter via modeling of the spatial cooling age patterns to understand long-term evolution of the central Mongolian landscape.

Chapter 2 applies a newly developed laboratory analytical methodology to evaluate the long-standing problem of dispersion encountered in (U-Th-Sm)/He thermochronology. This “continuous ramped heating” technique is especially applicable for handling dispersed cooling-age datasets, which are typically obtained in slowly-cooled settings, such as Mongolia or many cratonic terranes. (U-Th-Sm)/He dating is a low-temperature technique applicable to U and Th-bearing accessory minerals such as apatite (Farley,

2000; Farley, 2002; Wolf et al., 1996; Zeitler et al., 1987) and zircon (Reiners, 2005; Reiners et al., 2004). It is based on the robust accumulation of ^{4}He over geologic time due to the radioactive decay of the U and Th series, as well as Sm. Bulk mineral ages determined using (U-Th-Sm)/He analyses of apatite and zircon can constrain thermal histories in the range ~50 to ~85˚C and ~150 to ~180˚C, respectively. These temperatures are commonly seen by rocks that have cooled within the upper 3 to 10 kilometers of the crust (assuming 20˚C/km geotherm) and (U-Th-Sm)/He apparent ages are regarded as proxies for tectonic or erosional unroofing, or alternatively burial heating during sedimentation (e.g. Ehlers and Farley, 2003).

Alpha-induced radiation damage has been shown to have major effects on cooling ages in both apatite (Flowers et al., 2009; Gautheron et al., 2009; Shuster et al., 2006) and zircon (Guenthner et al., 2013). Radiation damage is proportional to the effective Uranium content (eU; *see* Flowers et al. 2009) and modulates the closure temperature of the mineral in combination with cooling rate and grain size. Some of the dispersion and age 'inversion' between fission-track and (U-Th)/He data often seen in slowly cooled settings can be partially attributed to radiation damage (Fitzgerald et al., 2006; Flowers, 2009; Flowers and Kelley, 2011). Dispersion seems to afflict slowly-cooled rocks more often and in greater severity, and therefore has some fundamental relationship with cooling rate. However, dispersion has also been attributed to alpha-ejection effects (Farley et al., 1996), variations in mineral grain size (Farley, 2000), chemical composition (Djimbi et al., 2015) and parent isotope zonation (Farley et al., 2011; Fox et al., 2014; Hourigan et al., 2005), U-Th grain boundary enrichment (Murray et al., 2014), external He

implantation (Spiegel et al., 2009), alpha-emitting mineral inclusions or fluid inclusions (Farley, 2002; Vermeesch et al., 2007), and voids that act as diffusive "traps" (Zeitler et al., 2016, in press). These factors have all been recognized as contributing to dispersion but little has been done to provide an adequate method for dealing with scattered ages or establishing age correction protocols. The standard practice is to perform careful mineral separation and pick grains under high magnification in an attempt to mitigate some of the more obvious contributors to dispersion (i.e. poor grain quality and inclusions) and then analyze multiple single grains from a sample to assess replication and possibly average scatter. This is often ineffective, and even if these steps are taken, workers may still fall short in identifying the root cause of dispersion.

Conventionally an apatite sample is placed in a heating apparatus in a high-vacuum extraction line where it is isolated and then heated to a temperature of about 1000°C for 10-15 minutes. The extracted gas is purified and the total released ^{4}He is measured with a mass spectrometer. The heating is often unmonitored in routine work and it is assumed that all of the gas is extracted when high temperatures are sustained for a period of time that has been established from previous diffusion experiments on well-behaved laboratory age standards. Occasionally upon reheating a grain there is additional gas that is re-extracted and this is taken as an indication that the sample is poor quality and contains unidentified fluid inclusions or other retentive U-Th-rich mineral phases. Unlike these approaches, the continuous ramped heating (CRH) technique evaluated here utilizes static-gas measurement during uninterrupted heating of the sample, i.e. the sample in the heating chamber is left open to the extraction line and mass spectrometer, and the

evolved ^{4}He released during incremental heating is constantly measured as heating progresses. This permits rapid assessment of the characteristic sigmoidal release pattern that is associated with diffusive He loss during a linear heating schedule. The exact shape and position of the sigmoidal He release profile depends on grain size, kinetics (activation energy and diffusivity), and the heating rate. This method has the potential to discriminate between samples that are well-behaved, conforming to the expected behavior for apatite and showing complete gas exhaustion by 800-900°C (at 20°C/min rate), and "bad actors" that show complicated release patterns or extraneous helium components that are delayed to higher temperatures than those expected for volume diffusion. Screening using this method has the ability to reliably identify anomalous grain pathologies and has the potential to correct ages by removing spurious helium gas components.

Chapter 3 deals with the other lithospheric end member, Archean-Paleoproterozoic cratons, the oldest and thickest lithosphere preserved on Earth. Cratons are generally thought to have stabilized early in their history and passively endured since, with little regard to the marginal tectonics going on around them. Questions remain about the timescale and nature of craton stability through deep time and whether cratonic histories are inherently uninteresting or if they record more turbulent intervals of transition driven by peripheral or deep-seated tectonic processes. The nucleus of the North American craton has been conventionally viewed as a highly stable feature that has persisted for billions of years through a long and exceptionally quiescent "Middle Age" that spanned the time between craton consolidation by ~2.5 to 2.0 Ga and much more recent and

modest epeirogenic activity in the Phanerozoic. However, the physical evidence for stability is principally rooted in just this Phanerozoic record, and for significant parts of the craton, direct measurements are lacking, forming an observational gap exceeding a billion years. This is especially true for thermochronologic data, which are sensitive to the kind of processes, such as significant uplift and exhumation, heat-flow changes, and deformation that are indicators of stability or lack thereof.

Cratonization occurs after the cessation of orogenic building during terrane assembly and cold, thick lithosphere is formed. Stability describes the lack of penetrative deformation (i.e. magmatism and tectonism) or significant vertical motion due to mantle dynamics. Stability in cratons reflects the achievement of buoyancy equilibrium marked by cold, thick lithosphere and roots that resist tectonic and mantle alteration due to their unique thermo-chemical properties and elevated mechanical viscosity (Jordan, 1978). Simple isostasy predicts that stability occurs in the transition to cratonization and that exhumation and burial record this progression in the absence of significant vertical motion. Common mechanisms invoked for the stabilization of cratons are chemical buoyancy, an associated high viscosity lithospheric root with respect to the underlying mantle, and a high brittle yield stress for cratonic lithosphere compared to oceanic lithosphere (Cottrell et al., 2004; Lenardic et al., 2003). Stabilization in cratons is generally cited as occurring at the end of the Archean when voluminous K-rich granites were emplaced, causing differentiation of heat-producing elements (HPEs) into the upper crust (Jaupart et al., 2014), finalizing the thermal, petrologic, and density balance necessary for maintaining competent, strong lithosphere.

$^{40}Ar/^{39}Ar$ thermochronology of potassium feldspars in granitic rocks and thermal-history data from the southern Canadian Shield of North America (the Laurentian craton core: western Ontario, Saskatchewan, and southern Baffin Island) suggest that cratonic terranes may have been more active than has been realized. These data demonstrate that from approximately >1.5 to ~1.0 Ga, these rocks were at temperatures of ~200-250°C and cooled at rates of <0.5°C/Ma. Cooling then resumed at a faster pace after 1.0 Ga, presumably reaching the surface in the early Phanerozoic. If the traditional view of cratons is adhered to, then their typical low heat flow, and therefore low geothermal gradients of 10-20°C/km have been established since the Paleoproterozoic. Assuming a normal cratonic geothermal gradient and monotonic cooling – this would place these rocks in the middle crust at ~1 Ga. This raises questions about what sort of history could support the notion that rocks were nearly isothermal for a few hundred million years in the mid-crust and then subsequently exhumed? Conceivably these rocks may not have been in the mid-crust, but nearer to the surface and reheated, followed by discreet exhumation during Paleozoic-Mesozoic episodes of continental-scale dynamic topography. Moreover, a combination of factors may be able to explain thermal histories, such as decaying mantle temperatures, modest burial, or higher geothermal gradients in the Proterozoic.

This Proterozoic interval is often referred to as the "Boring Billion" (Holland, 2006), a time of unprecedented calm in the tectonic and biologic record. Adhering to the standard cratonic evolutionary view, some regions such as the Hearne-Rae domain near Lake

Athabasca in western Canada show evidence of rapid multi-stage exhumation to the surface following peak metamorphism during the Proterozoic, with little tectonic activity recorded since that time other than nominal, episodic reheating and cooling driven by convective mantle fluctuations (Flowers et al., 2008; Flowers et al., 2006a; Flowers et al., 2006b). K-feldspar $^{40}Ar/^{39}Ar$ MDD data suggest this is not the case at other highly constrained locations, which bears the implication that not all cratons were created equal and that isolated tectonic events may have affected some cratonic lithosphere and not other terranes. A better-constrained Proterozoic thermal history offers the ability to improve understanding of the stability paradigm or potentially relax this view in favor of a more dynamic alternative. This has implications beyond solid-Earth dynamics alone, because ideas about long-lived cratonic stability have been incorporated into models for the evolution of life and Earth's surface environment (Brasier and Lindsay, 1998; Lindsay and Brasier, 2002).

References

Allen, P. A., 2011, Geodynamics: Surface impact of mantle processes: Nature Geosci, v. 4, no. 8, p. 498-499.

Ault, A. K., Flowers, R. M., and Bowring, S. A., 2009, Phanerozoic burial and unroofing history of the western Slave craton and Wopmay orogen from apatite (U–Th)/He thermochronometry: Earth and Planetary Science Letters, v. 284, no. 1-2, p. 1-11.

Blackburn, T. J., Bowring, S. A., Perron, J. T., Mahan, K. H., Dudas, F. O., and Barnhart, K. R., 2012, An Exhumation History of Continents over Billion-Year Time Scales: Science, v. 335, no. 6064, p. 73-76.

Brasier, M., and Lindsay, J., 1998, A billion years of environmental stability and the emergence of eukaryotes: new data from northern Australia: Geology, v. 26, no. 6, p. 555-558.

Braun, J., 2002a, Estimating exhumation rate and relief evolution by spectral analysis of age–elevation datasets: Terra Nova, v. 14, no. 3, p. 210-214.

-, 2002b, Quantifying the effect of recent relief changes on age-elevation relationships: Earth and Planetary Science Letters, v. 200, no. 3-4, p. 331-343.

-, 2005, Quantitative constraints on the rate of landform evolution derived from low-temperature thermochronology: Reviews in Mineralogy and Geochemistry, v. 58, no. 1, p. 351-374.
Braun, J., Guillocheau, F., Robin, C., Baby, G., and Jelsma, H., 2014, Rapid erosion of the Southern African Plateau as it climbs over a mantle superswell: Journal of Geophysical Research: Solid Earth, v. 119, no. 7, p. 6093-6112.
Braun, J., and Robert, X., 2005, Constraints on the rate of post-orogenic erosional decay from low-temperature thermochronological data: application to the Dabie Shan, China: Earth Surface Processes and Landforms, v. 30, no. 9, p. 1203-1225.
Braun, J., Robert, X., and Simon-Labric, T., 2013, Eroding dynamic topography: Geophysical Research Letters, v. 40, no. 8, p. 1494-1499.
Brown, R. W., Summerfield, M. A., and Gleadow, A. J., 1994, Apatite fission track analysis: Its potential for the estimation of denudation rates and implications for models of long-term landscape development: Process models and theoretical geomorphology, p. 23-53.
Cottrell, E., Jaupart, C., and Molnar, P., 2004, Marginal stability of thick continental lithosphere: Geophys. Res. Lett., v. 31, no. 18, p. L18612.
Djimbi, D. M., Gautheron, C., Roques, J., Tassan-Got, L., Gerin, C., and Simoni, E., 2015, Impact of apatite chemical composition on (U-Th)/He thermochronometry: An atomistic point of view: Geochimica et Cosmochimica Acta, v. 167, p. 162-176.
Dodson, M. H., 1973, Closure temperature in cooling geochronological and petrological systems: Contributions to Mineralogy and Petrology, v. 40, p. 259-274.
Ehlers, T. A., and Farley, K. A., 2003, Apatite (U–Th)/He thermochronometry: methods and applications to problems in tectonic and surface processes: Earth and Planetary Science Letters, v. 206, no. 1, p. 1-14.
Farley, K. A., 2000, Helium diffusion from apatite; general behavior as illustrated by Durango fluorapatite: Journal of Geophysical Research, v. 105, no. B2, p. 2903-2914.
Farley, K. A., 2002, (U-Th)/He Dating: Techniques, Calibrations, and Applications: Reviews in Mineralogy and Geochemistry, v. 47, no. 1, p. 819-844.
Farley, K. A., Shuster, D. L., and Ketcham, R. A., 2011, U and Th zonation in apatite observed by laser ablation ICPMS, and implications for the (U–Th)/He system: Geochimica et Cosmochimica Acta, v. 75, no. 16, p. 4515-4530.
Farley, K. A., Wolf, R. A., and Silver, L. T., 1996, The effects of long alpha-stopping distances on (U-Th)/He ages: Geochimica et Cosmochimica Acta, v. 60, no. 21, p. 4223-4229.
Fitzgerald, P. G., Baldwin, S. L., Webb, L. E., and O'Sullivan, P. B., 2006, Interpretation of (U–Th)/He single grain ages from slowly cooled crustal terranes: A case study from the Transantarctic Mountains of southern Victoria Land: Chemical Geology, v. 225, no. 1-2, p. 91-120.
Flowers, R., Bowring, S., Mahan, K., Williams, M., and Williams, I., 2008, Stabilization and reactivation of cratonic lithosphere from the lower crustal record in the western Canadian shield: Contributions to Mineralogy and Petrology, v. 156, no. 4, p. 529-549.

Flowers, R., Mahan, K., Bowring, S., Williams, M., Pringle, M., and Hodges, K., 2006a, Multistage exhumation and juxtaposition of lower continental crust in the western Canadian Shield: Linking high‐resolution U‐Pb and 40Ar/39Ar thermochronometry with pressure‐temperature‐deformation paths: Tectonics, v. 25, no. 4.

Flowers, R. M., 2009, Exploiting radiation damage control on apatite (U–Th)/He dates in cratonic regions: Earth and Planetary Science Letters, v. 277, no. 1-2, p. 148-155.

Flowers, R. M., Bowring, S. A., and Reiners, P. W., 2006b, Low long-term erosion rates and extreme continental stability documented by ancient (U-Th)/He dates: Geology, v. 34, no. 11, p. 925-928.

Flowers, R. M., and Kelley, S. A., 2011, Interpreting data dispersion and "inverted" dates in apatite (U–Th)/He and fission-track datasets: An example from the US midcontinent: Geochimica et Cosmochimica Acta, v. 75, no. 18, p. 5169-5186.

Flowers, R. M., Ketcham, R. A., Shuster, D. L., and Farley, K. A., 2009, Apatite (U–Th)/He thermochronometry using a radiation damage accumulation and annealing model: Geochimica et Cosmochimica Acta, v. 73, no. 8, p. 2347-2365.

Fox, M., McKeon, R. E., and Shuster, D. L., 2014, Incorporating 3‐D parent nuclide zonation for apatite 4He/3He thermochronometry: An example from the Appalachian Mountains: Geochemistry, Geophysics, Geosystems, v. 15, no. 11, p. 4217-4229.

Gautheron, C., Tassan-Got, L., Barbarand, J., and Pagel, M., 2009, Effect of alpha-damage annealing on apatite (U–Th)/He thermochronology: Chemical Geology, v. 266, no. 3, p. 157-170.

Guenthner, W. R., Reiners, P. W., Ketcham, R. A., Nasdala, L., and Giester, G., 2013, Helium diffusion in natural zircon: Radiation damage, anisotropy, and the interpretation of zircon (U-Th)/He thermochronology: American Journal of Science, v. 313, no. 3, p. 145-198.

Holland, H. D., 2006, The oxygenation of the atmosphere and oceans: Philosophical Transactions of the Royal Society B: Biological Sciences, v. 361, no. 1470, p. 903-915.

Hourigan, J. K., Reiners, P. W., and Brandon, M. T., 2005, U-Th zonation-dependent alpha-ejection in (U-Th)/He chronometry: Geochimica et Cosmochimica Acta, v. 69, no. 13, p. 3349-3365.

Jaupart, C., Mareschal, J. C., Bouquerel, H., and Phaneuf, C., 2014, The building and stabilization of an Archean Craton in the Superior Province, Canada, from a heat flow perspective: Journal of Geophysical Research: Solid Earth.

Jordan, T. H., 1978, Composition and development of the continental tectosphere: Nature, v. 274, no. 5671, p. 544-548.

Lenardic, A., Moresi, L. N., and Muhlhaus, H., 2003, Longevity and stability of cratonic lithosphere: Insights from numerical simulations of coupled mantle convection and continental tectonics: J. Geophys. Res., v. 108, no. B6, p. 2303.

Lindsay, J. F., and Brasier, M. D., 2002, Did global tectonics drive early biosphere evolution? Carbon isotope record from 2.6 to 1.9 Ga carbonates of Western Australian basins: Precambrian Research, v. 114, no. 1–2, p. 1-34.

Mancktelow, N. S., and Grasemann, B., 1997, Time-dependent effects of heat advection and topography on cooling histories during erosion: Tectonophysics, v. 270, no. 3, p. 167-195.
Murray, K. E., Orme, D. A., and Reiners, P. W., 2014, Effects of U–Th-rich grain boundary phases on apatite helium ages: Chemical Geology, v. 390, p. 135-151.
Reiners, P. W., 2005, Zircon (U-Th)/He thermochronometry: Reviews in Mineralogy and Geochemistry, v. 58, no. 1, p. 151-179.
Reiners, P. W., Spell, T. L., Nicolescu, S., and Zanetti, K. A., 2004, Zircon (U-Th)/He thermochronometry: He diffusion and comparisons with 40 Ar/39 Ar dating: Geochimica et cosmochimica acta, v. 68, no. 8, p. 1857-1887.
Shuster, D. L., Flowers, R. M., and Farley, K. A., 2006, The influence of natural radiation damage on helium diffusion kinetics in apatite: Earth and Planetary Science Letters, v. 249, no. 3-4, p. 148-161.
Spiegel, C., Kohn, B., Belton, D., Berner, Z., and Gleadow, A., 2009, Apatite (U–Th–Sm)/He thermochronology of rapidly cooled samples: The effect of He implantation: Earth and Planetary Science Letters, v. 285, no. 1-2, p. 105-114.
Stüwe, K., White, L., and Brown, R., 1994, The influence of eroding topography on steady-state isotherms. Application to fission track analysis: Earth and Planetary Science Letters, v. 124, no. 1-4, p. 63-74.
Vermeesch, P., Seward, D., Latkoczy, C., Wipf, M., Günther, D., and Baur, H., 2007, α-Emitting mineral inclusions in apatite, their effect on (U–Th)/He ages, and how to reduce it: Geochimica et Cosmochimica Acta, v. 71, no. 7, p. 1737-1746.
Wagner, G. A., Reimer, G. M., Jäger, E., and Mineralogia, I. d. G. e., 1977, Cooling Ages Derived by Apatite Fission-track, Mica Rb-Sr and K-Ar Dating: The Uplift and Cooling History of the Central Alps, Società Cooperativa Tipografica.
Wolf, R. A., Farley, K. A., and Silver, L. T., 1996, Helium diffusion and low-temperature thermochronometry of apatite: Geochimica et Cosmochimica Acta, v. 60, no. 21, p. 4231-4240.
Zeitler, P. K., Enkelmann, E., Thomas, J. B., Watson, E. B., Ancuta, L. D., and Idleman, B. D., 2016, in press, Solubility and trapping of helium in apatite: Geochimica et Cosmochimica Acta.
Zeitler, P. K., Herczeg, A. L., McDougall, I., and Honda, M., 1987, U-Th-He dating of apatite: A potential thermochronometer: Geochimica et Cosmochimica Acta, v. 51, no. 10, p. 2865-2868.

CHAPTER 1

Relict topography of the Hangay Mountains in central Mongolia: Quantifying long-term exhumation and relief change of an old landscape

Kalin T. McDannell[a]*, Peter K. Zeitler[a], and Bruce D. Idleman[a]

[a]*Department of Earth and Environmental Sciences, Lehigh University, 1 W Packer Ave., Bethlehem, PA 18015, USA*

*Corresponding author: ktm211@lehigh.edu

Submitted to Earth and Planetary Science Letters
For resubmission to Tectonics

Keywords: Thermochronology, (U-Th)/He, Hangay, Mongolia, landscape evolution, Pecube

CHAPTER ABSTRACT

The Hangay Mountains are a high-elevation, low-relief landscape within the greater Mongolian Plateau of central Asia. Bedrock apatite (U-Th-Sm)/He single-grain ages span ~70 to 200 Ma, with a mean of 122.7 ± 24.0 (2σ) and detrital apatite samples from the Selenga and Orkhon Rivers, north of the Hangay Mountains, yield dominant (U-Th-Sm)/He age populations of ~115 to 130 Ma as well as an older population not seen in the Hangay granitic bedrock data. These low-temperature data imply regional exhumation in the Mesozoic with limited erosion of <1-2 km since the Jurassic-Cretaceous, and suggest that significant rapid exhumation of central Mongolia during the Late Cenozoic is unlikely. Apatite (U-Th-Sm)/He age-elevation patterns suggest long-term thermal stability of the upper crust, and thermal model inversions require moderate relief lowering of a few hundred meters during Mesozoic exhumation to produce the observed cooling ages in the Hangay region. Topographic relief decayed rapidly during the Cretaceous. Alpine cirques and intact moraines are indicative of more recent, climate-driven erosion in the higher peaks of the western Hangay. These data support the notion that in the absence of strong tectonic or climate forcing, erosion is limited and remnant landscapes can persist over 10s-100s of millions of years in a state of disequilibrium.

1. Introduction

The topographic evolution of landscapes offers a top-down perspective on understanding mountain-belt development through time. In recent decades, we have begun to understand that deformation, erosional unroofing, and climate can be coupled in active settings and that their system dynamics inherently regulate landscape geometries, e.g. (Molnar and England, 1990; Zeitler et al., 2001). Studies of exhumation in active mountains have shown that orogenesis can take place quite rapidly, at rates and durations consistent with plate convergence, and that surface processes can remove large relief rapidly (Montgomery and Brandon, 2002). Contrarily, ancient mountains and the records of their origins are often different from their modern counterparts, making the analysis of orogenic and topographic development a challenge. Since most continents are dominated by youthful landscapes, especially at tectonic margins, regions that show little evidence of modern tectonic or surficial change may offer a unique opportunity to constrain the longer timescale landscape morphology and provide information about landscape decay.

Erosion and landscape evolution in active regions are primarily controlled by tectonic uplift on orogenic timescales, e.g. (Koppes and Montgomery, 2009). In slowly eroding landscapes, where there is little tectonism, isostasy is a primary contributor to exhumation. As mountains mature their crustal root is consumed and orogenic relief is reduced while isostatic rebound further enhances erosional exhumation. Under typical crustal and mantle density conditions, reduction of surface topography by 1 km requires the erosion of ~5.5 km from the crustal column (Braun and Robert, 2005). The overall density structure of the lithosphere, in turn, controls the magnitude and distribution of

isostatic adjustment to erosion, with less buoyant lithosphere demonstrating an inhibited isostatic response, e.g. Fischer (2002). Post-orogenic topography has also been found to survive over extended timescales when sediment mobilization shear stresses are low and the fluvial system is transport-limited (Baldwin et al., 2003). These phenomena allow topographic and geodynamic aberrations to persist over hundred million-year timescales, rather than disappear within tens of millions of years after tectonism ceases.

Clues to the exhumation and relief history of a landscape are held in the thermochronologic record of surface rocks across both short and long topographic wavelengths (Braun, 2002 and references therein). Topography affects the upper-crustal thermal structure, with the severity of the thermal disturbance decreasing with depth and proportionally with the topographic wavelength (Braun, 2002). At long topographic wavelengths (10s-100s km), isotherms conform to the broad shape of the topography and cooling ages become independent of elevation, whereas at very short wavelengths (≤10 km) low-temperature isotherms are strongly controlled by the surface topography. In equilibrated topography, rocks that are exposed at peaks have traveled a greater distance after crossing the closure isotherms and therefore a cooling age increase with altitude is expected and provides a direct estimate of the exhumation rate (Braun, 2002). Sampling at short wavelengths (valleys) can be used to directly estimate the mean exhumation rate when higher temperature systems are used or in regions characterized by slow exhumation. An observed positive age-elevation relationship (AER) becomes flattened with respect to steady-state topography if there has been relief growth, or steepened and even inverted if topographic relief has been reduced (Braun, 2002). Therefore, short

wavelength AERs are suitable for exhumation-rate estimation, while long topographic wavelengths can be used to estimate relief change (Braun and Robert, 2005).

Inferences about topographic change and the erosion history of the crust can be made from spatial patterns in thermochronometric data. Here, we explore the ability of the apatite (U-Th-Sm)/He thermochronometer to constrain long-term, long-wavelength exhumation and relief evolution in the Hangay Mountains of central Mongolia, where there is a lack of penetrative deformation, limited mass transport, and the climate has become increasingly arid from the late Mesozoic through the Cenozoic; see Caves et al. (2014).

2. Tectonic Setting

The Hangay Mountains are a high-elevation (>3500-4000 m) region in the Asian continental interior and offer the unique opportunity to study an old landscape in a setting affected by recent tectonism (fig. 1). The Hangay sit within the Mongolian Plateau (2.6 million km^2) between the Siberian craton to the north and the Tarim and North China cratons to the south. The Hangay are also situated between the Altai transpressional zone and northern extensional zone of the Khövsgöl and Baikal rifts. In a broader context, the Hangay and outlying mountain ranges are all high-elevation topography juxtaposed against the low-elevation Siberian craton.

Broad, low-relief topographic surfaces that stand prominently above median continental base level are common features of continental interiors. How these apparently

epeirogenic areas reach and maintain high elevations is puzzling because of their great distance from plate boundaries. The uplifted high topography of the Mongolian Plateau (and central Mongolia) has mainly been ascribed as a distal expression of the India-Asia collision (Molnar and Tapponnier, 1975), although other mechanisms include, Pacific plate subduction (Yanovskaya and Kozhevnikov, 2003), localized mantle plume activity (Windley and Allen, 1993), asthenospheric upwelling or support (Chen et al., 2015; Cunningham, 2001; Petit et al., 2008; Tiberi et al., 2008), and mafic underplating (e.g. Petit et al., 2002).

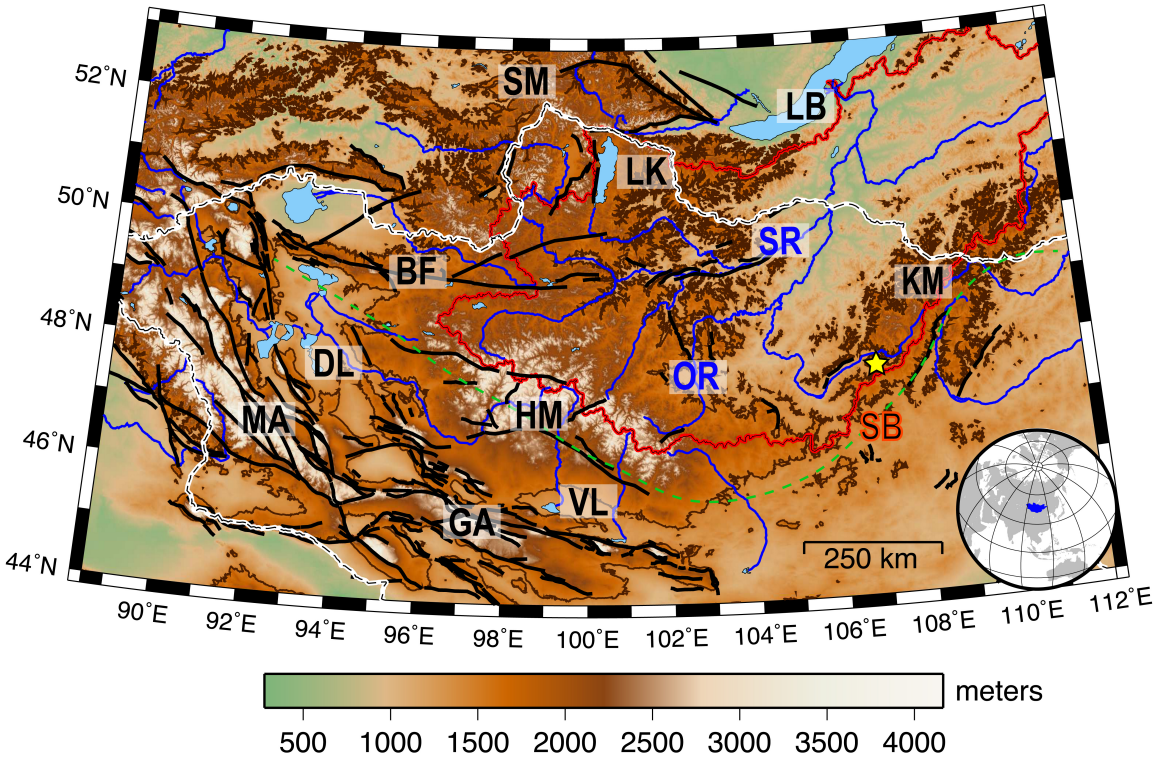


Figure 1: Regional map showing areas of high topography within Mongolia and southern Russia. The mean elevation in this view extent is 1500 ± 563 m and shows that the Hangay, Khövsgöl, Khentiyn, and Sayan Mountains (Russia) are a region of long-wavelength, high topography that has been dissected by the Selenga River network that drains the northern flank of the Hangay into Lake Baikal. Note that the deformation patterns vary regionally, i.e. the strong, large fault control in the Sayan versus the diffuse, smaller faults of the Hangay. The dark brown line denotes the 1500 m topographic contour. Regional fault systems are also shown; the sinistral Bulnai (BF) is

the major strike-slip fault north of the Hangay separating the Sayan/Khövsgöl from the Hangay. Blue lines are major permanent streams draining higher elevations and the red line denotes the Selenga River system drainage divide. Heavy white line is Mongolian political border. Green dashed line is approximate Mongol-Okhotsk Ocean suture from Van der Voo et al. (2015). Yellow star is Ulaanbaatar, the capital city. (MA=Mongolian Altai; GA=Gobi Altai; DL=Depression of Lakes; VL=Valley of Lakes; HM=Hangay Mountains; LK=Lake Khövsgöl; KM=Khentiyn Mountains; SM=Sayan Mountains; OR=Orkhon River; SR=Selenga River; LB=Lake Baikal; SB=Selenga basin).

The basement rocks of the Hangay Mountains are Archean to Early Proterozoic and composed of metamorphic units unconformably overlain by Cambrian through Devonian meta-sedimentary rocks. The crystalline and sedimentary rocks were intruded by Permian and Jurassic post-orogenic granitoids and underwent deformation during major Late Paleozoic through Mid-Mesozoic compression related to collision of Mongolia with the Siberian craton (Zorin, 1999). Hangay batholith granites yield zircon U-Pb crystallization ages of 242-260 Ma (Yarmolyuk et al., 2008).

The ranges in central Mongolia and southern Russia form the northernmost extent of the Central Asian Orogenic Belt (CAOB), which was a long-lived accretionary system, ca. 1000-250 Ma (Windley et al., 2007). The Mongol-Okhotsk Ocean was located between the Siberian and Mongolian (Amuria) blocks during Paleozoic-Mesozoic time and closed rapidly along a scissor-like suture during the Late Jurassic-Early Cretaceous in the eastern CAOB (Cogné et al., 2005; Van der Voo et al., 2015; Zorin, 1999). Yang et al. (2014) use basin analysis to assess the Jurassic-Cretaceous transition and propose that a brief (ca. 10 Ma), but significant orogeny occurred in the Late Jurassic-Early Cretaceous driven by collision of Siberia with the Kolyma-Omolon block. Seismic analysis in the Tugrug Basin in the Valley of Lakes also supports a rapid change from orogenic thickening to collapse in the Late Jurassic (Johnson et al., 2015), while

thermochronologic data from the Tian Shan, Altai, and Sayan Mountains confirm regional cooling during the initial stages of the Mongol-Okhotsk orogeny at about 150 Ma, with orogenic collapse occurring afterwards around 100 Ma (Glorie and De Grave, 2016).

2.1 Regional thermochronology

During the Middle to Late Mesozoic, parts of central Asia were characterized by a topographic planation surface. The Hangay Mountains, Sayan-Baikal ranges, and the Altai systems all show preserved Jurassic through Paleogene peneplain surfaces at elevations ranging from a few hundred meters to up to 4000 m (Cunningham, 2001; De Grave et al., 2009; Glorie and De Grave, 2016; Jolivet et al., 2007; Vassallo et al., 2007; West et al., 2013). In the Hangay Mountains, Valley of Lakes, and Gobi Altai rocks from relict erosional surfaces have Jurassic-Early Cretaceous apatite fission-track (AFT) ages (Jolivet et al., 2007; Vassallo et al., 2007). The similarity in AFT ages at peak summits in the Mongolian-Gobi Altai, Hangay, and the adjoining Valley of Lakes piedmont suggests that cooling below ca. 110°C occurred at roughly the same time across this region and these surfaces were at the same elevation in the crustal column (see fig. 5) and Jolivet et al. (2007). Central Mongolia also shares similarities with mountains in neighboring southern Russia. The mountains around Lake Baikal record AFT ages between ~140-100 Ma and rapid cooling in the Early Cretaceous, indicated by thermal-history modeling of AFT length distributions (Jolivet et al., 2009; van der Beek et al., 1996). AFT ages from the Siberian Altai and Western Sayan of Russia are Jurassic to Cretaceous in age (De Grave et al., 2009; Glorie and De Grave, 2016).

2.2 Long and short-term erosion rates

Thermal models for the Sayan suggest long-term erosion rates of 17.5 m/Ma, while ^{10}Be cosmogenic data suggest short-term (10^5 years) rates of 12-20 m/Ma (Jolivet et al., 2013). ^{10}Be cosmogenic data from basins in the eastern Hangay also show erosion rates between 12-20 m/Ma (Hopkins, 2012). Short and long-term rates are similar and imply an extended period of low erosion since the Mesozoic across Mongolia and southern Russia.

Climate has long been recognized as a major driver of tectonic-erosional feedbacks. Stratigraphy and basin analysis of the Tian Shan shows that the aforementioned Late Mesozoic tectonic reorganization shut off the monsoonal system in central Asia and aridification occurred through the Late Jurassic (Hendrix et al., 1992; Jolivet et al., 2015). Much of the aridification in central Asia is attributed to the uplift of the Tibetan Plateau and corresponding intraplate mountain belts extending to the north towards the Siberian craton (Molnar et al., 2010). This region of Asia has been arid through the end Mesozoic and Cenozoic. The observed shifts in regional isotopic aridity signatures support the timing of Hangay surface uplift to be at least Oligocene, and Late Miocene for the Altai range (Caves et al., 2014).

The existence of ~700 m of local paleo-relief is documented in central Mongolia through stratigraphic relationships between basalt flows and granitic bedrock (Smith et al., 2016). Basalt ^{40}Ar/^{39}Ar ages constrain the minimum age of the Hangay landscape to the Oligocene, while ^{14}C dating shows that material in lacustrine deposits overlying basalt

flows near Tariat are as young as ~5 Kya (Logachev et al., 1982). The ages of tilted sediments and volcanic rocks exposed on the flanks of the Hangay also support Oligocene doming and surface uplift of the Hangay, which is also broadly coincident with the initiation of regional volcanic activity (Cunningham, 2001). Basalt vesicle paleo-altimetry shows the surface of the Hangay may have been modestly uplifted by up to 1 km over the past ~10 Ma (Sahagian et al., 2016).

2.3 Hangay geomorphology

The central Mongolian fluvial network comprises alluvial streams with high sediment loads and limited transport ability due to many factors, including prolonged high aridity and spatially variable fluvial network integration. The Selenga River has a large drainage network (447,000 km^2) that sources the entire northern flank of the Hangay and most of central Mongolia and flows north into Lake Baikal, contributing a large volume of the lake water supply. The Orkhon River is one of the major Selenga tributaries flowing out of the glaciated eastern Hangay (see figure 1).

Geomorphic observations coupled with dated basalt stratigraphy (Ancuta et al., 2012) allow minimum incision rates to be calculated in the Hangay region. The Orkhon River headwaters show rates of ~20 m/Ma through the late Pliocene to Holocene, while Orkhon tributaries show late Pliocene through Holocene rates of ~30-60 m/Ma. At the Orkhon River waterfall (Ulaan Tsutgalan) basalts are ~700 Ka in age and yield incision rates of ~35 m/Ma. The northern flank of the Hangay show rates of ~10 m/Ma in 13-14 Ma basalts exposed along the Tamir River, a tributary of the Orkhon. The Chuluut River

valley, to the west, shows variable incision rates of 10-23 m/Ma over the past ca. 8-10 Ma. Basalt incision rates are similar to the aforementioned cosmogenic erosion rates in adjacent drainages and those estimated at Egiin Davaa in the central Hangay of ~25-77 m/Ma over the past 9 Ma (Smith et al., 2016). Basalt damming of river valleys in the past few million years establish that isolated flows caused accelerated incision, but overall these rates are comparable to those seen in old orogens such as the Appalachians (Matmon et al., 2003; McKeon et al., 2014).

The Hangay Mountains were extensively glaciated in the Pleistocene during the Last Glacial Maximum (Lehmkuhl et al., 2004). Evidence for this exists in the form of well-defined cirques and preserved moraine deposits. There are currently no permanent alpine glaciers in the Hangay, but cryoplanation features, patterned ground, and other glacial features exist at high elevations and advocate a more recent climate-driven erosion signal in the past few million years.

3. (U-Th)/He methods

Granitic bedrock and detrital sediments were collected for apatite (U-Th)/He (AHe) analysis throughout central Mongolia. Samples underwent standard mineral separation techniques using heavy liquids for apatite (see appendix A) and individual grains were picked under a stereographic microscope and placed into niobium carrier packets. Apatites were then loaded into the helium extraction system in the noble gas laboratory at Lehigh University where they were heated in a resistance furnace and He abundance was measured using a Balzers quadrupole mass spectrometer. Apatites were then sent to the

University of Arizona geochronology lab of Dr. Peter Reiners for U, Th, and Sm measurements using isotope-dilution ICP-MS.

4. (U-Th)/He results

4.1 Bedrock (U-Th)/He data

Granitoid bedrock samples were collected across the Hangay and areas to the north (figure 2, see suppl. table S1 and S4 for data). We dated 106 single-crystal aliquots of apatite (44 bedrock samples) and also report 12 multi-grain aliquots (5 bedrock samples) dated at Lehigh University during pilot Mongolia sampling from Landman (2007). Bedrock ages that were older than reported Hangay U-Pb ages of ~250 Ma were discarded as outliers for mean age calculations. However, there is a lack of age control for granitoids to the north, and those found in the Altai in southwest Mongolia have older zircon U-Pb populations spanning 289-317 Ma and 350-398 Ma (Cai et al., 2015), considerably older than the ~240-250 Ma granites in the Hangay. This allows for the possibility that there are some older granites that were exhumed previous to those in the Hangay. We would also like to note that age dispersion in slowly-cooled settings is a common issue, and although we ran a variable number of replicate grains per sample, meaningful statistics are difficult to justify in any case with such low *N*. We report average ages only for the graphical purpose of looking at broad, regional age patterns. Furthermore, for the purposes of the modeling (in later sections) it is a requirement to model single grains, not averages, regardless of statistical treatment because each analyzed grain is unique in its kinetic properties.

Single-grain ages replicate well within the central Hangay and cluster around ~100-120 Ma at various elevations with a few exceptions, while data outside the Hangay show greater dispersion. The cooling ages from the north flank of the range are marginally younger than elsewhere in the higher elevations (<100 Ma), which correlates well with the focus of modern precipitation. This regional cooling age pattern is similar to that of the Dabie Shan in China (Reiners et al., 2003) where regional age gradients were evaluated and significant differences were found between the range core and flanks, with a progressive younging of cooling ages towards the mountain interior. A subsequent modeling study suggested a twofold decrease of topographic relief over the past ~100 Ma to produce these age patterns (Braun and Robert, 2005).

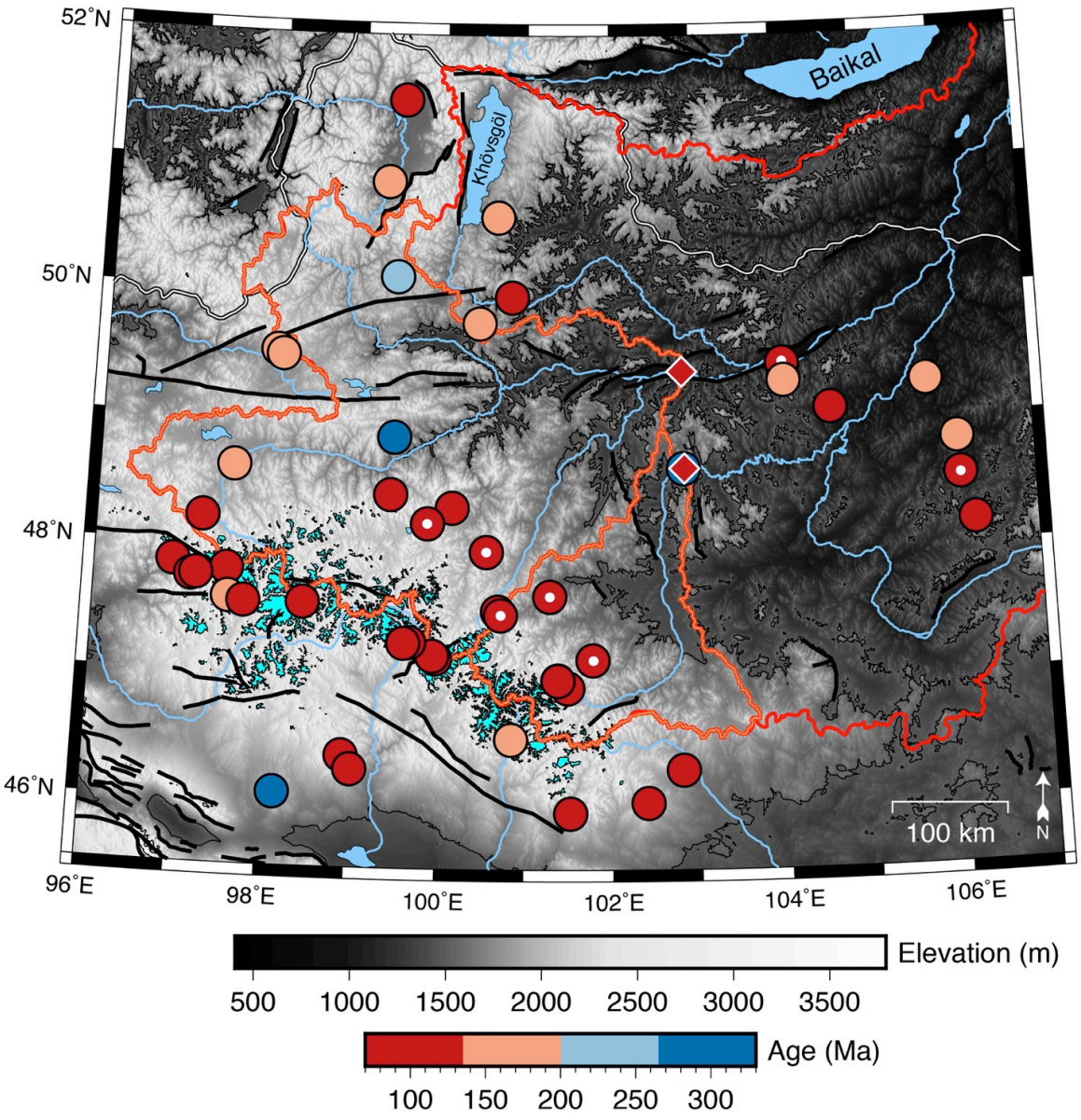


Figure 2: Granitic bedrock mean AHe ages across the Hangay Mountains and north-central Mongolia colored by age. The majority of cooling ages in the Hangay are ca. 100-120 Ma, with a slightly younger grouping <100 Ma on the north flank (red/white center). Off the Hangay, ages are similar, albeit with greater scatter and an older constituent greater than ca. 120 Ma. Detrital sample locations are shown as diamonds. The Selenga watershed is shown by the red line and sub-catchments with respect to detrital samples for the Selenga and Orkhon are the orange lines. Light blue region in the high Hangay denotes areas glaciated in the LGM. Gray-scale 90 m DEM with 1500 m contour to mark higher elevations above the regional background. Mongolian fault network shown by heavy black lines.

4.2 Detrital (U-Th)/He data

The lower reaches of the Orkhon and Selenga Rivers were sampled to survey regional detrital apatite cooling ages (suppl. table S2 for data). The corresponding watersheds of the sampled locations can be seen in figure 2. The motivation for detrital dating was also to establish the age distribution that may be expected from bedrock ages, and to assess any dominant subsets. The Selenga and Orkhon Rivers (fig. 3) show similar age distributions with dominant peaks at ~115-120 Ma for the Selenga and a broad peak centered at ~130 Ma for the Orkhon (this central value is very likely controlled by the low number of data).

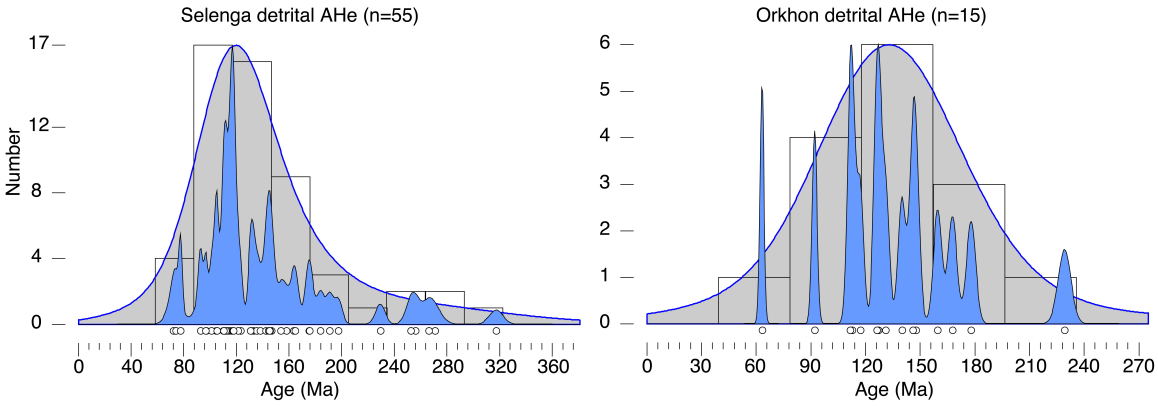


Figure 3: Selenga and Orkhon River detrital apatite (U-Th)/He cooling age populations shown by kernel density estimator (KDE) (smooth, gray envelope) and probability density functions (PDF) (shaded blue) from DensityPlotter (Vermeesch, 2012) using a Gaussian kernel and adaptive bandwidth (varied based on local data density). White dots show individual grain ages for the datasets. The y-axis is number of grains.

5. Modeling

5.1 Detrital apatite (U-Th)/He modeling

Inference of the probability distribution of the number of age components was performed via BayesMix using Reversible Jump Markov-Chain Monte Carlo methods (Jasra et al., 2006). There are two major age components identified in the Selenga River sample with

an expected model mean of 124 ± 29 Ma, representing 83% of the detrital population and an older component at 227 ± 51 Ma, representing 17% of the population (200,000 iterations, post burn-in). The Orkhon sample is low *n* and less resolved, but mixture modeling reveals a single component maximum posterior peak at 131 ± 29 Ma, showing overall agreement between both rivers. The Selenga detrital population contains a few dates that may reflect the end of CAOB orogenic exhumation, while the majority of grains are from the last major exhumation event in the early Cretaceous during Mongol-Okhotsk suturing. The notable outcome from the detrital dating is that the area supplying sediment to these two locations contains an older age component that is not reflected in the Hangay bedrock samples, implying that the older ages are potentially coming from bedrock in the lower reaches of the catchments or that older cooling ages are sourced from glacially eroded relict surfaces.

The hypsometry of the Selenga and Orkhon catchments relative to the detrital sample locations are quite different (fig 4). Both drainage basins have been glaciated (see fig. 2), but the glaciation is limited in extent compared to the overall basin areas. Based on the hypsometric integral, the Orkhon basin would be ‘mature’ while the Selenga would represent a younger stage of development. Nevertheless, caution is required during interpretation because the influence of tectonics or fluvial/glacial processes, along with basin size and tectonic activity can render basin hypsometry non-unique (Brocklehurst and Whipple, 2004).

Assuming uniform erosion and a positive trend AER, the observed elevation distribution in a catchment should produce a predicted age probability density function (PDF) that matches the hypsometry (Brewer et al., 2003; Ruhl and Hodges, 2005; Stock et al., 2006). If there is non- uniform erosion in a catchment then the predicted age PDF will be out of phase with the hypsometric curve or have multiple peaks corresponding to the areas of the catchment that are being more heavily eroded (Stock et al., 2006).

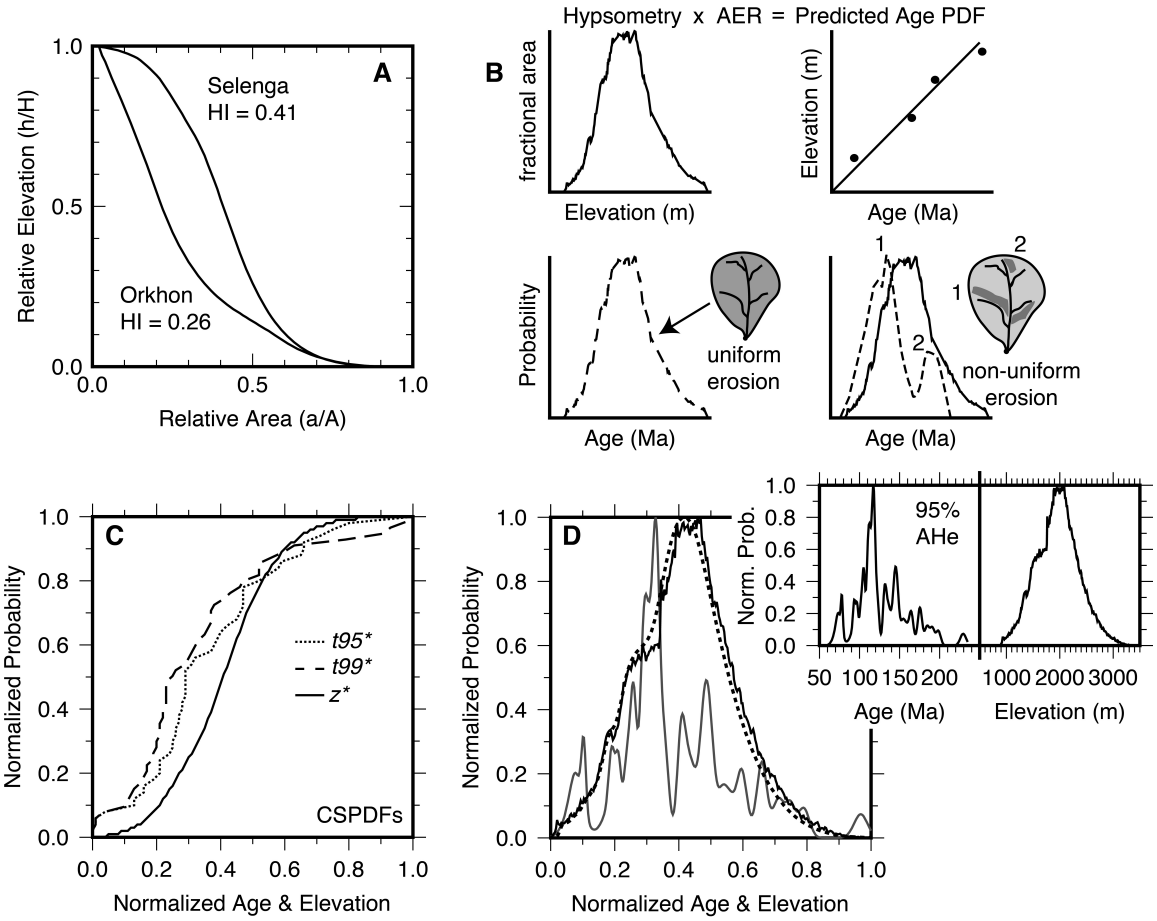


Figure 4: A) Hypsometry of the Selenga and Orkhon sub-basins sampled for detrital AHe. B) Schematic diagram illustrating the relationship between detrital thermochronometer data and the hypsometry of a catchment given an assumed positive age-elevation relationship where cooling ages should match the hypsometric curve if erosion is uniform, i.e. all points on the topography produce cooling ages that correspond to the basin AER. If there is non-uniform erosion, then the elevations on the landscape contributing sediments will affect the SPDF curve accordingly, modified after Stock et al. (2006). C) Normalized CSPDF curves of detrital ages (dashed lines, t*)

and catchment elevations (solid line, z*) for the Selenga and Orkhon Rivers, using 95 and 99% of the detrital dataset for the Selenga River, after Ruhl and Hodges (2005). D) SPDF curves for normalized age (gray) and elevation (solid black line) distributions with inset age and elevations. Dashed line is the 'ideal' age SPDF obtained from inverting the observed age SPDF and hypsometric curves with respect to the regional AER from the northern Hangay. Small inset panels show ages for 95% of the detrital AHe dataset and the elevations in the Selenga sub-basin.

The same would be true if the positive AER assumption is violated or relief change has occurred. Whipp et al., (2009) showed through 3D thermal modeling that an increase in relief causes a shift in the detrital age population towards older ages relative to steady-state relief, whereas a relief decrease would have an opposite trend. This is directly linked to the higher or lower effective denudation rate between each respective relief change scenario. Figure 4 shows plots of probability density functions (PDF) of cooling ages (after Stock et al., 2006; Ruhl and Hodges, 2005) expressed as:

(1)

$$PDF = \frac{1}{\sigma t_m \sqrt{2\pi}} \exp\left[-\frac{1}{2}\left(\frac{t - t_m}{\sigma t_m}\right)^2\right]$$

Where t is the PDF of the age, t_m is the measured age with the analytical uncertainty, σ. The synoptic probability function (SPDF) is the summation of all individual grain PDFs multiplied by the reciprocal of the number of detrital grains normalized to unity. The cumulative synoptic probability function (CSPDF) represents the probability that the age takes on a value less than or equal to t, the PDF of the cooling age. The CSPDFs are normalized hypsometric curves of elevation, z^*, and cooling age, t^*, and assuming uniform erosion, should overlap. To minimize the mismatch between normalized age and elevation curves due to uncertainty in cooling ages, both the 95% and 99% detrital SPDF were used to construct the t^* CSPDFs, which effectively removes a small component of

the older age signal. The $CSPDF_{t*}$ curves are slightly offset from the $CSPDF_{z*}$ curve for the Selenga basin, suggesting some non-uniform erosion. The Orkhon basin curves are not shown due to the limited number of dated grains.

We solve for the expected uniform erosion AER by dividing the observed detrital PDF by the hypsometry to obtain the slope of the ideal AER to match the hypsometry. This produces a predicted slope of 0.068 that is then compared to a bedrock age-elevation transect on the north flank of the Hangay, which yields a slope of 0.060 (dashed predicted age SPDF curve in fig. 4c). Another short transect from the valley floor to the Orkhon headwaters cirque yields a slope of 0.059. Near Otgon Tenger Uul, the highest elevation peak in the glaciated interior of the Hangay, age-elevation transects are shown in figure 5 using our data and those of West et al. (2013), Jolivet et al. (2007), and Landman (2007). Here, AER slopes are greater but still similar to the predicted and measured AER slopes in the Selenga basin. The slight mismatch in the PDF curves could be due to:

1) Sampling bias or outlier ages: The Selenga basin sources not only the Hangay, but lower elevations to the north that have a slightly older, albeit scattered, cooling age signal and therefore are eroding more slowly than the Hangay. Bias could be introduced from the dating process itself or be naturally occurring if a higher proportion of 'younger' Hangay sediments were being supplied to the lower reaches of the basin. Naturally occurring bias may be a reflection of alpine cirque cutting and higher erosion along steeper slopes of the Hangay. There is also the possibility of sampling other Mesozoic-Paleozoic bedrock and older, recycled sediments. If this is the case, it would seem that this is a fairly small proportion of

dated grains. Alternatively, some of these slowly-cooled apatites could be 'bad actor' outliers that are skewing the age PDF; this situation is apparent in the 95% $CSPDF_{t*}$ curve, which more closely matches the hypsometry by removing only the oldest ages from the detrital population.

2) Detrital under-sampling: The Selenga CSPDFs are reminiscent of those presented by Ruhl and Hodges (2005) for the Marsyandi trunk stream in Nepal where there is also departure of the $CSPDF_{t*}$ from the elevation range. This was attributed to sediments not capturing the full bedrock age signal in a very large catchment. This could very well be the case here as well, since the sampled Selenga catchment is >95000 km^2 in size.

3) The 'spike' in the measured detrital PDF is the only main point of deviation between PDFs and occurs at a large step in the hypsometric curve, which roughly aligns with the shift from the background low-lying elevations in the deeper basin to the elevated landscape of the Hangay. This shift likely signifies a regional, preferential 'cooling age zone' that is the current focus of incision at the crossover into higher elevations of the Hangay where more sediment of the primary detrital peak is being sourced. In line with this, the mismatch between hypsometry and the age CSPDF may also signify a change in erosion rate at ~120-130 Ma, which agrees to first-order with the West et al. (2013) apatite fission-track AER (see fig. 5).

The detrital age range for a catchment is also proportional to the time needed to erode the total relief in the source region (Brewer et al., 2003; Ruhl and Hodges, 2005). The large

spread in observed detrital ages suggests that erosion has been slow, low magnitude, and operative over a prolonged period since the Mesozoic. Narrow or broad age spread is interpreted as rapid or slow erosion rate, respectively (Stock and Montgomery, 1996). In a simplistic 1-D case where lateral advection is ignored, an erosion rate over the time represented by the detrital population can be calculated by simply dividing the total catchment relief by the cooling age range, which in this case is quite long, >150 Ma. Long-term slow erosion and low modern relief suggest that the shallow isotherms have conformed to the topography, and a simple 1-D technique is adequate for erosion rate estimation (Whipp et al., 2009). To reduce the influence of potential outlier ages, only cooling ages falling within 95% of the detrital population mean were used. The detrital apatites from the Selenga catchment that source the majority of the western Hangay and northern Mongolia show a time-integrated erosion rate of, $\dot{E} \approx 17$ m/Ma, which decreases to ~10 m/Ma if the entire detrital dataset is used. This is in agreement with the independently derived basalt incision rates for the late Cenozoic and previous thermochronologic and cosmogenic estimates for the region cited in section 2, all in accordance with a long-term history of slow denudation.

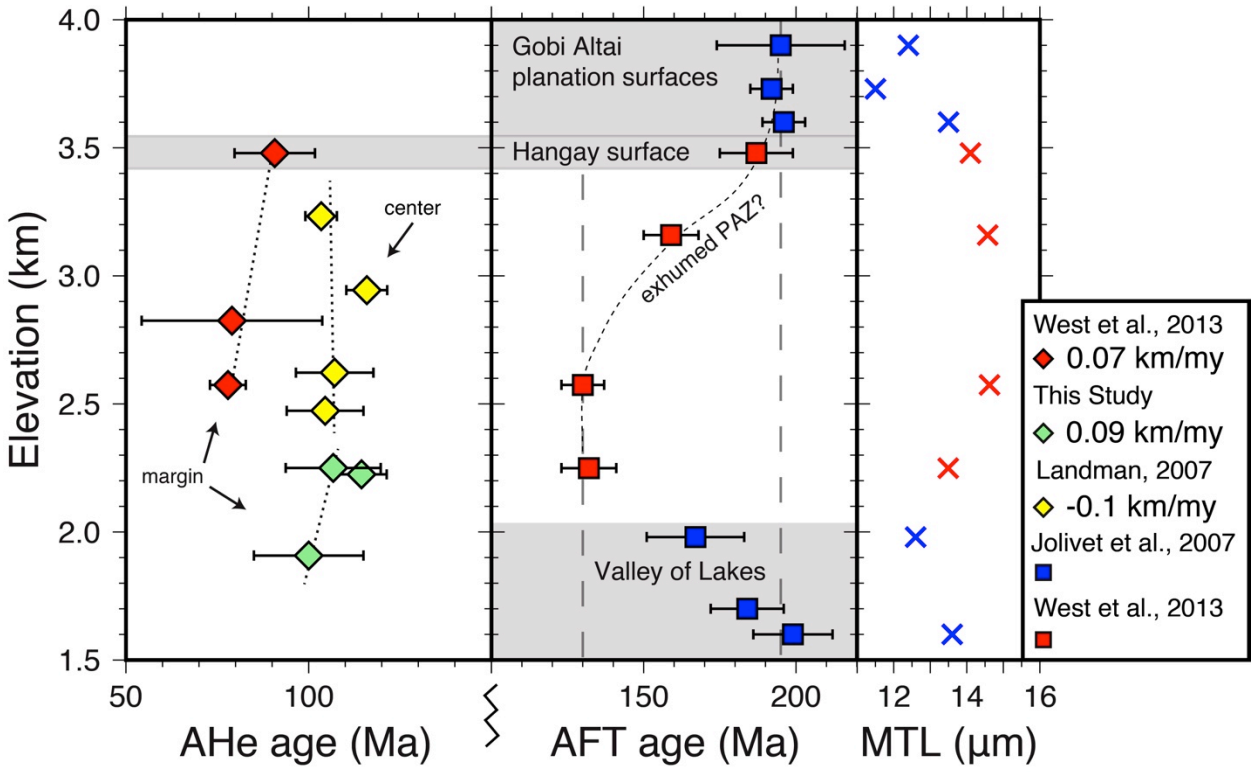


Figure 5: Apatite AERs (left panel) from the western Hangay near Otgontenger (highest peak) incorporating a short transect from this study and from West et al. (2013) and Landman (2007) datasets. Positive AERs suggest valley-scale topographic wavelengths do not affect low-T isotherms. Right panels show AFT and mean fission-track lengths (MTL) for Jolivet et al. (2007) and West et al. (2013) datasets. Planation surfaces in the Gobi Altai, Valley of Lakes, and W. Hangay (gray) are all similar in age suggesting regionally coincident exhumation and that highest elevations are preserved remnants from an older event. West et al. AFT transect suggests the period between ~180-130 Ma being governed by a moderate exhumation rate.

Conversely, paleo-relief can also be estimated from the detrital cooling age range using the AER of a catchment (Stock and Montgomery, 1996). On the large scale in the slowly-eroding Hangay, isotherms would presumably now be parallel to the surface, however, assuming horizontal isotherms, the exposed bedrock ages divided by the modern relief yields the change in cooling age with elevation. By the same token, the detrital age range divided by the AER provides estimates of the paleo-relief. The apatite fission-track AER of West et al. (2013) spans 46.34 ± 0.24 Ma over 1.23 ± 0.01 km of modern elevation (using 10 m elevation errors from 90 m DEM) in the western Hangay. Using the 95%

spread about the mean detrital age approximates catchment paleo-relief of 3.39 ± 0.1 km, or a 0.79 ± 0.1 km decrease in relief in the time represented by the detrital data.

The size of our detrital age sample population is too small to allow a definitive assessment, although assumptions of widespread steady-state erosion in the Hangay are seemingly invalidated. It is reasonable to suspect that the landscape has experienced variable, finite erosion since the Cretaceous that has been more focused in certain areas of the landscape. The continued existence of the remnant planation surfaces across the Hangay is further evidence that an erosional steady state has yet to be reached. The recent surface uplift has potentially complicated the erosional history and provided a 'regional knickpoint' at the uplifted Hangay margins for focused incision. Knickpoints in river profiles are evident near the Hangay margin at ~2000-2500 m elevation (West et al., 2013). The eastern Hangay and Orkhon watershed contain the majority of Cenozoic valley-filling basalts that have dammed many valleys and locally disrupted the fluvial system by resetting base level in the last ca. 10-15 Ma. Our observations and those in West et al. (2013) agree and support modern precipitation gradients, modest glaciation, and recent surface uplift as the cause of erosional variability in this setting.

5.2 Thermo-kinematic modeling

We are interested in not only the long-term exhumation of the region but also the relief evolution through time. We performed modeling analogous to the Dabie Shan study to ascertain the topographic and thermal histories necessary to produce the observed AHe dataset for central Mongolia using Pecube. Pecube (Braun, 2003) is a finite-element

thermo-kinematic model that solves the 3D heat transport equation in a crustal block with the allowance of a time-variable surface boundary condition (topography) including the effects of isostasy. In our Pecube inversion we adopt spatially constant material properties for the crust (suppl. table S3) and a sub-region of central Mongolia is modeled as a single uplifting block, as the entire Hangay and thermochronology dataset coverage are too large to model efficiently. For age prediction the RDAAM model of Flowers et al. (2009) is incorporated for apatite (U-Th)/He and all single grain age replicates are used in modeling the western Hangay. A SRTM digital elevation model resampled to 1 km resolution of central Mongolia was used as the topographic input.

During a Pecube model inversion, the use of a two-step Neighborhood Algorithm (NA) inverse approach is employed, where during the sampling stage the multi-dimensional prior model space is efficiently sampled to find the best-fitting parameter combinations that produce the lowest user-defined misfit between observed and predicted data (Sambridge, 1999a). The appraisal stage then allows robust measures of parameter resolution to be extracted in the form of Bayesian marginal posterior probability functions (PPDF) during resampling of the model ensemble (Sambridge, 1999b). During the sampling stage an initial model ensemble is randomly generated using the prior parameter range (assumed uniform distribution) of the Pecube variables. The misfit is assessed and Voronoi cells are created about nearest neighbor models that are subdivided after successive iterations as the algorithm focuses on regions of lower misfit by resampling the previous iteration. We employed an objective function or χ^2 misfit of the form:

(2)

$$\mu = \sum_{i=1}^{n} \left(\frac{m_i - o_i}{\sigma_i} \right)^2$$

Where μ is the misfit value, n is the number of data, and for each datapoint i, o_i is the observed age, m_i is the model age, and σ_i the observed age error. During the NA appraisal stage the entire sampling-stage ensemble is resampled to gain Bayesian estimates of parameter values and assess the resolution of the lowest misfit via the Likelihood function, L, to assess the likelihood of different model predictions, given in the simplified form as (Glotzbach et al., 2011):

(3)

$$L = \exp(-\frac{1}{2}\chi^2)$$

Pecube-NA inversions have been applied successfully to high-relief regions that have experienced relatively high exhumation rates and recent relief development such as the European Alps, e.g. (van der Beek et al., 2010). There has been varying success in applying this approach to determine relief histories accurately. Difficulties are often attributed to incomplete sampling of topography at multiple wavelengths, and the insensitivity of low-temperature thermochronometers to rapid topographic change and

high exhumation rates (Valla et al., 2010). Valla et al. (2010) explored the efficacy of estimating denudation rates and relief histories using the Pecube-NA inversion and the resolving power of the AFT and AHe low-temperature thermochronometers. They suggest that settings where relief development is approximately two to three times higher than background exhumation rates, or where background exhumation rates are generally low, as being more suitable for relief-change investigations.

6. Discussion and interpretation

The thermochronologic data suggest low background exhumation rates have been sustained over the past ~100 m.y., so here we test the sensitivity and resolving power of the Pecube-NA using a modest data subset in the western Hangay. We use representative values for crustal thickness, basal temperature, etc. for Mongolia (suppl. table S3) and our data input consists of replicate single grain AHe cooling ages and those reported in West et al., (2013). Inversion results are presented in figure 6 and listed in table 1 (run 1-C is in the supplement). We ran ~10,000 models for each inversion with a resampling rate between ~60-70% to obtain adequate convergence and sampling of the model space.

We ran a sensitivity test Pecube-NA inversion (suppl. fig. S3) to evaluate if exhumation rates and relief could be adequately constrained for the Hangay, where values for erosional timescale, relief amplitude, and exhumation rate timing were set and ran through a forward Pecube model to produce synthetic AHe and AFT cooling ages (using blanket 6% and 10% 2σ errors, respectively). These synthetic ages were then used as input in a Pecube inversion (results shown in table 1) to determine if the true values could

be recovered. The sensitivity test recovered the true parameter values and the overall misfit was very good, given the higher synthetic age errors. The higher chi-square misfit that is shown in Table 1 for the full inversions is higher due to a few ages producing bad fits at high elevations (~10% misfit) and because we used our real analytical age errors (~2-3%), which reduced the variance, i.e. made finding allowable model scenarios more difficult.

We report results for two inversions that simulate the last 150 Ma in the western Hangay (see figs. 7 and 8 for location), one (run 1-TSW) where the major exhumation phase timing is fixed using the thermal history of West et al. (2013) and the optimal basal temperature or thermal gradient is investigated, and the other (run 1-C) allows the end of the exhumation phase to be a free parameter (see supplementary material). The second model with the unrestricted exhumation phase was mainly for comparative purposes, as delayed or prolonged exhumation may have been possible in different parts of Mongolia during the end of the Mongol-Okhotsk orogeny in the Jurassic through the Cretaceous.

Table 1: Pecube-NA inversion results

Resolution sensitivity test				**Inversion Results**	
Free Inversion Parameter	**Units**	**Prior Range**	**Min. μ value**	**True value**	**Mean ± SD**
τ (erosional timescale)	Myr	0:1000	750.1	750	608 ± 260
Relief amplitude, *R*	-	0:1	0.50	0.5	0.57 ± 0.23
Exhumation change timing, E-timing	Myr	100:80	90.4	90	90.2 ± 5.5
Exhumation rate 1, E_1	km Myr^{-1}	-	-	0.1	-
Exhumation rate 2, E_2	km Myr^{-1}	-	-	0.03	-
Number of models	8512				
Lowest misfit, μ	1.8E-06				
Misfit type	χ^2				
Free parameters	3				
Models/Iterations	112/75				
Resample rate	68%				

Variables	**Run 1-TSW**	**Mean ± SD**	**Run 1-C**	**Mean ± SD**
Number of models	10224		9504	
Lowest misfit	1334.2		1325.5	
Misift type	χ^2		χ^2	
Number of Data	28		28	
τ	**930** (0:1000)	890.6 ± 110	**482** (0:1000)	491.7 ± 43
R	**1.58** (0:2)	1.62 ± 0.08	**1.24** (0:2)	1.20 ± 0.07
E-timing	130	-	**116.5** (130:100)	116.0 ± 1.1
E_1	**0.13** (0:0.8)	0.21 ± 0.09	**0.22** (0:0.5)	0.23 ± 0.03
E_2	**0.0071** (0:0.1)	0.0064 ± 0.0029	**0.0056** (0:0.1)	0.0078 ± 0.0046
Tb (basal temp, C)	**860.5** (600:950)	760.7 ± 92.8	850	
Time Step	1		1	
Run time (Ma)	150		150	
Free parameters	5		5	
Models/Iterations	144/70		144/65	
Resample Rate	63%		70%	

Table 1: Pecube-NA inversion results for sensitivity test and full inversions. Values separated by a colon are the prior search ranges during the NA sampling stage while those in bold are the best-fit parameter values (lowest misfit). Mean and standard deviation represent the resampling results from the NA appraisal of the model ensemble. See text and supplement for details.

Model inversion 1-TSW (fig. 6) shows paleo-relief greater than ~60% (1.62 ± 0.08) of the modern is required to explain the AHe ages. The evolution of relief is examined at the model start and how it has evolved since that time controlled by the τ (erosional/relief-change timescale) parameter. Relief amplitude and relief-change timescale are positively correlated and the large value for τ suggests exponentially rapid relief evolution following the main exhumation phase.

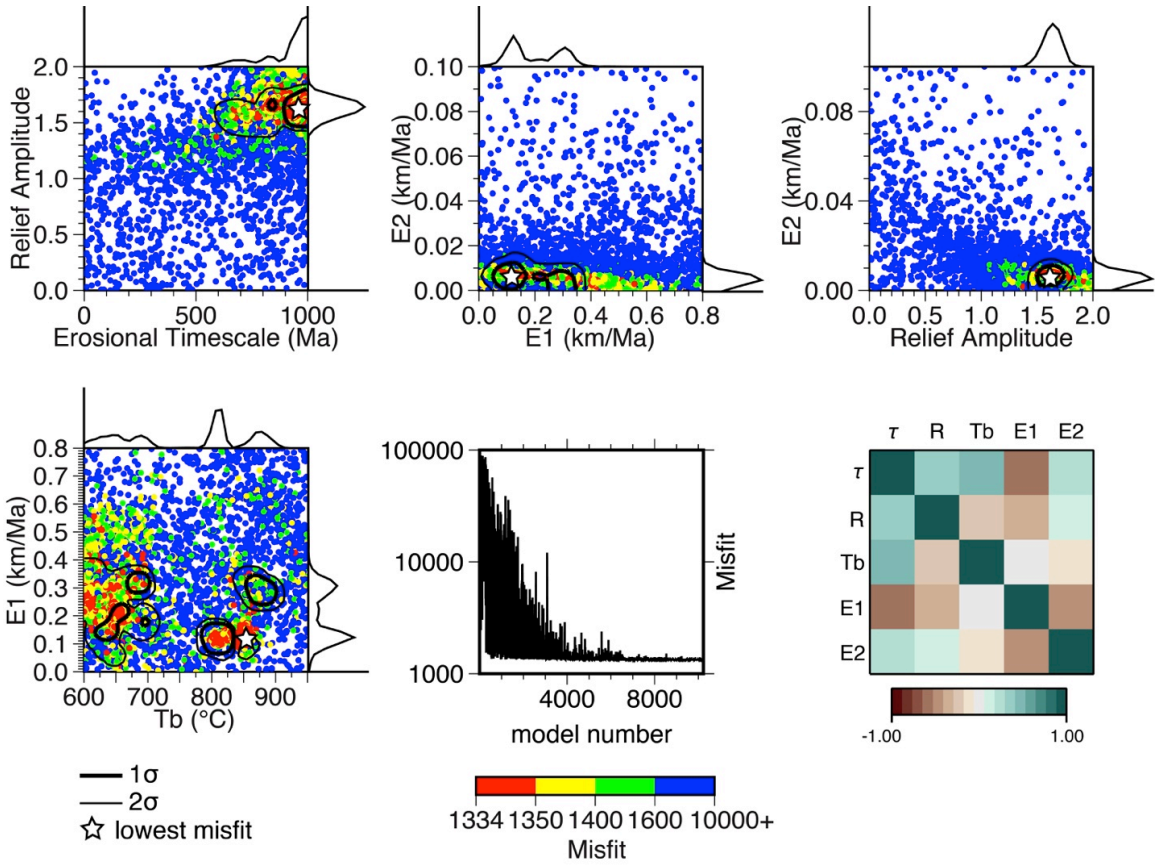


Figure 6: Pecube-NA inversion results for Run 1-TSW. Scatter plots are 2-D projections of the 5 dimensional parameter space on planes defined by combinations of two parameters. 1-D posterior curves show probability density within the parameter search range. See supplementary material for additional plots of other variables. Each dot represents a forward model from the inversion and is colored by the χ^2 misfit value. Stars denote the lowest misfit model while heavy/thin black lines are 1σ (67% confidence) and 2σ (95% confidence) errors, respectively. Bottom middle panel shows misfit evolution and convergence during the inversion and the bottom right shows the correlation matrix between difference parameters between -1 to +1 signifying strong (negative) anti-correlation or positive correlation, with values near zero having no relationship. Pecube physical modeling domain shown in fig. 7 and fig. 8 inset box, see text for discussion.

Inversion 1-C results are in good agreement with inversion 1-TSW, where the only difference is in the delayed timing in exhumation rate change at 116 Ma, which appropriately constrains the predicted relief reduction to be slightly lower. A two-stage exhumation scenario was applied for simplicity and because more complicated exhumation histories are unnecessary to explain the data. If exhumation is shorter in duration, i.e. 150 to 130 Ma versus 150 to ~115 Ma, the required paleo-relief is also

greater. Modeling results suggest exhumation was never extremely rapid during this time, on the order of ~100-200 m/Ma during the primary phase and very low since the Early Cretaceous at ≤10 m/Ma. The E1-E2 scatterplot shows that the secondary phase of exhumation is required to be very low at ~6 ± 3 m/Ma, regardless of what the E1 exhumation rate is. The geothermal gradient, which is controlled by the basal temperature of the crust, Tb, shows two distinct regions of either a cooler or hotter Moho temperature where neither has a relationship with E1, but anti-correlation exists between *R* and E2. The best-fit model has a basal temperature of 860°C, which is in agreement with local geochemical data (Ionov et al., 1998) and produces a geothermal gradient in agreement with paleo- and modern estimates of 15 and 21°C/km, respectively.

The misfit values reported for the full inversions are higher than the sensitivity inversion because the sensitivity test allowed much greater variance in the synthetic age uncertainties. The full inversions used the analytical error, which is typically ≤2 Ma. The observed versus predicted ages are very good, generally within 2%, with a few exceptions where the reported AHe age is slightly old (~10%) compared to the predicted age, which drove the misfit up. The reported multi-grain aliquot AHe data from West et al. (2013) were over-predicted and were the main contributors to the higher overall misfit values.

Observed versus predicted cooling ages are shown in figure 7 for inversion 1-TSW in the western Hangay. The major discrepancy in age agreement (higher associated misfit) lies between the West et al. (2013) multi-grain aliquot AHe ages and those modeled at high

elevations. This is likely due to the cooling age 'averaging' bias from using multiple grains, and in combination with the known scatter in slowly cooled samples, produces ages that do not adequately represent the 'true' single grain cooling ages. In this instance it seems that the West et al. (2013) ages are biased young in comparison to nearby samples from this study. This leads to the inability to predict the observed age accurately, given the other best-fit model conditions. The same can also be said for 'bad actor' apatites whose outlier pathologies are not readily explained by radiation damage and are potentially skewing ages older.

The elevation for the highest samples is also under-predicted which could be convolved with the errors associated with the age prediction itself or indicates that the predicted relief evolution is too simplistic and does not fully capture the nuanced topography. The latter may very well be the case since the relict planation surfaces represent fragments of topography that were never eroded and are thus difficult to reproduce numerically.

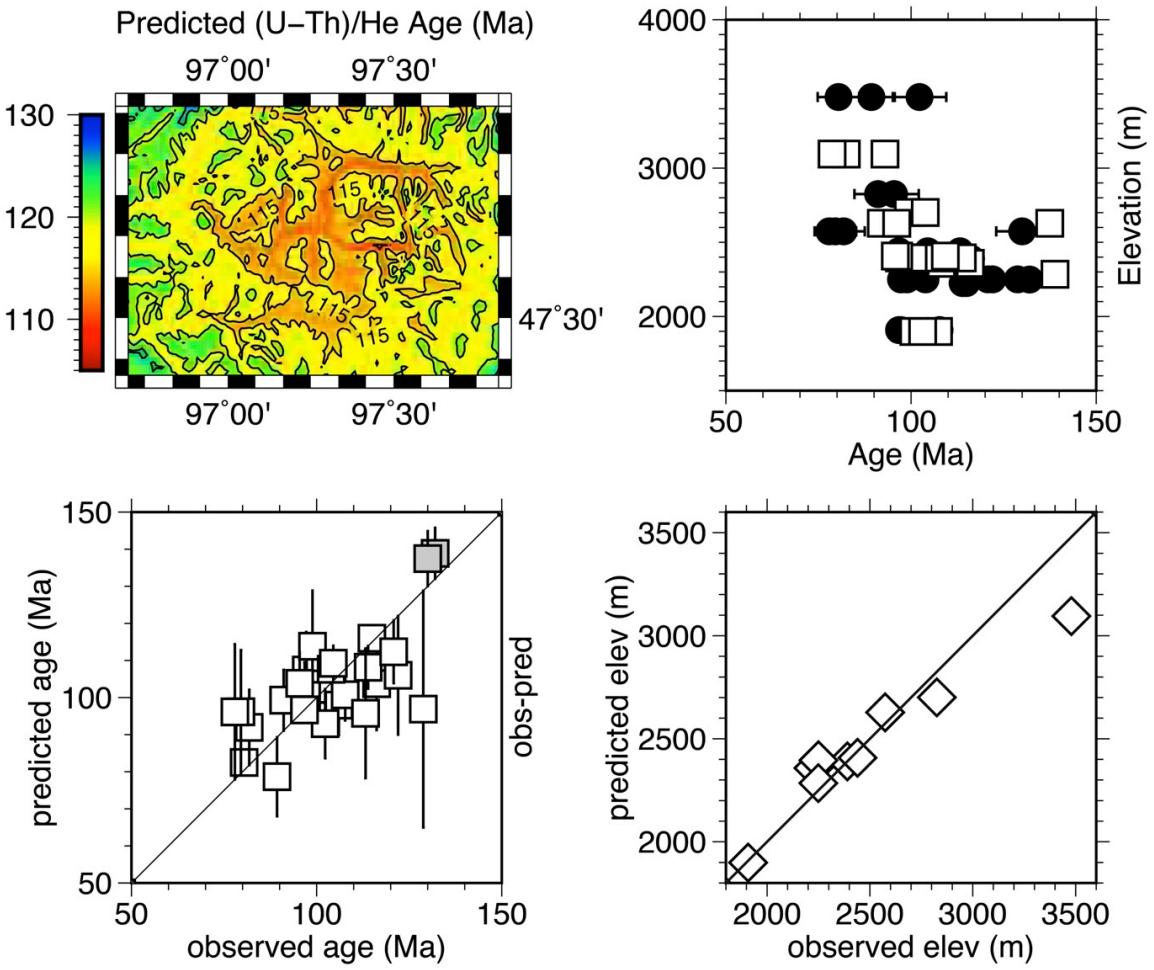


Figure 7: Top left: contoured age map (5 Ma interval) of Pecube-NA Run 1-TSW in the western Hangay (see fig. 8 for location, inset box). Top right: Observed and predicted cooling ages and corresponding elevations are in good agreement using the modeled best-fit or maximum likelihood inversion parameters, except mainly at the highest elevations. Black circles are observed single-grain age replicates with errors, while squares are predicted cooling ages. Bottom left: 1-to-1 line for predicted vs. observed cooling ages; gray squares are AFT samples. Second y-axis on the right plots lines showing the absolute difference between predicted ages that were better numerical fits to observed ages, and those that were not. Bottom right: observed versus predicted elevations.

An extrapolation of the model results in the western Hangay to the entire orogen can be seen in figure 8, where the optimum model parameters were fixed and forward modeled while incorporating observed replicate single grain AHe cooling ages from across the Hangay. The models were resampled at the 10 km length scale to smooth age patterns and contoured to permit more general comparisons of regional spatial patterns. All of the

model parameters were fixed using the lowest misfit values of inversion 1-TSW, except the effective elastic thickness, to examine the influence on model cooling ages. The best-fit model using a Te of 6.1 km from Bayasgalan et al. (2005) is shown in the upper right and the other panels show results using elastic thicknesses of 0 (local isostasy), 15, and 20 km. Local isostasy (Te = 0) produces uniform predicted ages across the Hangay, closely following the topography but with less age variation in the broad sense. Increasing Te yields a concentric 'bulls-eye' pattern of increasing cooling ages away from the range center with less topographic adherence. For comparison, a model of steady-state topography employing the best-fit exhumation rates shows expected age uniformity across the entire region and ages consistently older than those under relief-loss conditions. However, a steady-state topography model would likely require a slightly different exhumation history than the prescribed best-fit history of the inversion. The overall misfits for each model are fairly similar and fit the data within analytical error (reduced chi-squared misfit 0.8-0.9), demonstrating that varying Te has little effect on the match between observed and predicted ages for low exhumation rates. However, at the orogen-scale an elastic thickness of 20 km yields a marginally better misfit compared to the other models, which agrees with the findings of Bayasgalan et al. (2005) that the strength of the lithosphere increases away from the central Hangay.

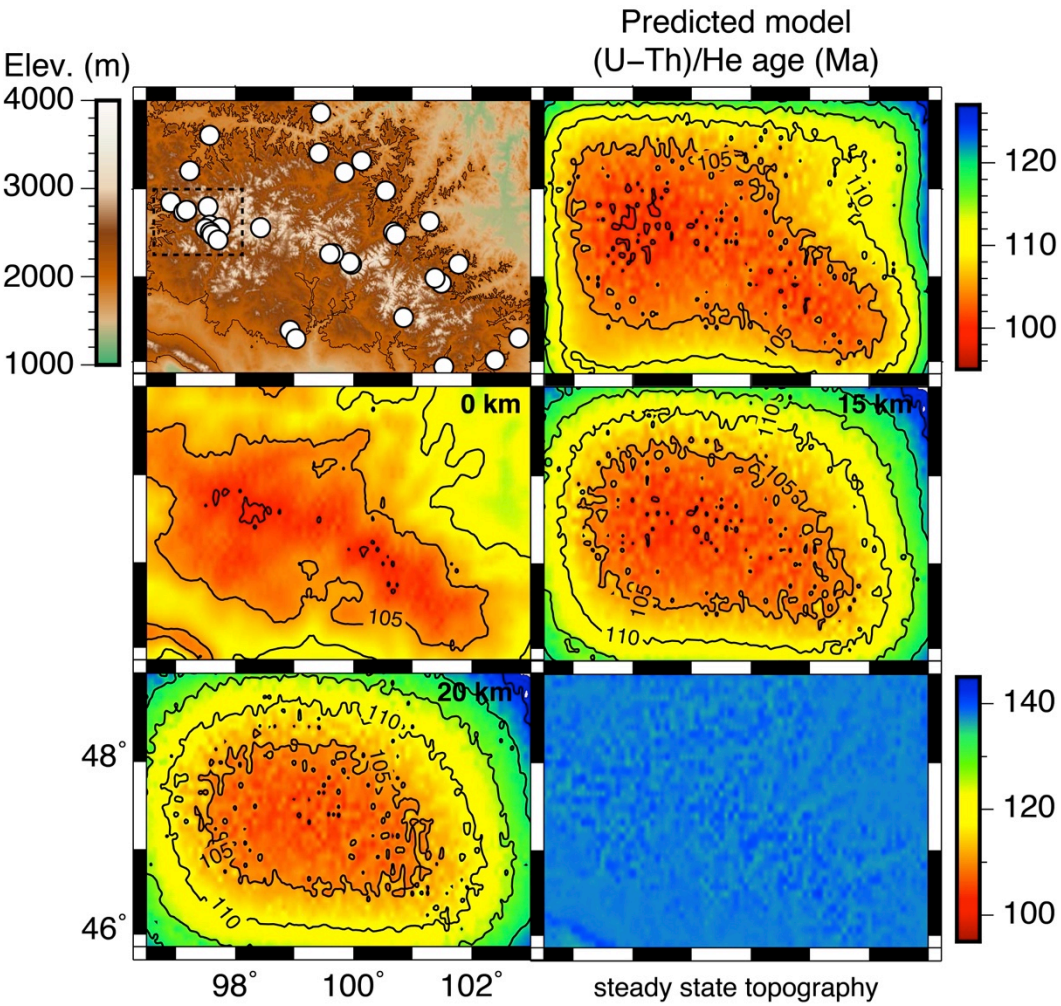


Figure 8: Pecube forward model age predictions using inversion run 1-TSW best-fit parameter values with the main exhumation stage from 150-130 Ma after West et al. (2013) thermal history model. Inset box shows location of western Hangay bounds used in Pecube-NA inversion. Regional forward models are resampled at 10 km to smooth ages and are shown with a 5 Ma contour interval. (Top left) Elevations from 90m SRTM DEM (2000 m elev. contoured) with white dots showing sample locations used in Pecube modeling of the entire Hangay, (top right) the ages predicted by the best-fit model results of inversion 1-TSW shown in table 1 (Te = 6.1 km). Other panels show the effects of varying the effective elastic thickness (Te) while holding all other best-fit variables constant. Note the age scale change for the steady-state topography model.

Some first-order assumptions about the regional relief history of the Hangay can be made. Apatite helium cooling ages from this study indicate regional Mesozoic cooling based on spatial relationships across central Mongolia. Relief lowering can expose younger ages at high peaks while valley bottoms are older, producing an orogen-scale

inverted age-elevation relationship but maintaining valley-scale positive age-elevation relationships. The steep trend of the positive age-elevation relationship also suggests a smaller elastic-plate thickness. This behavior has been documented in old, post-orogenic mountains in other regions of central Asia with similar exhumation histories, such as the Dabie Shan. This is observed in the Hangay as well, where cooling ages are generally uniform in the mountain core, while off the higher topography and into the surrounding lower elevations ages are slightly older.

The regional bedrock cooling age trends and the detrital data point to relief reduction following the last major tectonic event in the Late Jurassic-Early Cretaceous. Cooling-age patterns are explained by preferential exposure of younger rocks at higher elevations through summit relief lowering from isostatically-enhanced erosion of the Hangay Mountains during the initial post-orogenic phase in the Cretaceous. One could argue that instead of relief lowering, recent surface uplift accompanied by some amount of erosion could produce similar age patterns. There is no evidence to support a Cenozoic history involving accelerated, high magnitude erosion of the Hangay. Moderately higher erosion rates are only found in isolated glacial valleys.

7. Conclusions

The tectonic reorganization during the early to mid-Mesozoic resulted in the suturing of Mongolia and collision with the Siberian craton. This tectonism created the high mountains in central Mongolia, which were then rapidly eroded through the Cretaceous, which remained as an erosional remnant landscape throughout the Cenozoic. Detrital

cooling age erosional proxies agree to first-order with thermo-kinematic models and indicate extended low erosion since the end Mesozoic and that Jurassic-Early Cretaceous paleo-relief was greater than the present. Exhumation rates estimated from Pecube inversions suggest a period of moderate exhumation in the Early Cretaceous followed by low rates of ~10 m/Ma since that time. This history agrees with shorter-term cosmogenic estimates of erosion and implies that the Hangay have been subject to a long regime of very slow erosion, similar to other old orogenic landscapes, such as the Appalachians in the eastern USA. The high topography of the Hangay has experienced some degree of recent enhanced erosion in the form of recent alpine glaciation, but it has been fairly minimal in amount and regional extent.

The collapse of the Mongol-Okhotsk orogeny in the Cretaceous and synchronous rapid relief reduction produced the observed pattern of progressively older cooling ages away from the highest topography of the Hangay. The magnitude of relief loss in the model inversions is highly correlated with the timing of the shift to very low exhumation rates, with a more extended high-rate period, i.e. delayed exhumation rate change, requiring less relief loss. Relief has presumably been stable throughout the Cenozoic due to high aridity, with a modest amount of surface uplift probably occurring in the Oligocene-Miocene. Holding the current landscape geometry fixed through time, the current approximated mountain relief compared to background elevations outside of the Hangay is on the order of 2500 m, which would be approaching 4000 m in the Mesozoic using the modeled paleo-relief. An approximate 50-60% addition to the modern relief would produce ancient elevations in the Hangay approaching 6000 m at the highest peaks,

roughly on par with the modern Tian Shan to the southwest (see supplement for location). This mountain belt is an excellent example of a relict erosional landscape and demonstrates that mature topography can endure for prolonged periods when there is little forcing from tectonics, climate, or surface processes.

Acknowledgements

The authors thank Frédéric Herman and David Whipp for discussions and for supplying various bits of code. Jean Braun and Malcolm Sambridge for conversations about Pecube and the Neighborhood Algorithm. Thanks to Matthew Fox for Pecube and inverse detrital modeling assistance. We would also like to thank Alex Pacheco of Lehigh University HPC for support with the Corona computing cluster where preliminary inversions were performed. Final inversions were run through XSEDE and the SDSC Gordon/Comet clusters and the UT-Austin TACC Stampede cluster. This study was part of McDannell's Ph.D. research and was supported by a grant from the National Science Foundation CD program grant EAR-1009702.

References

Ancuta, L., Carlson, R., Idleman, B., Zeitler, P., 2012. Volcanic stratigraphy, 40Ar/39Ar Geochronology and Geochemistry of Hangay Dome Volcanic Rocks, Central Mongolia, AGU Fall Meeting Abstracts, pp. 2586.

Baldwin, J.A., Whipple, K.X., Tucker, G.E., 2003. Implications of the shear stress river incision model for the timescale of postorogenic decay of topography. Journal of Geophysical Research: Solid Earth (1978–2012), 108(B3).

Bayasgalan, A., Jackson, J., McKenzie, D., 2005. Lithosphere rheology and active tectonics in Mongolia: relations between earthquake source parameters, gravity and GPS measurements. Geophysical Journal International, 163(3): 1151-1179.

Braun, J., 2002. Quantifying the effect of recent relief changes on age-elevation relationships. Earth and Planetary Science Letters, 200(3-4): 331-343.

Braun, J., 2003. Pecube: a new finite-element code to solve the 3D heat transport equation including the effects of a time-varying, finite amplitude surface topography. Computers & Geosciences, 29(6): 787-794.

Braun, J., Robert, X., 2005. Constraints on the rate of post-orogenic erosional decay from low-temperature thermochronological data: application to the Dabie Shan, China. Earth Surface Processes and Landforms, 30(9): 1203-1225.

Brewer, I., Burbank, D., Hodges, K., 2003. Modelling detrital cooling-age populations: Insights from two Himalayan catchments. Basin Research, 15(3): 305-320.

Brocklehurst, S.H., Whipple, K.X., 2004. Hypsometry of glaciated landscapes. Earth Surface Processes and Landforms, 29(7): 907-926.

Cai, K. et al., 2015. A synthesis of zircon U–Pb ages and Hf isotopic compositions of granitoids from Southwest Mongolia: Implications for crustal nature and tectonic evolution of the Altai Superterrane. Lithos, 232: 131-142.

Caves, J.K., Sjostrom, D.J., Mix, H.T., Winnick, M.J., Chamberlain, C.P., 2014. Aridification of Central Asia and uplift of the Altai and Hangay Mountains, Mongolia: Stable isotope evidence. American Journal of Science, 314(8): 1171-1201.

Chen, M., Niu, F., Liu, Q., Tromp, J., 2015. Mantle-driven uplift of Hangai Dome: New seismic constraints from adjoint tomography. Geophysical Research Letters, 42(17): 6967-6974.

Cogné, J.-P., Kravchinsky, V.A., Halim, N., Hankard, F., 2005. Late Jurassic-Early Cretaceous closure of the Mongol-Okhotsk Ocean demonstrated by new Mesozoic palaeomagnetic results from the Trans-Baikal area (SE Siberia). Geophysical Journal International, 163(2): 813-832.

Cunningham, W.D., 2001. Cenozoic normal faulting and regional doming in the southern Hangay region, Central Mongolia: implications for the origin of the Baikal rift province. Tectonophysics, 331(4): 389-411.

De Grave, J. et al., 2009. Multi-method chronometry of the Teletskoye graben and its basement, Siberian Altai Mountains: new insights on its thermo-tectonic evolution. Geological Society, London, Special Publications, 324(1): 237-259.

Fischer, K.M., 2002. Waning buoyancy in the crustal roots of old mountains. Nature, 417(6892): 933-936.

Glorie, S., De Grave, J., 2016. Exhuming the Meso–Cenozoic Kyrgyz Tianshan and Siberian Altai-Sayan: A review based on low-temperature thermochronology. Geoscience Frontiers, 7(2): 155-170.
Glotzbach, C., Van Der Beek, P.A. and Spiegel, C. (2011) Episodic exhumation and relief growth in the Mont Blanc massif, Western Alps from numerical modelling of thermochronology data. Earth and Planetary Science Letters 304, 417-430.
Hendrix, M.S. et al., 1992. Sedimentary record and climatic implications of recurrent deformation in the Tian Shan: Evidence from Mesozoic strata of the north Tarim, south Junggar, and Turpan basins, northwest China. Geological Society of America Bulletin, 104(1): 53-79.
Hopkins, C.E., 2012. Beryllium-10 derived erosion rates from the Hangay Mountains, Mongolia: landscape evolution in a periglacially-dominated continental interior, Georgia Institute of Technology, 48 pp.
Ionov, D.A., O'Reilly, S.Y., Griffin, W.L., 1998. A geotherm and lithospheric section for central Mongolia (Tariat region). Mantle dynamics and plate interactions in East Asia: 127-153.
Jasra, A., Stephens, D., Gallagher, K., Holmes, C., 2006. Analysis of geochronological data with measurement error using Bayesian mixtures. Mathematical Geology, 38(3): 269-300.
Johnson, C. et al., 2015. Subsurface evidence for late Mesozoic extension in western Mongolia: tectonic and petroleum systems implications. Basin Research, 27(3): 272-294.
Jolivet, M. et al., 2013. Geomorphic Mesozoic and Cenozoic evolution in the Oka-Jombolok region (East Sayan ranges, Siberia). Journal of Asian Earth Sciences, 62: 117-133.
Jolivet, M. et al., 2015. The Upper Jurassic–Lower Cretaceous alluvial-fan deposits of the Kalaza Formation (Central Asia): tectonic pulse or increased aridity? Geological Society, London, Special Publications, 427: SP427. 6.
Jolivet, M. et al., 2009. How old is the Baikal Rift Zone? Insight from apatite fission track thermochronology. Tectonics, 28(3).
Jolivet, M. et al., 2007. Mongolian summits: an uplifted, flat, old but still preserved erosion surface. Geology, 35(10): 871-874.
Koppes, M.N., Montgomery, D.R., 2009. The relative efficacy of fluvial and glacial erosion over modern to orogenic timescales. Nature Geoscience, 2(9): 644-647.
Landman, R.L., 2007. Petrologic constraints on the sources of granites from the Hangay Mountains, central Mongolia, Amherst College, 73 pp.
Lehmkuhl, F., Klinge, M., Stauch, G., 2004. The extent of Late Pleistocene glaciations in the Altai and Khangai Mountains. In: Ehlers, J., Gibbard, P.L. (Eds.), Developments in Quaternary Sciences. Elsevier, pp. 243-254.
Logachev, N.A., Devyatkin, E.V., Malaeva, E.M., al., e., 1982. Cenozoic Deposits in the Taryat Basin and in the Chulutu R. Valley, Central Khangai. Izv. AN SSSR. Ser. Geol., no. 8: 76-86.
Matmon, A. et al., 2003. Temporally and spatially uniform rates of erosion in the southern Appalachian Great Smoky Mountains. Geology, 31(2): 155-158.
McKeon, R.E., Zeitler, P.K., Pazzaglia, F.J., Idleman, B.D., Enkelmann, E., 2014. Decay of an old orogen: Inferences about Appalachian landscape evolution from low-

temperature thermochronology. Geological Society of America Bulletin, 126(1-2): 31-46.
Molnar, P., Boos, W.R., Battisti, D.S., 2010. Orographic controls on climate and paleoclimate of Asia: thermal and mechanical roles for the Tibetan Plateau. Annual Review of Earth and Planetary Sciences, 38(1): 77.
Molnar, P., England, P., 1990. Late Cenozoic uplift of mountain ranges and global climate change: chicken or egg? Nature, 346(6279): 29-34.
Molnar, P., Tapponnier, P., 1975. Cenozoic tectonics of Asia: effects of a continental collision. Science, 189(4201): 419-426.
Montgomery, D.R., Brandon, M.T., 2002. Topographic controls on erosion rates in tectonically active mountain ranges. Earth and Planetary Science Letters, 201(3): 481-489.
Petit, C., Deverchere, J., Calais, E., San'kov, V. and Fairhead, D. (2002) Deep structure and mechanical behavior of the lithosphere in the Hangai-Hovsgol region, Mongolia: new constraints from gravity modeling. Earth and Planetary Science Letters 197, 133-149.
Petit, C., Tiberi, C., Deschamps, A., Déverchere, J., 2008. Teleseismic traveltimes, topography and the lithospheric structure across central Mongolia. Geophysical Research Letters, 35(11).
Reiners, P.W. et al., 2003. Post-orogenic evolution of the Dabie Shan, eastern China, from (U-Th)/He and fission-track thermochronology. American Journal of Science, 303(6): 489-518.
Ruhl, K.W., Hodges, K.V., 2005. The use of detrital mineral cooling ages to evaluate steady state assumptions in active orogens: An example from the central Nepalese Himalaya. Tectonics, 24(4): TC4015.
Sahagian, D., Proussevitch, A., Ancuta, L.D., Idleman, B.D., Zeitler, P.K., 2016. Uplift of Central Mongolia Recorded in Vesicular Basalts. The Journal of Geology, 124(4): 435-445.
Sambridge, M., 1999a. Geophysical inversion with a neighbourhood algorithm—I. Searching a parameter space. Geophysical Journal International, 138(2): 479-494.
Sambridge, M., 1999b. Geophysical inversion with a neighbourhood algorithm—II. Appraising the ensemble. Geophysical Journal International, 138(3): 727-746.
Smith, S.G., Wegmann, K.W., Ancuta, L.D., Gosse, J.C., Hopkins, C.E., 2016. Paleotopography and erosion rates in the central Hangay Dome, Mongolia: Landscape evolution since the mid-Miocene. Journal of Asian Earth Sciences, 125: 37-57.
Stock, G.M., Ehlers, T.A., Farley, K.A., 2006. Where does sediment come from? Quantifying catchment erosion with detrital apatite (U-Th)/He thermochronometry. Geology, 34(9): 725-728.
Stock, J.D., Montgomery, D.R., 1996. Estimating palaeorelief from detrital mineral age ranges. Basin Research, 8(3): 317-327.
Stosch, H.G., Ionov, D.A., Puchtel, I.S., Galer, S.J.G. and Sharpouri, A. (1995) Lower crustal xenoliths from Mongolia and their bearing on the nature of the deep crust beneath central Asia. Lithos 36, 227-242.

Tiberi, C. et al., 2008. Asthenospheric imprints on the lithosphere in Central Mongolia and Southern Siberia from a joint inversion of gravity and seismology (MOBAL experiment). Geophysical Journal International, 175(3): 1283-1297.
Valla, P.G., Herman, F., van der Beek, P.A., Braun, J., 2010. Inversion of thermochronological age-elevation profiles to extract independent estimates of denudation and relief history — I: Theory and conceptual model. Earth and Planetary Science Letters, 295(3-4): 511-522.
van der Beek, P., Delvaux, D., Andriessen, P., Levi, K., 1996. Early Cretaceous denudation related to convergent tectonics in the Baikal region, SE Siberia. Journal of the Geological Society, 153(4): 515-523.
van der Beek, P.A. et al., 2010. Inversion of thermochronological age–elevation profiles to extract independent estimates of denudation and relief history — II: Application to the French Western Alps. Earth and Planetary Science Letters, 296(1–2): 9-22.
Van der Voo, R., van Hinsbergen, D.J.J., Domeier, M., Spakman, W., Torsvik, T.H., 2015. Latest Jurassic–earliest Cretaceous closure of the Mongol-Okhotsk Ocean: A paleomagnetic and seismological-tomographic analysis. Geological Society of America Special Papers, 513.
Vassallo, R. et al., 2007. Uplift age and rates of the Gurvan Bogd system (Gobi-Altay) by apatite fission track analysis. Earth and Planetary Science Letters, 259(3,Äì4): 333-346.
Vermeesch, P., 2012. On the visualisation of detrital age distributions. Chemical Geology, 312: 190-194.
West, A.J. et al., 2013. Links between climate, erosion, uplift, and topography during intracontinental mountain building of the Hangay Dome, Mongolia. Geochemistry, Geophysics, Geosystems, 14(12): 5171-5193.
Whipp, D., Ehlers, T., Braun, J., Spath, C., 2009. Effects of exhumation kinematics and topographic evolution on detrital thermochronometer data. Journal of Geophysical Research: Earth Surface, 114(F4).
Windley, B.F., Alexeiev, D., Xiao, W., Kröner, A., Badarch, G., 2007. Tectonic models for accretion of the Central Asian Orogenic Belt. Journal of the Geological Society, 164(1): 31-47.
Windley, B.F., Allen, M.B., 1993. Mongolian plateau: Evidence for a late Cenozoic mantle plume under central Asia. Geology, 21(4): 295-298.
Yang, Y.-T., Guo, Z.-X., Song, C.-C., Li, X.-B., He, S., 2014. A short-lived but significant Mongol–Okhotsk collisional orogeny in latest Jurassic–earliest Cretaceous. Gondwana Research.
Yanovskaya, T., Kozhevnikov, V., 2003. 3D S-wave velocity pattern in the upper mantle beneath the continent of Asia from Rayleigh wave data. Physics of the Earth and Planetary Interiors, 138(3): 263-278.
Yarmolyuk, V. et al., 2008. The age of the Khangai batholith and the problem of batholith formation in Central Asia. Doklady Earth Sciences, 423(1): 1223-1228.
Zeitler, P.K. et al., 2001. Erosion, Himalayan geodynamics, and the geomorphology of metamorphism. GSA Today, 11(1): 4-9.
Zorin, Y.A., 1999. Geodynamics of the western part of the Mongolia-Okhotsk collisional belt, Trans-Baikal region (Russia) and Mongolia. Tectonophysics, 306(1): 33-56.

Appendix A1: Methodology – (U-Th)/He thermochronology

Igneous bedrock samples went through standard procedures for rock crushing, sieving (<250 microns), Frantz magnetic splitting, and heavy-liquid separation using lithium polytungstate and methylene iodide. Unbroken, symmetric apatite grains without visible inclusions were selected under a high-power petrographic microscope. Samples were digitally photographed in order to record their 3D morphology for determination of alpha-correction factors using a cylindrical geometry. Note: the use of spherical or cylindrical geometry will generate differences in the calculated eU (Flowers et al., 2009) due to volumetric and U-Th concentration considerations. Grains were then placed in small Nb tubes whose ends were crimped and loaded into the extraction system in the Lehigh University noble gas geochronology lab. ^{4}He and the ^{3}He spike were measured using a Balzers bakeable quadrupole mass spectrometer designed for UHV operation, fitted with both Faraday and electron-multiplier detectors, providing a wide dynamic range. For helium extraction, a double-vacuum resistance furnace was used for heating, and an all-metal sample dropper permits multiple samples to be loaded for sequential analysis in the resistance furnace. Helium evolved from heated samples was purified in an all-metal extraction line pumped by an ion pump during routine operation as well as a 70 l/s turbo-molecular pump with a small rotary backing pump used during bake-out. An SAES getter in the extraction line removes active gases, while a smaller SAES getter in the mass spectrometer volume is used to minimize hydrogen loads. Reservoirs containing a ^{3}He spike and a ^{4}He/^{3}He standard are attached to the line behind all-metal pipettes while two temperature-stabilized capacitance manometers provide the precise, accurate

pressure measurements needed for spike preparation (the extraction line ^{4}He blank is $1x10^{-16}$ moles or less).

^{4}He was measured by isotope dilution, using a ^{3}He spike, and also by manometric peak-height comparison against a mass-discrimination standard. Generally these approaches agree to better than 1% and the dual calibrations provide an internal crosscheck. Over periods spanning the analysis of sample batches, the $^{4}He/^{3}He$ ratio for the standard was precise to within 0.3%, with a value of about 0.795 (the true $^{4}He/^{3}He$ ratio of standard is 1.000). For the current spike preparation, the size of a typical spike is 4×10^{-13} moles.

Following helium extraction, U, Th, and Sm measurements were obtained from the University of Arizona in the laboratory operated by Dr. Peter Reiners, where samples were dissolved, spiked, and analyzed using isotope-dilution ICP-MS. U, Th, and Sm were measured on the same aliquots of apatite that were used for He determinations, eliminating any uncertainties contributed by weighing errors and sample heterogeneity.

A mean age of 31.85 ± 0.24 Ma (2 SE, n = 78) has been acquired for the Durango apatite age standard over repeated experiments in the LU laboratory. McDowell et al. (2005) obtained a direct (U-Th)/He age of 31.13 ± 0.42 (2 SE). Commonly, a 5-7% (2σ) error is applied to helium ages based on the pooled long-term reproducibility of the Durango apatite standard and additional uncertainties associated with the alpha-ejection correction factor applied to unknowns.

Appendix A2: Coupled Pecube-Neighborhood Algorithm modeling

The conventional volume diffusion model of Farley (2000) has typically been used for apatite age prediction, and in the case of grains with low (<20-30 ppm) effective uranium (eU) content, (Flowers et al., 2009) and/or rapid cooling this model is satisfactory and does not require more sophisticated age prediction models that account for compositional or radiation damage effects, e.g. (Flowers et al., 2009; Gautheron et al., 2009). Since the last major tectonic event in the Cretaceous, Hangay rocks have resided in the uppermost few kilometers of the crust, placing them at the lower-temperature end of the He partial retention zone (HePRZ). Since radiation damage tends to suppress partial He loss, the closure temperature varies in proportion to the eU and cooling rate, thus contributing to the observed apatite cooling age dispersion commonly seen in slowly cooled settings. The Flowers et al. (2009) radiation damage model was incorporated for age prediction within Pecube for modeling of our Mongolia data. Pecube and previous applications are reviewed thoroughly in Braun et al. (2012). Here we summarize some of the main features relevant to this study.

The sampling stage has typically been performed iteratively but here we use the MPI-enabled parallelized version of the code that does away with 'formal iterations' and instead of the misfit being assessed at the end of an iteration, it is continuously assessed during the inversion, leading to more efficient algorithm performance (Rickwood and Sambridge, 2006). The number of iterations, the number of models in each iteration step, and the resampling rate all control the NA-sampler stage and influence the NA search. Although there are no specific rules for these configurations, a lower resampling rate

allows faster convergence, albeit with the danger of prematurely converging on local minima, while a greater resampling rate allows more thorough exploration of the ensemble space but is slower to converge. Generally, inversions with a greater number of free parameters require a larger number of iterations to fully converge on the lowest misfit.

In the case of χ^2 misfit, the simplified form of the *log (L)* is equal to -0.5 multiplied by the misfit value (Glotzbach et al., 2011). The motivation for examining individual model misfit during the appraisal stage is that the lowest misfit can be misleading, for example, the lowest misfit may be identified for an individual parameter, but in the multi-dimensional case the overall misfit is a combination of several parameters where the identified best fit may have a single parameter value that is associated with a large misfit due to trade-offs in multi-dimensional space. Posterior probability accounts for this, although it is a function of all parameters, it may be integrated over one or more parameters to examine the best estimate of that parameter independent of the others in the form of a 1-D marginal PPDF curve. Parameters plotted as 2-D marginals examine potential correlative tradeoffs between different parameters. In the case of a purely Gaussian PDF the results can be interpreted as a mean/mode value at the peak maximum, and in the case of a skewed PDF, the mode is at the maximum probability peak of the PPDF curve.

The relief amplitude, *R,* in Pecube is fairly simplistic as it assumes the planform geometry of the topography does not change, only the amplitude varies, i.e. valleys and

ridges do not migrate laterally, (Valla et al., 2010; van der Beek et al., 2010). This assumption is justified in equilibrated landscapes with low erosion. R is defined as the ratio between the relief amplitude (Δh_i) when rocks passed through the closure isotherms and the modern-day relief amplitude (Δh_0). Where:

$$R = \frac{\Delta h_i}{\Delta h_0}$$

According to the model definition, when $R = 0$ the initial topography is a plateau (no relief); for $R < 1$ relief has grown from the past to present; while for $R > 1$ relief has decreased from past to present (Beucher et al., 2012; Valla et al., 2010). The relief-change or erosional timescale, τ, is a function that describes how relief evolves through time, either in an exponential or linear fashion, where 0 is a linear change in relief in the model (see below). When values are highly positive, relief change will take place rapidly at the model onset, and if τ is highly negative the relief change will take place close to present day (Beucher et al., 2012).

$$\Delta h_t = \Delta h_0 + \left[(R-1)\Delta h_0 \frac{1-e^{\left(-\frac{t\tau}{t_f{}^2}\right)}}{1-e^{\left(-\frac{\tau}{t_f}\right)}} \right]$$

Appendix A3: Inversion resolution tests

We initially tested whether moderate relief change could be adequately modeled in a slow exhumation setting using the Pecube-NA. We set background exhumation rates from exhumation phase, E1, from 180-90 Ma at 0.1 km/Ma and a second slower phase, E2, from 90-0 Ma at 0.03 km/Ma. The relief amplitude (R) is set to 0.5 (50% of modern relief), and the erosional timescale, τ, to 750 Ma. These variables are fixed and a Pecube forward model predicts model AHe and AFT cooling ages output at the same locations as observed data applying 7% AHe and 10% AFT age errors. The model ages and respective errors are then supplied back into two NA inversions, one where the relief amplitude is the only free parameter varying between 0-2, and the other with τ, R, and the timing of exhumation rate change (E-timing) set free. This second test is to examine the ability to identify the true parameter values and any tradeoff effects. The second resolution test initially allowed E1 and E2 as free parameters but in later inversions the background exhumation rates were fixed because in all initial tests the "true" rates were quickly identified.

The relief-only sensitivity test inversion was set to run for >6000 total models with 96 models in an initial iteration and 96 models in each subsequent iteration with a 96% resampling rate. Convergence on the true value of R = 0.5 was found within a few hundred models but the algorithm was allowed to run to ~850 models before the run was stopped due to adequate convergence. This result verifies that in the case of well-known thermo-kinematic parameters and high quality thermochronometric data, relief growth in

a post-orogenic setting can be resolved accurately to within <2% in a short number of iterations, in this example the best 50 models resulted in an R = 0.49 ± 0.02 (1σ).

The resolution test inversion for τ, R, and E-timing was run with an initial and subsequent pool of 112 models over 75 iterations with a 68% resampling rate for a total of 8504 models (fig. 7). The lowest misfit values matched the true values very accurately, suggesting the absence of synthetic noise in the resolution test. The model appraisal shows that relief amplitude and E-timing were well resolved with a mode and standard deviation of 0.57 ± 0.23 for *R* and mean of 90.2 ± 5.5 Ma, respectively. The relief-change timescale showed considerable scatter but was within one standard deviation of the true value. Trade-offs between parameter combinations can be seen in supplementary figure S2-C. Under fixed exhumation rates, relief amplitude decreases non-linearly as the relief-change timescale increases, while the timing of exhumation rate change is positively correlated with both relief amplitude and relief-change timescale.

Appendix A: References

Beucher, R., Beek, P., Braun, J., Batt, G.E., 2012. Exhumation and relief development in the Pelvoux and Dora-Maira massifs (western Alps) assessed by spectral analysis and inversion of thermochronological age transects. Journal of Geophysical Research: Earth Surface, 117(F3).

Braun, J. et al., 2012. Quantifying rates of landscape evolution and tectonic processes by thermochronology and numerical modeling of crustal heat transport using PECUBE. Tectonophysics, 524-525: 1-28.

Farley, K.A., 2000. Helium diffusion from apatite; general behavior as illustrated by Durango fluorapatite. Journal of Geophysical Research, 105(B2): 2903-2914.

Flowers, R.M., Ketcham, R.A., Shuster, D.L., Farley, K.A., 2009. Apatite (U–Th)/He thermochronometry using a radiation damage accumulation and annealing model. Geochimica et Cosmochimica Acta, 73(8): 2347-2365.

Gautheron, C., Tassan-Got, L., Barbarand, J., Pagel, M., 2009. Effect of alpha-damage annealing on apatite (U–Th)/He thermochronology. Chemical Geology, 266(3): 157-170.

Glotzbach, C., Van Der Beek, P.A., Spiegel, C., 2011. Episodic exhumation and relief growth in the Mont Blanc massif, Western Alps from numerical modelling of thermochronology data. Earth and Planetary Science Letters, 304(3): 417-430.

Idleman, B.D., Zeitler, P.K., 2014. Rapid characterization of noble-gas kinetics using continuous heating and gas accumulation, 14th International Conference on Thermochronology, Chamonix, France.

Lysak, S., Dorofeeva, R., 2003. Thermal state of lithosphere in Mongolia. Russ. Geol. Geophys 44, 893-903.

McDowell, F.W., McIntosh, W.C., Farley, K.A., 2005. A precise 40 Ar–39 Ar reference age for the Durango apatite (U–Th)/He and fission-track dating standard. Chemical Geology, 214(3): 249-263.

Rickwood, P., Sambridge, M., 2006. Efficient parallel inversion using the Neighbourhood Algorithm. Geochemistry, Geophysics, Geosystems, 7(11).

Stachnik, J.C., Meltzer, A., Souza, S., Munkhuu, U., Tsaagan, B., Russo, R.M., 2014. Lithospheric Structure Beneath the Hangay Dome, Central Mongolia, American Geophysical Union. AGU T21A-4555, San Francisco.

Valla, P.G., Herman, F., van der Beek, P.A., Braun, J., 2010. Inversion of thermochronological age-elevation profiles to extract independent estimates of denudation and relief history — I: Theory and conceptual model. Earth and Planetary Science Letters, 295(3-4): 511-522.

van der Beek, P.A. et al., 2010. Inversion of thermochronological age–elevation profiles to extract independent estimates of denudation and relief history — II: Application to the French Western Alps. Earth and Planetary Science Letters, 296(1–2): 9-22.

Appendix B: Supplementary figures and tables

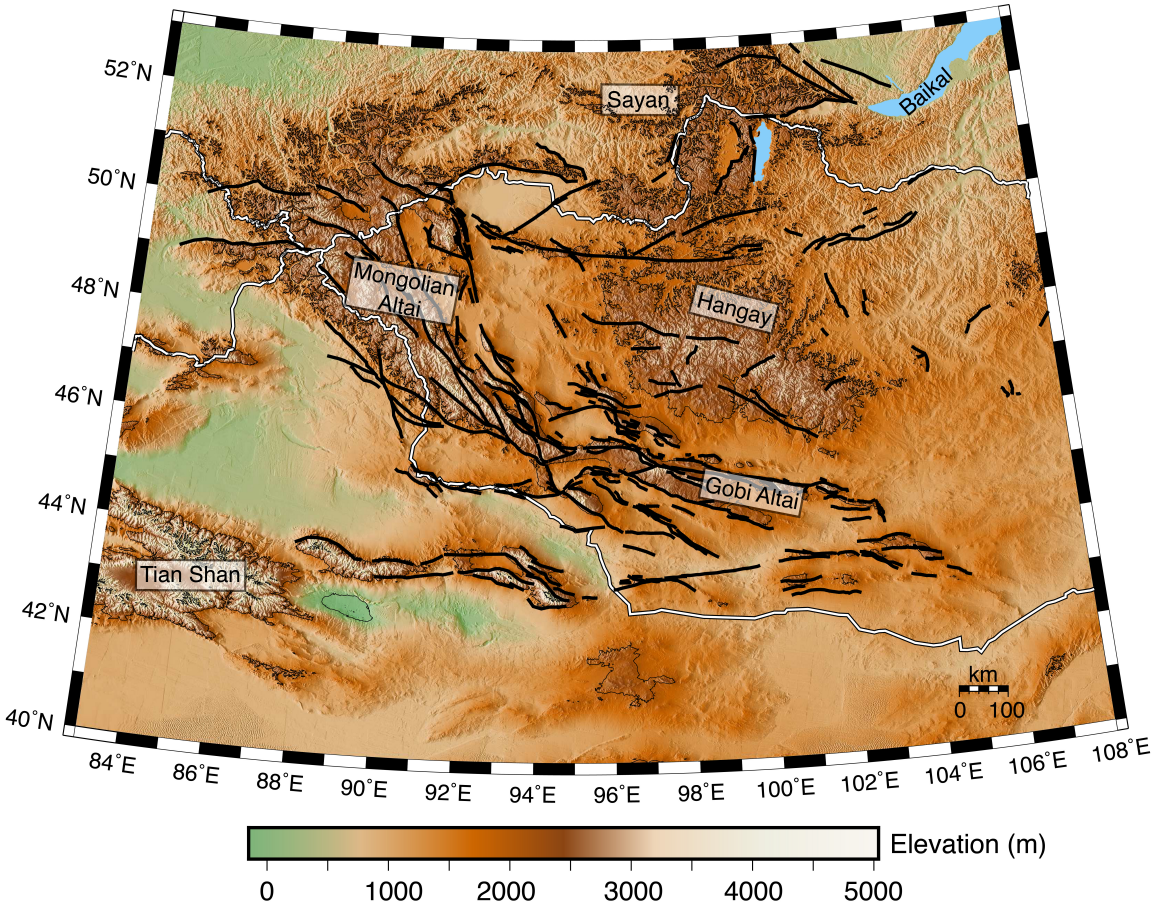


Figure B1: Regional digital elevation model (90 m resolution) showing major physiographic features and mountain ranges of north-central Asia. Most high elevation regions are also shown in figure 1 of Chapter 1. The Tian Shan range to the SW of Mongolia in China (and Kazakstan to the northwest) is shown with highest elevations at over 4000-5000 m in this view. Major regional fault systems shown by heavy black lines. Map is contoured every 2000 m.

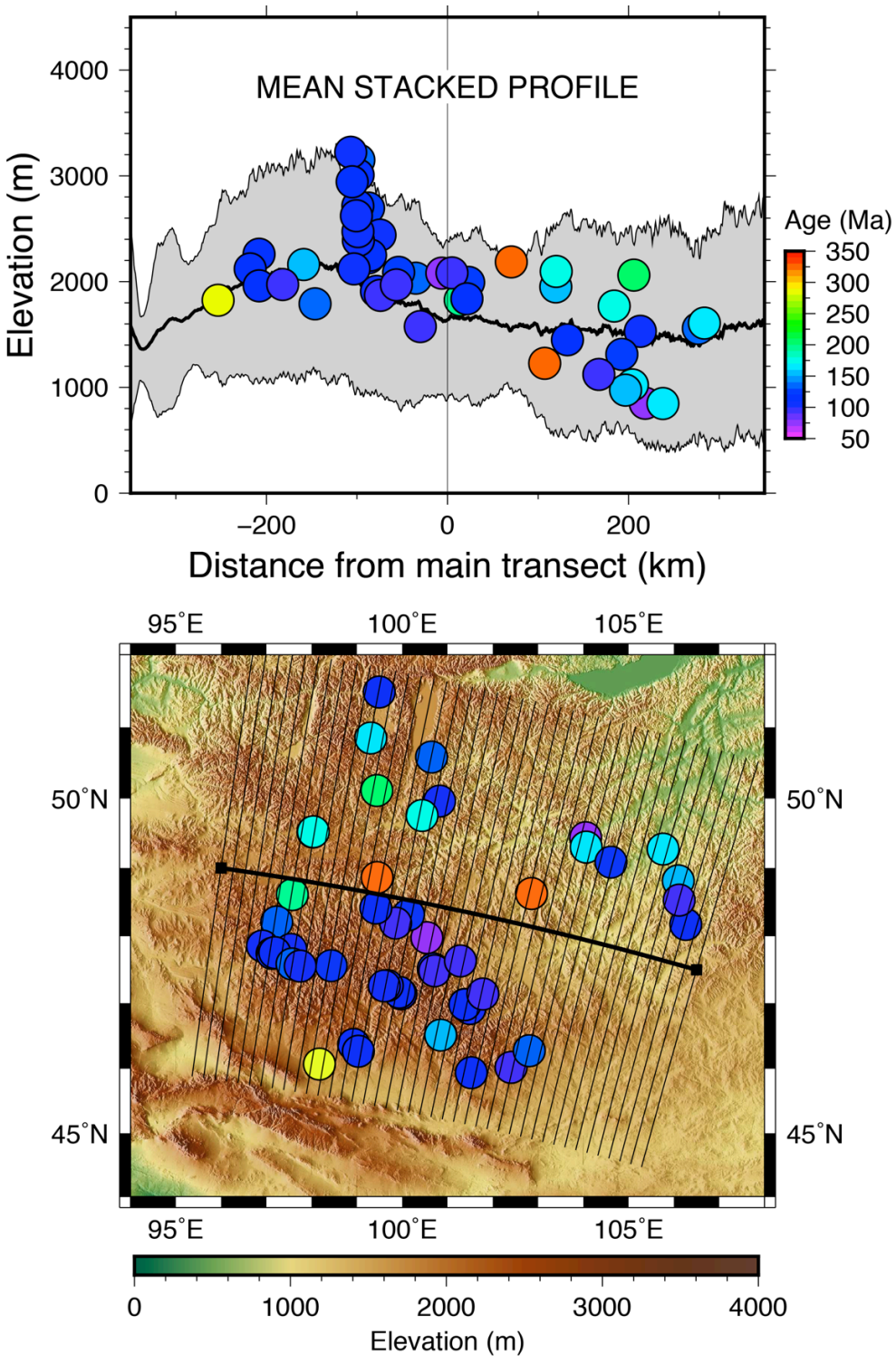


Figure B2: Upper panel, stacked elevation transects over 700 km across central Mongolia with min/max elevations encountered from the sampled 90m DEM shown in the gray envelope, black line is the mean elevation. Sample points colored by arithmetic mean age from single grain replicates.

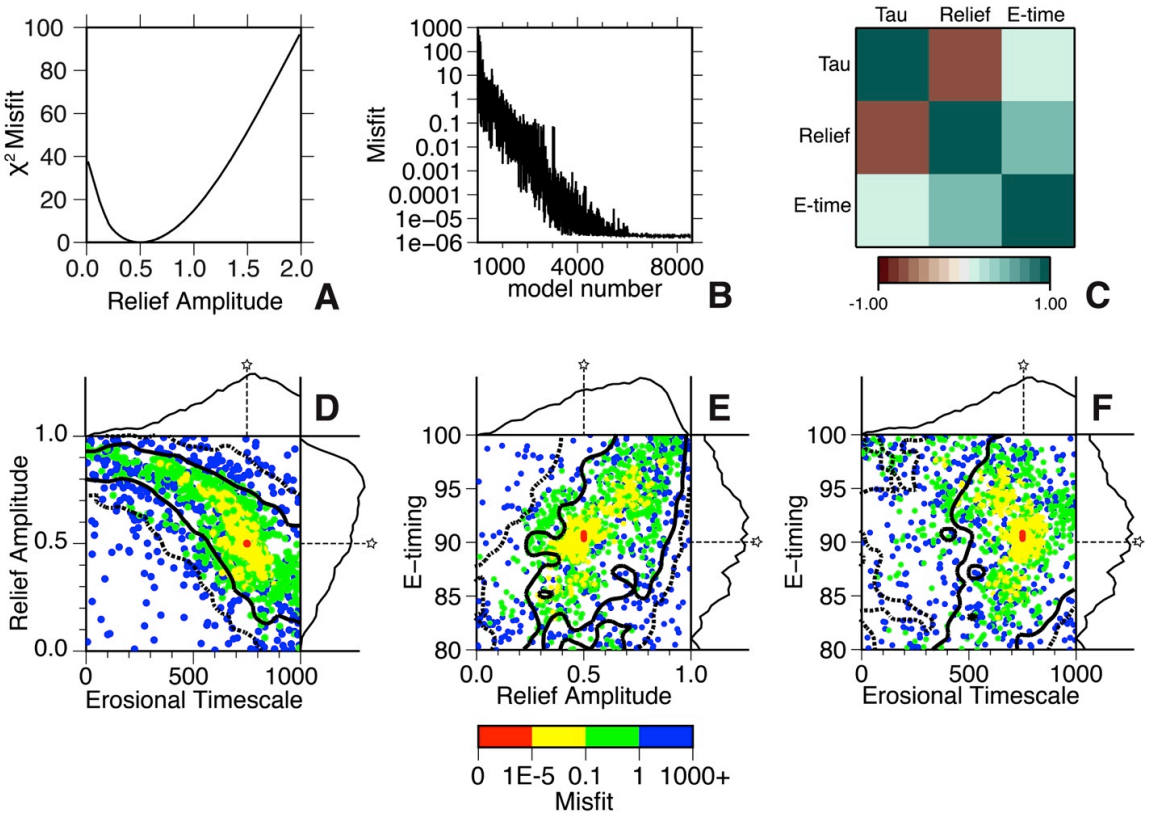


Figure B3: Pecube-NA resolution test of variables controlling relief to assess the ability to resolve relief change in this type of slow exhumation setting. For tests, a two-phase exhumation scenario was used with fixed rates of 100 m/Ma and 30 m/Ma. (A) Relief amplitude-only sensitivity test showing least-squares misfit and relief amplitude between 0 (no relief) to 2 (two times modern relief) with a defined misfit minima at the true value of 0.5x the modern relief in the Hangay. (B) Misfit evolution over inversion duration for resolution test #2 where τ, R, and E-timing are allowed free, exhibiting optimal convergence after >6000 models. (C) Correlation matrix for the free inversion parameters using NA-plot (Sambridge, 1999b). Values approaching (-1)+1 show greater (anti)-correlation while values near 0 show no relationship or dependence. Erosional timescale and relief amplitude are highly anti-correlated, while both the exhumation rate change timing and relief amplitude have a slight positive correlation with erosional timescale. These trends can also be seen in the PPDFs in panels D to F. (D-F) Scatter plots showing misfit between τ, R and E-timing, the 2D PPDF 1-sigma (solid) and 2-sigma (dashed) contours shown as overlays and the corresponding 1D marginal PPDF curves for each parameter on the corresponding axes. In each case the star marks both the 'true value' and the respective lowest misfit of the 1D PPDF, which in this synthetic example is also the mean or modal value.

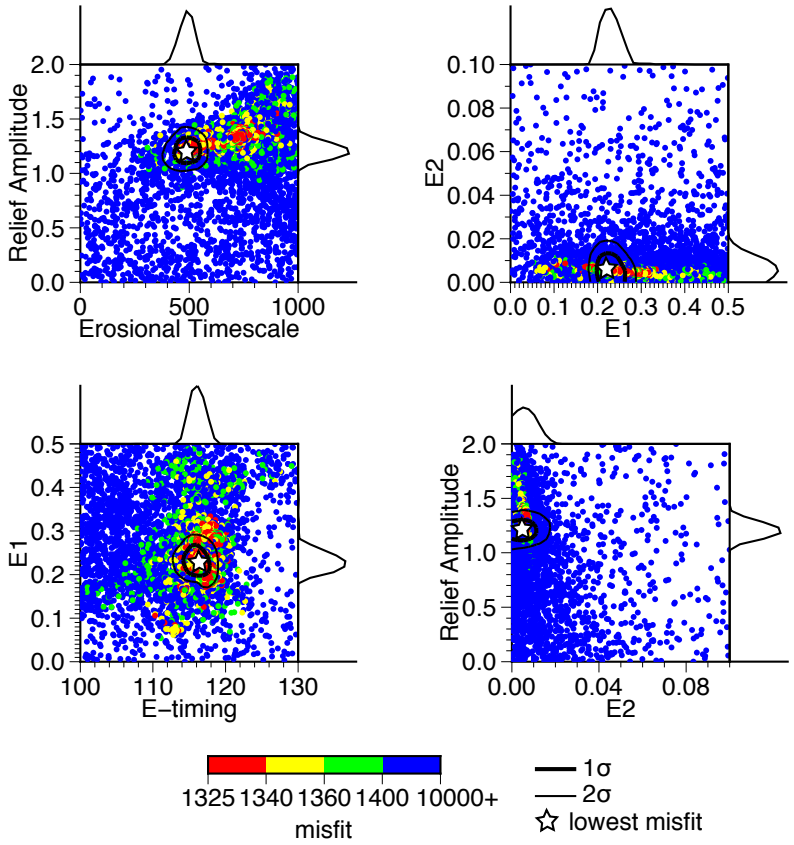


Figure B4: Pecube-NA Run 1-C inversion results for 9504 models. The same figure scheme as figure 6 in Chapter 1 main text. The difference between Run 1-TSW is that the exhumation rate change timing is allowed free in this inversion.

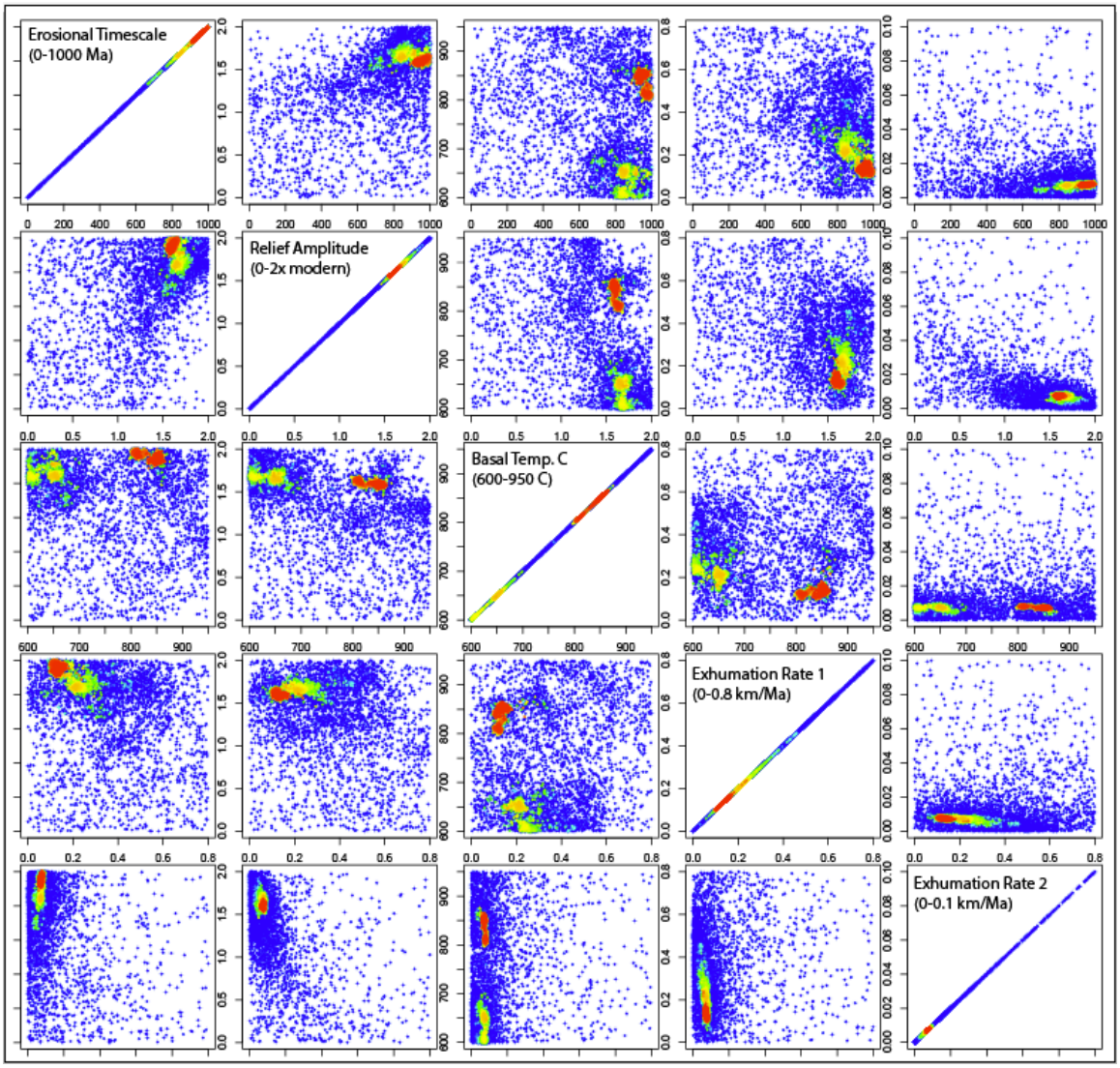


Figure B5: Scatter plot matrix of the 5 dimensional parameter space for Pecube-NA inversion run 1-TSW of 10224 total models; each dot is a forward model colored by the χ^2 misfit. Cooler colors are higher misfit and warmer colors are lower misfit. The x-axis for each plot in every row is the same and is plotted against all other variables; the y-axis is also the same in each column. Parameter plotted against itself where dots are 1:1 line. NOTE: Parameters are both top to bottom (x-axes) and left to right (y-axes): τ (erosional or relief-change timescale; prior 0-1000 Ma), where a value of 0 is linear change and increased positive values indicate greater (i.e. faster) exponential change; R (relief amplitude; prior 0-2) where 0 = no (flat) topography, 1 = modern topography, and 2 = double the modern topography; Tb (basal temperature; prior 600-950°C); E1 (exhumation rate 1; prior 0-0.8 km/my); and E2 (exhumation rate 2; prior 0-0.1 km/my).

Supplementary Tables

Table S1: Mongolian bedrock apatite (U-Th)/He data

Table 1: New granitic bedrock single-grain apatite (U-Th-Sm)/He data for Mongolia

Sample	*Corr. Age (Ma)*	*± 1σ (Ma)*	U (ppm)	Th (ppm)	Sm (ppm)	4He (mol)	Rs (um)	eU cyl (ppm)*	Raw Age (Ma)	Ft
11KWW04-1	*109.99*	*1.19*	21.3	62.3	77.4	1.111E-13	68.8	35.9	86.41	0.78
11KWW04-1c	*128.36*	*0.91*	18.4	74.5	92.2	8.743E-14	60.3	35.9	96.46	0.75
11KWW04-2	*68.86*	*2.54*	5.5	17.0	23.6	1.360E-14	58.9	9.5	51.51	0.74
11KWW04-2c	*106.08*	*2.05*	23.6	85.3	95.4	1.699E-13	74.3	43.7	84.74	0.80
11KWW04-3	*206.92*	*1.69*	30.4	104.0	61.0	1.643E-13	53.4	54.8	149.32	0.72
12MN09-1	~~*283.10*~~	*3.21*	8.7	24.8	111.5	8.092E-14	58.7	14.6	212.54	0.75
12MN09-2	~~*321.80*~~	*3.62*	7.2	29.0	95.7	7.788E-14	56.3	14.0	237.14	0.73
12MN09-3	~~*377.44*~~	*4.29*	8.3	26.8	100.8	3.910E-14	44.6	14.6	254.41	0.67
12MN11-1	*143.85*	*1.97*	126.7	69.3	104.4	3.552E-13	58.6	142.9	109.33	0.76
12MN11-2	*155.13*	*2.07*	114.4	58.8	80.7	3.387E-13	59.1	128.2	118.32	0.76
12MN11-3	*122.92*	*1.59*	86.5	83.1	88.5	1.478E-13	51.6	106.1	89.09	0.72
12MN11c	*127.56*	*1.63*	121.5	55.5	92.1	2.059E-13	52.7	134.6	93.60	0.73
12MN16c	*118.35*	*1.18*	2.0	11.4	152.0	5.053E-14	86.6	4.7	97.97	0.83
12MN18	*160.26*	*2.14*	8.3	5.9	206.5	2.561E-14	56.0	9.7	120.64	0.75
12MN22-1	*190.41*	*2.78*	8.7	5.2	245.7	2.124E-14	51.2	10.0	139.27	0.73
12MN22-3	~~*333.65*~~	*5.36*	7.9	7.8	187.7	6.623E-14	61.2	9.7	258.05	0.77
12MN22c	*227.28*	*4.31*	7.4	7.0	178.8	3.325E-14	58.6	9.1	173.40	0.76
12MN26-1	*148.15*	*1.74*	17.4	25.0	84.8	2.889E-13	95.4	23.3	125.80	0.85
12MN26-2	*163.75*	*2.08*	7.8	32.2	199.2	2.052E-14	47.5	15.4	112.74	0.68
12MN26-3	*151.27*	*1.95*	9.3	6.1	18.7	5.116E-14	70.3	10.8	120.94	0.80
12MN27-1	~~*286.49*~~	*3.30*	8.1	30.5	116.5	4.330E-14	46.4	15.3	195.98	0.68
12MN27-2	*176.00*	*2.01*	9.7	24.7	105.8	3.532E-13	109.8	15.5	152.52	0.86
12MN27-3	*181.65*	*2.14*	4.6	18.1	104.6	7.359E-14	79.9	8.8	147.96	0.81
12MN29-1	*159.26*	*2.40*	13.8	36.0	151.8	9.236E-14	64.4	22.3	122.99	0.77
12MN29-2	*207.30*	*3.12*	5.7	19.2	97.2	3.221E-14	51.1	10.2	147.63	0.71
12MN29-3	*205.89*	*3.09*	6.3	14.8	111.2	4.919E-14	58.6	9.8	154.96	0.75
12MN30-1	*128.39*	*1.63*	30.9	61.8	174.6	3.607E-14	43.7	45.4	85.92	0.66
12MN30-2	*127.69*	*1.59*	16.0	32.2	150.9	9.093E-14	75.6	23.6	102.95	0.80
12MN30-3	*137.35*	*1.65*	34.9	83.3	192.6	1.253E-13	50.9	54.5	97.81	0.71
12MN32-1	*96.73*	*1.11*	8.8	44.1	118.7	4.404E-14	61.7	19.1	73.07	0.75
12MN32-2	*97.19*	*1.12*	9.2	39.2	71.1	4.967E-14	65.6	18.4	74.89	0.77
12MN32-3	*107.71*	*1.24*	7.5	33.1	84.4	3.080E-14	59.4	15.3	80.51	0.74
12MN33-1	*114.93*	*1.37*	12.5	71.7	122.9	2.590E-13	87.7	29.3	94.90	0.82
12MN33-3	*113.95*	*1.37*	13.2	73.8	94.1	1.539E-13	71.9	30.5	89.78	0.78
12MN34-1	*104.53*	*1.30*	35.2	207.3	83.9	6.094E-14	46.5	83.9	70.27	0.67
12MN34-2	*96.70*	*1.05*	27.3	161.2	214.5	5.801E-14	49.4	65.2	67.06	0.69
12MN34-3	*113.23*	*1.22*	26.6	137.3	131.2	6.359E-14	48.9	58.9	78.36	0.69
12MN36-1	*128.82*	*1.49*	13.4	87.5	266.9	6.667E-14	54.0	33.9	92.56	0.71
12MN36-1c	*122.00*	*1.95*	12.1	62.9	128.2	1.080E-13	72.6	26.9	96.54	0.79
12MN36-2	*97.29*	*1.12*	7.2	39.9	50.5	4.815E-14	66.7	16.6	75.06	0.77
12MN36-2c	*120.89*	*1.94*	10.2	70.9	252.9	3.462E-13	92.7	26.9	100.30	0.83
12MN36Ac	*98.87*	*1.01*	11.0	70.7	230.3	3.491E-13	98.2	27.6	83.00	0.84
12MN36Bc	*103.97*	*1.05*	12.0	71.9	208.5	1.627E-13	75.8	28.9	82.45	0.80
12MN42c	*139.51*	*4.17*	4.7	11.3	175.5	1.802E-14	56.7	7.3	104.05	0.74
12MN44-1	*104.04*	*1.16*	6.0	12.3	334.2	2.137E-14	62.0	8.8	80.24	0.77
12MN44-1c	*101.59*	*1.69*	4.1	8.8	291.2	2.175E-14	65.0	6.2	79.48	0.78
12MN44-2	*165.22*	*1.77*	3.9	7.7	279.4	1.383E-13	106.4	5.7	143.33	0.87
12MN44-2c	*116.17*	*2.12*	4.7	8.4	310.3	2.204E-14	67.2	6.6	92.01	0.79
12MN44-3	*157.44*	*1.72*	4.6	9.3	272.7	2.990E-14	66.1	6.8	123.82	0.78
12MN44-3c	*106.03*	*1.90*	5.0	7.3	307.0	1.127E-14	56.1	6.7	79.77	0.75
12MN47-1	*107.72*	*1.36*	12.6	31.5	51.6	5.613E-14	62.4	20.0	82.32	0.76
12MN47-2	*119.02*	*1.49*	42.9	106.9	113.2	4.484E-14	43.2	68.0	78.65	0.66
12MN47-3	*108.39*	*1.35*	26.6	81.2	71.2	1.332E-13	61.0	45.7	82.01	0.75
12MN48c	*115.57*	*2.19*	8.8	42.8	408.7	2.504E-14	48.3	18.8	80.15	0.69

Table S1 (*continued*)

Sample	*Corr. Age (Ma)*	*± 1σ (Ma)*	U (ppm)	Th (ppm)	Sm (ppm)	4He (mol)	Rs (um)	eU cyl (ppm)*	Raw Age (Ma)	Ft
12MN49c	*176.47*	*1.88*	13.8	25.8	172.6	9.307E-14	67.2	19.8	138.47	0.78
12MN49c	*129.07*	*2.12*	14.6	36.0	233.3	2.930E-14	51.6	23.1	92.68	0.71
12MN50-1	*79.43*	*1.01*	67.5	117.6	333.8	6.252E-14	46.4	95.1	54.69	0.68
12MN50-2	*128.63*	*1.67*	57.2	65.9	425.3	1.413E-13	55.2	72.6	95.42	0.74
12MN50-3	*112.21*	*1.47*	39.6	42.9	314.6	4.630E-14	46.2	49.7	77.79	0.69
12MN51-1	~~*259.85*~~	*3.04*	6.4	25.5	75.9	8.944E-14	68.1	12.4	203.11	0.78
12MN51-2	*118.67*	*1.60*	82.9	91.9	334.1	1.286E-13	48.6	104.5	83.71	0.70
12MN51-3	*104.73*	*1.41*	59.0	60.3	230.6	1.235E-13	53.8	73.1	76.92	0.73
12MN54-1	*103.99*	*1.50*	69.8	39.6	184.8	1.230E-13	51.7	79.1	75.67	0.72
12MN54-2	*128.49*	*1.79*	67.5	36.6	161.7	7.119E-14	45.4	76.1	88.97	0.69
12MN54-3	*193.87*	*2.71*	84.7	65.3	212.4	1.335E-13	40.6	100.0	126.81	0.65
12MN59c	*115.57*	*2.19*	41.7	59.2	461.1	3.368E-13	79.4	55.6	107.38	0.82
14MN02c	*99.69*	*1.55*	82.3	68.2	632.9	5.867E-14	42.2	98.3	64.42	0.66
14MN04c	*124.47*	*2.81*	11.3	25.4	132.4	2.224E-14	51.0	17.3	89.13	0.71
14MN05c	*90.75*	*1.30*	53.1	142.6	432.0	6.557E-14	43.4	86.6	60.20	0.66
14MN05c	~~*487.40*~~	*10.58*	17.3	39.6	143.2	2.547E-13	62.1	26.6	374.95	0.76
14MN07c	*105.40*	*1.16*	19.0	45.9	35.8	4.696E-14	56.2	29.8	77.82	0.73
14MN07c	*94.11*	*1.09*	14.9	40.9	67.6	3.021E-14	54.0	24.5	68.45	0.72
14MN08c	*70.10*	*0.88*	117.0	89.8	158.7	9.536E-14	48.9	138.1	49.81	0.71
14MN08c	*70.67*	*1.48*	116.5	92.5	144.1	4.682E-14	41.5	138.2	46.71	0.66
14MN09c	*109.87*	*1.63*	16.1	62.2	315.2	3.076E-14	46.2	30.7	91.67	0.68
14MN09c	*100.84*	*2.01*	10.3	33.2	202.1	2.444E-14	54.2	18.1	73.55	0.72
14MN09-1c	*142.77*	*6.38*	10.3	29.9	208.8	1.154E-13	80.1	17.3	116.65	0.81
14MN10c	*95.75*	*1.82*	12.0	45.0	18.2	3.550E-14	56.6	22.5	70.44	0.73
14MN11c	~~*187.16*~~	*2.86*	1.6	6.6	181.0	1.591E-14	64.9	3.2	145.95	0.78
14MN11c	*126.41*	*5.87*	1.3	4.0	139.8	2.819E-15	49.6	2.3	90.59	0.71
14MN12c	*257.41*	*8.57*	7.3	24.9	345.3	4.390E-14	51.1	13.2	184.48	0.71
14MN12c	~~*389.06*~~	*7.55*	7.3	23.3	333.2	5.861E-14	53.1	12.8	283.81	0.72
14MN13c	*81.40*	*1.06*	43.3	23.7	41.6	4.258E-14	50.0	48.9	58.47	0.71
14MN13c	*123.10*	*2.57*	34.0	27.8	22.1	4.498E-14	48.7	40.5	87.25	0.70
14MN14c	*177.03*	*2.58*	8.4	63.6	346.8	8.141E-14	61.7	23.3	133.71	0.75
14MN14c	~~*503.55*~~	*10.93*	6.0	40.3	281.7	2.983E-13	75.0	15.4	403.66	0.79
14MN15-1c	*81.13*	*1.63*	36.5	73.1	42.7	5.505E-14	51.8	53.7	58.27	0.71
14MN15-2c	*70.13*	*1.42*	39.3	63.4	79.6	1.655E-13	75.4	54.2	56.61	0.80
14MN15c	*61.04*	*0.65*	20.3	68.7	106.4	3.066E-14	54.0	36.4	44.22	0.72
14MN16c	*160.43*	*3.91*	1.0	3.4	87.5	5.925E-15	60.1	1.8	122.31	0.76
14MN17c	*26.99*	*0.42*	27.6	36.0	86.4	3.034E-14	52.7	36.1	19.63	0.72
14MN17c	*126.96*	*2.81*	4.3	10.3	137.7	8.143E-14	92.7	6.7	107.20	0.84
14MN18c	~~*519.79*~~	*5.34*	1.1	4.3	108.9	2.832E-14	62.6	2.2	394.23	0.77
14MN18c	*211.29*	*2.53*	0.7	2.6	70.9	3.698E-14	96.4	1.3	173.83	0.85
14MN18c	*145.32*	*3.41*	1.1	4.3	131.9	7.292E-15	61.2	2.1	111.52	0.76
14MN18-1c	*138.98*	*6.21*	1.0	3.5	119.4	1.140E-14	73.2	1.8	112.00	0.80
14MN19c	*156.99*	*3.62*	7.8	12.5	453.9	1.136E-14	44.3	10.7	107.77	0.68
14MN20c	*98.25*	*1.45*	8.5	40.1	76.9	1.071E-14	43.5	18.0	64.45	0.65
14MN20c	*193.06*	*4.25*	9.6	24.8	144.9	8.133E-14	63.7	15.4	148.88	0.77
MN15-27c	*286.60*	*9.48*	7.9	1.1	214.1	4.550E-14	62.2	8.2	224.02	0.78
MN15-28c	*111.38*	*3.63*	6.9	21.5	65.1	1.891E-14	57.8	12.0	82.58	0.74
MN15-28c	*112.40*	*5.04*	7.5	21.4	92.4	2.136E-14	58.0	12.6	83.62	0.74
MN15-29c	*93.78*	*3.11*	33.9	25.1	275.0	3.531E-14	51.7	39.8	63.79	0.72
MN15-29c	*101.80*	*4.59*	40.1	49.2	323.8	3.930E-14	44.9	51.7	69.25	0.68
MN15-30c	*124.37*	*4.05*	15.5	33.4	205.2	1.587E-14	41.4	23.4	80.71	0.65
MN15-30c	*136.60*	*6.14*	17.4	28.3	168.6	2.525E-14	47.3	24.1	94.76	0.69

Table S1 (*continued*)

Egiin Davaa (#7-8) & Hangay Batholith (#5), Mongolia, bedrock apatite multi-grain aliquots dated at Lehigh University: from Landman, 2007

Sample	*Corr. Age (Ma)*	*± 1σ (Ma)*	U (ppm)	Th (ppm)	Sm (ppm)	4He (mol)	Rs (um)	eU (ppm)	Raw Age (Ma)	Ft
RL7-1a (n=3)	*107.90*	*7.96*	19.5	27.9	428.8	9.316E-14	51.4	26.1	75.76	0.72
RL7-1b (n=4)	*99.40*	*7.45*	8.5	10.0	150.8	7.124E-14	60.6	10.9	73.58	0.75
RL7-1c (n=4)	*102.70*	*7.51*	17.1	14.8	228.7	5.424E-14	45.0	20.5	66.98	0.68
RL7-3b (n=3)	*119.80*	*9.01*	5.1	14.7	79.2	3.581E-13	107.2	8.6	102.95	0.86
RL7-3c (n=3)	*111.90*	*8.58*	10.1	27.5	187.9	1.724E-13	72.1	16.6	87.96	0.79
RL5-4a (n=3)	*93.30*	*6.97*	19.8	31.1	152.3	2.823E-13	77.2	27.1	74.53	0.81
RL5-4b (n=4)	*106.20*	*7.97*	10.6	19.6	75.4	2.852E-13	83.9	15.2	86.14	0.82
RL5-4c (n=3)	*114.00*	*8.50*	23.1	37.3	153.4	9.194E-14	45.6	31.9	75.72	0.68
RL5-2a (n=3)	*99.60*	*7.38*	19.3	47.8	89.2	1.379E-13	60.7	30.5	72.32	0.74
RL5-2c (n=3)	*114.60*	*8.65*	57.6	111.2	237.1	2.509E-13	51.3	83.8	79.08	0.70
RL8-3a (n=3)	~~*413.40*~~	*30.81*	13.1	20.0	219.9	3.713E-13	57.4	17.8	303.03	0.75
RL8-3b (n=3)	~~*439.10*~~	*32.52*	18.4	60.5	274.8	3.024E-13	59.2	32.6	325.37	0.74

± 1σ is analytical uncertainty from propagated error of He, U, Th, and Sm analyses along with Ft and blank measurements

*effective Uranium content for cylindrical geometry, eU from Flowers et al., 2009; Rs is spherical equivalent radius

Ft is correction for diffusive alpha-loss after Farley, 1996

Samples with 'c' suffix denote those run via controlled ramped heating (CRH method), see Chapter 2

Samples in bold had high 4He gas re-extracts after initial analysis

Strikethrough samples are excluded because ages are much older than Hangay granite U-Pb ages

Table S2: Detrital (U-Th)/He data for the Selenga and Orkhon Rivers, Mongolia

Table S2: Selenga and Orkhon River detrital apatite (U-Th-Sm)/He data

Selenga Sample	Corr. Age (Ma)	± 1σ (Ma)	U (ppm)	Th (ppm)	Sm (ppm)	4He (mol)	Rs (um)	eU (ppm)	Raw Age (Ma)	Ft
12MGS04-E1	132.82	1.97	16.9	36.9	671.3	1.743E-13	91.65	25.6	111.88	0.841
12MGS04-E3	190.80	2.71	1.4	6.3	206.4	3.328E-14	95.69	2.9	162.28	0.849
12MGS04-E4	114.45	5.16	1.0	2.0	0.3	1.594E-15	55.31	1.5	84.09	0.733
12MGS04-E6	175.77	2.67	3.1	5.4	142.9	3.187E-14	71.23	4.4	140.80	0.799
12MGS04-E8	131.16	2.12	1.5	38.4	210.5	4.054E-14	77.63	10.6	104.30	0.795
12MGS04-E9	116.37	5.02	0.1	1.3	0.2	5.660E-16	59.51	0.4	85.73	0.736
12MGS04-E10	252.68	4.22	12.8	3.6	172.9	2.211E-13	97.23	13.6	216.66	0.855
12MGS04-E11	110.06	1.63	33.3	90.0	208.2	1.897E-13	80.36	54.4	89.73	0.814
12MGS04-E12	175.01	2.54	4.2	16.9	197.5	4.860E-14	80.59	8.2	142.90	0.815
12MGS04-E14	114.05	1.85	5.7	4.5	37.2	1.756E-14	72.71	6.7	91.64	0.802
12MGS04-E15	135.52	1.99	12.8	54.9	133.6	1.534E-13	76.26	25.7	108.84	0.802
12MGS02	92.61	4.08	21.0	52.0	153.5	2.132E-14	44.86	33.2	62.43	0.673
12MGS03	163.65	2.72	104.1	50.4	80.7	5.006E-13	73.93	115.9	132.43	0.807
12MGS04	157.85	2.57	52.9	33.3	54.1	7.611E-13	91.92	60.7	133.59	0.845
12MGS05	123.15	1.98	25.6	37.2	233.4	1.113E-13	66.55	34.4	96.57	0.783
12MGS07	164.73	2.66	4.2	16.5	621.9	1.219E-14	47.29	8.1	115.90	0.702
12MGS08	121.31	1.99	1.9	5.1	169.9	1.520E-14	74.98	3.1	98.44	0.810
12MGS09	153.73	2.38	11.6	39.4	198.7	9.836E-14	67.88	20.9	120.19	0.780
12MGS10	146.82	2.48	0.8	3.0	298.4	5.288E-15	54.55	1.5	112.15	0.763
12MGS12	229.35	3.67	9.2	28.4	269.1	8.049E-14	59.19	15.8	172.89	0.751
12MGS13	138.27	2.19	5.5	21.9	260.5	3.422E-14	59.95	10.6	104.35	0.753
12MGS14	317.39	5.14	4.6	12.4	286.2	5.111E-14	60.58	7.5	243.02	0.762
12MGS15	73.47	2.79	1.1	3.6	760.2	1.140E-15	44.99	1.9	54.87	0.746
12MGS16	117.53	1.97	9.2	31.9	1114.3	9.883E-15	44.97	16.7	80.58	0.684
12MGS01-2	96.89	1.49	18.3	64.8	39.5	7.514E-14	64.55	33.5	74.44	0.767
12MGS02-2	142.54	2.23	18.6	64.7	126.0	5.990E-14	58.41	33.8	106.00	0.742
12MGS03-2	175.53	8.78	1.5	8.4	76.4	4.600E-15	41.82	3.5	113.50	0.645
12MGS04-2	105.24	1.63	20.3	54.3	20.0	8.154E-14	62.98	33.1	80.58	0.764
12MGS05-2	111.21	1.79	33.1	37.4	115.8	2.030E-13	68.54	41.8	87.86	0.789
12MGS06-2	146.66	2.66	2.2	6.6	55.6	2.057E-14	71.31	3.7	116.45	0.793
12MGS07-2	117.39	2.02	46.6	15.8	133.2	2.298E-13	71.86	50.4	94.50	0.803
12MGS08-2	72.16	5.11	7.5	11.3	31.3	1.298E-14	54.27	10.2	52.93	0.732
12MGS10-2	104.50	1.76	58.2	44.4	95.9	7.165E-14	46.02	68.6	72.42	0.691
12MGS11-2	74.22	4.91	3.4	13.0	38.3	3.246E-15	42.37	6.4	48.29	0.650
12MGS12-2	145.33	3.83	2.6	7.1	44.5	9.970E-15	55.03	4.3	106.65	0.732
12MGS13-2	113.65	2.08	5.0	17.5	129.2	2.004E-14	56.29	9.1	83.80	0.736
12MGS14-2	116.54	1.80	35.7	101.6	35.3	8.620E-14	49.31	59.6	81.67	0.699
12MGS15-2	117.37	1.77	24.6	77.9	107.4	7.207E-14	53.61	42.9	84.98	0.723
12MGS16-2	130.79	2.03	23.2	85.2	21.4	6.109E-14	50.34	43.3	92.11	0.703
12MGS01-3	78.02	1.22	24.0	46.8	121.2	1.444E-14	42.24	35	51.05	0.653
12MGS02-3	118.01	1.85	32.3	73.5	51.7	3.050E-14	41.83	49.6	76.57	0.647
12MGS03-3	144.43	2.19	9.8	32.0	47.6	2.951E-14	57.69	17.4	106.99	0.739
12MGS04-3	184.41	2.72	10.5	52.2	61.0	2.026E-13	78.6	22.7	148.56	0.804
12MGS05-3	266.93	4.61	8.2	2.4	84.5	3.505E-14	54.1	8.8	198.71	0.740
12MGS06-3	112.56	1.78	13.0	38.0	37.4	1.690E-14	42.33	21.9	73.13	0.648
12MGS07-3	198.32	2.99	17.2	55.3	175.7	4.336E-14	45.49	30.2	133.81	0.672
12MGS08-3	118.21	2.00	6.5	9.8	5.6	1.037E-14	48.14	8.8	82.49	0.696
12MGS09-3	101.44	1.58	5.3	12.8	69.2	9.446E-15	50.27	8.3	71.76	0.706
12MGS10-3	93.28	1.52	5.7	21.4	56.8	4.376E-15	39.4	10.8	58.05	0.621
12MGS11-3	97.26	7.44	1.3	5.3	14.0	3.423E-15	53.08	2.5	69.56	0.714
12MGS12-3	105.82	2.02	8.7	17.9	54.7	4.084E-15	34.59	12.9	61.57	0.580
12MGS15-3	145.94	3.85	1.0	3.7	9.4	1.710E-15	43.39	1.9	95.74	0.654
12MGS16-3	110.72	1.80	44.9	67.0	63.4	2.518E-14	36.34	60.6	66.88	0.602

Table S2 (*continued*)

Orkhon Sample	Corr. Age (Ma)	± 1σ (Ma)	U (ppm)	Th (ppm)	Sm (ppm)	4He (mol)	Rs (um)	eU (ppm)	Raw Age (Ma)	Ft
12MGO03-Z1	140.21	2.09	10.3	15.8	344.7	2.173E-14	51.99	14.0	101.80	0.724
12MGO03-Z2	168.13	2.43	3.3	9.0	35.2	3.364E-14	72.76	5.4	133.80	0.794
12MGO03-Z3	148.02	2.13	14.6	53.4	28.7	7.941E-14	61.91	27.2	112.00	0.755
12MGO03-Z5	63.31	1.08	0.9	6.7	96.7	2.418E-15	62.64	2.5	48.09	0.759
12MGO03-Z6	117.49	1.90	17.8	9.9	276.1	6.608E-14	66.18	20.1	92.43	0.785
12MGO03-Z7	146.43	2.11	26.0	126.3	137.2	1.710E-13	59.63	55.6	109.03	0.743
12MGO03-Z8	160.12	2.30	22.5	100.0	217.1	1.116E-13	57.42	46.0	117.98	0.735
12MGO03-Z9	178.34	2.55	7.6	28.7	127.8	7.750E-14	64.81	14.3	137.13	0.767
12MGO03-Z10	127.42	1.96	29.1	35.3	126.5	1.965E-13	74.75	37.3	102.65	0.804
12MGO03-Z11	92.25	1.35	17.2	37.6	332.8	1.364E-13	79.13	26.0	75.09	0.813
12MGO03-Z12	113.08	1.79	83.3	66.0	324.5	1.452E-13	53.81	98.8	83.10	0.733
12MGO03-Z14	131.50	1.99	34.0	48.7	379.9	6.459E-14	50.64	45.4	94.03	0.713
12MGO03-Z15	126.82	1.90	33.8	58.8	46.1	6.504E-14	48.83	47.6	88.89	0.699
12MGO03-Z16	111.75	1.77	36.2	32.1	38.5	8.024E-14	62.18	43.7	85.89	0.767

Table S3: Bedrock sample locations and mean ages

Table S3: Mongolian bedrock sample locations and mean (U-Th)/He ages

Sample	Longitude (DD)	Latitude (DD)	Elevation (m)	Mean Age (Ma)	1 S.E.
11KWW04	98.43149	47.56130	2695	124	23
12MN09	102.85576	48.62807	1228	327	27
12MN11	100.64848	50.58302	1558	137	7
12MN16	99.49230	51.48810	1587	-	-
12MN18	99.30450	50.85050	1607	-	-
12MN22	99.43890	50.11140	2061	209	15
12MN26	98.02777	49.52010	1950	154	5
12MN27	98.03717	49.52312	2096	179	2
12MN29	97.57150	48.61240	1826	191	16
12MN30	97.22990	48.20980	2032	131	3
12MN32	96.91240	47.85390	1908	101	4
12MN33	97.12630	47.74460	2225	114	0.4
12MN34	97.53950	47.80410	2440	105	5
12MN36	97.18490	47.75640	2250	112	6
12MN42	97.56593	47.58624	3149	-	-
12MN44	97.74680	47.55593	2390	107	12
12MN47	98.92677	46.37360	2259	112	4
12MN48	99.03072	46.26778	2120	-	-
12MN49	100.84712	46.51558	2161	153	24
12MN50	101.49387	46.91762	2120	107	7
12MN51	101.38090	46.97923	3008	112	6
12MN54	101.38182	46.97630	2715	116	27
12MN59	106.26272	48.17420	1450	-	-
14MN02	101.78238	47.13675	1870	-	-
14MN04	100.68382	47.51389	2088	-	-
14MN05	100.71835	47.48491	1969	-	-
14MN07	101.28596	47.63231	1575	-	-
14MN08	100.54628	47.97729	2080	70	1
14MN09	100.13952	48.31841	1992	126	13
14MN10	99.85471	48.19311	2083	-	-
14MN11	99.41685	48.41427	1838	157	30
14MN12	99.44515	48.86182	2186	-	-
14MN13	100.82367	49.96175	1530	102	21
14MN14	100.43731	49.75661	1769	-	-
14MN15	104.05012	49.43802	850	71	6
14MN16	104.06229	49.30243	1024	-	-
14MN17	104.61073	49.08473	1312	-	-
14MN18	105.76070	49.27403	847	165	20
14MN19	106.09676	48.81374	974	-	-
14MN20	106.11541	48.53217	1122	98	47

Table S3 (*continued*)

Sample	Longitude (DD)	Latitude (DD)	Elevation (m)	Mean Age (Ma)	1 S.E.
MN15-27	98.17137	46.07203	1824	-	-
MN15-28	101.52622	45.94054	1960	112	1
MN15-29	102.40330	46.02081	1972	98	4
MN15-30	102.80430	46.27676	1790	130	6
RL7-1**	99.97167	47.14167	3223	103	5
RL7-3	99.93587	47.16233	2944	116	6
RL5-4	99.66898	47.26480	2473	105	5
RL5-2	99.60178	47.25804	2622	107	6
RL8-3	99.92587	47.17497	2562	-	-

*1 SE: from component single grain age std. dev. (ignoring analytical unc.)
**Std. Dev./S.E. propagated from multi-grain aliquot analytical errors in RL samples
dashes signify grains with only one analysis, or discarded because of outlier/analytical error (RI
and in figures, ages with only one grain are reported in place of mean

Table S4: Pecube fixed thermal model parameters

Table S4: Model parameters used in Pecube-NA inversions

Fixed Parameter	Value	Units	Reference
Model initiation	150	Myr	
Basal Moho temperature, *Tb*	850	°C	Ionov et al., 1998; Ancuta et al., 2012
Volumetric heat production, *H*	0.7	$\mu W\ m^{-3}$	Lysak and Dorofeeva, 2003
Radiogenic heat production, *A*	8	$°C\ Myr^{-1}$	
Thermal diffusivity, κ	25	$km^2\ Myr^{-1}$	
Specific heat capacity, *Cp*	800	$J\ kg^{-1}\ K^{-1}$	
Surface Temperature, *Ts*	0	°C	
Atmospheric lapse rate	0	$°C\ km^{-1}$	
Crust/Mantle density, *ρc/ρm*	2800/3300	$kg\ m^{-3}$	
Crustal Thickness, *Zc*	49	km	Stachnik et al., 2014
Effective elastic thickness, *Te*	6.1	km	Bayasgalan et al., 2005
Model domain	80 x 60	km	
1 km grid resolution	0.00833	degrees	
Vertical node spacing	1	km	

CHAPTER 2

Screening apatites for (U-Th)/He thermochronometry via continuous ramped heating: Helium age components and implications for age dispersion

Kalin T. McDannell[a]*, Peter K. Zeitler[a], Darwin G. Janes[a], Bruce D. Idleman[a], and Annia K. Fayon[b]

[a]*Department of Earth and Environmental Sciences, Lehigh University, Bethlehem, PA 18015*
[b]*Department of Earth Sciences, University of Minnesota, Minneapolis, MN 55455*

*Corresponding author: ktm211@lehigh.edu

For submission to *Geochimica et Cosmochimica Acta*

Keywords: apatite, screening, dispersion, helium, diffusion, thermochronology

CHAPTER ABSTRACT

Old, slowly-cooled apatites often yield dispersed helium ages due to factors such as parent zonation, He implantation, radiation damage, crystal defects, and fluid inclusions. Careful grain selection and conducting replicate analyses can mitigate the impact of some of these effects. However, these approaches add costs in time and resources and have proven insufficient for understanding age dispersion, including its possible causes and means of making age corrections to poorly-behaved samples. We assess a new technique utilizing static-gas measurement during continuous ramped heating (CRH) as a means to rapidly screen apatite samples. In about the time required for a conventional total-gas analysis, this method can discriminate between samples showing the expected volume-diffusion behavior for ^{4}He in apatite, and those showing anomalous release patterns inconsistent with their use in thermochronologic applications. This method also has the potential to quantify and discriminate between the radiogenic and extraneous ^{4}He fractions released by a sample, allowing ages to be corrected. Well-behaved examples such as the Durango standard and other apatites with good age reproducibility show the expected smooth, sigmoidal gas release profiles predicted for volume diffusion using typical apatite kinetics, with complete exhaustion by ~900°C for linear heating at 20°C/minute. Secondary factors such as U and Th zoning and alpha-loss distribution have a relatively minor impact on such profiles. In contrast, samples that show anomalous behavior and greater age dispersion show significant helium release deferred to higher temperatures. We report on screening results for a range of samples, assessing the degree to which CRH screening can reliably identify misbehaving grains and correct their ages.

1. Introduction

Since the suggestion that (U-Th)/He ages of apatite might function as a thermochronometer (Zeitler et al., 1987), many advances have been made in documenting the fundamental diffusion systematics of helium in this phase (e.g., Farley et al., 1996; Wolf et al., 1996; Warnock et al., 1997; Farley, 2000; Shuster et al., 2006). This includes understanding that the diffusion length scale appears to be the physical grain dimension, quantifying the alpha-ejection process and means of correcting for it, measuring the range of diffusion kinetics seen in natural samples, and assessing the impact that zoning in U and Th can have on measured apatite He ages. More recently, it has been shown that radiation damage (e.g., Shuster et al., 2006; Flowers et al., 2009) can act as an important control on effective diffusivity, with damage acting to impede diffusion.

It has become very apparent through work on various sample suites from different geologic settings, (e.g. Fitzgerald et al., 2006; Peyton et al., 2012) that additional factors must be involved in controlling He abundances in natural samples, because datasets often yield age dispersion beyond what radiation damage, grain size, and zoning can explain. Other documented factors that can in some cases have a significant impact include He implantation, (e.g. Spiegel et al., 2009), U-Th-rich grain boundary phases, (e.g. Murray et al., 2014), fluid and mineral inclusions, (e.g. Farley, 2002; Vermeesch et al., 2007), and broken grains, (e.g. Beucher et al., 2013; Brown et al., 2013). In some cases, quantification of these factors has permitted more sophisticated explanations for what had been perplexing, dispersed data, (e.g. Green et al., 2006; Flowers and Kelley, 2011), but in many cases unexplained dispersion remains. Most recently, this has turned attention to

factors that could change diffusion kinetics by altering the apatite crystal lattice, across a range of spatial scales, ranging from substitutions associated with variable chemical composition (Djimbi et al., 2015), vacancy damage (Gerin et al., 2017), deformation-induced microstructures (Fayon and Hansen, 2015), or crystallographic voids (Zeitler et al., 2016, in press).

Here we take an empirical approach to the problem of age dispersion and assess an alternative experimental method for characterizing ^{4}He components in apatite. This continuous ramped heating (CRH) method (Idleman and Zeitler, 2014) employs continuous heating and static-mode measurement of evolved gas, and was initially implemented by McDannell et al. (2015). This technique permits efficient screening of apatite samples through characterization of diffusive loss during heating, as the method allows an entire diffusion experiment to be carried out in the same amount of time as is usually taken for a conventional gas extraction and second "re-extract" step. Continuously heated samples that outgas by volume diffusion (VD) during a linear heating schedule produce a characteristic sigmoidal ^{4}He cumulative-loss curve, with the exact shape and position of these curves (in loss vs. heating space) controlled by sample kinetics, grain size, and heating rate (see discussion and figure 1, below). Modifications to diffusive behavior by factors such as alpha-ejection, radiation damage, and parent isotope zoning lead to relatively subtle changes to the sigmoidal release curve form. However, as we demonstrate, anomalous samples with poor single-grain age reproducibility commonly yield complex cumulative-loss curves that have multiple inflection points or are displaced from those of other apatites analyzed under the same

experimental conditions. The CRH approach can discriminate between apatites showing expected volume-diffusion behavior and those that show complicated release during degassing. We conclude that (1) simple behavior is required for obtaining good, well-replicated ages, and that (2) in some cases, screening can be used to correct dispersed age datasets.

2. Continuous Ramped Heating (CRH) Method and Sample Assessment

2.1 Analytical Procedures

Apatite samples for ^{4}He analysis via the CRH method were obtained using standard processing: crushing, sieving, and density- and magnetic-separation procedures. Grains were picked under a Nikon SMZ800 microscope at ~95x magnification and then examined under an Olympus BH2-UMA polarized petrographic microscope to inspect for inclusions at up to 500x. Grains were digitally photographed in order to record their 3D sizes and shapes for determination of alpha-correction factors. Individual grains were placed in small niobium microtubes whose ends were crimped, and then loaded into the extraction system's sample dropper that permits multiple samples to be readied for sequential analysis in a resistance furnace. Samples were degassed of their ^{4}He in the Lehigh University noble-gas laboratory and parent U-Th-Sm isotopes were subsequently measured by dissolution and isotope dilution of sample aliquots by ICP-MS at the laboratory of Dr. Peter Reiners at the University of Arizona following the procedures of Reiners and Nicolescu (2006).

For noble-gas analysis, samples were outgassed using a water-cooled double-vacuum

resistance furnace that was held idle at 200°C between runs. The extraction line includes two temperature-stabilized capacitance manometers used in monitoring pressure and preparing spikes and calibration shots. The extraction line ^{4}He blank is typically 1 x 10^{-16} moles or less for conventional analyses, however for the CRH technique the blank is generally between ~1 x 10^{-15} to ~1 x 10^{-14} moles because of the "open system" conditions between the furnace and the rest of the extraction line. A reservoir containing a $^{4}He/^{3}He$ standard is attached to the extraction line ^{4}He is measured by manometric peak-height comparison against pipetted aliquots of a mass-discrimination standard having accurately known quantities of ^{3}He and ^{4}He. This approach agrees to better than 1% with samples amounts determined using our ^{3}He spike, and is preferred because under high hydrogen loads the spike determinations become unreliable due to interferences at m/e=3. Typical variations in ^{4}He sensitivity (mol/A) over a day are about 0.5%.

Apatites were heated in the resistance furnace using a linearly ramped, rate-controlled heating schedule from 200°C to 1150°C at a rate of 20°C/minute. During CRH experiments, raw release data (cumulative time and ^{4}He signal) were collected by the mass spectrometer every 21.5 s over a cycle of ~133 data blocks. SAES getters in the extraction line and in the mass spectrometer volume sorb active gases during heating, while the degassed helium from apatite grains was measured simultaneously. Sensitivity hysteresis (Lieszkovszky et al., 1990) due to increased hydrogen released at furnace temperatures between 400-600°C was apparent. Hydrogen suppression of He ionization in the mass spectrometer source was a result of background hydrogen load buildup due to repeated heating cycles and exposure of the furnace to the entire extraction line during

sample outgassing. To alleviate these effects, the furnace was allowed to cool for one hour between runs back to 200°C, and to inhibit active gas interference, the furnace went through extended 1 to 2 hour bake-outs at 1350°C every three to four sample runs (it should be noted that this is not required for laser heating, which is better suited for routine analysis). For samples other than the Mongolian suite, to more easily handle possible sensitivity variations, we began injecting a $^{4}He/^{3}He$ calibration shot as soon as the ^{4}He signal stabilized at the end of runs, in effect using the method of standard additions to determine sample amounts.

2.2 Data reduction

Individual mass spectrometer measurements were treated mathematically as square-pulse heating steps using the average temperature experienced during the measurement cycle. Raw mass spectrometer times were equated to temperature using a heating ramp rate of 20°C/minute (~7.5°C/block) and raw ^{4}He measurements were translated to cumulative fractional loss, *f,* and then numerically differentiated to incremental fractional loss per temperature step, *df* **(fig. 1)**. The *f*-curve displays the cumulative liberation of ^{4}He that progresses with increasing temperature (normalized to unity), while the *df*-curve shows the incremental gas release that intuitively emphasizes the temperature zone where the majority of apatite degassing occurs (for a given set of heating conditions). In early experiments using furnace heating, a lag of up to ~75°C between the sample and the thermocouple at the base of the furnace crucible was apparent in Arrhenius data and is supported by measurements of the crucible interior temperature using a secondary thermocouple. The temperature was measured for the sample crucible and the thermal lag

offset was determined between the target temperature and the actual temperature during a 20°C/min heating schedule. Therefore all quoted temperatures and figures reference the corrected measurements. Despite the temperature offset, we have confidence in the overall form of the cumulative loss and Arrhenius curves from Durango release patterns. However, we refrain from calculating kinetic parameters from furnace data due to the precise but inaccurate temperatures.

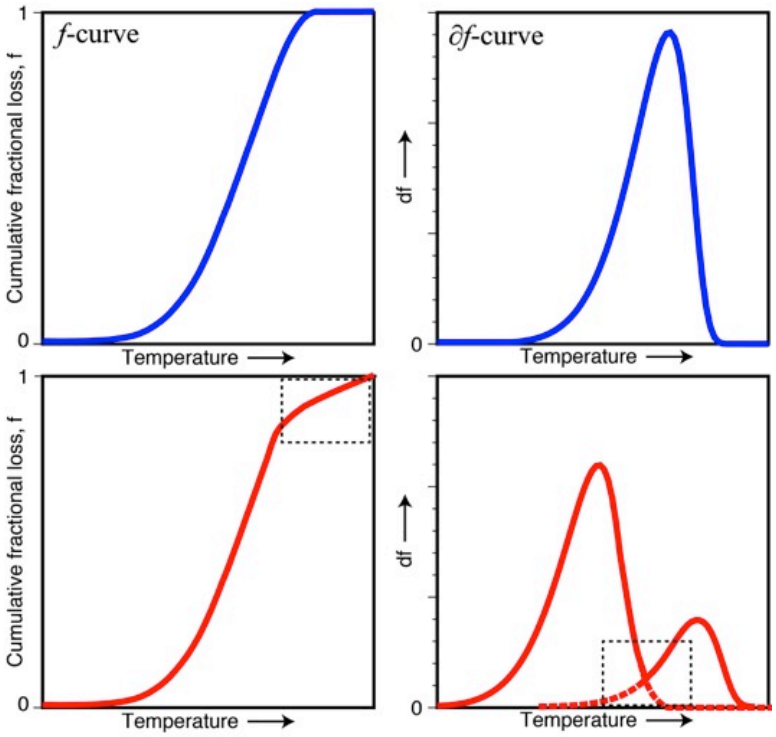


Figure 1. Schematic sigmoidal shape of an expected, smooth cumulative fractional loss (*f*-curve) that is differentiated to produce the *df*-curve (top). Bottom shows *f* and *df* plots for a hypothetical sample showing some anomalous behavior – flattened high-temperature *f*-curve segment and a secondary gas component at the peak shoulder (denoted by dashed box). This example would be a candidate for VD model peak fitting (see section 2.4) where the observed data are honored up to the second minor peak, which is then removed. Note that the total area under the *df*-curve must be 1, so multiple peak *df*-curves act to lower overall peak height and broaden the gas-release interval relative to a unimodal curve.

2.3 Expected behavior

In general, He diffusion in apatite obeys thermally activated volume diffusion where the crystal size is the diffusion domain and He outgassing produces a sigmoidal release curve. Increasing the activation energy (E_a) will narrow the *df*-curve peak and shift it to warmer temperatures while a decrease in E_a will broaden the peak and shift it to cooler temperatures for a given heating rate (**fig. 2**). Higher E_a produces a narrower peak (steeper *f*-curve) for any given release temperature. Holding E_a constant, an increase in diffusivity will narrow the peak and shift it to cooler temperatures, while decreasing diffusivity will broaden the peak and shift it to warmer temperatures (**fig. 2**). Grain size and heating rate also shift release curves, where smaller grains and faster heating rate lead to earlier He release, and vice versa for larger grains and slower heating schedules. In net, the interplay of these variables will modify the locations of the *f*- and *df*-curves and their shapes. Another point to note is that since the *df*-curves must conserve an area equal to 1, any secondary He components or complexities in release will act to lower and broaden any observed peaks (**fig. 1**).

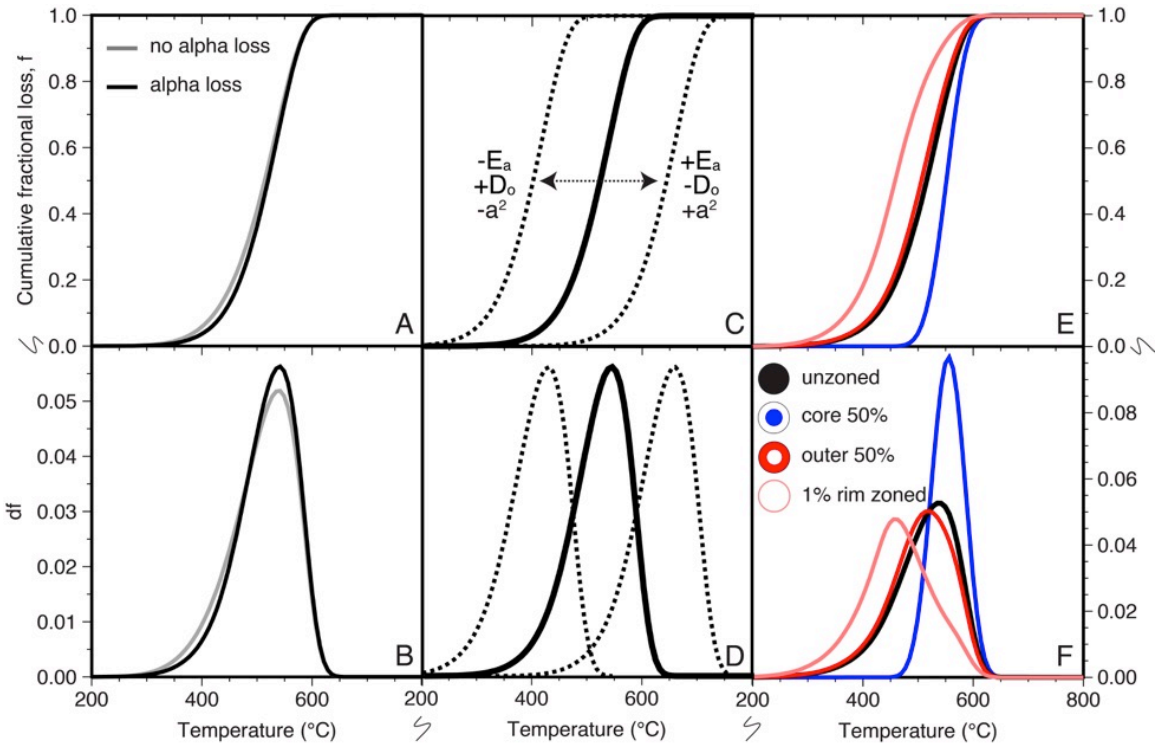


Figure 2. A) Cumulative fractional diffusive loss (*f*-curve) derived from Crank-Nicolson 1D implicit finite-difference diffusion model, using spherical geometry for a 100 µm radius apatite under simulated laboratory conditions of 20°C/minute heating rate (21.5 s time step) and Durango apatite diffusion kinetics; curves illustrate the difference between alpha and no-alpha loss cases. (B) *df*-curve peak shows gas release with increasing temperature and the minor delayed release effect of alpha-loss profile. (C) Variation in grain size (diffusion domain, a^2), heating rate, or changes to diffusivity (D_o) and activation energy (E_a) can shift the cumulative release curve in loss-temperature space, (D) the same effects on the *df*-curve peak. (E) the effects of inner-grain and outer-grain U-Th zoning on the *f*-curve, and (F) the same zoning effects on *df*-curves. Legend in F refers to hypothetical spherical grains to illustrate zoned regions of apatites (i.e. core 50% = U-Th only in grain interior) that are colored according to their respective curves.

To constrain some possible behaviors that might be observed due to volume diffusion, 1D finite-difference modeling was carried out using an implicit Crank-Nicolson solution. These models consider the effects of heterogeneous parent distribution and alpha-ejection on concentration profiles using a spherical diffusion domain geometry for a 100 µm grain radius and show the variation in cumulative loss curve form **(fig. 2)**. Standard Durango He diffusion kinetics of Farley (2000), i.e. E_a = 138 kJ/mol (33 kcal/mol) and ln D_o/a^2 = 13 m^2/s (D_o of 50 cm^2/s), and the experimental heating conditions experienced by

unknowns were used as model constraints. The cumulative fractional loss curves (**fig. 2A**) represent the impact of non-flat concentration profiles and show relatively minor shifts in curve form between an alpha loss versus a non-alpha loss scenario as gas is incrementally released with increased heating. The derivative of the fractional loss curve (**fig. 2B**) shows incremental fractional loss per temperature step (*df*) in peak form, and visually one can see that in the case of alpha-loss, the outer edge of the crystal where helium has been lost due to energetic U, Th, and Sm alpha-recoil results in delayed release of He, displacing gas to the peak top when compared to the no-alpha-loss case. Modeling the effects of parent isotope zoning in instantaneously-cooled grains shows mostly subtle variability in peak shape between unzoned and outer 1% and 50% rim-zoned examples, with deflection of the peak top to cooler temperatures related to enhanced outer grain zoning (fig. 1E-F). The grain-core 50% zoning example is markedly different, with a steep, narrow peak shifted to higher temperatures where delayed diffusion occurs over a short temperature span. The main outcomes to note are that VD predicts only smooth, unimodal behavior during outgassing, and that results are sensitive only to extreme zoning patterns.

Another point to note is that for a 20˚C/min ramp rate, outgassing is predicted by simple VD kinetics to occur between ~400-500°C, with complete exhaustion by ~600°C. This gas release is much earlier than what is observed with Durango apatite, as well as other examples obeying expected VD behavior and is a manifestation of the well-known deviation from linear Arrhenius behavior at temperatures > 280-325°C (Farley, 2000; Shuster et al., 2006). Thus, compared to simple modeled VD, natural samples experience

lowered diffusivity at higher temperatures.

2.4 Peak fitting

We used a volume-diffusion model to fit observed *df*-curves as a means of assessing cumulative loss curves and the degree to which they deviate from the expected smooth patterns predicted from theory and from analysis of well-behaved samples (see below). The purpose of this peak fitting was to distinguish between expected and anomalous gas components, and was not meant to extract kinetic information from the fitting parameters. By using a curve of the form associated with a temperature-activated diffusive process, we explored whether it is possible to correct anomalous total-gas ages by removing extraneous components. A purely diffusive process would predict only smooth, unimodal release behavior over a fairly limited temperature range, so any abrupt gas "spikes," *df*-curve bimodality, or delayed release to high temperatures would all signify anomalous behavior inconsistent with the expectations underpinning thermochronological use of the total-gas age.

He fractional loss and *df*-curves from apatite unknowns were fit to a predicted VD model by using the sample grain radius and modifying E_a, D_o, and the *df*-curve amplitude. In cases of complex release behavior this predicted curve was used to remove portions of the superfluous ^{4}He signal, i.e. spikes or late-release gas. The latter is schematically shown in figure 1 where VD and extraneous gas components are separated from one another. When using the VD model for quantifying components, as much of the observed data as possible was retained, using only the portion of the VD model that overlapped

with high-temperature release, or underlay lower-temperature spikes. Generally, when comparing unknowns to the VD model, activation energies required for good fits were commonly lower (~26 kcal/mol) with respect to accepted values for Durango apatite. This effect is due to the Arrhenius non-linearity above ~300°C that leads to lower diffusivities at higher temperatures, resulting in somewhat greater helium retentivity compared to expectations based on the lower-temperature gas release.

We propagated all analytical uncertainties from He, U, Th, and Sm measurements and those associated with the F_T (alpha-loss) and blank correction for conventional (U-Th)/He ages. We then used the VD model to correct conventional ages for grains that showed intermediate and anomalous He release. Apatite *df*-curves were initially smoothed using a median filter and the early-release (filtered) data were honored up to the high-temperature limb of the *df*-curve or to the point at which there was deviation from simple, smooth behavior. The VD model curve was then projected for the high-temperature portion of the curve using both an E_a of 25 and 35 kcal/mol to capture the potential range in *df*-curve slope (i.e. clipped amount of extra gas) at high temperatures. To estimate the error on CRH-corrected model ages, the extraneous gas amounts were removed from the total, averages and standard deviations were calculated for each E_a fit, and errors were then propagated following our conventional total-gas protocol. The 1-sigma error is typically on the order of ~2-5% for CRH age corrections, but can be higher (>10%) for curves that are more difficult to correct (i.e. ambiguous peaks or very noisy *df* signals). The errors inherent in performing CRH corrections are difficult to quantify because *df*-curves are unique for each grain. Moreover, any deviations from simple behavior are variable in

severity from grain to grain, making more disturbed curves generally harder to assess and usually requiring greater correction, see **figure 5E** vs. **figure 5C**. We fully acknowledge that error estimation is an issue requiring more rigorous study, and as this paper is mainly focused on application of the CRH method for screening, we do not address this further.

2.5 Samples

CRH experiments were performed on previously analyzed single crystals from various sample suites. Samples that were evaluated using this technique include slowly-cooled apatites (≤1°C/Ma) from central Mongolia, the central Appalachian Mountains in Pennsylvania, and the Sierra Nevada; rapidly-cooled examples (~10°C/Ma) from Tibet; and Durango and Mt. Dromedary apatites from volcanic rocks typically used as thermochronologic age standards (all shown in **Table 1**).

Table 1: Apatite sample suites for CRH method application

Sample Provenance	Host rock	Cooling Rate (°C/Ma)	Typical eU (ppm)	Exp. U-Th/He Age (Ma)	Obs. Age Range (Ma)
MN: Hangay Mtns. Mongolia	granite/diorite	~0.3-0.5	<10-135 30 (avg)	122.7 ± 24.0 (2σ)	~80-220
APL: Appalachians PA	granite	~0.4	< 10-25	164.1 ± 5.1 & 183.2 ± 7.4 (2σ)	~85-245
R: Sierra Nevada, CA	granodiorite	~0.8-1.3	~65 (avg)	~40-50	~35-90
MDC: Mt. Dromedary	monzonite	~1.5-2	~62 (avg)	86.6 (mean)*	77.8-100.8
NB: Namche Barwa, Tibet	gneiss	~10-15	~10-40	~2-8	~10-200
DUR: Durango, Mexico	rhyolite tuff	>10	~60 (avg)	31.44 ± 0.18 (2σ)	–

Table 1. Samples characterized by the CRH method: Apatites from the Hangay Mountains in Mongolia, central Appalachian Mountains in the eastern USA; Namche Barwa, Tibet; Durango, Mexico; and Mt. Dromedary, Australia. DUR is commonly used as the U-Th/He age standard. MDC is an apatite fission-track age standard yielding a date of 98.7 ± 1.1 Ma (Green, 1985). *Persano (2003) presents ages of 77.8-100.8 Ma with a mean of 86.6 Ma from rocks at Mt.

Brown that are near Dromedary but are not the same unit. Samples increase in cooling rate down the table. References for sample groups: Hangay, Mongolia: McDannell (2017); Appalachians samples CHFD and SCDM: McKeon et al. (2014); Sierra Nevada: (Fayon and Hansen, 2015); Mt. Dromedary: Persano (2003); Namche Barwa: Zeitler et al. (2014); Durango: McDowell et al. (2005). Expected U-Th/He age refers to the cooling age that is the typical result during conventional He analysis that is either internally consistent analytically or determined from comparison to other thermochronometric or geologic data. The observed age range is the scatter that is commonly associated with each sample during He dating.

Durango, Mexico

CRH experiments were carried out on internal fragments (180-250 μm) of the Durango fluorapatite (U-Th)/He age standard from the rapidly cooled volcanics of the Cerro de Mercado mine in Durango City, Mexico (McDowell et al., 2005). The careful study of McDowell et al. (2005) yields an age of 31.44 ± 0.18 Ma (2σ). Durango is appropriate for use as an age standard because it is rapidly cooled and the large cm-scale crystal size allows internal portions of crystals that have not experienced alpha-loss to be utilized. However, Durango is an atypical apatite because of the high effective uranium (eU) content (eU = [U+0.235×Th]; Flowers et al. 2009), unusual Th/U, and strong zoning in U and Th, e.g. (Boyce and Hodges, 2005).

Hangay Mountains, Mongolia

The Hangay Mountains apatite samples are from Permo-Triassic granitoids in central Mongolia, presented in McDannell (2017). These rocks are representative of a slowly-cooled terrane that has experienced denudation rates over the past ~100 Ma comparable to other ancient settings such as the Appalachians. Cooling rates through the mid-to-late Cretaceous were <1°C/Ma when (U-Th)/He cooling ages were set (McDannell, 2017). Ages are typically ~100 Ma in the Hangay Mountains and slightly older and much more variable in the outlying region. These apatites display a range of eU and grain size and

the entire dataset for screened grains using the CRH method are presented in the supplementary material.

Namche Barwa, Tibet

Zeitler et al., (2014) presented apatite (U-Th)/He data for the Namche Barwa antiform of Tibet, where rocks underwent rapid cooling and exhumation from about 10 to 5 Ma. Previous single-grain (U-Th)/He ages for NB-07 from Zeitler et al. (2014) have a mean age of 12.5 ± 0.5 Ma (n=20) and those indicated in McDannell et al. (2015) were ~11, ~14, and ~25 Ma, where nearby samples yield ages of 6.7 to 8.6 Ma. Previously analyzed NB-54 single-grain ages were ~14, ~55, and ~204 Ma, and nearby samples yield ages of ~2-7 Ma.

Sierra Nevada, California

Fayon and Hansen (2015) presented preliminary apatite (U-Th)/He results for grains taken from a small-scale brittle shear zone and undeformed country rock of the Round Valley Peak granodiorite in the Sierra Nevada of California. There are multiple shear zones (~8) cutting the Round Valley Peak granodiorite between Big McGee Lake and Hopkins Pass, potentially related to emplacement of the Mono Creek granite. Fayon and Hansen (2015) results suggest cooling-age dispersion increases with deformation, and attribute this to increased dislocation density within the crystal lattice. In their study, deformed sample 1989s24 showed single-grain ages ranging from 36 to 87 Ma with a mean of 57.9 ± 19.5 Ma, whereas the undeformed bedrock apatites yield less dispersed ages between 37 to 42 Ma, with a mean age of 40.4 ± 1.7 Ma.

Appalachian Mountains, Pennsylvania, USA

McKeon et al. (2014) presented (U-Th)/He data that showed signs of problematic behavior from slowly-cooled terranes of the Appalachian Mountains in the eastern USA. Scattered (U-Th)/He results from other studies of Appalachian samples are common and well documented, (e.g. Littlefield, 2010; Spotila et al., 2004; Taylor and Fitzgerald, 2011). Physical and chemical abrasion of Appalachian grains suggests that some are afflicted by severe crystal-core U-Th zonation, contributing to dispersed cooling ages (McKeon, 2012). Further detailed LA-ICPMS 3D grain mapping showed that these apatites can exhibit significant and complex U-Th zonation (Fox et al., 2014). Previous analyses of grains APL-CHFD-00 and APL-SCDM-00 yield pooled ages of 164.1 ± 5.1 and 183.2 ± 7.4 (2σ), and total age uncertainties of 79 and 14 Ma (2σ), respectively (McKeon et al., 2014). The McKeon et al. (2014) apatites are from granitic rocks and sample CHFD has low, pooled eU <10 ppm, while the eU for sample SCDM is 26 ppm, which is about the typical apatite value. Under Appalachian cooling rates of 0.4°C/Ma, CHFD apatites experienced closure near ~50°C, however SCDM apatite closure would be offset about 12°C warmer, under slow cooling conditions, which equates to an additional 30 Ma of cooling for SCDM grains and is verified by published ages.

Mt. Dromedary, Australia

MDC rocks were emplaced during opening of the Tasman Sea in the Cretaceous and are now exposed along the southeastern Great Escarpment margin of Australia (Ollier, 1982). Mt. Dromedary (GA1550) apatites are from the same locale as the biotite K-Ar and

$^{40}Ar/^{39}Ar$ age standard (98.5 ± 0.5 Ma; McDougall and Wellman, 2011), and apatite fission-track age standard (98.7 ± 1.1 Ma; Green, 1985). Dromedary apatite He ages typically range between ~80-90 Ma and nearby at Brown Mountain to the SW, apatite cooling ages range between 77.8 to 100.8 Ma, with an average of ~86 Ma (Persano, 2003; Persano et al., 2005), suggesting the Australian margin developed rapidly after rifting. MDC apatites are old and underwent cooling rates on the order of ~1.5 to 2°C/Ma through the apatite He partial retention zone (Persano, 2003). The cooling rates near Mt. Dromedary equate to closure temperatures of ~68-69°C using the RDAAM model (Flowers et al., 2009), while conventional Durango kinetics yield a closure temperature ~10°C lower.

3. Results

Apatite grains for all sample suites were selected via typical He-dating microscope picking methods as previously described. Additionally, grains were also picked that contained evident fluid or mineral inclusions for the purpose of documenting their CRH degassing character. We placed the samples we investigated using the CRH method into three broad categories, (1) expected, (2) intermediate, and (3) anomalous, based on diffusive behavior during outgassing (**fig. 4**). These categories are semi-quantitative, based on empirical performance, comparison to Durango apatite patterns, and descriptive statistics. Using our laboratory heating protocol, apatites showing expected behavior should release between ~5% to 95% of ^{4}He between ~450 to 800°C and be totally exhausted by ~900°C, as is observed in the degassing behavior of a reference group of Durango standard grains (n=15), (**fig. 3**) and a subset of well-behaved Mongolian

apatites. Durango apatite shows very systematic, smooth release that varies slightly only due to grain size dependence.

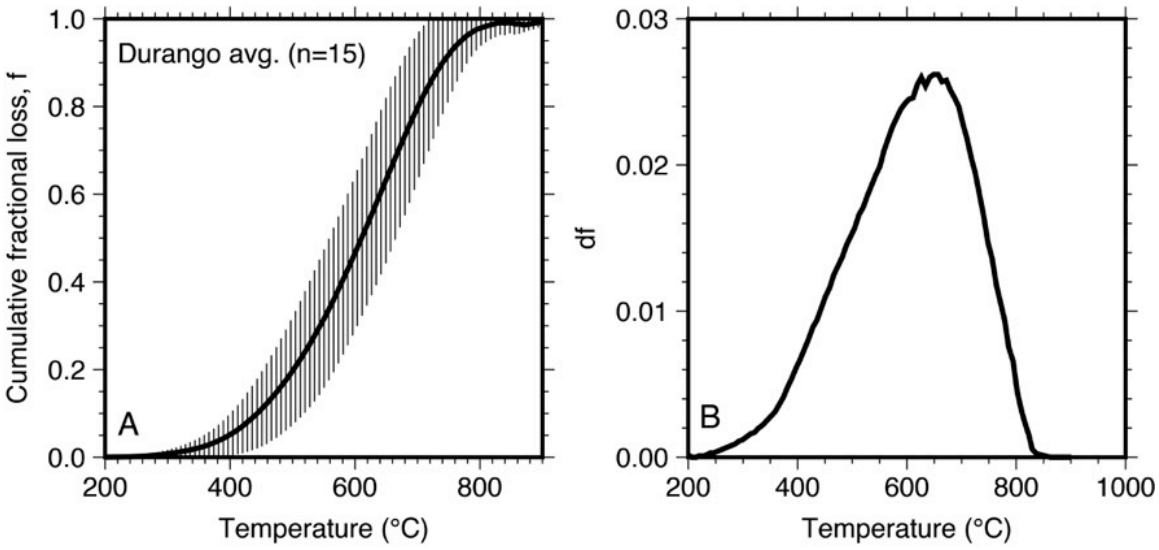


Figure 3. A) Plot of the mean cumulative *f* with increasing temperature following a 20°C/min heating rate for Durango apatite (n=15) shown with two standard deviations. Real Apatites obeying simple diffusion behavior should be totally exhausted of ^{4}He by ~850-900°C under a 20°C/min heating rate. See text for discussion. B) The average *df*-curve for same grains as in panel A. Note that Durango apatites obey smooth, simple diffusive behavior. Durango internal shards are 180-250 μm, with a spherical equivalent radius (R_s) of ~100 μm.

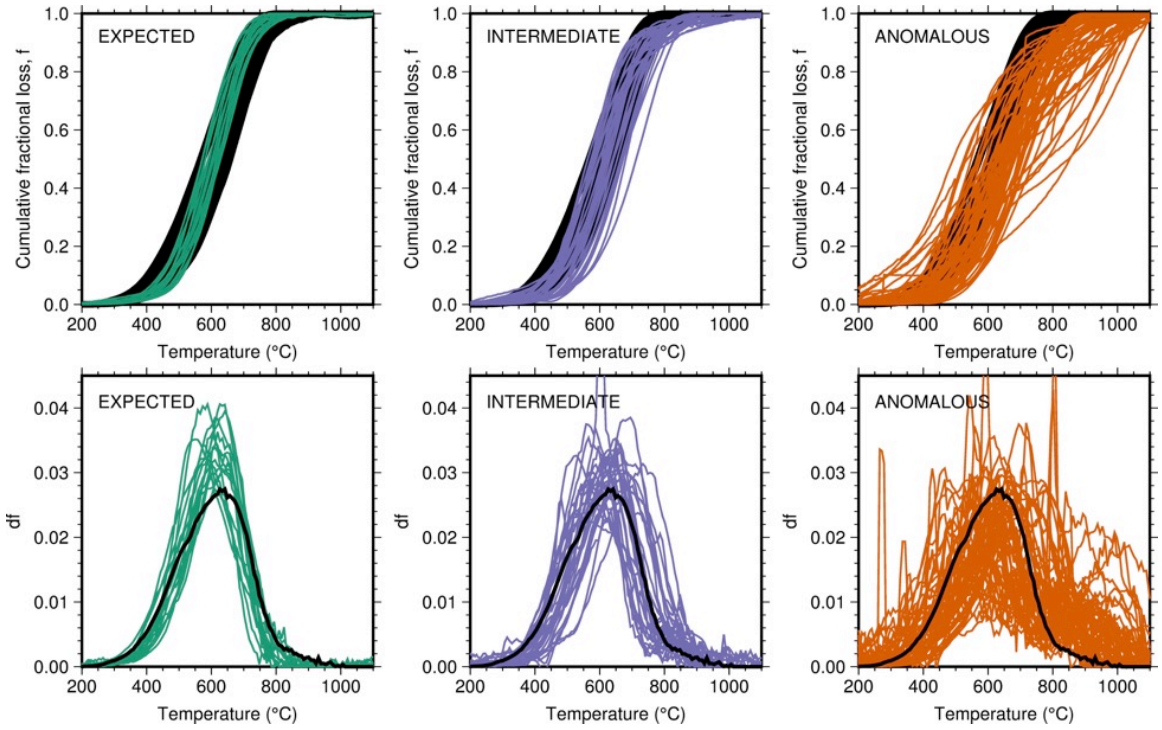


Figure 4. Summary of the CRH (U-Th)/He screening results for the apatite suites shown in Table 1. Apatites that follow expected, smooth behavior are shown in green, intermediate grains are shown in purple, and grains that exhibit anomalous diffusive loss are shown in orange. Black envelope (upper plots) represents 16 Durango apatites (180-250 μm sieve size) for comparison. Cumulative *f*-curves suggest 'expected' grains are completely outgassed by ~900°C, while intermediate examples show more flattened release at high-temperature due to excess gas, but are nonetheless exhausted by ~950-1000°C. Anomalous grains have a less sigmoidal, and sometimes linear approach to high-temperature and some are still outgassing past 1000°C. *df*-curves (bottom plots) smoothed using a 3 pt. moving average. Black curve is an example Durango apatite for comparison.

Anomalous apatites are designated as apatite grains that show inflections in *f*-curves (represented as multi-modal *df*-curve peaks), significant gas spikes, or any severe deviation from smooth release, while intermediate apatites may show some subtle irregularities. Note that small spikes or "tails" of gas late in the derived *df*-curves that are only a few percent or less of the total sum of ^{4}He are still atypical with respect to VD predictions, yet do little to affect the estimated cooling age, as they are still within the normal bounds of apatite (U-Th)/He reproducibility and fall into an "intermediate" category between expected and anomalous behaviors. ^{4}He signal strength becomes a

concern when evaluating CRH results from younger and/or lower-eU samples, and is especially problematic as *df*-curves can become noisy and make it difficult to identify anomalous degassing behavior.

We assessed 122 apatite grains in total using the CRH method, and if the expected and intermediate results are grouped together then about half of the grains we analyzed demonstrate expected, smooth diffusive behavior and the other half exhibited clearly anomalous outgassing characteristics. Note this overall summary does not necessarily apply to apatite He diffusion behavior in general since our results reflect our choice of samples – we intentionally chose several samples that we knew showed problematic behavior. Below, we examine our results from different geologic settings in more detail. Errors in He ages are reported as analytical uncertainty for the majority of cases unless otherwise noted in figures or tables.

3.1 Mongolia CRH results

Mongolian examples make up the majority of our CRH screening results and display a range of behaviors (see figure 6 for all curves). Peak fitting of Mongolian apatites (**fig. 5**) show observed *df*-curves with VD model predictions. In cases where gas spikes and/or high-temperature excess gas were present, fitting necessitated the removal of these components (**fig. 5C-F**). Grain 14MN09-d157 (**fig. 5C**) is an example of the 12-point median filter that was used to smooth *df*-curves and the VD correction was applied to the peak shoulder to remove excess helium. This grain has a conventional (U-Th)/He age of

109.87 ± 1.63 Ma and a >15% reduction in age following CRH correction (91.6 ± 1.8 Ma).

Sample 12MN22 (**fig. 5D**) has a conventional single grain He age of 190.41 ± 3.35 Ma and one grain (12MN22-d158) degassed using the CRH method yields a total-gas age of 227.10 ± 4.87 Ma, with similar grain size and eU between both grains. If the gas spike and slight high-temperature irregularities are removed from the *df*-curve, the CRH single-grain He age recalculates to 204.7 ± 4.5 Ma. The difference in arithmetic mean between conventional (U-Th)/He and CRH corrected ages produces a ~5% mean age reduction and shows better internal age consistency. This apatite is an example of a purposely degassed grain with inclusions, while a third grain from this sample that contained visible inclusions was also purposely degassed under conventional extraction line conditions and gave a much older age >300 Ma.

Sample 12MN36 (**fig. 5E**) generally exhibits smooth release, and was dated using conventional (U-Th)/He analysis (n=2) and also underwent CRH analysis (n=4). This sample does display slight eU-age correlation and no clear trend in grain size with age is observed. The grain shown in the figure corrects from 98.87 ± 1.41 Ma to ~83 Ma when the small gas "tail" is removed. Conventional ages for this sample range from ~96-130 with a mean of 111.97 ± 1.5 Ma, and after CRH correction the mean is 108.61 ± 1.5 Ma; although the mix of conventional and CRH analyses makes any further inter-comparison difficult.

Cases where irregular behavior was observed, such as in **fig. 5F**, the volume-diffusion model was fit to the entire observed *df*-curve. Sample 14MN18 conventional (U-Th)/He cooling age replicates are ~139, ~145, ~211 without CRH correction and display slight grain size-age correlation and roughly the same eU between each grain (single-grain age in **fig. 5F** is 211.29 ± 3.28). The two younger ages for sample 14MN18 demonstrate expected behavior (not shown), while the ~211 Ma grain indicated here deviates from smooth release between ~400-600°C and corrects to 172.6 ± 10.4 Ma and is ~35% larger than the other grains. In all 14MN18 cases, the level of correction is moderate and where there is greater scatter it can usually be explained by grain size or eU.

Table 2: Mongolian samples (subset) for age correction

Sample	(U-Th)/He Age (Ma)	± 1σ (Ma)	CRH model age (Ma)	± 1σ (Ma)	Rs (um)	eU cyl. (ppm)
12MN36-1-conv	*128.82*	*1.49*			54.0	33.9
12MN36-2-conv	*97.29*	*1.12*			66.7	16.6
12MN36-1c-d159	122.00	2.29	(95.8)	2.2	72.6	26.9
12MN36-2c-d159	120.89	2.28	(64.0)	2.3	92.7	26.9
12MN36Ac-d158	98.87	1.41	(82.7)	2.3	98.2	27.6
12MN36Bc-d158	103.97	1.47	(97.8)	1.7	75.8	28.9
Mean ± 1σ (Ma)	*111.97 ± 1.74*		*85.1 ± 2.12*			
12MN44-1-conv	*104.04*	*1.16*			62.0	8.8
12MN44-2-conv	*165.22*	*1.77*			106.4	5.7
12MN44-3-conv	*157.44*	*1.72*			66.1	6.8
12MN44-1c-d159	101.59	1.96	(64.0)	9.6	65.0	6.2
12MN44-2c-d159	116.17	2.41	(59.5)	1.8	67.2	6.6
12MN44-3c-d159	106.03	2.17	(61.2)	2.2	56.1	6.7
Mean ± 1σ (Ma)	*125.08 ± 1.91*		*61.5 ± 5.8*			
14MN09-d165	134.74	2.25	(94.1)	2.1	46.2	30.7
14MN09-d157	109.87	1.63	(91.6)	1.8	54.2	18.1
14MN09-1-d162	142.77	6.53	(124.9)	5.4	80.1	17.3
Mean ± 1σ (Ma)	*126.13 ± 4.10*		*103.5 ± 3.5*			
14MN15-1c-d165	81.13	1.83	(65.4)	1.6	51.8	53.7
14MN15-2c-d165	70.13	1.60	-	-	75.4	54.2
14MN15c-d157	61.04	0.89	(48.7)	1.3	54.0	36.4
Mean ± 1σ (Ma)	*70.77 ± 1.50*		*57.1 ± 1.5*			
14MN18c-d158	211.29	3.28	(172.6)	10.4	96.4	1.3
14MN18c-d165	145.32	3.70	(126.2)	3.4	61.2	2.1
14MN18-1c-d162	138.98	6.36	(131.1)	5.6	73.2	1.8
Mean ± 1σ (Ma)	*165.20 ± 4.03*		*143.30 ± 6.1*			
12MN22-1-conv	*190.41*	*2.78*			51.2	10.0
12MN22-3-conv	~~333.65~~	5.36	inclusions present		61.2	9.7
12MN22c-d158	227.28	4.31	(204.7)	4.5	58.6	9.1
Mean ± 1σ (Ma)	*208.84 ± 3.63*		-	*New mean: 197.6 ± 3.7*		
11KWW04-1-conv	*109.99*	*1.19*			68.8	35.9
11KWW04-2-conv	*68.86*	*2.54*			58.9	9.5
11KWW04-3-conv	*206.92*	*1.69*			53.4	54.8
11KWW04-1c	128.36	2.41	(122.6)	4.2	60.3	35.9
11KWW04-2c	106.08	2.05	(85.8)	2.2	74.3	43.7
Mean ± 1σ (Ma)	*124.04 ± 2.04*		*104.2 ± 3.3*			

Table 2: Subset of Mongolian apatites for CRH age correction. Sample names in bold are those that were degassed using the CRH method while those with the –conv suffix were analyzed via conventional total gas analysis. All 1-sigma errors are propagated from He, U, Th, Sm

measurements, the Ft correction, and extraction line blanks. CRH corrected model ages also include uncertainties in fitting procedures using VD model curve with activation energies of 25 and 35 kcal/mol, further explained in text. Mean age 1-sigma uncertainties are calculated from propagation of analytical uncertainties only. Rs = apatite spherical equivalent radius in microns; eU = effective Uranium content for spherical geometry. All Mongolia results are shown in figure 6.

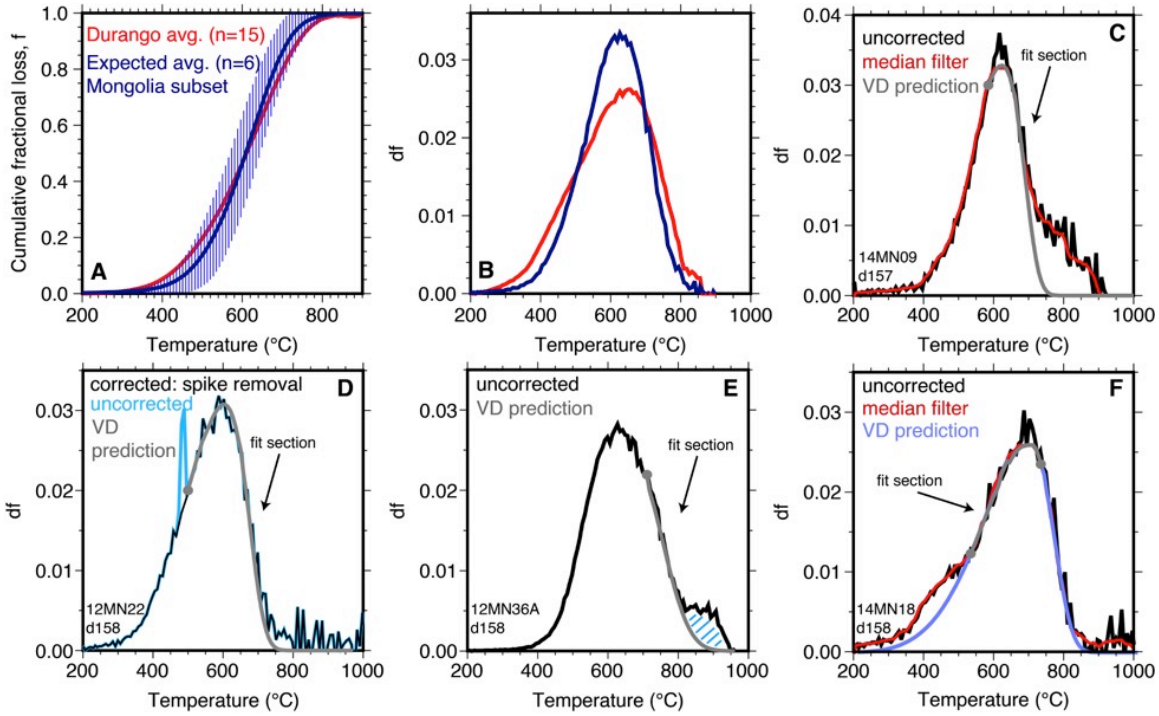


Figure 5. Comparison of expected behavior, Durango behavior, and fitting examples**.** (A) Subset of Mongolian apatites (mean ± 2 standard deviation of fractional loss values) that show expected, smooth behavior compared to the Durango average (same as fig. 4). Note the alpha vs. no-alpha profile difference between the cumulative *f*-curves. (B) *df*-curve difference between the Mongolian and Durango group averages. Panels C-F: Examples of peak fitting applied to Mongolian apatites where *df*-curves are analyzed to yield the corrected CRH age. Minor fitting examples using: manual gas spike removal and minor gas component above 800°C (D), keeping observed data until the shoulder where the VD model is utilized to remove excess He at high-temperature (E), and in panel F the VD prediction is shown for the entire observed *df*-curve as well as the region that is used in fitting. The peak fitting in F shows VD model correction and removal of early, abnormal "bump."

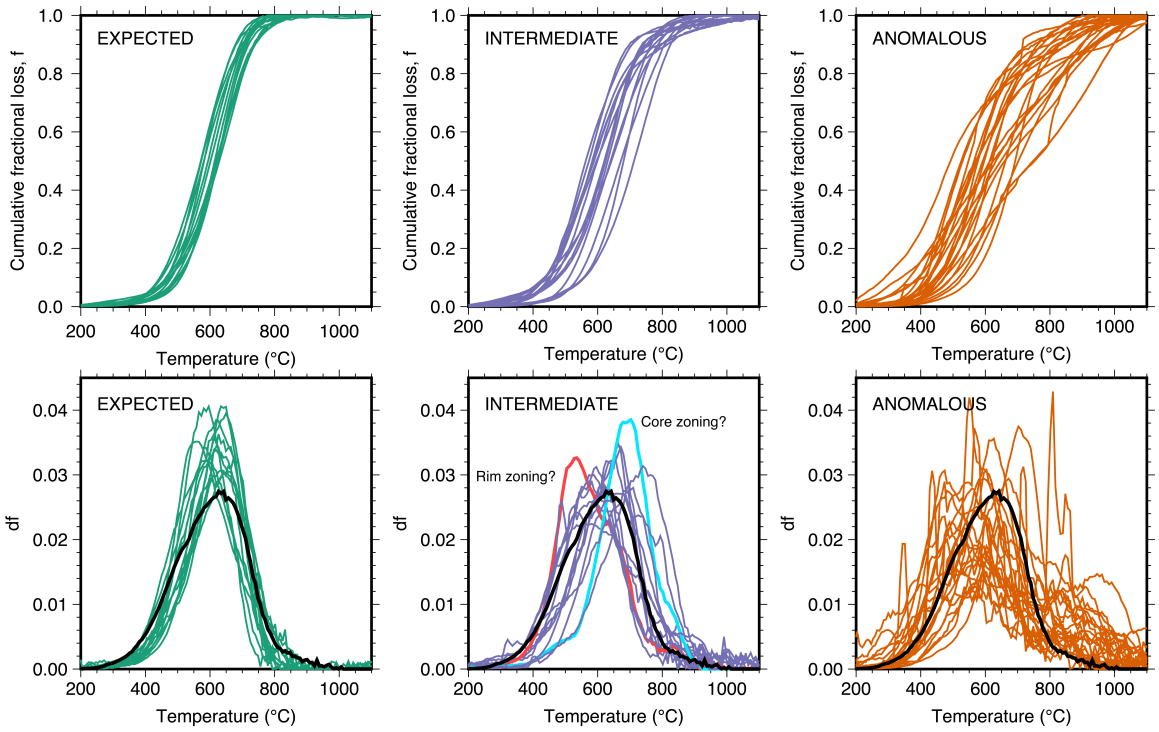


Figure 6: Summary of *f* and *df*-curves from Mongolia with same scheme as figure 4. In these examples the grains that follow smooth expected behavior in green are tightly grouped and *df*-curves are very similar to a representative Durango curve shown in black. The intermediate group shows more variability in release behavior and the blue and red curves appear to match the isotopic-zoning model results for core and rim zoning to first-order (core example is sample 14MN08-d157, conventional He age of ~70 Ma; CRH corrected to ~65 Ma). Anomalous results show non-smooth release with many gas spikes and deferred release beyond what is typically expected, i.e. see Durango. *df*-curves are smoothed using a 3-point moving average.

3.2 Namche Barwa CRH results

Apatite samples NB-07-26 and NB-54 from Namche Barwa were investigated using the CRH method (**fig. 7**). NB-54 screening shows some abnormal behavior and in this study we obtained ages between ~10 to ~17 Ma using conventional total-gas analysis (mean age of 15.36 ± 0.42 Ma, including a much older grain with an age of ~30 Ma). In the absence of screening, and without regional age control, it would appear that this sample reproduces moderately well with some outliers. However, ages nearby suggest that despite this, all of the ages are still too old, as they should produce cooling ages <10 Ma.

Sample NB-07 is even more dispersed with a mean age of 22.07 ± 0.52 Ma and much older than surrounding ages.

For the purposes of extracting extraneous components and correcting ages, *df*-curves are first smoothed using a 12-point median filter, followed by VD peak-fitting, then the size of the diffusive component of the outgassed ^{4}He was determined. This component was then used to calculate CRH-corrected ages (**Table 3**). NB-54-d159 has a very disturbed *df*-curve without a discernible peak or obvious correction scheme and therefore was excluded from CRH correction. Other grains that showed highly deferred release or that had no apparent peak were also not corrected.

The CRH-corrected ages show much better internal age agreement and agreement with surrounding cooling ages. The CRH correction results in a ~45% decrease in the mean NB-54 He age and a ~70% reduction to the mean NB-07 age. For those samples we did not model, if one uses the area of fractional-loss space normally spanned by Durango apatites and makes an age correction based on that amount, the old ages correct to reasonable dates (denoted by stars in **Table 3**). We report this an interesting observation but we would not recommend using ages obtained with such an approach.

Table 3: Samples NB54 and NB07 age correction

Sample	(U-Th)/He Age	± 1σ (Ma)	CRH model age (Ma)	± 1σ (Ma)	Rs (μm)	eU (ppm)
NB54-1	13.89	0.30	(9.3)	0.3	54.35	11.4
NB54-2	17.08	0.39	*	*	45.59	14.9
NB54-4	10.43	0.20	(5.9)	0.3	79.22	10.5
NB54-5	10.81	0.22	(8.3)	0.3	71.25	7.8
NB54-6	13.92	0.26	(9.0)	0.5	60.90	20.1
NB54-7	11.81	0.23	(8.4)	0.4	60.89	12.2
NB-54-d159	29.61	0.89	*	*	58.07	8.7
Mean age: 15.36 ± 0.42 [± 13, 2σ]			*(8.2) ± 0.4* [± 2, 2σ]			
Exp. age:	***~2-7***					
NB07-2	9.72	0.19	(5.8)	0.2	57.63	39.1
NB07-4	11.80	0.23	(7.1)	0.2	50.72	55.3
NB07-6	27.54	0.65	*	*	43.47	12.7
NB07-7	24.81	0.47	-	-	52.70	55.2
NB07-8	12.41	0.24	*	*	57.42	44.2
NB07-9	46.11	0.93	-	-	36.54	42.9
Mean age: 22.07 ± 0.52 [± 28, 2σ]			*(6.4) ± 0.2* [± 2, 2σ]			
Exp. age:	***~6-9***					

Table 3. Sample NB54 and NB07 ages before and after CRH correction. NB-54 shows He ages that are consistent albeit with a few outliers, but nevertheless too old given the surrounding cooling ages (expected age ~2-9 Ma) even if outliers are removed. Zeitler et al. (2014) NB-07 mean age is 12.5 ± 0.5 Ma (n=20). Using peak fitting the ages then can be corrected and end up being in much better agreement with local data and each other. CRH corrected ages with stars discussed in text and dashes were those that were unable to be corrected. NB-07 had fewer grains that had obvious peaks and most were deferred to temperatures well beyond VD norms, so were excluded from correction. (U-Th)/He age is the age using the standard measured total gas ^{4}He amount. CRH age is corrected using peak fitting and removal of surplus gas. 1σ errors on U-Th/He ages are analytical error propagated from uncertainties from He, U, Th, Sm and Ft and blank corrections (and error in CRH correction). Mean ages are the arithmetic mean and reported 2-sigma errors are calculated from the standard deviation of component measured/CRH ages only, discounting analytical uncertainty.

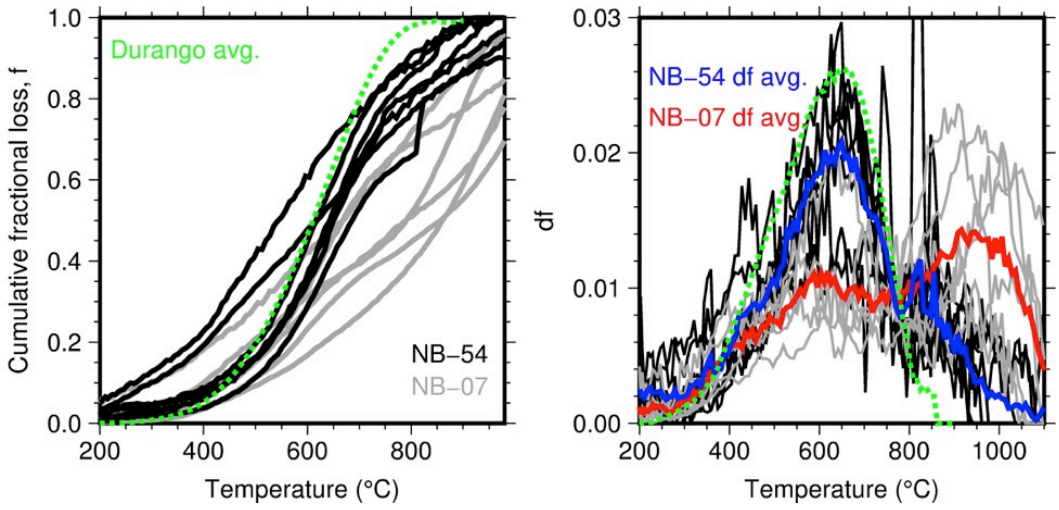


Figure 7. Cumulative fractional loss and smoothed (3 pt. moving average) *df*-curves for Tibetan samples NB-07-26 and NB-54. Conventional He ages obtained in the NB group ranged from 9.72 ± 0.19 to 46.11 ± 0.93 Ma. Helium signals for these samples were low, which yield noisy *df*-curves. NB-07 displays a substantial gas component delayed to high-temperature; see red curve for average of release bundle. NB-54 looks much better overall (see blue avg. curve compared to green Durango curve), but has elevated early release and minor secondary gas as well. Note that most of these apatites (mainly NB-07) never quite reached 100% ^{4}He loss, even above 1100°C.

3.3 Sierra Nevada CRH results

Screening results for the relatively undeformed sample R9515 and deformed sample 1989s24 are shown in **Table 4** and **figure 8** and demonstrate that screening using CRH can differentiate between grains that display expected-to-intermediate behavior and anomalous examples that also show dispersed ages. Apatite grains from the relatively undeformed sample R9515 show results that fall broadly into our "intermediate" category, showing behavior similar to the average Durango apatite, with smooth release and total degassing by about 900°C, albeit with a steepened approach to f=1 due to a small amount (<5%) of high-temperature gas. Sample 1989s24 vastly deviates from smooth diffusive behavior (**fig. 8C**) and the *df*-curve reveals a spurious high-temperature gas tail representing ~40% of the total gas on average. Sierra apatites also show very

distinct spikes intermittently during degassing that are generally a small amount of gas, however in addition to a low ^{4}He signal this can complicate release curve categorization and the uncertainty in the age correction that is applied.

Table 4: Sierra Nevada samples 1989s24 (deformed) and R9515 (undeformed) age correction

Sample	(U-Th)/He Age (Ma)	± 1σ (Ma)	CRH model age (Ma)	± 1σ (Ma)	Rs (μm)	eU (ppm)
1989s24-01	50.49	1.25	(27.4)	1.0	74.8	96.4
1989s24-04	59.73	1.47	(31.0)	1.2	65.6	75.1
1989s24-05	63.18	1.56	(40.6)	1.3	51.3	57.9
1989s24-07	103.49	2.51	(47.7)	1.9	51.0	39.1
Mean age:	69.22 ± 1.77	± 47 (2σ)	(36.7) ± 1.4	± 18 (2σ)		
1989s24: Fayon & Hansen (2015)						
Mean age: 57.90 ± 19.50		**Range: 36 to 87**				
R9515-03	64.56	1.55	(59.2)	1.3	52.1	50.8
R9515-04	36.93	0.90	(33.6)	0.7	46.4	85.8
R9515-05	49.35	1.20	(42.7)	1.1	37.6	41.4
R9515-06	39.18	0.95	(32.2)	1.0	56.5	73.8
R9515-07	42.10	1.01	(35.9)	1.3	72.4	69.9
R9515-08	38.59	0.93	(32.9)	1.0	77.6	61.8
Mean age:	45.12 ± 1.11	± 21 (2σ)	(39.4) ± 1.1	± 21 (2σ)		
w/o R95-03:	41.23 ± 1.00	± 5 (2σ)	(35.5) ± 1.1	± 4 (2σ)		
R9515: Fayon & Hansen (2015)						
Mean age: 40.40 ± 1.70		**Range: 37 to 82**				

Table 4. CRH age correction results for Sierra Nevada samples 1989s24 (deformed) and the relatively undeformed sample R9515. (U-Th)/He age and error are calculated as conventional analyses ages while the CRH corrected ages are screened and the *df*-curves are fit with a VD correction. The gas amount is then reduced and the age is recalculated. Compared to the Fayon and Hansen (2015) results, CRH means are corrected slightly younger, as even the 'undeformed'

sample still shows some irregular behavior. After CRH correction the mean ages are identical within error. Curves are shown in fig. 7. All 1-sigma errors are propagated from analytical He, U, Th, Sm measurements, Ft correction, extraction line blanks, and errors associated with CRH curve fitting. Reported 2-sigma errors are calculated from the standard deviation of component measured/CRH ages only, discounting analytical uncertainty.

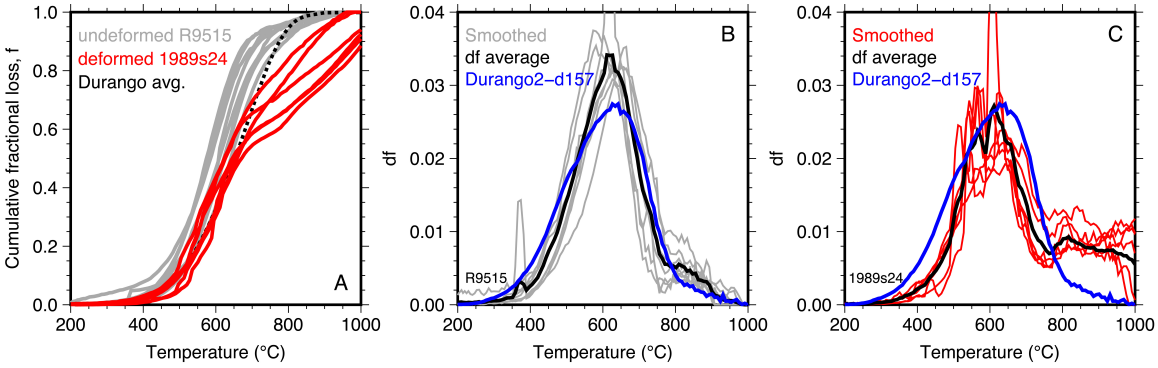


Figure 8. Screening results for two samples from the Round Valley Peak granodiorite in the Sierra Nevada: the relatively undeformed R9515, and the deformed apatite, 1989s24, where the latter shows considerable age scatter, originally introduced in Fayon and Hansen (2015). A) Cumulative *f*-loss with increasing temperature for multiple R9515 samples (gray lines) and sample 1989s24 (red lines). Here R9515 is relatively well-behaved. Black dashed line is the *f*-loss of an averaged bundle of 15 Durango apatites. B) Smoothed (3 pt. moving average) *df*-curves for R9515 in gray, while the black line shows the average behavior of the group. A typical Durango is shown for comparison (blue curve) and the R9515 'intermediate/expected' group is similar in behavior to the Durango example. C) Same as B but for the deformed sample 1989s24, where there is an irregular, narrow peak shape and clearly a high-temperature component that deviates from both smooth, expected behavior and Durango behavior.

3.4 Appalachians CRH results

Screening results for Appalachian samples APL-CHFD-00 (n=7) and APL-SCDM-00 (n=9) show cumulative *f*-curves shifted towards higher temperatures when compared to *f*-curves from an averaged bundle of Durango apatites (n=15) and a smaller subset of well-behaved (n=6) Mongolian apatites (**fig. 9**). Appalachian SCDM *df*-curves display greater displacement towards high-temperature and consistently show a small extraneous gas component, while CHFD curves are both less displaced with respect to Durango and have less high-temperature perturbation. Peaks for most grains are also wider at the peak top,

when compared to other analyzed samples. The SCDM grains have an average high eU of 46 ppm and average Rs of 106 μm, while CHFD grains have an average eU of 26 ppm and an average Rs of 79 μm. Conventional He ages from this study range from 59.86 ± 4.02 (1σ) Ma to 443.64 ± 28.78 for sample SCDM and 169.71 ± 11.29 Ma to 239.82 ± 15.84 Ma for sample CHFD. There is also a very strong positive age-grain size relationship for SCDM apatites that is maintained after CRH correction.

Table 5: Appalachian samples SCDM and CHFD age corrections

Sample	(U-Th)/He Age (Ma)	± 1σ (Ma)	CRH model age (Ma)	± 1σ (Ma)	Rs (μm)	eU (ppm)
APL_SCDM_01	190.34	12.64	(158.1)	16.7	116.5	30.1
APL_SCDM_02	443.64	28.78	(301.6)	36.6	126.0	20.0
APL_SCDM_03	59.86	4.02	(44.7)	7.1	78.7	153.1
APL_SCDM_04	146.57	9.77	(113.6)	9.3	96.4	42.0
APL_SCDM_05	219.08	14.51	(153.4)	16.8	106.4	25.2
APL_SCDM_06	338.69	22.18	(271.0)	34.0	115.2	21.8
APL_SCDM_07	172.97	11.50	(132.7)	15.3	105.3	44.6
APL_SCDM_08	127.57	8.52	(96.0)	8.1	96.2	53.2
APL_SCDM_09	265.11	17.48	(227.5)	24.0	109.3	23.2
Mean age ± 1σ	218.20 ± 16.03		166.5 ± 21.3			
APL-SCDM-00: McKeon et al. (2014)						
Pooled age: 183.2 ± 7.4 (2σ)						
APL_CHFD_01	219.86	14.55	(174.7)	11.0	38.4	129.8
APL_CHFD_02	239.82	15.84	(214.7)	11.5	81.4	10.5
APL_CHFD_03	184.78	12.28	(157.7)	9.2	83.3	5.1
APL_CHFD_04	216.76	14.34	(129.1)	7.8	88.9	12.1
APL_CHFD_05	169.71	11.29	(149.5)	8.2	81.8	6.6
APL_CHFD_06	174.90	11.63	(169.8)	8.5	90.9	6.0
APL_CHFD_07	186.90	12.42	(177.8)	9.3	88.4	11.8
Mean age ± 1σ	198.96 ± 13.29		167.6 ± 9.4			
APL-CHFD-00: McKeon et al. (2014)						
Pooled age: 164.1 ± 5.1 (2σ)						

Table 5. Appalachian samples SCDM and CHFD. CRH correction produces mean age reductions of up to ~20%. Conventional (U-Th)/He ages are shown with CRH ages in parentheses denoting ages after CRH correction. After correction both granites show approximately the same mean age. All errors are propagated from analytical He, U, Th, Sm measurements, Ft correction, extraction line blanks, and errors associated with CRH curve fitting.

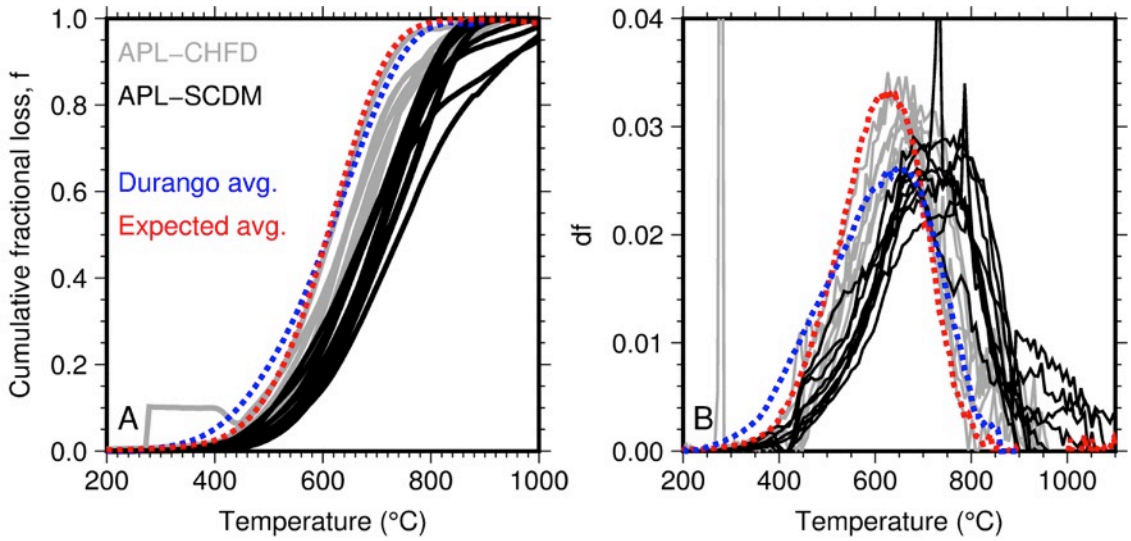


Figure 9. Screening results for Appalachian apatites from SE Pennsylvania. A) Cumulative *f*-curves are offset to higher temperatures compared to Mongolian subset observing expected behavior (dashed red curve, n=6) and Durango average (dashed blue curve, n=15), with sample APL-CHFD being more delayed and still releasing He at temps. >1000°C. If APL grains were kinetically the same as Durango or expected examples they should approximately overlap. APL spherical equivalent radii are ~70-100 μm, smaller or roughly equal to Durango fragments, therefore a shift to higher T is unlikely to be controlled by grain size.

3.5 Mt. Dromedary CRH results

Screening results for the Mt. Dromedary Complex apatites show ^{4}He release offset to higher temperature for the majority of grains, displaying similar behavior to Appalachian grains **(fig 10)**. Conventional ages obtained in our study range from 72.88 ± 1.90 Ma to 84.86 ± 2.21 Ma, with an average age of 77.59 ± 4.10 Ma (without CRH correction). These apatites cluster much better in age and release behavior than the APL apatites, but there is a negative correlation between age and grain size and a slight positive trend between eU and age. Overall, our results that include CRH age correction yield ages slightly younger than previously published ages. Grains that underwent CRH treatment

yield a characteristically high, average eU of 61 ppm (average Rs of 80 μm), which implies high levels of radiation damage. Durango apatite is also high eU, typically ~40-60 ppm, but over half the age and cooled very rapidly.

Table 6: Mount Dromedary sample GA-1550 age correction

Sample	(U-Th)/He Age (Ma)	± 1σ (Ma)	CRH model age (Ma)	± 1σ (Ma)	Rs (um)	eU cyl. (ppm)
GA1550_01	75.76	1.97	*70.7*	3.2	74.9	63.1
GA1550_02	76.75	2.00	*68.2*	2.3	81.8	52.5
GA1550_03	72.88	1.90	(62.4)	2.1	99.2	74.1
GA1550_04	73.49	1.91	(60.3)	2.5	91.2	53.4
GA1550_05	83.91	2.19	(77.5)	3.5	76.0	66.7
GA1550_06	84.86	2.21	(70.9)	3.1	57.3	72.4
GA1550_07	74.00	1.92	(61.5)	3.0	91.8	45.0
GA1550_08	79.07	2.06	(72.0)	4.0	69.4	64.5
Mean ± 1σ (Ma)	77.59 ± 2.02		67.9 ± 3.0			
Total uncertainty:	± 9 (2σ)		± 12 (2σ)			
Total range (Ma):	68 to 87		56 to 80			

Table 6. CRH age correction for MDC samples. GA1550-1 and GA1550-2 follow expected behavior while the rest of grains display intermediate behavior. The first two 'expected' behavior samples were corrected for consistency (in italics), however their total-gas ages are still reasonable and have very little influence on the mean age calculation when used in place of CRH model ages. All of these samples had small corrections with minor gas tails removed in most cases. These ages could be viewed as a generous estimate, although the conventional ages and CRH model ages overlap at the 2-sigma level. All errors are propagated from analytical He, U, Th, Sm measurements, Ft correction, extraction line blanks, and errors associated with CRH curve fitting. Total uncertainty is calculated from component total-gas and CRH ages only, discounting 1-sigma analytical errors. Total age range is using the 2-sigma uncertainty.

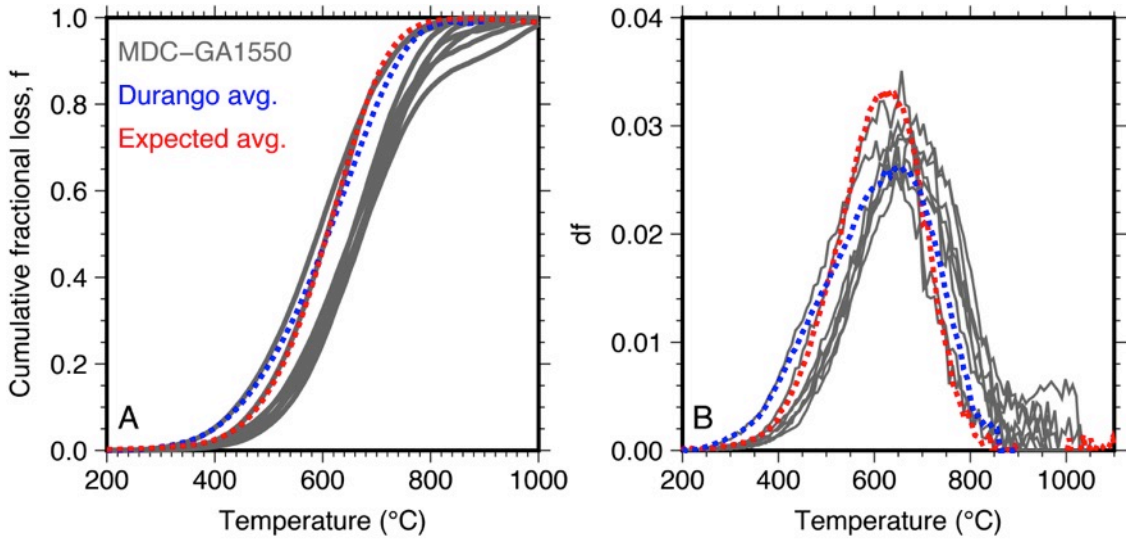


Figure 10. Cumulative fractional loss and *df*-curves for Mt. Dromedary samples (GA-1550). Notice relatively consistent behavior with release deferral to higher temperature. Two apatites are clearly offset from the rest of the group and align well with an expected group of Mongolian samples (red curve) and the Durango average (blue curve). The two MDC curves that overlay with Durango and expected results (GA1550-1 and GA1550-2) have identical ages of 75.76 ± 1.97 Ma and 76.75 ± 2.00 Ma. Overall, the behavior of MDC samples is similar to the APL suite.

4. Discussion

4.1 General observations

All *df*-curves show release of a component of He that is consistent with volume-diffusion behavior, including anomalous apatite samples. The CRH method also seems quite sensitive in that modestly deferred, early release attributed to alpha-ejection and diffusive-loss profiles can be distinguished from curves predicted for internal shards of Durango apatite with uniform ^{4}He concentration, (cf., fig. 2A, B; and natural samples in fig.4). Durango CRH behavior demonstrates smooth release, which should be anticipated for grains that have low age dispersion. It is also worth noting that most grains in the intermediate and expected groups often overlay with Durango *df*-curves, which suggests kinetic similarity or consistent diffusive loss under the same heating conditions in different apatite suites. Apatites that follow expected, smooth behavior represent about

half of the total pool of our analyzed apatites; this is reduced marginally if Durangos are excluded. However, as a reminder we did choose some grains that would not normally be used for conventional He dating. The majority of grains displaying anomalous degassing behaviors are classified by delayed release at high-temperature or multiple *df* peaks, with gas spikes as a tertiary feature that can muddle an otherwise simple release shape.

4.2 Gas spikes

A number of our samples showed anomalous gas release in the form of sharp spikes. These could possibly be related to fluid-inclusion decrepitation, as seen in the results from apatite 12MN22, which was an apatite purposely chosen because it contained numerous visible inclusions (**fig. 5)**. The 'popping' of inclusions and gas liberation is not confined to any particular temperature range, though it seems more common at lower temperatures. This could simply be due to the location of the inclusion within a grain, so inclusions near the crystal rim have a far greater chance to decrepitate, while more internally located fluid inclusions might not decrepitate as readily.

4.3 High-temperature release

Very small inclusions of more refractory minerals like zircon might lead to high-temperature He release. Alternatively, volume defects that have trapped He could act as the source for secondary gas components liberated at high temperatures. A variant of this model would involve He trapped in small fluid inclusions located deep within crystals that, unable to decrepitate, instead serve as a drawn-out higher-temperature source of gas that obscures the late release pattern.

4.4 Evidence for kinetic variability

The release characteristics of the MDC and APL apatites are suggestive of radiation damage (concomitant with slow-cooling, old ages, and eU) causing displacement of release curves to higher temperatures. The transferal of loss curves towards higher temperature is likely due to these apatite grains being more retentive (lower D_o), which broadens the *df* peak and shifts it warmer. The grain size for APL samples are approximately equal to, or less than Durango; therefore grain size is unlikely to be a primary control, see **figure 9 and Table 5**. APL and MDC apatites show delayed CRH behavior and the lack of a convincing grain size relationship for most grains in the presence of high eU implies that radiation damage effects on diffusivity surpass other known controls, in accordance with Shuster et al. (2006). Irregular zoning patterns previously observed in these grains, such as those discussed in Fox et al., 2014, may not be resolved via screening or are not readily discriminated from other minor fluctuations in diffusion kinetics.

4.5 Evidence for the role of deformation and apatite microstructures

The Sierra Nevada results tentatively support the hypothesis of Fayon and Hansen (2015) that structural damage produces crystal dislocations that can trap He or impede its diffusion. The difference between relatively deformed and undeformed samples is very apparent in the cumulative loss curves, with increased deformation leading to more anomalous behavior and a greater secondary gas component at high-temperature. It is remarkable that grains from a particular sample (e.g. Sierra deformed and undeformed grains) show repeated consistency in their release patterns, suggesting that when grains

are poorly behaved that this is pattern is upheld for all grains in a sample. This may be particularly true for grains that have experienced brittle grain deformation of similar magnitude. The bimodal nature of some apatite grain CRH release looks reminiscent of multi-domain diffusion in K-feldspar when viewed on an Arrhenius plot; see Lovera et al. (1989). This could signify a quasi-segregated diffusion domain caused by deformation or radiation damage-induced defects that is not activated until high-temperature, thus potentially representing a dual-E_a system. Recent work by Gerin et al. (2017) also documents the He trapping properties of deformation-induced point defects. More investigation would be required to verify these assertions and to explore whether He trapping by dislocations obeys a quantifiable relationship related to thermal history, or whether it is simply a matter of inheriting traps established well before closure to diffusive He loss.

4.6 Support for the re-extract protocol

During conventional apatite (U-Th)/He analyses some laboratories perform He re-extracts on apatite grains, where after initial heating the sample is heated again under the same temperature conditions or to even higher temperature to ensure that the grain is fully outgassed, e.g. (Wolf et al., 1996). If the second reheat produces significant ^{4}He (>1-1.5% of He blank), then this is taken as a sign of anomalous behavior and is either noted during reporting or the data are simply considered unreliable due to unidentified mineral inclusions and discarded, e.g. (Farley, 2002). Hot blank re-extraction is crudely analogous to CRH assessment in the sense that degassed helium after reheats is commonly associated with abnormal behavior, just as anomalous high-temperature

component gas that can be observed during screening is not associated with smooth, expected behavior. Our observations of He release deferred to higher temperatures than expected for VD support the re-extraction approach, however it can not protect against samples showing gas spikes.

4.7 Future directions

CRH screening allows rapid characterization of diffusive behavior and is a successful step towards better identifying the underlying causes of cooling age dispersion. Most labs already take steps to avoid included grains for example, however it is not always clear if this approach has been successful. Our results suggest that for screening, the CRH method could be an additional step that allows recognition of undetected fluid or mineral during heating. In some instances, this technique allows the correction of ages where anomalous or extraneous components of ^{4}He are identified. There are further strides that can be taken to improve upon the approach. The CRH method outlined here used a resistance furnace for heating where thermal lag precluded acquiring kinetics from individual apatites. The benefits of using laser heating going forward would be many, including better temperature control and the gain of kinetic information for each apatite grain in a short, ~45 minute heating experiment. This is a much better approach than time-intensive step-heating experiments. Laser heating also allows the loading of multiple samples at one time, resulting in more efficient throughput and diminishes the size of the heating chamber to allow much better gas cleanup and reduction of active gas interference in the static mode. Most importantly a laser would negate the need for extensive bake-outs due to cleaner extraction line conditions and be much better suited

for routine analysis. The CRH methodology, by extension could also be applied to zircon using laser heating, as opposed to using a furnace, which would be ineffective with regard to time and sample throughput.

To investigate mechanisms or origins of anomalous release, one simple approach could include systematically degassing grains with visible fluid or mineral inclusions to document specific release behaviors or potential interferences caused by volatile gas components. Mavrogenes et al. (2005) and Gaboury et al. (2008) show pressure curves from *in vacuo* decrepitation of quartz fluid inclusion volatiles, namely CO_2, show strong peaks at ~300˚C and later at ~500˚C with greater aqueous contributions. They also demonstrate that quadrupole mass spectrometer monitoring records strong pressure peaks near ~575-600˚C due to alpha-to-beta phase transitioning of quartz during heating. They use this observation to argue that mineral strength (Young's modulus) also plays a role in decrepitation during heating. Along those same lines, a structural mechanism may also have some applicability to apatite and help to explain the cause of some of the observed gas spikes in apatite release curves.

5. Conclusions

The CRH method is a simple analytical technique that provides a means to rapidly characterize apatite diffusive behavior. Analyses of Durango apatite standard and samples having little or no age dispersion show simple gas-release behavior consistent with diffusive loss of their ^{4}He at lower temperatures (samples should be completely exhausted by 900˚C using a 20˚C/minute ramp rate while heating). Examples that show

complicated release patterns or degas well beyond these temperatures suggest that confounding factors such as fluid inclusion decrepitation, impeding of diffusion by crystallographic defects or voids developed through grain deformation, and radiation damage are likely sources of extraneous helium. We have shown examples of anomalous apatites that display unique helium release styles that may be related to such mechanisms. Complex parent U-Th zoning is difficult to verify using CRH screening, however lower diffusivity can be inferred for old, slow-cooled apatites relative to lower eU examples: apatite *df*-curves that are shifted by ~100°C warmer relative to Durango or good actors are suggestive of high radiation damage. Our results suggest that about half of apatites analyzed using the CRH method demonstrated expected-to-intermediate behavior, although that is specific to this dataset where characterization of He diffusion behaviors was the principal motivation for sample selection. The value of CRH application to (U-Th)/He dating is not only the ability to use degassing character to distinguish between apatites that obey volume diffusion and those that do not, but also offer insight into the underlying mechanisms that are the root cause of abnormal behavior by examining release patterns and ultimately, use this information to correct dispersed age datasets.

Acknowledgements

This research did not receive any specific grant from funding agencies in the public, commercial, or not-for-profit sectors. We thank B. Tikoff and L. Goodwin from the University of Wisconsin – Madison for samples from the Sierra Nevada shear zones; we also thank P. Reiners and the Arizona Radiogenic Dating Laboratory for providing the preliminary ages for the Sierra samples.

References

Beucher, R., Brown, R.W., Roper, S., Stuart, F. and Persano, C. (2013) Natural age dispersion arising from the analysis of broken crystals: Part II. Practical application to apatite (U–Th)/He thermochronometry. Geochimica et Cosmochimica Acta 120, 395-416.

Boyce, J. and Hodges, K. (2005) U and Th zoning in Cerro de Mercado (Durango, Mexico) fluorapatite: Insights regarding the impact of recoil redistribution of radiogenic 4 He on (U–Th)/He thermochronology. Chemical Geology 219, 261-274.

Brown, R.W., Beucher, R., Roper, S., Persano, C., Stuart, F. and Fitzgerald, P. (2013) Natural age dispersion arising from the analysis of broken crystals. Part I: Theoretical basis and implications for the apatite (U–Th)/He thermochronometer. Geochimica et Cosmochimica Acta 122, 478-497.

Djimbi, D.M., Gautheron, C., Roques, J., Tassan-Got, L., Gerin, C. and Simoni, E. (2015) Impact of apatite chemical composition on (U-Th)/He thermochronometry: An atomistic point of view. Geochimica et Cosmochimica Acta 167, 162-176.

Dodson, M.H. (1973) Closure temperature in cooling geochronological and petrological systems. Contributions to Mineralogy and Petrology 40, 259-274.

Farley, K.A. (2000) Helium diffusion from apatite; general behavior as illustrated by Durango fluorapatite. Journal of Geophysical Research 105, 2903-2914.

Farley, K.A. (2002) (U-Th)/He Dating: Techniques, Calibrations, and Applications. Reviews in Mineralogy and Geochemistry 47, 819-844.

Farley, K.A., Shuster, D.L. and Ketcham, R.A. (2011) U and Th zonation in apatite observed by laser ablation ICPMS, and implications for the (U–Th)/He system. Geochimica et Cosmochimica Acta 75, 4515-4530.

Farley, K.A., Wolf, R.A. and Silver, L.T. (1995) (U-Th)/He dating; overview of the system and analytical techniques. Abstracts with Programs - Geological Society of America 27, 37-37.

Farley, K.A., Wolf, R.A. and Silver, L.T. (1996) The effects of long alpha-stopping distances on (U-Th)/He ages. Geochimica et Cosmochimica Acta 60, 4223-4229.

Fayon, A.K. and Hansen, L. (2015) Effects of deformation on apatite (U-Th)/He single-grain ages, GSA Annual Meeting. The Geological Society of America, Baltimore, MD, USA, p. 293.

Fitzgerald, P.G., Baldwin, S.L., Webb, L.E. and O'Sullivan, P.B. (2006) Interpretation of (U–Th)/He single grain ages from slowly cooled crustal terranes: A case study from the Transantarctic Mountains of southern Victoria Land. Chemical Geology 225, 91-120.

Flowers, R.M. and Kelley, S.A. (2011) Interpreting data dispersion and “inverted” dates in apatite (U–Th)/He and fission-track datasets: An example from the US midcontinent. Geochimica et Cosmochimica Acta 75, 5169-5186.

Flowers, R.M., Ketcham, R.A., Shuster, D.L. and Farley, K.A. (2009) Apatite (U–Th)/He thermochronometry using a radiation damage accumulation and annealing model. Geochimica et Cosmochimica Acta 73, 2347-2365.

Fox, M., McKeon, R.E. and Shuster, D.L. (2014) Incorporating 3‐D parent nuclide zonation for apatite 4He/3He thermochronometry: An example from the Appalachian Mountains. Geochemistry, Geophysics, Geosystems 15, 4217-4229.
Gautheron, C., Tassan-Got, L., Barbarand, J. and Pagel, M. (2009) Effect of alpha-damage annealing on apatite (U–Th)/He thermochronology. Chemical Geology 266, 157-170.
Gerin, C., Gautheron, C., Oliviero, E., Bachelet, C., Djimbi, D.M., Seydoux-Guillaume, A.-M., Tassan-Got, L., Sarda, P., Roques, J. and Garrido, F. (2017) Influence of vacancy damage on He diffusion in apatite, investigated at atomic to mineralogical scales. Geochimica et Cosmochimica Acta 197, 87-103.
Gaboury, D., Keita, M., Guha, J. and Lu, H.-Z. (2008) Mass spectrometric analysis of volatiles in fluid inclusions decrepitated by controlled heating under vacuum. Economic Geology 103, 439-443.
Green, P. (1985) Comparison of zeta calibration baselines for fission-track dating of apatite, zircon and sphene. Chemical Geology: Isotope Geoscience section 58, 1-22.
Green, P.F., Crowhurst, P.V., Duddy, I.R., Japsen, P. and Holford, S.P. (2006) Conflicting (U–Th)/He and fission track ages in apatite: enhanced He retention, not anomalous annealing behaviour. Earth and Planetary Science Letters 250, 407-427.
Hourigan, J.K., Reiners, P.W. and Brandon, M.T. (2005) U-Th zonation-dependent alpha-ejection in (U-Th)/He chronometry. Geochimica et Cosmochimica Acta 69, 3349-3365.
Idleman, B.D. and Zeitler, P.K. (2014) Rapid characterization of noble-gas kinetics using continuous heating and gas accumulation, 14th International Conference on Thermochronology, Chamonix, France.
Lieszkovszky, L., Filippelli, A.R. and Tilford, C.R. (1990) Metrological characteristics of a group of quadrupole partial pressure analyzers. Journal of Vacuum Science & Technology A 8.
Littlefield, K.V. (2010) (U-Th)/He analysis of denudation rates and exhumation histories in southern West Virginia, Geology and Geography. West Virginia University, Morgantown, WV.
Lovera, O.M., Richter, F.M. and Harrison, T.M. (1989) The 40Ar/39Ar Thermochronometry for Slowly Cooled Samples Having a Distribution of Diffusion Domain Sizes. Journal of Geophysical Research 94, 17917-17935.
Mavrogenes, J., Bodnar, R., Graney, J., McQueen, K. and Burlinson, K. (1995) Comparison of decrepitation, microthermometric and compositional characteristics of fluid inclusions in barren and auriferous mesothermal quartz veins of the Cowra Creek gold district, New South Wales, Australia. Journal of Geochemical Exploration 54, 167-175.
McDannell, K.T., Idleman, B.D. and Zeitler, P.K. (2015) Characterization of helium diffusion behavior from continuous heating experiments: Sample screening and identification of multiple 4He components, AGU Fall Meeting. American Geophysical Union, San Francisco, CA.
McDannell, K.T. (2017) Methods and application of deep-time thermochronology: Insights from slowly cooled terranes of Mongolia and the North American craton,

Earth and Environmental Sciences. Lehigh University, Bethlehem, Pennsylvania, p. 261.
McDougall, I. and Wellman, P. (2011) Calibration of GA1550 biotite standard for K/Ar and 40 Ar/39 Ar dating. Chemical Geology 280, 19-25.
McDowell, F.W., McIntosh, W.C. and Farley, K.A. (2005) A precise 40 Ar–39 Ar reference age for the Durango apatite (U–Th)/He and fission-track dating standard. Chemical Geology 214, 249-263.
McKeon, R.E. (2012) Apatite U-Th/He Thermochronometry in Slowly Eroding Landscapes: Addressing Age Dispersion to Understand Appalachian Topographic Development, Earth and Environmental Sciences. Lehigh University.
McKeon, R.E., Zeitler, P.K., Pazzaglia, F.J., Idleman, B.D. and Enkelmann, E. (2014) Decay of an old orogen: Inferences about Appalachian landscape evolution from low-temperature thermochronology. Geological Society of America Bulletin 126, 31-46.
Meesters, A. and Dunai, T. (2002) Solving the production–diffusion equation for finite diffusion domains of various shapes: Part II. Application to cases with α-ejection and nonhomogeneous distribution of the source. Chemical Geology 186, 347-363.
Murray, K.E., Orme, D.A. and Reiners, P.W. (2014) Effects of U–Th-rich grain boundary phases on apatite helium ages. Chemical Geology 390, 135-151.
Ollier, C. (1982) The Great Escarpment of eastern Australia: tectonic and geomorphic significance. Journal of the Geological Society of Australia 29, 13-23.
Persano, C. (2003) A combination of apatite fission track and (U-Th)/He thermochronometers to constrain the escarpment evolution in south eastern Australia: a case study of high elevation passive margins. University of Glasgow.
Persano, C., Stuart, F.M., Bishop, P. and Dempster, T.J. (2005) Deciphering continental breakup in eastern Australia using low‐temperature thermochronometers. Journal of Geophysical Research: Solid Earth 110.
Peyton, S.L., Reiners, P.W., Carrapa, B. and DeCelles, P.G. (2012) Low-temperature thermochronology of the northern Rocky Mountains, western USA. American Journal of Science 312, 145-212.
Reiners, P.W. and Farley, K.A. (2001) Influence of crystal size on apatite (U–Th)/He thermochronology: an example from the Bighorn Mountains, Wyoming. Earth and Planetary Science Letters 188, 413-420.
Reiners, P.W. and Nicolescu, S. (2006) Measurement of parent nuclides for (U-Th)/He chronometry by solution sector ICP-MS, ARHDL Report 3.0 ed. University of Arizona.
Shuster, D.L., Flowers, R.M. and Farley, K.A. (2006) The influence of natural radiation damage on helium diffusion kinetics in apatite. Earth and Planetary Science Letters 249, 148-161.
Spiegel, C., Kohn, B., Belton, D., Berner, Z. and Gleadow, A. (2009) Apatite (U–Th–Sm)/He thermochronology of rapidly cooled samples: The effect of He implantation. Earth and Planetary Science Letters 285, 105-114.
Spotila, J.A., Bank, G.C., Reiners, P.W., Naeser, C.W., Naeser, N.D. and Henika, B.S. (2004) Origin of the Blue Ridge escarpment along the passive margin of Eastern North America. Basin Research 16, 41-63.

Taylor, J.P. and Fitzgerald, P.G. (2011) Low-temperature thermal history and landscape development of the eastern Adirondack Mountains, New York: Constraints from apatite fission-track thermochronology and apatite (U-Th)/He dating. Geological Society of America Bulletin 123, 412-426.

Vermeesch, P., Seward, D., Latkoczy, C., Wipf, M., Günther, D. and Baur, H. (2007) α-Emitting mineral inclusions in apatite, their effect on (U–Th)/He ages, and how to reduce it. Geochimica et Cosmochimica Acta 71, 1737-1746.

Warnock, A.C., Zeitler, P.K., Wolf, R.A. and Bergman, S.C. (1997) An evaluation of low-temperature apatite U-Th/He thermochronometry. Geochimica et Cosmochimica Acta 61, 5371-5377.

Wolf, R.A., Farley, K.A. and Kass, D.M. (1998) Modeling of the temperature sensitivity of the apatite (U-Th)/He thermochronometer. Chemical Geology 148, 105-114.

Wolf, R.A., Farley, K.A. and Silver, L.T. (1996) Helium diffusion and low-temperature thermochronometry of apatite. Geochimica et Cosmochimica Acta 60, 4231-4240.

Zeitler, P.K., Enkelmann, E., Thomas, J.B., Watson, E.B., Ancuta, L.D. and Idleman, B.D. (2016, in press) Solubility and trapping of helium in apatite. Geochimica et Cosmochimica Acta.

Zeitler, P.K., Herczeg, A.L., McDougall, I. and Honda, M. (1987) U-Th-He dating of apatite: A potential thermochronometer. Geochimica et Cosmochimica Acta 51, 2865-2868.

Zeitler, P.K., Meltzer, A.S., Brown, L., Kidd, W.S.F., Lim, C. and Enkelmann, E. (2014) Tectonics and topographic evolution of Namche Barwa and the easternmost Lhasa block, Tibet. Geological Society of America Special Papers 507.

Appendix A: Full (U-Th)/He dataset using the CRH method

Supplemental table 1: Conventional (U-Th)/He results and CRH corrections for all apatite suites

MN Sample	Corr. Age (Ma)	± 1σ (Ma)	U ppm	Th ppm	Sm ppm	4He (mol)	Rs (um)	eU cyl. ppm	Raw Age (Ma)	Ft	CRH age	± 1σ (Ma)
11KWW04-1c	128.36	2.41	18.4	74.5	92.2	8.743E-14	60.3	35.9	96.46	0.75	122.6	4.2
11KWW04-2c	106.08	1.99	23.6	85.3	95.4	1.699E-13	74.3	43.7	84.74	0.80	85.8	2.1
12MN11c	127.56	2.06	121.5	55.5	92.1	2.059E-13	52.7	134.6	93.60	0.73	114.9	2.6
12MN16c	118.35	1.67	2.0	11.4	152.0	5.053E-14	86.6	4.7	97.97	0.83	63.6	2.1
12MN22c	227.28	4.87	7.4	7.0	178.8	3.325E-14	58.6	9.1	173.4	0.76	204.7	4.5
12MN36-1c	122.00	2.29	12.1	62.9	128.2	1.080E-13	72.6	26.9	96.54	0.79	95.8	2.2
12MN36-2c	120.89	2.28	10.2	70.9	252.9	3.462E-13	92.7	26.9	100.3	0.83	64.0	2.3
12MN36Ac	98.87	1.41	11.0	70.7	230.3	3.491E-13	98.2	27.6	83.00	0.84	82.7	2.3
12MN36Bc	103.97	1.47	12.0	71.9	208.5	1.627E-13	75.8	28.9	82.45	0.80	97.8	1.7
12MN42c	139.51	4.17	4.7	11.3	175.5	1.802E-14	56.7	7.3	104.0	0.74	-	-
12MN44-1c	101.59	1.96	4.1	8.8	291.2	2.175E-14	65.0	6.2	79.48	0.78	64.0	9.6
12MN44-2c	116.17	2.41	4.7	8.4	310.3	2.204E-14	67.2	6.6	92.01	0.79	59.5	1.8
12MN44-3c	106.03	2.17	5.0	7.3	307.0	1.127E-14	56.1	6.7	79.77	0.75	61.2	2.2
12MN48c	115.57	2.19	8.8	42.8	408.7	2.504E-14	48.3	18.8	80.15	0.69	55.8	2.9
12MN49c	176.47	2.56	13.8	25.8	172.6	9.307E-14	67.2	19.8	138.4	0.78	131.8	4.2
12MN49c	129.07	2.12	14.6	36.0	233.3	2.930E-14	51.6	23.1	92.68	0.71	106.7	2.4
12MN59c	115.57	2.53	41.7	59.2	461.1	3.368E-13	79.4	55.6	107.3	0.82	74.0	3.9
14MN02c	99.69	1.55	82.3	68.2	632.9	5.867E-14	42.2	98.3	64.42	0.66	95.3	4.6
14MN04c	124.47	2.81	11.3	25.4	132.4	2.224E-14	51.0	17.3	89.13	0.71	63.5	2.7
14MN05c	90.75	1.30	53.1	142.6	432.0	6.557E-14	43.4	86.6	60.20	0.66	86.2	6.3
14MN05c	487.40	10.58	17.3	39.6	143.2	2.547E-13	62.1	26.6	374.9	0.76	306.0	37.4
14MN07c	105.40	1.56	19.0	45.9	35.8	4.696E-14	56.2	29.8	77.82	0.73	-	-
14MN07c	94.11	1.44	14.9	40.9	67.6	3.021E-14	54.0	24.5	68.45	0.72	-	-
14MN08c	70.10	1.12	117.0	89.8	158.7	9.536E-14	48.9	138.1	49.81	0.71	63.9	1.3
14MN08c	70.67	1.64	116.5	92.5	144.1	4.682E-14	41.5	138.2	46.71	0.66	65.6	3.1
14MN09c	134.74	2.25	16.1	62.2	315.2	3.076E-14	46.2	30.7	91.67	0.68	94.1	2.1
14MN09c	100.84	1.63	10.3	33.2	202.1	2.444E-14	54.2	18.1	73.55	0.72	91.6	1.8
14MN09-1c	142.77	6.53	10.3	29.9	208.8	1.154E-13	80.1	17.3	116.6	0.81	124.9	5.4
14MN10c	95.75	1.82	12.0	45.0	18.2	3.550E-14	56.6	22.5	70.44	0.73	58.5	1.9
14MN11c	190.56	2.90	1.6	6.6	181.0	1.591E-14	64.9	3.2	145.9	0.78	96.8	11.5
14MN11c	126.41	5.98	1.3	4.0	139.8	2.819E-15	49.6	2.3	90.59	0.71	98.0	7.4
14MN12c	257.41	8.99	7.3	24.9	345.3	4.390E-14	51.1	13.2	184.4	0.71	198.6	9.4
14MN12c	389.06	8.45	7.3	23.3	333.2	5.861E-14	53.1	12.8	283.8	0.72	253.3	12.1
14MN13c	81.40	1.33	43.3	23.7	41.6	4.258E-14	50.0	48.9	58.47	0.71	44.4	2.7
14MN13c	123.10	2.84	34.0	27.8	22.1	4.498E-14	48.7	40.5	87.25	0.70	48.1	2.0
14MN14c	177.03	2.59	8.4	63.6	346.8	8.141E-14	61.7	23.3	133.7	0.75	124.4	9.4
14MN14c	503.55	10.93	6.0	40.3	281.7	2.983E-13	75.0	15.4	403.6	0.79	-	-
14MN15-1c	81.13	1.83	36.5	73.1	42.7	5.505E-14	51.8	53.7	58.27	0.71	65.4	1.6
14MN15-2c	70.13	1.60	39.3	63.4	79.6	1.655E-13	75.4	54.2	56.61	0.80	-	-
14MN15c	61.04	0.89	20.3	68.7	106.4	3.066E-14	54.0	36.4	44.22	0.72	48.7	1.3
14MN16c	160.43	3.91	1.0	3.4	87.5	5.925E-15	60.1	1.8	122.3	0.76	142.9	4.7
14MN17c	~~26.99~~	1.24	27.6	36.0	86.4	1.019E-14	52.7	36.1	19.63	0.72	error	error
14MN17c	126.96	2.81	4.3	10.3	137.7	8.143E-14	92.7	6.7	107.2	0.84	-	-
14MN18c	519.79	7.34	1.1	4.3	108.9	2.832E-14	62.6	2.2	394.2	0.77	498.9	22.4
14MN18c	211.29	3.28	0.7	2.6	70.9	3.698E-14	96.4	1.3	173.8	0.85	172.6	10.4
14MN18c	145.32	3.70	1.1	4.3	131.9	7.292E-15	61.2	2.1	111.5	0.76	126.2	3.4
14MN18-1c	138.98	6.36	1.0	3.5	119.4	1.140E-14	73.2	1.8	112.0	0.80	131.1	5.6
14MN19c	156.99	3.62	7.8	12.5	453.9	1.136E-14	44.3	10.7	107.7	0.68	77.7	4.8

14MN20c	98.25	1.45	8.5	40.1	76.9	1.071E-14	43.5	18.0	64.45	0.65	80.2	1.9
14MN20c	193.06	4.25	9.6	24.8	144.9	8.133E-14	63.7	15.4	148.8	0.77	122.0	12.9
MN15-27c	286.60	9.48	7.9	1.1	214.1	4.550E-14	62.2	8.2	224.0	0.78	168.4	23.2
MN15-28c	111.38	3.79	6.9	21.5	65.1	1.891E-14	57.8	12.0	82.58	0.74	75.7	22.4
MN15-28c	112.40	5.16	7.5	21.4	92.4	2.136E-14	58.0	12.6	83.62	0.74	77.2	3.8
MN15-29c	93.78	3.25	33.9	25.1	275.0	3.531E-14	51.7	39.8	63.79	0.72	68.2	2.4
MN15-29c	101.80	4.70	40.1	49.2	323.8	3.930E-14	44.9	51.7	69.25	0.68	83.5	3.6
MN15-30c	124.37	4.24	15.5	33.4	205.2	1.587E-14	41.4	23.4	80.71	0.65	117.1	4.4
MN15-30c	136.60	6.28	17.4	28.3	168.6	2.525E-14	47.3	24.1	94.76	0.69	131.0	4.8
NB Sample	**Corr. Age (Ma)**	**± 1σ (Ma)**	**U ppm**	**Th ppm**	**Sm ppm**	**4He (mol)**	**Rs (um)**	**eU sph. ppm**	**Raw Age (Ma)**	**Ft**	**CRH age**	**± 1σ (Ma)**
NB07-2	9.72	0.19	30.3	37.3	271.7	4.985E-15	57.6	39.1	7.27	0.75	5.8	0.2
NB07-4	11.80	0.23	42.8	53.1	525.7	5.635E-15	50.7	55.3	8.44	0.71	7.1	0.2
NB07-6	27.54	0.65	11.6	4.8	86.1	1.547E-15	43.5	12.7	18.63	0.68	-	-
NB07-7	24.81	0.47	42.6	53.7	274.5	1.367E-14	52.7	55.2	17.97	0.72	-	-
NB07-8	12.41	0.24	35.5	37.1	351	7.069E-15	57.4	44.2	9.28	0.75	-	-
NB07-9	46.11	0.93	38.3	19.6	374.4	6.364E-15	36.5	42.9	28.45	0.62	-	-
NB54-1	13.89	0.30	6.6	20.4	301.2	1.680E-15	54.4	11.4	10.13	0.73	9.3	0.3
NB54-2	17.08	0.39	8.4	27.7	377.6	1.401E-15	45.6	14.9	11.57	0.68	-	-
NB54-4	10.43	0.20	6.3	17.9	175.9	5.201E-15	79.2	10.5	8.47	0.81	5.9	0.3
NB54-5	10.81	0.22	4.7	13.5	181.8	2.219E-15	71.3	7.8	8.56	0.79	8.3	0.3
NB54-6	13.92	0.26	11.9	34.7	460.5	4.647E-15	60.9	20.1	10.54	0.76	9.0	0.5
NB54-7	11.81	0.23	7.1	21.6	199.4	2.370E-15	60.9	12.2	8.91	0.76	8.4	0.4
NB54-d159	29.61	0.89	4.8	16.2	256.9	3.217E-15	58.1	8.7	22.47	0.76	-	-
SN Sample	**Corr. Age (Ma)**	**± 1σ (Ma)**	**U ppm**	**Th ppm**	**Sm ppm**	**4He (mol)**	**Rs (um)**	**eU sph. ppm**	**Raw Age (Ma)**	**Ft**	**CRH age**	**± 1σ (Ma)**
1989s24-01	50.49	1.25	87	40.1	189.8	1.662E-13	74.8	96.4	40.85	0.80	27.4	1.0
1989s24-04	59.73	1.47	64.9	43.4	206.3	9.318E-14	65.6	75.1	46.67	0.78	31.0	1.2
1989s24-05	63.18	1.56	51	29.4	182.3	3.710E-14	51.3	57.9	45.66	0.72	40.6	1.3
1989s24-07	103.49	2.51	31.7	31.5	102.9	4.241E-14	51.0	39.1	74.33	0.71	47.7	1.9
R9515-03	64.56	1.55	37.7	55.8	95.9	3.125E-14	52.1	50.8	46.49	0.72	59.2	1.3
R9515-04	36.93	0.90	67.8	76.6	90	2.094E-14	46.4	85.8	25.44	0.69	33.6	0.7
R9515-05	49.35	1.20	31.8	40.9	74.5	9.742E-15	37.6	41.4	30.49	0.62	42.7	1.1
R9515-06	39.18	0.95	57.7	68.6	114	3.472E-14	56.5	73.8	29.10	0.74	32.2	1.0
R9515-07	42.10	1.01	50.4	82.8	145.9	8.733E-14	72.4	69.9	33.53	0.80	35.9	1.3
R9515-08	38.59	0.93	46.7	64.4	111	1.000E-13	77.6	61.8	31.29	0.81	32.9	1.0
APL Sample	**Corr. Age (Ma)**	**± 1σ (Ma)**	**U ppm**	**Th ppm**	**Sm ppm**	**4He (mol)**	**Rs (um)**	**eU sph. ppm**	**Raw Age (Ma)**	**Ft**	**CRH age**	**± 1σ (Ma)**
SCDM_01	190.34	12.64	29.9	1.0	211.7	7.033E-13	116.5	30.1	167.5	0.88	158.1	16.7
SCDM_02	443.64	28.78	19.8	1.0	128.0	1.653E-12	126.0	20.0	395.7	0.89	301.6	36.6
SCDM_03	59.86	4.02	151.6	6.5	1047	4.707E-13	78.7	153.1	49.21	0.82	44.7	7.1
SCDM_04	146.57	9.77	41.6	1.5	276.2	4.028E-13	96.4	42.0	125.4	0.85	113.6	9.3
SCDM_05	219.08	14.51	25.0	0.9	151.9	5.081E-13	106.4	25.2	190.5	0.87	153.4	16.8
SCDM_06	338.69	22.18	21.6	0.9	141.3	1.093E-12	115.2	21.8	297.4	0.88	271.0	34.0
SCDM_07	172.97	11.50	44.2	1.7	317.4	7.216E-13	105.3	44.6	150.1	0.87	132.7	15.3
SCDM_08	127.57	8.52	51.2	8.3	361.9	5.221E-13	96.2	53.2	109.0	0.85	96.0	8.1
SCDM_09	265.11	17.48	23.0	1.0	152.1	6.895E-13	109.3	23.2	230.8	0.87	227.5	24.0
CHFD_01	219.86	14.55	123.3	27.6	1256	8.279E-14	38.4	129.8	141.2	0.64	174.7	11.0
CHFD_02	239.82	15.84	9.9	2.9	200.1	9.496E-14	81.4	10.5	198.2	0.83	214.7	11.5
CHFD_03	184.78	12.28	4.8	1.2	62.7	3.571E-14	83.3	5.1	153.3	0.83	157.7	9.2
CHFD_04	216.76	14.34	11.4	3.1	186.2	8.319E-14	88.9	12.1	119.7	0.84	129.1	7.8
CHFD_05	169.71	11.29	6.0	2.3	86.0	3.861E-14	81.8	6.6	140.6	0.83	149.5	8.2
CHFD_06	174.90	11.63	6.0	0.2	152.1	5.405E-14	90.9	6.0	148.5	0.85	169.8	8.5

CHFD_07	186.90	12.42	11.7	0.5	87.3	1.081E-13	88.4	11.8	157.1	0.84	177.8	9.3
MDC Sample	**Corr. Age (Ma)**	**± 1σ (Ma)**	**U ppm**	**Th ppm**	**Sm ppm**	**4He (mol)**	**Rs (um)**	**eU sph. ppm**	**Raw Age (Ma)**	**Ft**	**CRH age**	**± 1σ (Ma)**
GA1550_01	75.76	1.97	41.1	93.7	328.6	1.576E-13	74.9	63.1	60.72	0.80	70.7	3.2
GA1550_02	76.75	2.00	34.0	78.8	288.0	1.585E-13	81.8	52.5	62.83	0.82	68.2	2.3
GA1550_03	72.88	1.90	49.7	103.7	311.7	3.817E-13	99.2	74.1	61.98	0.85	62.4	2.1
GA1550_04	73.49	1.91	34.1	82.0	295.0	2.432E-13	91.2	53.4	61.53	0.84	60.3	2.5
GA1550_05	83.91	2.19	43.6	98.2	280.6	1.682E-13	76.0	66.7	67.52	0.80	77.5	3.5
GA1550_06	84.86	2.21	48.5	101.5	355.4	8.608E-14	57.3	72.4	62.98	0.74	70.9	3.1
GA1550_07	74.00	1.92	28.2	71.2	239.6	1.749E-13	91.8	45.0	61.95	0.84	61.5	3.0
GA1550_08	79.07	2.06	42.5	93.3	294.5	1.363E-13	69.4	64.5	62.20	0.79	72.0	4.0
DURANGO	**Corr. Age (Ma)**	**± 1σ (Ma)**	**U ppm**	**Th ppm**	**Sm ppm**	**4He (mol)**	**Rs (um)**	**eU sph. ppm**	**Th/U**	**Ft**	**CRH age**	**± 1σ (Ma)**
DUR-1-d158	30.95	0.37	10.8	202.7	169.8	3.287E-13	127	58.4	18.8	NA	-	-
DUR-2-d158	32.87	0.40	9.7	197.8	168.8	2.781E-13	90	56.2	20.3	NA	-	-
DUR-3-d158	31.87	0.38	10.1	180.8	137.3	3.302E-13	110	52.6	18.0	NA	-	-
DUR-4-d158	33.10	0.40	8.5	171.5	149.2	2.137E-13	100	48.8	20.3	NA	-	-
DUR-1-d159	34.99	0.60	10.1	202.3	165.2	4.042E-13	100	57.7	20.0	NA	32.2	0.6
DUR-2-d159	33.17	0.57	9.2	185.8	152.3	2.913E-13	100	52.8	20.3	NA	-	-

* these are all age data for all samples that were dated, some were ran using CRH method but not analyzed

Corr age = corrected age using Ft correction for alpha-loss after Farley et al., 1996

all 1-sigma errors are propagated from uncertainty in He, U, Th, Sm, Ft calculation, and blank correction

CRH model ages propagate additional uncertainty in Ea 25/35 kcal/mol high-T df-curve correction, see text

Rs = spherical equivalent radius, eU = effective Uranium content ([U+0.235*Th] from Flowers et al., 2009

CHAPTER 3

Instability of the Canadian Shield during the Late Proterozoic

Kalin T. McDannell[a]*, Peter K. Zeitler[a], and David A. Schneider[b]

[a]*Earth and Environmental Sciences Department, Lehigh University, 1 W Packer Ave., Bethlehem PA, 18015, USA*

[b]*Department of Earth and Environmental Sciences, University of Ottawa, 120 University, Ottawa ON, Canada*

For submission to *Earth and Planetary Science Letters*

Keywords: craton, thermochronology, $^{40}Ar/^{39}Ar$, Laurentia, stability

CHAPTER ABSTRACT

Cratons are generally considered to be terranes that have remained tectonically quiescent for billions of years. Actual evidence for stability is mainly founded on the Phanerozoic sediment record and low-temperature thermochronology, however for significant parts of Canada, stability has been inferred due to the lack of an extensive rock record in both time and space. We used $^{40}Ar/^{39}Ar$ multi-diffusion domain analysis of K-feldspar to constrain cratonic thermal histories across an intermediate (~150-350°C) temperature range in an attempt to link known high-temperature geochronology that resolves orogenesis and metamorphism with lower-temperature data suited for upper crustal burial and unroofing histories. This work is focused on understanding the transition from Archean-Paleoproterozoic crustal growth to stability, and how uninterrupted that record is throughout Earth's Proterozoic "Middle Age." Intermediate-temperature thermal histories of cratonic rocks at well-constrained localities within the southern Canadian Shield of North America challenge the stability worldview because rocks were at elevated temperatures in the Proterozoic. Feldspars from granitic rocks collected at the surface cooled at rates of <0.5°C/Ma following intrusion, seemingly characteristic of cratonic lithosphere, however modeled thermal histories suggest that at ~1.1-1.0 Ga these rocks were near ~200°C – signaling either reheating, or rocks being at mid-crustal depths assuming a normal cratonic geothermal gradient. Subsequently, after 1 Ga, the regions undergo further cooling such that they were at or near the surface (<< 60°C) in the early Paleozoic. Explaining mid-crustal residence at ~1 Ga is challenging. A widespread, prolonged reheating history via burial is not supported by stratigraphic information, however assuming a purely monotonic history requires a very large amount of

exhumation at 1 Ga. A possible explanation may be found in evidence of magmatic underplating that thickened the crust, driving uplift and erosion. The timing of this coincides with Mid-Continent extension and Grenville orogenesis. $^{40}Ar/^{39}Ar$ MDD data demonstrate that this technique can be successfully applied to older rocks and fill in a large observational gap, and that these data also raise questions about the evolution of cratons during the Proterozoic and the nature of cratonic stability through deep time.

1. Introduction

1.1 The nature of cratons and stabilization

Cratons are made of tectonically quiescent, ancient continental lithosphere that have characteristically thick, chemically depleted mantle and low heat flow (Foley, 2008; Jordan, 1978, 1981; Lee et al., 2011; Rudnick and Nyblade, 1999). Cratons are first-order features important to understanding the evolution of Earth, and in particular the dynamics of continental interiors. While intrinsically interesting because they record the secular evolution of the continents and a cyclic response to mantle dynamics, cratons are also important because the emergence of the biosphere and atmosphere and fundamental environmental changes such as oceanic oxygenation and nitrification have been ascribed to the emergence of stable continental landmasses, with cratonization being integral to these geo-biological developments (Brasier and Lindsay, 1998; Knoll, 2003; McKenna, 1972).

The conventional understanding is that cratons have persisted since the initiation of plate tectonics on Earth, which may have been as early as the Hadean or as late as the Neoproterozoic (Korenaga, 2013 and references therein), and have acted as nuclei for subsequent continental amalgamation. Early crustal formation was likely accomplished through subduction melting of basaltic slabs (Tappe et al., 2011) and the assembly of Archean lithosphere through models requiring shallow melting at spreading centers or water-driven flux melting at convergent margins (Martin, 1986; Rudnick, 1995; Taylor and McLennan, 1995). There are important geochemical and mechanical changes that occur after initial lithosphere formation that produce the complex petrology and

architecture preserved today, including processes such as high volatile melt depletion of Archean peridotites (James and Fouch, 2002; Pollack, 1986), and subducted slab stacking and underplating during lithospheric mantle root formation (Bostock, 1998; Carlson et al., 2005; Helmstaedt and Schulze, 1989; Wyman and Kerrich, 2002).

"Cratonization" refers to the collective result of sporadic mafic magma injection into the crust over 100 m.y. timescales, resulting in net crustal growth and thickening through underplating that is marked by the pervasive dike swarms across cratonic terranes (Nelson, 1991). The stabilization of cratonic lithosphere is thought to occur during volatile mobilization in the upper mantle during magmatism and growth of the continental crust (Pollack, 1986). The "stability" of cratons is typically defined as their resistance to internal deformation, limited magmatism, and the lack of significant vertical motions beyond those related to deeper mantle dynamics (Pollack, 1986). Stability is often attributed to the presence of thick (>150-250 km), buoyant Archean or Early Proterozoic mantle lithosphere that is resistant to deformation and recycling due to its cold temperature, high viscosity, and depleted chemical composition (Carlson et al., 2005; Cottrell et al., 2004; Jordan, 1978; Lenardic and Moresi, 1999; Pearson et al., 1995a; Rudnick and Nyblade, 1999). Chemical depletion of mantle peridotite results from removal of Fe-rich basaltic melts and volatiles (H_2O and CO_2), which are crucial for stability in that they offset negative thermal buoyancy and enhance mantle viscosity (Herzberg and Rudnick, 2012; Jordan, 1978; Kelly et al., 2003).

The crust is also critical for cratonic stability and Flowers et al. (2004) argue that long-term exhumation within cratons is a function of crustal heat production and initial lithospheric mantle temperatures. Jaupart et al. (2014) arrived at a similar conclusion but emphasized the importance of Archean-Early Proterozoic differentiation of heat-producing elements into the upper crust and subsequent removal as a means of increasing overall lithospheric strength. Crustal mineralogy, including metamorphic reactions involving garnet (e.g. Williams et al., 2014) play a key role in lower crustal densification and maintenance of crustal buoyancy. Reversal of this process may occur during upper mantle and lower-crustal hydration and metasomatism, which can alter densities and cause uplift, supporting significant surface topography in regions that are otherwise tectonically inactive (e.g. Jones et al., 2015). Some cratonic keels show evidence for metasomatism and refertilization (e.g. Carlson et al., 2004; Pearson et al., 1995b) that can ultimately result in keel destruction through continued lithospheric thinning, root removal, and melt metasomatism (Lee et al., 2011), e.g. the Tanzanian (Weeraratne et al., 2003) and North China cratons (Griffin et al., 1998; Menzies and Xu, 1998). This demonstrates that the cratons preserved today exist in part by managing to evade or survive tectonic reworking through time.

The interval between 1.7 to 0.75 Ga has been referred to as "Earth's Middle Age," (Cawood and Hawkesworth, 2014) or the "Boring Billion" (Holland, 2006), a time of geological, biologic, and environmental stability that is attributed in part to secular cooling of the mantle and the development of a strong continental lithosphere. This period of pervasive stability was initiated during the Columbia/Nuna supercontinent cycle

from ~2.1-1.3 Ga (Meert, 2012; Rogers and Santosh, 2002) and endured until protracted breakup of Rodinia between ~0.86-0.57 Ga (Li et al., 2008). Rodinia was the supercontinent that existed at the end of the Mesoproterozoic and its primary reconstructions are based mainly on correlating ~1.1 Ga orogenic belts that occur on numerous modern continents (Dalziel et al., 2000; Hoffman, 1991). Rodinia was formed through widespread Grenvillian contractional orogenesis from ~1.3-1.0 Ga, and reconstructed paleogeography demonstrates that the entire eastern and southwestern margins of Laurentia experienced contraction, while the Laurentian core underwent continental-scale northeast-southwest extension, causing rifting and numerous dike swarms (Ernst and Bleeker, 2010; Timmons et al., 2001; Turner et al., 2016; Whitmeyer and Karlstrom, 2007).

The established view is that the majority of the Proterozoic represents a period of long-term stability for most cratons following early consolidation and exhumation during the Archean-Proterozoic transition. This is founded mainly on the lack of geologic events recorded in the long interval between initial Archean cratonization and subsequent epeirogenic activity in the Phanerozoic. The large time gap corresponds to the Great Unconformity, which in some places signifies over a billion years of time, e.g. Karlstrom and Timmons (2012). For the majority of this interval, time-temperature information is lacking. The scarcity of robust sedimentary information for many cratonic terranes during this time is also problematic for reconstructing the erosion record. Geochronologic study of cratons has usually been limited to high-closure temperature (>500°C) methods focused on understanding cratonization and metamorphism during orogenic suturing, or

alternatively, low-temperature closure (<100°C) methods for examining shallow exhumation and burial histories. From a thermochronological standpoint, the 1 to 2 billion-year gap in the Proterozoic record could simply reflect the lack of studies using methods that address the 500°C to 100°C temperature window.

1.2 Stability: record or lack thereof?

The geologic record of stability is mostly found in the more recent Phanerozoic history of cratonic continental interiors. Based on fragmented stratigraphic and low-temperature thermochronology data, cratons in particular seem to have experienced under two kilometers of vertical motion over many hundreds of millions of years (Ault et al., 2009, 2013; Blackburn et al., 2012; Flowers et al., 2012; Flowers et al., 2006b; Flowers and Schoene, 2010). Suggested mechanisms for modest observed epeirogenic motions include far-field lithospheric responses to subduction (Mitrovica et al., 1989) and dynamic topography induced by mantle flow (Forte et al., 2010; Gurnis, 1992; Hager et al., 1985). In central Canada the case for Proterozoic stability appears to be based mostly on the unobserved: a lack of orogenic activity and sedimentary records, and lack of disturbed (i.e. thermally reset) geochronological systems. Extensive work in the western Superior Province suggests that orogenic activity over the Kenoran interval ~2.75 to 2.65 Ga ceased by 2.6 Ga and transitioned shortly thereafter to a stable cratonic lithosphere by 2.5 Ga, with some immediate post-orogenic sedimentation occurring (e.g. the Huronian Supergroup; Percival et al., 2006; Percival et al., 2012). Internal deformation occurred during mantle plume activity in the form of the Matatchewan large igneous province (LIP) and dike swarm at ~2.48-2.45 Ga during proto-continental breakup (Ernst and

Bleeker, 2010) and 2.2 Ga emplacement of the Nipissing Sills fed by the Ungava plume. Very local deformation occurred as a result of counter-clockwise rotation of the western Superior Province along the Kapuskasing uplift at ca. 1.9 Ga that exposed the mid-lower crust (Evans and Halls, 2010). The next major events recorded are the ~1.86 Ga Penokean Orogeny along the southern Superior margin, a Himalayan-scale orogen that was synchronous with the Trans-Hudson Orogen (~1.9-1.8 Ga) to the north and northwest (Schulz and Cannon, 2007). Extension-related magmatism occurred later, such as the 1.27 Ga Mackenzie dikes, 1.24 Ga Sudbury mafic dike swarm, and the ~1.1 Ga Mid-Continental Rift (MCR) and Abitibi dike swarm related to Rodinia assembly and Grenville orogenesis. Subtle epeirogenic motions of up to ±1-2 km in the Phanerozoic followed these events (Feinstein et al., 2009; Flowers et al., 2012).

After initial cratonic stabilization, almost a billion years of thermal record is unaccounted for. An analogous, although somewhat younger, orogenic and stabilization sequence is recorded for the neighboring Trans-Hudson orogen (THO), where ~1.9 to 1.8 Ga granulite-facies metamorphic rocks (Alexandre et al., 2009; Flowers et al., 2008; Schneider et al., 2007) underlie Athabasca sediments deposited between ~1.7-1.6 Ga (Rainbird et al., 2007; Rayner et al., 2005). This was seemingly followed by quiescence until modest Phanerozoic epeirogenesis (Ault et al., 2009; Flowers et al., 2012). It is clear that certain locations on the North American craton, such as Athabasca, show that orogenic assemblages were completely exhumed fairly soon after orogenesis. However, many other parts of the Canadian Shield are lacking definitive information on post-orogenic activity in the Archean-Proterozoic.

2. K-feldspar multi-diffusion domain $^{40}Ar/^{39}Ar$ thermochronology

2.1 Linking high and low-temperature thermochronometers

Potassium feldspar is a useful mineral for $^{40}Ar/^{39}Ar$ dating because of its high K content, ubiquity in felsic rocks, and stability during *in vacuo* heating (McDougall and Harrison, 1999). K-feldspar is moderately retentive of radiogenic ^{40}Ar, and low-temperature ordered K-feldspars usually exhibit complex microstructures that lead to what has been termed multi-diffusion-domain (MDD) behavior, which means that most grains of K-feldspar contain a range of diffusion domains that can record a range of temperatures (Harrison et al., 1991; Lovera et al., 1989; Lovera et al., 1991; Zeitler, 1987). $^{40}Ar/^{39}Ar$ K-feldspar MDD analysis is able to determine continuous temperature-time (T-t) paths over the range ~150˚C to 350˚C and the shape of age spectra can distinguish between slow and rapid cooling. Continuous T-t paths can be established over this interval because the ^{39}Ar released during step heating can be used to independently determine the sample's specific diffusion kinetics and inherent domain-size distribution. These data can then be used to invert the observed $^{40}Ar/^{39}Ar$ age spectrum for the only remaining unknown, the thermal history. Modeling for thermal history is best done using an inverse approach to eliminate observer bias from forward modeling, and also speed up the recovery of a robust suite of thermal histories. K-feldspar $^{40}Ar/^{39}Ar$ thermochronology fills the middle-temperature range between higher temperature methods recording crystallization, such as U-Pb geochronology, and the low-temperature chronometers (apatite fission-track and U-Th/He) that record near-surface processes.

Samples were obtained from widespread localities (fig. 1 and fig. 5) within central Canada to investigate the intermediate thermal history gap. Craton interior samples are bracketed spatially by well-known histories in the northwest craton, i.e. Athabasca, and the Grenville to the southeast. Exposed granitic rocks and near-surface drill cores were chosen for their K-feldspar and because most have existing high- and low-temperature thermochronologic constraints. See the appendices for comprehensive information on rock samples, geochronologic context, and dating/modeling methods.

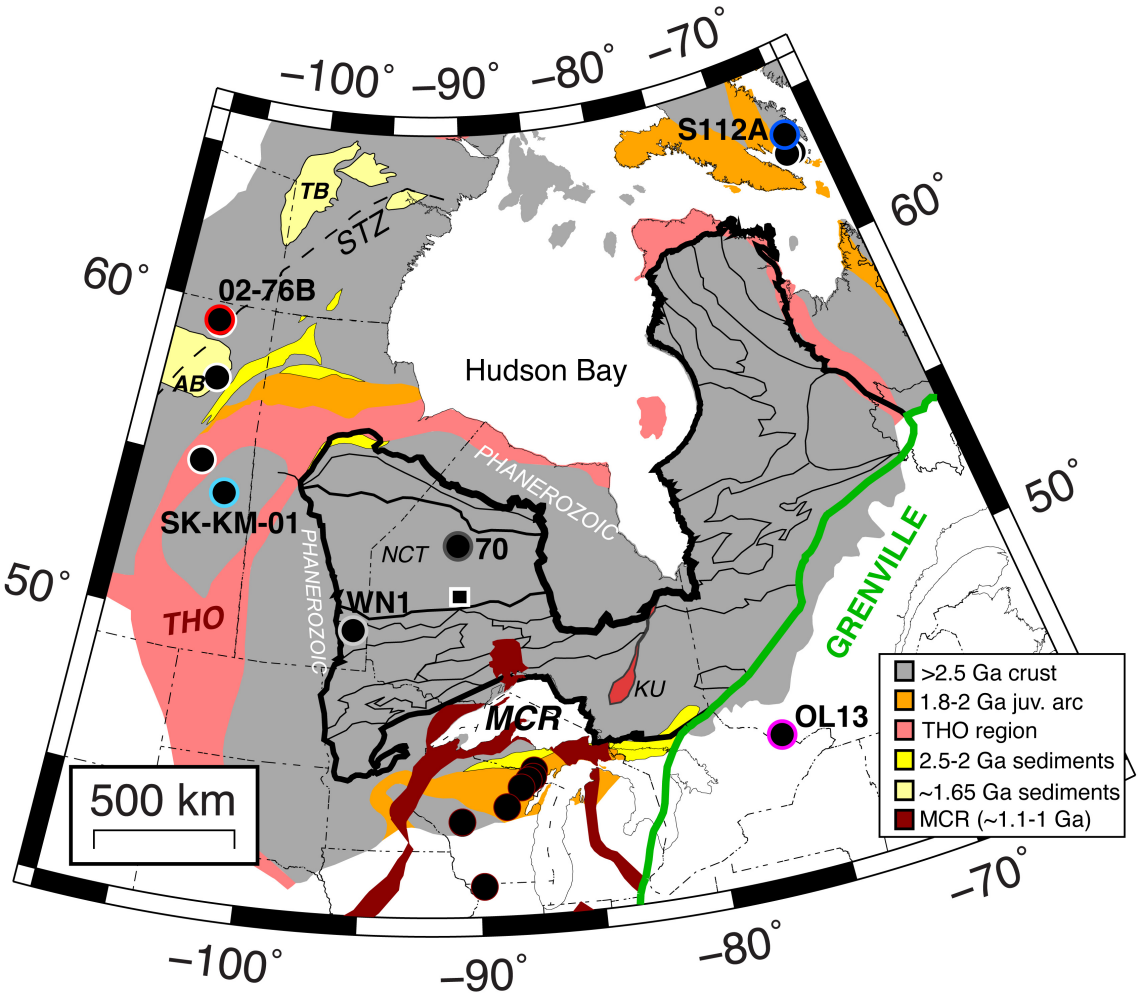


Figure 1. Map of Canadian Shield modified from Whitmeyer and Karlstrom (2007) with the Superior Province (outlined by heavy black line) and associated subterrane boundaries after Percival et al. (2006); actual western Superior craton boundary extends to THO beneath sedimentary cover. Red, blue, and pink outlined points match Ar/Ar age spectra and black dots show locations of other K-feldspar samples we have dated by $^{40}Ar/^{39}Ar$ MDD step-heating. All colored points correspond to samples and age spectra/thermal histories in figure 3. The sample located in the North Caribou Terrane (NCT) is #70. Black square in the NCT is an apatite (U-Th)/He sample from R. Flowers (pers. comm.) with a mean age (n=5) of 529.56 ± 60.49 (2σ) Ma. Samples and data south of the MCR are shown in appendix. Gray areas are >2.5 Ga Archean crust and orange regions are 2.0-1.8 Ga juvenile arcs of the Penokean orogen to the south, La Ronge to the northwest, and Torngat-Narsajuaq to the northeast. Light red shading reflects areas affected by the Trans-Hudson Orogen (THO). Darker yellow areas are 2.5-2.0 Ga miogeoclinal post-orogenic sediments. Light yellow are ~1.6-1.7 Ga sediments of the Athabasca Basin (AB) and the Thelon Basin (TB). STZ = Snowbird Tectonic Zone; THO = Trans Hudson Orogen; MCR = Mid Continent Rift (dark red shading), KU = Kapuskasing Uplift (shaded red). Green line is Grenville Province boundary.

2.2 $^{40}Ar/^{39}Ar$ MDD thermochronology results

Granitic rocks from various parts of the Canadian Shield including, the Western Superior Province (Ontario), and terranes affected by the THO (Saskatchewan and southern Baffin Island) yield $^{40}Ar/^{39}Ar$ spectra that reveal protracted histories of slow cooling during the Proterozoic 'middle age' (**fig. 2; see appendix for full dataset**). Information about $^{40}Ar/^{39}Ar$ dating methodology and modeling can be found in the supplementary material. Age spectra from the North Caribou Terrane (NCT) at the center of the western Superior craton (sample No. 70) exhibits ^{39}Ar release patterns that span from >2000 Ma to approximately 1100 Ma, whereas to the southwest in Manitoba, a Superior province sample (WN-1) reveals slow cooling from ca. 1700 Ma to nearly 1000 Ma. THO rocks in central Saskatchewan yield age spectra indicating slow cooling spanning the entire Mesoproterozoic and those from THO rocks on Baffin Island also show coeval slow cooling progressing further through the Neoproterozoic. An MDD sample from the Grenville Province in the Otter Lake region of Quebec (OL13) yields slow cooling through the Cambrian. Age spectra from the northern Athabasca Basin margin denote very rapid cooling at ~1.7 Ga (see fig. 3A and Flowers et al. 2006) and other $^{40}Ar/^{39}Ar$ data from the southern Athabasca basin are also in agreement (see appendix).

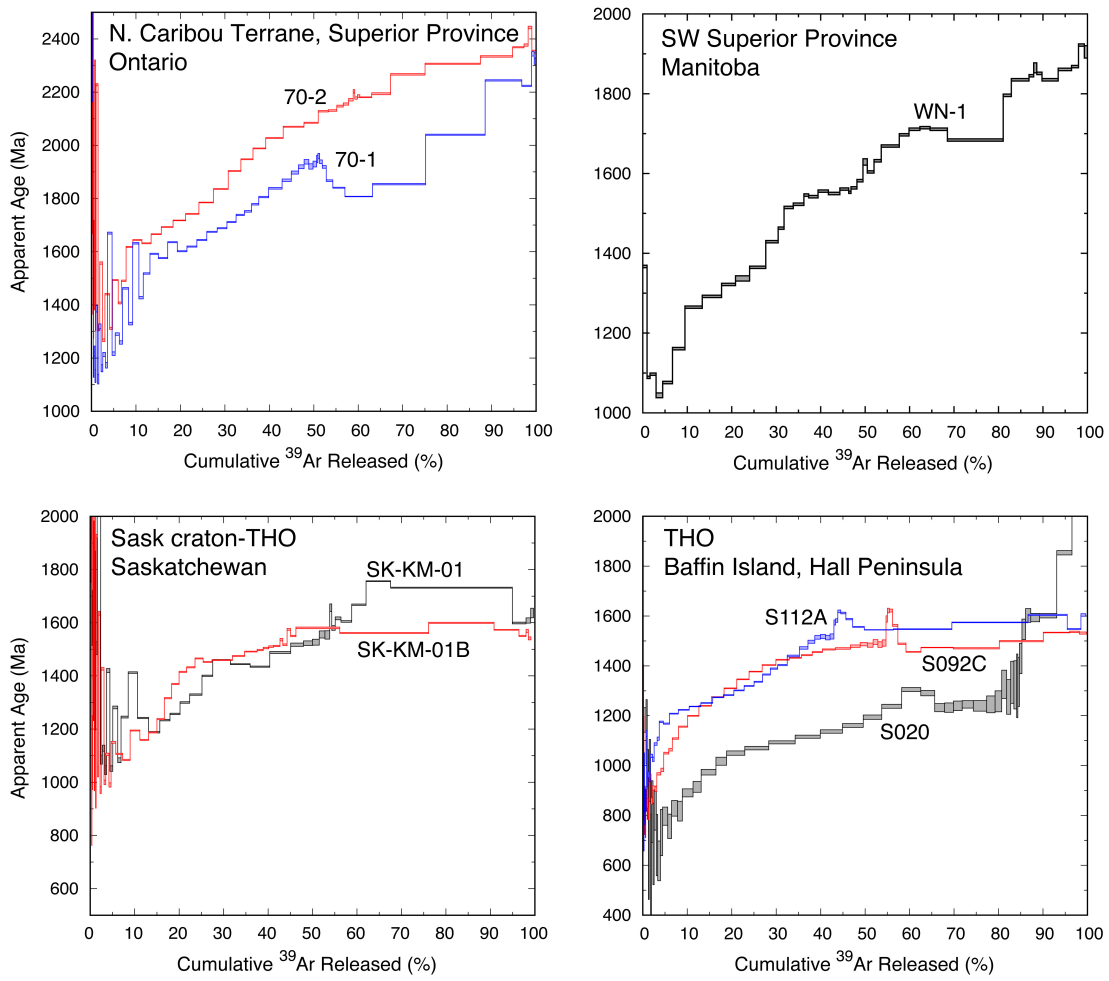


Figure 2. Subset of step-heated $^{40}Ar/^{39}Ar$ age spectra for K-feldspars from the Canadian Shield. Superior Province samples 70 and WN-1 illustrate slow cooling over ~800-900 m.y. The Sask craton sample SK-KM-01 replicates indicate slow cooling synchronous with Superior Province samples from ~1.6 to ~1.0 Ga. Baffin Island samples indicate slow cooling similar in duration to the SK sample, albeit further through the Neoproterozoic. Most samples have excess Ar in early release and experienced melting near 1100°C during heating experiments, typically at 50-70% ^{39}Ar loss. Note that under very slow cooling conditions, different age spectra can be produced from the same sample due to subtle differences in diffusion domain structure. All other age spectra are shown in appendix.

The most striking observation from these data is the consistent and geographically extensive slow-cooling signal recorded across the craton. This can be observed in the general "drooping" shape of age spectra indicative of partial Ar loss signifying slow cooling. Age gradients are large, collectively spanning the majority of the Proterozoic (2.5 to 0.54 Ga), amounting to ~500-600 million years or up to ~800-900 million years of

cooling in the Superior Province. These gradients are generally consistent with time-integrated slow cooling on the order of <0.5°C/Ma for cratonic rocks during the Proterozoic.

2.3 Thermal history data and modeling

We chose samples throughout the southern Canadian Shield to better resolve the intermediate thermal history of this region and link these data to existing high and low-temperature records. Rocks were selected from a broad area to assess potential differences (or lack thereof) in cooling signals across the interior craton.

The accepted ranges in K-feldspar kinetics (i.e. diffusivity and activation energies) from Lovera et al. (1997) were rigorously applied for diffusion domain modeling, which were input for thermal history inversions (see appendix). Thermal history modeling was performed only on samples that obey K-feldspar MDD theory, i.e. age spectra consistent with slowly-cooled feldspars should systematically increase in age from 0 to 100% cumulative ^{39}Ar release or alternatively, individual steps should remain consistent or equal in age during stepwise-degassing of ^{39}Ar, discounting low- or high-temperature excess Ar. Disturbed spectra with intermediate age maxima, saddle-shaped spectra, or high levels of age discordance between individual heating steps were excluded from modeling and interpretation. Thermal histories were assessed using the Arvert code, which employs a Monte Carlo approach driven by a Controlled Random Search algorithm (Price, 1977; Willet, 1997) (see appendix for details). The algorithm searches parameter space for misfit minima (thermal histories) that lead to better fits between

observed and predicted age spectra and additional mineral ages using a mean square weighted deviates (MSWD) objective function for assessing the agreement between individual age spectrum steps and model age spectrum steps. Explicit, constraining high-temperature information, variable heating and cooling rates, and additional apatite or zircon He ages can be included and modeled along with the feldspar age spectrum. It should be noted that $^{40}Ar/^{39}Ar$ age spectra were also obtained for rocks near the Mid-Continent Rift, however most of these samples produce disturbed spectra (e.g. intermediate age maxima), likely indicative of partial resetting, recrystallization, or hydrothermal alteration and were unable to be modeled.

2.3.1 Superior Province, Ontario

Sample #70 is a tonalite-trondjhemite granite from the Neoarchean North Caribou Terrane of the western Superior Province in Ontario Canada and is part of one of the oldest Archean cratons in North America; see Percival et al., (2006) for summary. Most of the rocks in this region record 3.1-2.6 Ga magmatic activity and hydrothermal alteration and a nearby sample yields zircon and titanite U-Pb ages of 2858 ± 5 Ma and 2854 ± 7 Ma, respectively (Van Lankvelt et al., 2016). Ti-in-zircon thermometry indicates zircon crystallization temperatures of 752 ± 37°C (Van Lankvelt et al., 2016). Apatite fission-track ages from this region of Ontario are ~350-450 Ma (Kohn et al., 2005; Lorencak, 2003).

Sample WN-1 is an Archean granodiorite from the Winnipeg River sub-province of the Superior craton from the Lac du Bonnet Batholith that was emplaced at 2665 ± 20 to

2568 ± 23 Ma (Everitt et al., 1996; Krogh et al., 1976). This sample was from 30.5 m depth from a borehole core and was previously dated via biotite $^{40}Ar/^{39}Ar$, yielding an age of 2291 ± 27 Ma (Hunt and Roddick, 1988), corresponding to a temperature of ~300°C at that time. An apatite sample (URL-6-2) at nearly the same depth/elevation as WN-1 has an AFT age of 373 ± 29 Ma (Feinstein et al., 2009). AFT data yield ages of ~370 to ~250 Ma, decreasing in age with depth.

Our K-feldspar $^{40}Ar/^{39}Ar$ monotonic thermal histories for the majority of samples in the southern craton indicate cooling rates of ~0.3°C/Ma from ~1.9 to 1.5 Ga and even slower cooling rates of <0.1°C/Ma from ~1.5 to ~1.1 Ga. Net cooling over this interval was only on the order of 100°C (fig. 3). Superior craton $^{40}Ar/^{39}Ar$ spectra from samples 70 and WN-1 display intermediate temperature thermal histories indicative of either: (1) prolonged mid-to-upper crustal residence during the Proterozoic, with time-integrated slow cooling on the order of ~0.1˚C/Ma, until ~1 Ga where marginally faster cooling resumed to bring these rocks to the surface, or (2) histories involving some amount of reheating during the Late Proterozoic **(fig. 3)**.

Sample 70 from the western Superior Province illustrates the non-unique nature of thermal history modeling and establishes the resolution and sensitivity of feldspar thermal histories (**see fig. 3D**). Three monotonic and six non-monotonic thermal history model inversions were performed under different starting conditions, i.e. permissible cooling rates, number of time nodes, explicit temperature constraints, and ran to varying degrees of convergence (see appendix for modeling methods). Both types of histories

overlap very well in the MDD constrained section of the model. However, models that allow any amount of reheating suggest that if it did occur it would have been between ~1.45 to ~1.1 Ga. High amounts of reheating (>>200°C) destroy T-t information and cause resetting of diffusion domains in K-feldspar, so our data imply that reheating of any amount between ~50° up to ~200°C is allowed, as any greater heating would have produced significantly different age spectra due to resetting. The best model runs favor minimal reheating of 50-75°C prior to 1 Ga, but still places this sample at temperatures of ~180-200°C near ~1.1-1.0 Ga.

2.3.2 Trans-Hudson Orogen, Saskatchewan

North-central Saskatchewan represents the transition from the exposed Shield bedrock to Phanerozoic cover of the Western Canada basin. Southern Saskatchewan is made up of multiple deformation fronts that welded the ~2.4 to 3.1 Ga Sask, Hearne, Rae, and Wyoming cratons during ~1.9-1.8 Ga Trans-Hudson orogenesis and suturing of Laurentian North America (Bickford et al., 2005). K-feldspars from the Athabasca Basin margin in the Chipman Domain of the Snowbird Tectonic Zone (samples 02-123A and 02-176B) are tightly constrained by existing high- and low-temperature thermochronological data (Flowers et al., 2006a; Flowers et al., 2006b) and stratigraphic constraints (Rainbird et al., 2007) and confirm the rapid cooling signal obtained in previous studies. Rocks here have been at or near the surface since ca. 1.6 Ga (Rainbird et al., 2007). Our Athabasca K-feldspar data clearly show excellent agreement with existing thermochronologic data and reinforce the validity of $^{40}Ar/^{39}Ar$ MDD for use on old rocks (fig. 3). Granitic drill core sample SK-KM-02 taken from shallow depth below

Phanerozoic sediments in Saskatchewan yield slightly disturbed spectra that may have been altered during post-depositional diagenesis; see Flowers et al. (2006b) and references therein. Sample SK-KM-01 results are able to be modeled and show either slow cooling from ~1.5 to ~1.1 Ga or modest reheating from ~1.3 to 1.1 Ga (sample furthest south; see fig. 1). The K-feldspar age spectrum from the southern Athabasca basin (SK-KM-03) shows some evidence of thermal alteration or, however the modeled T-t history aligns well with other samples from the northern Athabasca basin (see appendix for spectrum and modeled histories), whereas the central Saskatchewan sample from the Sask craton (SK-KM-01) exhibits a T-t history similar in style and timing to the Superior Province samples.

2.3.3 Trans-Hudson Orogen, Baffin Island

Baffin Island (Hall Peninsula) MDD samples (e.g. S112A in **fig. 3A**) display slow cooling and return thermal histories that are in internal agreement and completely consistent with other thermochronological data (e.g. Scott, 1999; Skipton et al., 2016a,b), suggestive of either slow cooling and exhumation towards the surface during Grenville time (~1.3-1.0 Ga), or histories involving reheating up to temperatures of ~200˚C between ~1.1-0.6 Ga. Proterozoic basin sediments exist in apparent thicknesses of over 2 km on northwestern Baffin Island in the Milne Inlet Trough and there is local evidence of non-depositional or erosional paleo-structural highs, faulting, and uplift prior to Paleozoic deposition (Kerr, 1979). The ~6 km thick sediments of the Bylot Supergroup (~1.27-0.72 Ga) on the northern Baffin Island shelf (Kah et al., 1999) are part of the Arctic Bylot Basins originally believed to have formed as a result of the Mackenzie rifting and igneous

event at ~1.27 Ga (Long and Turner, 2012), although these basins can also be interpreted as impactogens (see Sengor et al. 1978) forming from extension in response to far-field compressional effects of the Grenville during Rodinia assembly (Turner et al., 2016). The time from ~1.6-0.8 Ga represents a period of presumed erosion and intermittent sedimentation, with preserved sediments in excess of ~1-3 km on the northern Baffin Island margin (Kerr, 1979). Mackenzie and Franklin diabase intrusions also bracket these sediments. The Franklin-Thule LIP and dike swarm was emplaced in the Arctic, including Baffin Island, cutting through Bylot sediments during 0.75-0.725 Ga Rodinia breakup (Jackson et al., 1985) and is one of the largest LIPs in Earth history over five times greater than the Mid-Continental Rift area (Ernst et al., 2008). To the southeast, the Chidliak kimberlites of the Hall Peninsula were emplaced between 138-156 Ma, and preserved xenoliths show evidence of the now eroded Paleozoic cover (Heaman et al., 2012). The presence of Ordovician limestone on the western Baffin peninsula and apatite fission-track ages of ~200-440 Ma (McGregor et al., 2013) and apatite (U-Th)/He ages of ~200-400 Ma (Creason, 2015) indicate that the current southern Baffin bedrock was exposed (<100˚C) in the early Paleozoic. The $^{40}Ar/^{39}Ar$ thermal histories and geologic evidence favor a model where Baffin rocks were near the surface in the late Proterozoic and subsequently underwent episodic burial reheating and unroofing during the terminal phase of the Grenville orogeny into the Neoproterozoic.

2.3.4 Grenville Province, Quebec

Sample OL13 is a syenogranite from the Otter Lake region of Quebec, approximately 75-100 km northwest of Ottawa. This area underwent upper-amphibolite facies

metamorphism at temperatures and pressures of 700 ± 50°C and 6.5-7.5 kbar (Kretz, 1994) during the Elzivirian and Ottawan phases of the Grenville orogeny. Titanite from this sample was dated via U-Pb giving concordant ages of ~1.02 Ga for hornblende and hornblende-pyroxene granites (D. Schneider, unpubl. data), while yielding a biotite $^{40}Ar/^{39}Ar$ total-gas age of ~0.88 Ga (Schneider et al., 2013). A nearby sample has a hornblende Ar age of ~0.98 Ga, allowing the higher temperature Ar systems to constrain ~300-500°C from nearly 1000 Ma to 800 Ma. Collectively these data suggest post-orogenic cooling of ~2°C/Ma, and modestly slower cooling if K-feldspar $^{40}Ar/^{39}Ar$ data are incorporated. Our K-feldspar MDD monotonic thermal histories imply rapid cooling through ~250-200°C, followed by post-orogenic slower cooling of ~0.1-0.2°C (fig. 3B).

2.4 Summary of results

As for all thermochronometers, the application of the $^{40}Ar/^{39}Ar$ MDD method to resolve time-temperature histories over long time spans requires that diffusion mechanisms and kinetics determined in the laboratory over short timescales apply to much longer intervals; i.e., that there are no additional slow low-temperature mechanisms that become significant at billion year timescales. The overall agreement of our MDD results with other geochronology supports application of the method and that volume diffusion is dominant over very long timescales.

Independently constrained samples in the western craton at Lake Athabasca (sample 02-123A) and in the Grenville Province (sample OL-13) align with more 'traditional' views of craton stability and rapid post-orogenic decay, respectively, because their thermal

histories show rapid exhumation to the surface followed by relative stasis (fig. 3). Athabasca and Grenville K-feldspar data confirm that the $^{40}Ar/^{39}Ar$ MDD method can be reliably applied to very old rocks and that other K-feldspar samples are also broadly consistent with other constraining data. However, samples from across the southern Canadian Shield combine $^{40}Ar/^{39}Ar$ MDD K-feldspar data and high- and low-temperature thermochronology suggest much different histories (fig. 3B-D). Monotonic cooling-only scenarios exhibit broad agreement between locations in the central craton for a period of very slow cooling in the Meso- to Neoproterozoic, suggesting that these rocks were at elevated temperatures of ~200°C near 1 Ga and did not cool quickly to low temperatures. Scenarios allowing reheating (**see appendix for full results**) indicate that if heating occurred it was prior to 1 Ga, over a prolonged period of time (over ~200-300 Ma) coincident with the Grenville orogeny, and could have been approximately 50°C to 200°C in magnitude. However, both monotonic and reheating histories still suggest rocks were at elevated temperatures near 200°C in the late Proterozoic.

Rocks at temperatures of 200˚C in the late Proterozoic is an interesting problem. Invoking monotonic cooling and a normal cratonic geothermal gradient of 20˚C/km, would suggest that these rocks would be in the mid-crust at that time. If reheating occurred via long-term burial, thick sediment packages would be required, and given the relative synchronicity of reheating between different locations may also suggest similarities across the craton. Moreover, following peak reheating, rocks would then need to be re-exhumed. Therefore burial heating is an unlikely mechanism, although the next sections discuss possible contributing mechanisms to explain these thermal histories.

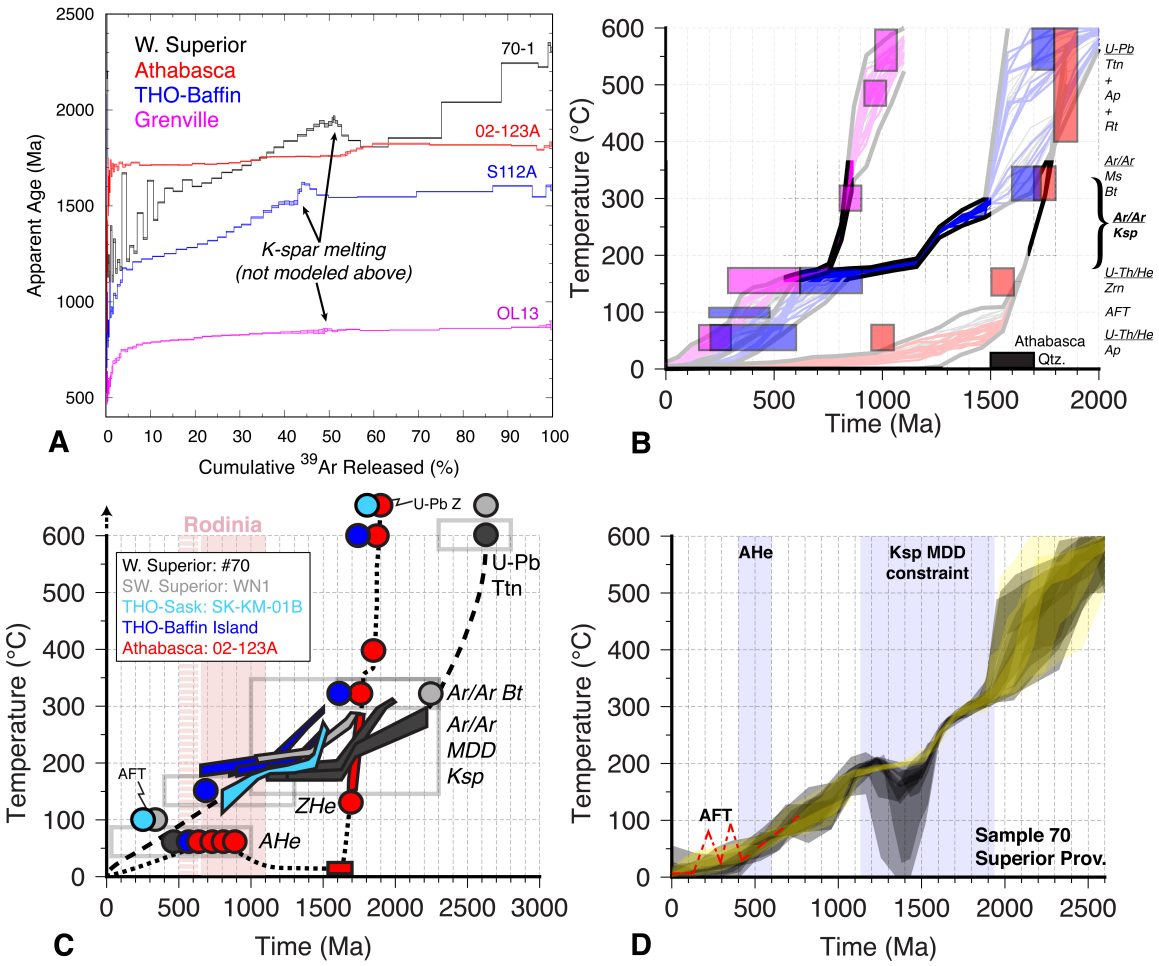


Figure 3. (A) K-feldspar MDD $^{40}Ar/^{39}Ar$ age spectra from Athabasca Basin sample (02-123A; red), THO-Baffin Island (S112A; blue), and the Grenville Province (OL13; pink). **(B)** Monotonic cooling-only T-t inversions corresponding to colored spectra in fig. 3A (sample 70 T-t monotonic and reheating-allowed results in fig. 3D). These show excellent agreement with independent higher and lower-temperature thermochronologic constraints shown by colored boxes. The MDD spectra can only constrain T-t histories from ~150 to 350°C, shown by the T-t envelopes for the 15 best solutions bounded by heavy black lines; steps with excess Ar early in gas release and those after K-feldspar melting at ~1100°C were not modeled. Black box is constraint given by depositional age range of Lake Athabasca sediments. Age constraints from Scott (1999); Flowers et al. (2006a, 2006b); Kennedy et al. (2010); McGregor et al. (2013); Schneider et al. (2013); Creason (2015); Hardie (2016); Skipton et al. (2016); full age constraint references are shown in appendix. **(C)** Summary of constrained T-t envelopes for monotonic-only K-feldspar MDD thermal histories of samples from the Western Superior Province (Samples 70 and WN-1: black/gray symbols), Sask craton sample SK-KM-01B from central Saskatchewan (light blue symbols), THO-Baffin Island samples (blue symbols), and a highly constrained Athabasca sample from the Chipman Domain (red symbols); refer to figure 2 for other age spectra that are not shown in fig. 3A. Colored dots correspond to bracketing high and low-temperature data for each sample. Gray boxes show the typical temperature range addressed by other thermochronologic systems. Notice truncated y-axis as U-Pb in zircon closure temperatures are in excess of 850-900°C. Pink band shows the time span of the Rodinia supercontinent from ~1.1 Ga

to breakup near ~0.7-0.6 Ga. Athabasca constraints from Flowers et al. (2006a; 2006b) Other age constraints from Krogh et al. (1976); Hunt and Roddick (1988); Naeser and Crowley (1999); Annesley et al. (1999); Van Lankvelt et al. (2016), Osadetz et al. (2002), see appendix for full references. **(D)** Sample #70 (from NCT, western Superior Province) thermal-history inversions showing the difference between three monotonic cooling models (yellow envelopes) and six models allowing reheating (black envelopes). Both sets of solutions place these rocks near temperatures of 300°C at ~1.8 Ga and 150-200°C at ~1.0-1.1 Ga. Regions explicitly constrained by Ar and apatite He data are shown. Dashed line shows Phanerozoic T-t path from burial/exhumation histories derived from AFT data of Lorencak et al. (2004) and Feinstein et al. (2009) during Paleozoic and Mesozoic burial of up to ~1.1-1.2 km from building of the Appalachians. Zrn = zircon, Ttn = titanite, Rt = Rutile; Ms = Muscovite; Bt = biotite; Ksp = K-feldspar; AHe = apatite (U-Th)/He; ZHe = zircon (U-Th)/He; AFT = apatite fission-track

3. Discussion

K-feldspar data from Athabasca agree with conventional views of cratonic stability where at ~1.9 Ga Laurentian assembly initiated rapid multi-stage exhumation of rocks to the surface, where they have remained for ~1.7 Ga (Flowers et al. 2006a;b). Thermal histories from the Archean-Paleoproterozoic southern Canadian Shield indicate rocks there were instead at temperatures near 200°C at 1 Ga (this also broadly applies to the histories at Baffin Island). So instead of rapid stabilization it appears that these rocks underwent very prolonged slow cooling. No matter how they were achieved, temperatures of 200˚C would represent depths of about 10 to 20 km using the range of Superior Province geothermal gradients from Jaupart et al. 2014 and about 6.5 km for 30°C/km.

3.1 Erosional exhumation via isostasy

These depths, and the temperatures they are based on, provide a serious challenge to conventional views of craton stability. Whether there was reheating or not, it is not feasible to obtain 10 km of exhumation through simple erosional isostatic return over the last 1 billion years, as reasonable values of upper/lower crustal and mantle densities, e.g.

(Schmandt et al., 2015) would require a crustal thickness of over 90 km at 1 Ga to permit this much total exhumation. The original estimated crustal thickness for the Superior Province is on the order of 50-60 km (Percival et al., 2006; Percival et al., 2012), which means that this magnitude of exhumation is highly unlikely without some post-Archean thickening of the crust. Erosion of this magnitude is also conceptually difficult, given the widely assumed low continental freeboard that one might infer from such slow cooling between ~2 Ga and 1 Ga. The "constant freeboard model" asserts that under isostatic equilibrium conditions the denudation of exposed cratonic terranes and accumulation of sediments on low-lying craton margins leads to continental elevations trending towards equilibrium with mean sea level over long timescales (Eriksson et al., 2006). This carries implications for the erosional potential at 1 Ga, where any significant craton topography had long since been removed and the continental interior would have to be above sea level for excess elevation to be isostatically balanced by crustal thickness.

Pressure-temperature estimates (**fig. 5**) show that large portions of the western Superior Province have been exhumed a total of 10-15 km (~4-6 kbar), whereas present Moho depths are ~40 km, suggesting that the maximum original crustal thickness was on the order of 50-60 km (Percival et al., 2006; Percival et al., 2012). Geothermal constraints and prior P-T studies were integrated and suggest that exposed metamorphic rocks of the North Caribou terrane in the Western Superior Province were eroded ~11 km (Jaupart et al., 2014). Given the known erosion levels and original crustal thickness, cooling from 200˚C at 1 Ga would require some amount of crustal addition and delayed exhumation after initial Archean stabilization. Abbott et al. (2000) estimate that the worldwide total

crustal erosion that occurred in Archean and early Proterozoic terranes ranged from 2.5-7.8 km and 1.7-4.4 km, respectively. This information along with petrologic observations and our K-feldspar MDD data suggest virtually all of the southern Canadian Shield exhumation would have been deferred to ~1 Ga.

3.2 Burial heating and geotherm variability

If burial is required to achieve 180-200˚C via reheating, significant accommodation space and a source of sediment is required. The Superior Province witnessed extreme deformation, from Grenvillian contraction (and foreland sedimentation) on one side and MCR extension on the other, over 300 m.y. from 1.3-1.0 Ga. If all or part of the reheating observed in inverse thermal history models was attributed to burial heating instead, one would have to explain how such a horizontally and vertically extensive package of sediments could be deposited at 1 Ga, far inboard of the Grenville orogen, and ultimately there would still be a reasonably thick rock column to remove afterwards, since our samples were collected from the surface. The extent of the Grenville foreland is not very well constrained and all surface evidence of it is gone, but it would have been mainly restricted to the eastern Superior margin (Krabbendam et al., 2008) and the eastern U.S. mid-continent (Hauser, 1993).

To estimate the effects of sedimentation heating, steady-state crustal geotherms were calculated as a result of 5 km of sediments overlying an eroded radiogenic upper crust (5 km removed) with a bulk heat production (A) of 2.5×10^{-6} W/m^3, surface temperature of 10˚C, basal heat flow of 30 mW/m^2, and assumed uniform thermal conductivity (K) of 3

W/(m·K) between the upper crust and sediments. Intracratonic basin depths would have to be considerable as temperatures of ~150-200˚C would only be reached at ~3-5 km depth. Heating of this magnitude could also be achieved via higher heat production from thinner sediment cover or a thicker radiogenic upper crust. This end-member scenario is possible, although no evidence of a basin of proper age exists and most of the preserved cratonic basins nearby contain sediments shed during initial cratonization and stabilization in the Archean-Paleoproterozoic during early assembly of Laurentia (Davidson, 2008). The central craton has undergone platform sedimentation numerous times since ~2 Ga and the sporadic sediments found scattered across the landscape suggest that most of Laurentia was buried by sediment at various times in the past (Davidson, 2008). Detrital zircon studies and paleo-current markers also reveal Proterozoic sediment transport was facilitated by large continental-scale fluvial networks, carrying sediments to the northwest craton (Slave-Athabasca region) shed from the Trans-Hudson orogen and later high topography of the Grenville orogen that buried the craton in a veneer of sediment up to 1 km thick in some areas (Rainbird et al., 2012; Rainbird et al., 1992; Rainbird et al., 1997). However, even without the encumbrance of vegetation restricting channelized fluvial flow, it is difficult to assert that the majority of the eastern Canadian Shield experienced sheet-like sediment deposition thick enough to substantially reheat MDD samples.

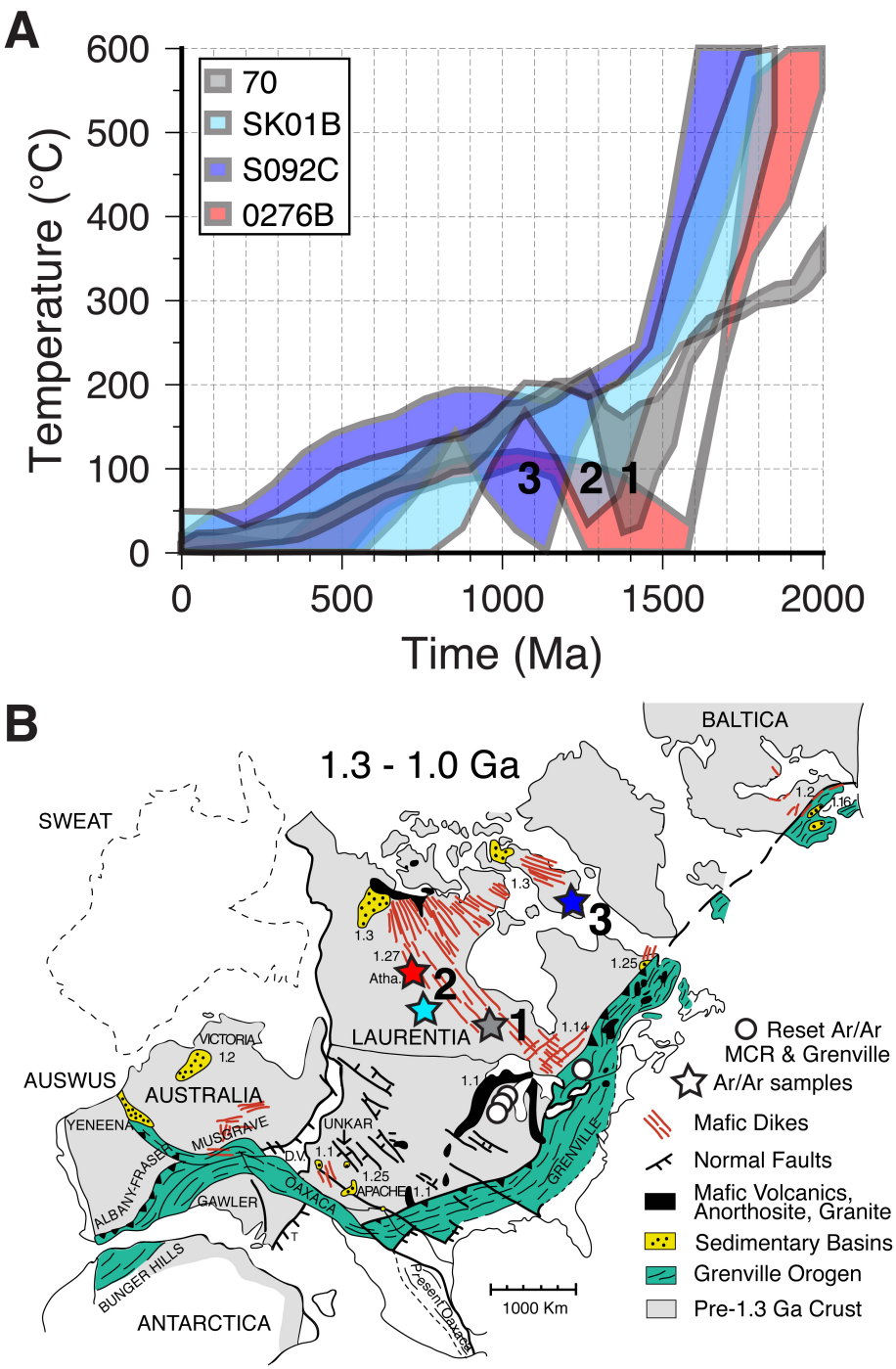


Figure 4. (**A**) Thermal history T-t envelopes allowing a single reheating episode; for the W. Superior (gray), Sask craton, sample SK-KM-01B (light blue), Baffin Island, sample S092C (dark blue), and Athabasca, sample 02-76B (red) for regional comparison. The Athabasca sample shows rapid cooling to the surface by ~1.7-1.6 Ga, whereas the other samples show cooling to near surface conditions, followed by sequential reheating with respect to increased distance from the Grenville orogen. The Athabasca K-feldspar requires a less distinctive reheating signal than the other examples and reheating could begin between ~1.55 to ~1.25 Ga. (**B**) The tectonic arrangement for the 1.3-1.0 time period is shown on the right with stars denoting Ar/Ar samples that were modeled in figure 3A; map modified from Karlstrom et al. (1999). Other Ar samples

reset by MCR heating/deformation and Grenville orogenesis are also shown. Two proposed configurations of Rodinia, SWEAT = southwestern U.S. – East Antarctica; AUSWUS = Australia – Western U.S.

Thermal histories for southern Canadian Shield samples suggest that if burial reheating occurred then there was variability in magnitude and timing (**fig. 4**). The initial rapid cooling to the surface of Athabasca sample 02-76B ($^{40}Ar/^{39}Ar$ MDD constraints between ~1.6 and ~0.45 Ga) gives way to subtle, prolonged reheating of up to ~100°C beginning as late as ~1.25 Ga. This history is in first-order agreement with a combination of histories proposed in Flowers et al. (2006b) from apatite and zircon U-Th/He data where rocks were exhumed to the near-surface and were either at temperatures of ~40°C for an extended time or underwent episodic reheating later in the Phanerozoic. Superior Province, THO-Sask craton, and THO-Baffin Island samples underwent distinctive cooling histories when compared to Athabasca, however they are similar to the **figure 3D** sample 70 example with respect to the range of model-allowed reheating and rocks still end up at elevated temperatures near ~200°C. The timing of reheating initiation for each sample in **figure 4** is markedly earlier when approaching the Grenville deformation front. It should be noted that the THO-Baffin Island signal at ~1 Ga is similar to the others in style albeit slightly delayed when compared to the samples in the southern Shield. It is worth noting that the Athabasca samples are indicative of rapid cooling to the surface and suggest maximum reheating was only on the order of ~100°C. If southern craton samples experienced similar histories then the maximum reheating would likely be of a similar magnitude, however thermal history solutions for these other areas suggest reheating that is double this amount, which is probably unreasonable for burial scenarios.

It seems improbable, at least under current views about cratonic evolution, that 200˚C temperatures at shallow depths could have been related to an abnormal geothermal gradient, and not burial, because thermal gradients approaching 40-50˚C or more would have been required and sustained on the order of a hundred million years or more to match thermal history model results. Most geothermal perturbations are short-lived; an estimate of the Paleoproterozoic steady-state geotherm of the Witwatersrand Basin is 27˚C/km with an increase to ~40˚C/km during ~2 Ga Bushveld magmatism and mafic underplating that lasted for <30 m.y. before returning to steady-state conditions (Frimmel, 1997). In addition, plume-head thermal diffusion effects on thick lithosphere have been modeled for the Great Meteor Hotspot of the northeastern U.S., and a 500˚C anomaly initially confined to the lower 50 km of the cratonic lithosphere decays to 80˚C at 200 km depth over 120 m.y., while the middle-to-upper crust feels very little perturbation at all (Eaton and Frederiksen, 2007). The thermal diffusivity through thick cratonic lithosphere is long (~10^9 years) and the amount of basal heat required to substantially heat the crust is high.

3.3 Magmatic underplating

Mafic underplating is integral to various models of Archean-Proterozoic geodynamics and crustal growth and reworking, where higher density material is added to the base of the crust (Hawkesworth et al., 2013; Thybo and Artemieva, 2013). The emplacement of 10-25 km of underplated material can rapidly thicken and add significant crustal volume under normal lithospheric thermal conditions (Cox, 1993; Furlong and Fountain, 1986).

Adiabatic decompression of the mantle forms melt that is typically a density of 3000-3100 kg/m^3, which falls between typical mantle and crustal densities, therefore increasing the potential for mafic melt trapping in the lower crust that displaces denser lithospheric mantle while producing uplift (Allen and Allen, 2013). The high seismic velocities observed in the lower crust of underplated regions seems to verify this (Thybo and Artemieva, 2013), and underplating has been proposed for other cratons such as the Karoo province of the South Africa that experienced crustal inflation and permanent uplift and surface erosion in the Phanerozoic (Cox, 1993).

3.3.1 Underplating at the Mid-Continent Rift

The Mid-Continental Rift affected the Superior craton at ~1.1 Ga and various models exist for initiation, either a hot mantle plume that impinged on the lower lithosphere founded on petrologic and geochemical data (Davis and Green, 1997; Nicholson and Shirey, 1990) or as a far-field extensional response to compressional stresses during the Grenville orogeny (Gordon and Hempton, 1986; Van Schmus and Hinze, 1985). Both models are still debated, however, recent studies favor the latter model (Levandowski et al., 2015; Whitmeyer and Karlstrom, 2007) or a combination of the two (Stein et al., 2015). Northward propagation of the MCR was inhibited by the strong Superior lithosphere, and the shape and position of the rift was influenced by the stable craton margin (Ola et al., 2016). There is evidence of basaltic underplating of the Archean lower crust during the 1.1 Ga failed rifting of the mid-continent (Behrendt et al., 1990; Tréhu et al., 1991), whereas lower crustal granulite xenoliths from northern Michigan also indicate a plume-derived source for underplating (Zartman et al., 2012). The rift itself shows a

~20 km depth discontinuity (potentially the base of the MCR volcanic package) and a 10-20 km thick layer between the lower crust and upper mantle interpreted as underplated magmatic material (Zhang et al., 2016). Other seismic studies also suggest that the crust is unusually thick at the MCR from reactivation during late stages of the Grenville orogeny (French et al., 2009; Shen et al., 2013). Geophysical modeling shows a similar Moho density contrast interpreted as thickened crust due to mafic underplating that is >15 km thick at the base of the southwestern Superior crust that occurred during ~1.8 Ga suturing of the Yavapai-Superior-Wyoming blocks during the THO (Thurner et al., 2015). Underplating has also been invoked in models of southern Laurentian deformation during the Grenville, where south-directed subduction and continental collision led to over-thickening, slab breakoff, and asthenospheric upwelling resulting in the Llano Uplift and erosion at ~1.12-1.07 Ga (Mosher et al., 2008).

3.3.2 Archean versus Proterozoic crust

Abbott et al. (2013) argue that undisturbed cratonic crust stabilized in the Archean is characterized by few internal seismic boundaries, the absence of high velocities in the lower crust, and a sharp Moho as a result of delamination of denser eclogite-facies rocks, while post-Archean basaltic lower crust is the result of underplating. Proterozoic crust is consistently thicker (40-55 km) and is characterized by higher lower crustal seismic velocities, when compared to Archean terranes (Durrheim and Mooney, 1991). The North Caribou Terrane is the core of the western Superior Province and is contrarily characterized by thicker crust (40-43 km), given its Archean affinity (Percival et al., 2012; Perry et al., 2002). The crust also thickens from 40 km in the NCT to 45 km

towards Lake Superior at the locus of MCR rifting. This is markedly different from the eastern Superior craton, which is ~35 km thick (Perry et al., 2002). The greater crustal thickness in the western Superior compared to the eastern Superior and thickening towards the MCR tentatively supports the compiled worldwide observations for post-Archean underplating and crustal thickening.

3.3.3 Underplating in the Superior Province

Despite a thicker crust in the western Superior Province, the lithospheric lid generally thickens eastward. There is a significant mafic crustal component present in the western Superior and eastern Ontario, suggesting highly heterogeneous crustal and mantle structure across the Superior Province, with a thickened crust in the southern Superior Province (Darbyshire et al., 2007). The lower crust-upper mantle anomaly that exists in the western Superior Province has been interpreted to be the result of Archean imbricate slab accretion of oceanic crustal material (in the Wabigoon subprovince) under the North Caribou Terrane during lithospheric assembly that appear as Moho-penetrating high-velocity regions in seismic profiles (Musacchio et al., 2004; White et al., 2003) (**fig. 5)**. Alternatively, Nitescu et al. (2006) hypothesize that the oceanic slab argument is not conclusive and that continuity in lower crustal densities align more with a model of post-accretionary thermal softening and lower crustal reworking. They also argue that the mass anomalies within the lower crust of the Wabigoon Province and those terranes to the south instead represent underplated dense, anisotropic mafic rocks from MCR extension and magmatism that modified the lower crust.

Thermobarometry and the compositional differences with depth (fertile vs. depleted) found between garnets in the Proterozoic Kyle Lake and Paleozoic-Mesozoic Attawapiskat kimberlites (just east of Kyle Lake) (**fig. 5**) in the western Superior Province signify a modified mantle composition or reworked structure between parts of the western province due to MCR extension and basalt emplacement (Scully et al., 2004; Smit et al., 2014). The thickened crust of the rift flanks experienced uplift due to increased buoyancy (Levandowski et al., 2015) and the "topographic doming" model of Allen et al. (1992) proposes MCR melting from a mantle plume source affected a large portion of the western Superior lower crust with underplating occurring up to 650 km from the rift itself (**fig. 5**). This model is reinforced by the aforementioned high-density, lower-crustal layer thickening towards the MCR and the presence of synchronous dikes (and kimberlites) north of Lake Superior (Ernst et al., 2008), which are typically believed to be the surface expression of underplated mafic rocks (Nelson, 1991). Magmatic underplating (~5 km thick) is also observed in the Davis Strait off of SE Baffin Island (Funck et al., 2007) and to the north in Baffin Bay (Suckro et al., 2012) but has been interpreted as a more recent Paleogene feature associated with Icelandic plume activity.

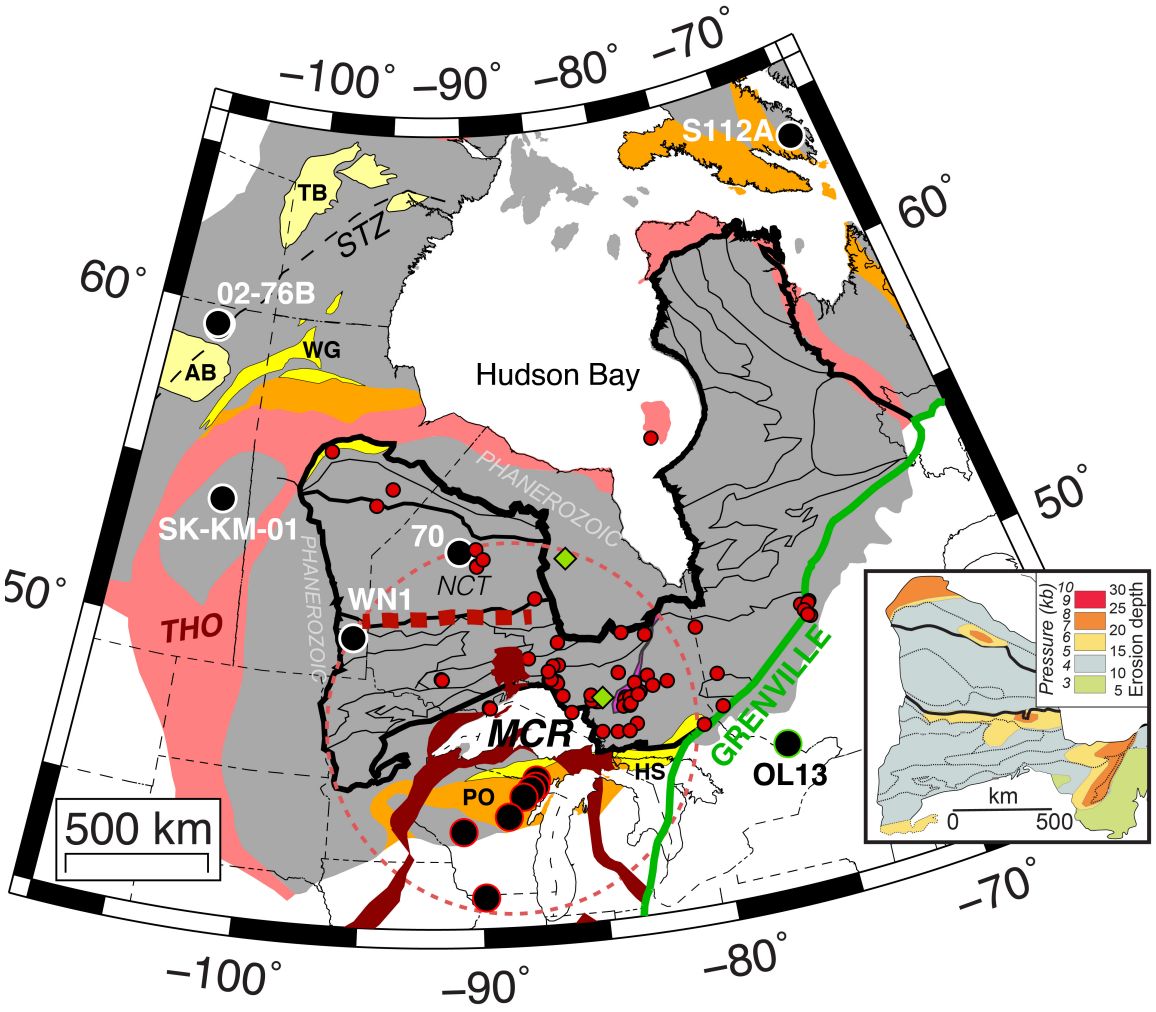


Figure 5. Map of the eastern Canadian Shield modified from Whitmeyer and Karlstrom (2007) with geologic sub-terranes of the Superior Province outlined in black from Percival et al. (2006). Inset map shows erosion depths in km and P-T estimates across the western Superior Province, adapted from Percival et al. (2012). K-feldspar MDD samples dated in this study via $^{40}Ar/^{39}Ar$ are shown by black dots and the Mid-Continent Rift likely disturbed those with red outlines (see appendix for age spectra). Red dots are from the Geological Survey of Canada Geochronology database and queried by location in the Superior Province and filtered by 0.95-1.2 Ga date range, representing ages (mainly mafic dikes) using various higher-T dating methods, i.e. K-Ar, Ar/Ar, U-Pb, Rb/Sr. Note: the red points in NW Superior are likely related to the ~1.26 Mackenzie dike swarm originating in the Slave craton up to 3000 km to the NW. The dark red dashed line near the southern NCT boundary is the high seismic velocity region from Musacchio et al. (2004) and gravity anomalies of Nitescu et al. (2006) interpreted as a result of MCR underplating. Red dashed circle is the region that could theoretically be affected by topographic doming up to 650 km away from the MCR nucleus, from model of Allen (1992). Gray areas are >2.5 Ga Archean crust and orange regions are 2.0-1.8 Ga juvenile arcs of the Penokean Orogen (PO) to the south, La Ronge to the northwest, and Torngat-Narsajuaq to the northeast. Pink shading reflects areas affected by the Trans-Hudson Orogen (THO). Darker yellow areas are 2.5-2.0 Ga miogeoclinal post-orogenic sediments. Light yellow are ~1.65 Ga sediments of the Athabasca Basin (AB) and the Thelon Basin (TB). Areas marked 'Phanerozoic' are Archean basement underlying younger sediments. Light green diamonds are Kyle Lake (north) and Abitibi kimberlites (south) of ~1.1

Ga age. MCR = Mid-Continent Rift and pink polygon is Kapuskasing uplift. The Grenville province boundary is dashed in green. STZ = Snowbird Tectonic Zone (between Rae craton to N and Hearne to the S); HS = Huronian Supergroup; WG = Wollaston Group; NCT = North Caribou Terrane.

The western Superior Province shows evidence of significant deformation occurring due to dike swarms and rifting from ~1.25-1.0 Ga from the Mackenzie plume and dike system (in the Slave Province far to the northwest; figs. 4 and 5) and the MCR mantle plume. This magmatism produced an underplated (>15 km), thickened crust at the MCR, which tapers to approximately ≤10 km thick to the north in the Western Superior Province. Magmatic underplating in the lower crust causes thickening and drives isostatic compensation to account for added mass. To model the appropriate crustal response, typical crustal densities, as well as those from Thurner et al. (2015) of 2950, 3100, and 3300 kg/m^3 for the crust, underplate, and mantle, respectively, are used to simulate isostatic uplift and erosion (**Table 1**). Using equations from Allen and Allen (2013), under normal lithospheric conditions with the surface at sea level, the pressure at depth, y_L at the base of the lithosphere is:

$$y_c\rho_c g + (y_L - y_c)\rho_m g \tag{1}$$

While the pressure at the same depth, under uplifted lithosphere with an underplate is given as:

$$y_c\rho_c g + H\rho_h g + (y_L - y_c - H + U)\rho_m g \tag{2}$$

Equation (3) describes the uplift (U) relationship under Airy isostasy conditions and the balance of lithospheric columns at the base of the lithosphere (compensation depth); where H is the underplate thickness, ρ_h is the density of the underplate, and ρ_m is the density of the mantle.

(3)

$$U = H\left(1 - \frac{\rho_h}{\rho_m}\right)$$

Erosional denudation (D) is included from (Brodie and White, 1994), where ρ_c is the crustal density:

(4)

$$D = H\left(\frac{\rho_m - \rho_h}{\rho_m - \rho_c}\right)$$

Underplate thicknesses of 3 to 10 km **(table 1)** produce respective isostatic uplift amounts of ~200 to ~900 m, resulting in ~1700 to 6000 m of denudation (assuming no change in surface elevation).

Table 1: Isostatic uplift and denudation for magmatic underplating

Underplate, H (m)	ρ_c (kg m^{-3})	ρ_h (kg m^{-3})	ρ_m (kg m^{-3})	Uplift, U (m)	Denudation, D (m)
3000	2800	3000	3300	273	1800
5000	2800	3000	3300	455	3000
10000	**2800**	**3000**	**3300**	**909**	**6000**
15000	2800	3000	3300	1364	9000
20000	2800	3000	3300	1818	12000
3000	2950	3100	3300	182	1714
5000	2950	3100	3300	303	2857
10000	2950	3100	3300	606	5714
15000	2950	3100	3300	909	8571
20000	2950	3100	3300	1212	11429

Table 1. The role of magmatic underplating of variable thickness and density is shown. The relation of crustal density changes inducing an isostatic response causing uplift and corresponding erosion at the surface. Mafic underplating of typical thicknesses for the crust between 3-20 km (variable density) can cause up to ~275-1800 m of uplift, resulting in ~2-12 km of erosion. Note: multiplying the underplate thickness by a factor of 0.6 yields the amount of denudation for typical crustal/mantle/underplate densities of 2800/3300/3000 kg/m^3. The 10 km underplate is in bold as a likely W. Superior example from geophysical and gravity data interpretations.

3.3.4 Summary of mechanisms to explain T-t histories

The key result is that ^{40}Ar/^{39}Ar K-feldspar MDD data establish that rocks in the southern Canadian Shield were at ~200°C at ~1 Ga. The preferred mechanism to provide the required exhumation is magmatic underplating, which is a feasible way to thicken the crust in the Proterozoic and cause an isostatic disturbance that would necessitate erosional re-equilibration. There are regional geophysical data that suggest that underplating occurred at this time and impacted a large area of over 1000 square kilometers near the Mid-Continental Rift. Assuming a 20°C/km geothermal gradient, monotonic cooling-only thermal histories for the western Superior Province indicate that the surface rocks from which our feldspar samples were taken were at depths of up to 10 km in the crust at ~1 Ga. Extreme crustal thicknesses would be required if rocks were simply isostatically exhumed over the past 1 billion years. Our data imply that if rocks

resided in the middle crust then the majority of craton unroofing was delayed until Rodinian-time near the end of the 'Boring Billion.' Reheating initiated prior to 1 Ga on the order of ~50°C up to 200°C is allowed by the $^{40}Ar/^{39}Ar$ MDD thermal histories and could be achieved through a few kilometers of sediment burial or significant warming of the middle-to-upper crust. However, the monotonic thermal histories are preferred as there is no sedimentary evidence to support burial in many areas, nor evidence of sustained, elevated upper- and mid-crustal reheating that would have to be on the order of a few tens to hundreds of millions of years. The time span of the Great Unconformity and physical lack of sediments would also suggest that erosion was the more dominant process across the exposed Laurentian shield at the end of the Proterozoic.

4. Conclusions

A previous observational gap was filled using $^{40}Ar/^{39}Ar$ MDD analysis of K-feldspar, which yielded interpretable results consistent with success in younger terranes. Results were tested using several samples where other constraints were available and produced thermal histories consistent with prior geochronologic and geologic information. This success gave us confidence to pursue unconstrained regions of the Canadian Shield where modeled thermal histories suggest rocks were at temperatures near ~200°C at approximately 1 Ga in the southern Shield. Baffin Island rocks show similar age gradients and thermal histories but the timing of slow cooling is slightly delayed with respect to the southern Canadian Shield. $^{40}Ar/^{39}Ar$ age spectra for most localities suggest slow cooling throughout the Earth's Middle Age. Assuming monotonic cooling, thermal-history solutions resolve a prolonged period of near-isothermal conditions throughout

most of the Proterozoic. If modest, geologically reasonable reheating is allowed, thermal-history solutions permit up to ~200°C of diachronous reheating during the span ~1.4 to ~0.8 Ga for rocks in the southern Canadian Shield and to the north at Baffin Island. In either case, rocks are at elevated temperatures near ~1 Ga in those scenarios and would require re-exhumation. However, Athabasca and Grenville rocks show much different histories of rapid cooling. Sedimentary data and high-temperature geochronology show that the western craton near Athabasca was exhumed to the surface much earlier in the Proterozoic – and our K-feldspar age spectra lend further support for this observation. Thermal histories and geologic evidence suggest that Grenville rocks were fully exhumed to the near surface in the Paleozoic.

Thermal histories allowing mid-Proterozoic unroofing to the near surface would require extreme and prolonged upper crustal heating, but there is no geologic evidence to support such cratonic histories. Reheating via burial does not provide adequate explanations for K-feldspar MDD data, and rocks would still require later unroofing given the timing of modeled heating episodes. The known levels of total erosion and P-T constraints on the total crustal thickness in the western Superior Province put limits on the regional exhumation history. Proterozoic slow cooling would require some amount of subsequent crustal thickening on the order of 10-15 km near 1 Ga to permit the necessary uplift and erosion levels to explain K-feldspar MDD data. Our preferred mechanism is that regional magmatic underplating due Mid-Continental rifting thickened the crust and caused exhumation beginning in the Neoproterozoic. This is supported by geophysical evidence of underplating and crustal thickening at the Mid-Continental Rift and the western

Superior Province, and when taken together with K-feldspar MDD thermal histories suggest previously unrecognized exhumation beginning in the Neoproterozoic. This large-scale denudation may have contributed to the development of the Great Unconformity in North America, preceding the recognized epeirogenic burial and exhumation episodes occurring during the early Phanerozoic.

Acknowledgements

We would like to thank Rebecca Flowers at the University of Colorado, Boulder for providing Athabasca samples and Ryan Morelli at the Saskatchewan Geologic Survey for facilitating access to granite cores. Thanks to Nancy Joyce of the Geological Survey of Canada geochronology lab for finding information about a long lost sample and thanks to Bruce Idleman for assistance in running the LU noble gas laboratory Ar extraction line, with sample preparation, and feldspar irradiation logistics.

References

Abbott, D., Sparks, D., Herzberg, C., Mooney, W., Nikishin, A., and Zhang, Y. S., 2000, Quantifying Precambrian crustal extraction: the root is the answer: Tectonophysics, v. 322, no. 1, p. 163-190.

Abbott, D. H., Mooney, W. D., and VanTongeren, J. A., 2013, The character of the Moho and lower crust within Archean cratons and the tectonic implications: Tectonophysics, v. 609, p. 690-705.

Alexandre, P., Kyser, K., Thomas, D., Polito, P., and Marlat, J., 2009, Geochronology of unconformity-related uranium deposits in the Athabasca Basin, Saskatchewan, Canada and their integration in the evolution of the basin: Mineralium Deposita, v. 44, no. 1, p. 41-59.

Allen, D. J., Hinze, W. J., and Cannon, W. F., 1992, Drainage, topographic, and gravity anomalies in the Lake Superior region: Evidence for a 1100 Ma mantle plume: Geophysical Research Letters, v. 19, no. 21, p. 2119-2122.

Allen, P. A., and Allen, J. R., 2013, Basin analysis: Principles and application to petroleum play assessment, John Wiley & Sons.

Ault, A. K., Flowers, R. M., and Bowring, S. A., 2009, Phanerozoic burial and unroofing history of the western Slave craton and Wopmay orogen from apatite (U–Th)/He thermochronometry: Earth and Planetary Science Letters, v. 284, no. 1-2, p. 1-11.

-, 2013, Phanerozoic surface history of the Slave craton: Tectonics, v. 32, no. 5, p. 1066-1083.

Behrendt, J. C., Hutchinson, D., Lee, M., Thornber, C., Trehu, A., Cannon, W., and Green, A., 1990, GLIMPCE seismic reflection evidence of deep-crustal and upper-mantle intrusions and magmatic underplating associated with the Midcontinent Rift system of North America: Tectonophysics, v. 173, no. 1-4, p. 595-615.

Bickford, M., Mock, T., Steinhart Iii, W., Collerson, K., and Lewry, J., 2005, Origin of the Archean Sask craton and its extent within the Trans-Hudson orogen: evidence from Pb and Nd isotopic compositions of basement rocks and post-orogenic intrusions: Canadian Journal of Earth Sciences, v. 42, no. 4, p. 659-684.

Blackburn, T. J., Bowring, S. A., Perron, J. T., Mahan, K. H., Dudas, F. O., and Barnhart, K. R., 2012, An Exhumation History of Continents over Billion-Year Time Scales: Science, v. 335, no. 6064, p. 73-76.

Bostock, M., 1998, Mantle stratigraphy and evolution of the Slave province: Journal of Geophysical Research: Solid Earth (1978–2012), v. 103, no. B9, p. 21183-21200.

Brasier, M., and Lindsay, J., 1998, A billion years of environmental stability and the emergence of eukaryotes: new data from northern Australia: Geology, v. 26, no. 6, p. 555-558.

Brodie, J., and White, N., 1994, Sedimentary basin inversion caused by igneous underplating: Northwest European continental shelf: Geology, v. 22, no. 2, p. 147-150.

Carlson, R. W., Irving, A. J., Schulze, D. J., and Hearn, B. C., 2004, Timing of Precambrian melt depletion and Phanerozoic refertilization events in the lithospheric mantle of the Wyoming Craton and adjacent Central Plains Orogen: Lithos, v. 77, no. 1, p. 453-472.

Carlson, R. W., Pearson, D. G., and James, D. E., 2005, Physical, chemical, and chronological characteristics of continental mantle: Rev. Geophys., v. 43, no. RG1001, p. 1-24.
Cawood, P. A., and Hawkesworth, C. J., 2014, Earth's middle age: Geology, v. 42, no. 6, p. 503-506.
Cope, N. J., 2012, Thermochronology and geochronology of the Otter Lake region, QC, Central Metasedimentary Belt, Grenville Province [Master of Science: Kent State, 117 p.
Cottrell, E., Jaupart, C., and Molnar, P., 2004, Marginal stability of thick continental lithosphere: Geophys. Res. Lett., v. 31, no. 18, p. L18612.
Cox, K., 1993, Continental magmatic underplating: Philosophical Transactions of the Royal Society of London A: Mathematical, Physical and Engineering Sciences, v. 342, no. 1663, p. 155-166.
Creason, C. G., 2015, Phanerozoic Exhumation History of Hall Peninsula, Baffin Island: Insights from Apatite and Zircon (U-Th-Sm)/He Thermochronology and 3D Thermokinematic Modeling [Master of Science: Dalhousie University, 138 p.
Dalziel, I. W., Mosher, S., and Gahagan, L. M., 2000, Laurentia - Kalahari collision and the assembly of Rodinia: The Journal of Geology, v. 108, no. 5, p. 499-513.
Darbyshire, F. A., Eaton, D. W., Frederiksen, A. W., and Ertolahti, L., 2007, New insights into the lithosphere beneath the Superior Province from Rayleigh wave dispersion and receiver function analysis: Geophysical Journal International, v. 169, no. 3, p. 1043-1068.
Davidson, A., 2008, Late Paleoproterozoic to mid-Neoproterozoic history of northern Laurentia: an overview of central Rodinia: Precambrian Research, v. 160, no. 1, p. 5-22.
Davis, D., and Green, J., 1997, Geochronology of the North American Midcontinent rift in western Lake Superior and implications for its geodynamic evolution: Canadian Journal of Earth Sciences, v. 34, no. 4, p. 476-488.
Durrheim, R. J., and Mooney, W. D., 1991, Archean and Proterozoic crustal evolution: Evidence from crustal seismology: Geology, v. 19, no. 6, p. 606-609.
Eaton, D. W., and Frederiksen, A., 2007, Seismic evidence for convection-driven motion of the North American plate: Nature, v. 446, no. 7134, p. 428-431.
Eriksson, P. G., Mazumder, R., Catuneanu, O., Bumby, A. J., and Ilondo, B. O., 2006, Precambrian continental freeboard and geological evolution: a time perspective: Earth-Science Reviews, v. 79, no. 3, p. 165-204.
Ernst, R., and Bleeker, W., 2010, Large igneous provinces (LIPs), giant dyke swarms, and mantle plumes: significance for breakup events within Canada and adjacent regions from 2.5 Ga to the Present: Canadian Journal of Earth Sciences, v. 47, no. 5, p. 695-739.
Ernst, R., Wingate, M., Buchan, K., and Li, Z.-X., 2008, Global record of 1600–700Ma Large Igneous Provinces (LIPs): implications for the reconstruction of the proposed Nuna (Columbia) and Rodinia supercontinents: Precambrian Research, v. 160, no. 1, p. 159-178.
Evans, D., and Halls, H., 2010, Restoring Proterozoic deformation within the Superior craton: Precambrian Research, v. 183, no. 3, p. 474-489.

Evans, D. A. D., 2013, Reconstructing pre-Pangean supercontinents: Geological Society of America Bulletin, v. 125, no. 11-12, p. 1735-1751.
Everitt, R., McMurry, J., Brown, A., and Davison, C., Geology of the Lac Du Bonnet batholith, inside and out: AECL's underground research laboratory, southeastern Manitoba, *in* Proceedings Field excursion B-5: guidebook. Geological Association of Canada–Mineralogical Association of Canada Joint Annual Meeting1996.
Feinstein, S., Kohn, B., Osadetz, K., Everitt, R., and O'Sullivan, P., 2009, Variable Phanerozoic thermal history in the Southern Canadian Shield: Evidence from an apatite fission track profile at the Underground Research Laboratory (URL), Manitoba: Tectonophysics, v. 475, no. 1, p. 190-199.
Flowers, R., Bowring, S., Mahan, K., Williams, M., and Williams, I., 2008, Stabilization and reactivation of cratonic lithosphere from the lower crustal record in the western Canadian shield: Contributions to Mineralogy and Petrology, v. 156, no. 4, p. 529-549.
Flowers, R., Mahan, K., Bowring, S., Williams, M., Pringle, M., and Hodges, K., 2006a, Multistage exhumation and juxtaposition of lower continental crust in the western Canadian Shield: Linking high‐resolution U‐Pb and 40Ar/39Ar thermochronometry with pressure‐temperature‐deformation paths: Tectonics, v. 25, no. 4.
Flowers, R. M., Ault, A. K., Kelley, S. A., Zhang, N., and Zhong, S., 2012, Epeirogeny or eustasy? Paleozoic-Mesozoic vertical motion of the North American continental interior from thermochronometry and implications for mantle dynamics: Earth and Planetary Science Letters, v. 317-318, no. 0, p. 436-445.
Flowers, R. M., Bowring, S. A., and Reiners, P. W., 2006b, Low long-term erosion rates and extreme continental stability documented by ancient (U-Th)/He dates: Geology, v. 34, no. 11, p. 925-928.
Flowers, R. M., Royden, L. H., and Bowring, S. A., 2004, Isostatic constraints on the assembly, stabilization, and preservation of cratonic lithosphere: Geology, v. 32, no. 4, p. 321.
Flowers, R. M., and Schoene, B., 2010, (U-Th)/He thermochronometry constraints on unroofing of the eastern Kaapvaal craton and significance for uplift of the southern African Plateau: Geology, v. 38, no. 9, p. 827-830.
Foley, S. C., 2008, Rejuvenation and erosion of the cratonic lithosphere: Nature Geoscience, v. 1, no. August 2008, p. 503-510.
Forte, A. M., Moucha, R., Simmons, N. A., Grand, S. P., and Mitrovica, J. X., 2010, Deep-mantle contributions to the surface dynamics of the North American continent: Tectonophysics, v. 481, p. 3-15.
French, S., Fischer, K., Syracuse, E., and Wysession, M., 2009, Crustal structure beneath the Florida‐to‐Edmonton broadband seismometer array: Geophysical Research Letters, v. 36, no. 8.
Frimmel, H. E., 1997, Chlorite thermometry in the Witwatersrand Basin: constraints on the Paleoproterozoic geotherm in the Kaapvaal Craton, South Africa: The Journal of Geology, v. 105, no. 5, p. 601-616.
Funck, T., Jackson, H. R., Louden, K. E., and Klingelhöfer, F., 2007, Seismic study of the transform‐rifted margin in Davis Strait between Baffin Island (Canada) and

Greenland: What happens when a plume meets a transform: Journal of Geophysical Research: Solid Earth, v. 112, no. B4.
Furlong, K. P., and Fountain, D. M., 1986, Continental crustal underplating: Thermal considerations and seismic - petrologic consequences: Journal of Geophysical Research: Solid Earth, v. 91, no. B8, p. 8285-8294.
Gordon, M. B., and Hempton, M. R., 1986, Collision-induced rifting: the Grenville Orogeny and the Keweenawan rift of North America: Tectonophysics, v. 127, no. 1-2, p. 1-25.
Griffin, W., Andi, Z., O'reilly, S., and Ryan, C., 1998, Phanerozoic evolution of the lithosphere beneath the Sino - Korean craton: Mantle dynamics and plate interactions in East Asia, p. 107-126.
Gurnis, M., 1992, Eustatic and Epeirogenic Motions by Mantle Convection: GSA TODAY, v. 2, no. 7.
Hager, B. H., Clayton, R. W., Richards, M. A., Comer, R. P., and Dziewonski, A. M., 1985, Lower mantle heterogeneity, dynamic topography and the geoid: Nature, v. 313, no. 6003, p. 541-545.
Harrison, T. M., Lovera, O. M., and Heizler, M. T., 1991, 40Ar/39Ar results for alkali feldspars containing diffusion domains with differing activation energy: Geochim. Cosmochim. Acta, v. 55, no. 5, p. 1435-1448.
Hauser, E. C., 1993, Grenville foreland thrust belt hidden beneath the eastern US midcontinent: Geology, v. 21, no. 1, p. 61-64.
Hawkesworth, C., Cawood, P., and Dhuime, B., 2013, Continental growth and the crustal record: Tectonophysics, v. 609, p. 651-660.
Heaman, L., Grütter, H., Pell, J., Holmes, P., and Grenon, H., U-Pb geochronology, Sr and Nd isotope compositions of groundmass perovskite from the Chidliak and Qilaq kimberlites, Baffin Island, Nunavut, *in* Proceedings 10th International Kimberlite Conference, Bangalore2012.
Helmstaedt, H. H., and Schulze, D. J., 1989, Southern African kimberlites and their mantle sample: implications for Archean tectonics and lithosphere evolution, *in* Ross, J., ed., Kimberlites and Related Rocks, Vol.1: Their Composition, Occurrence, Origin, and Emplacement, Volume 14, Geological Society of Australia Special Publication, p. 358-368.
Herzberg, C., and Rudnick, R., 2012, Formation of cratonic lithosphere: an integrated thermal and petrological model: Lithos, v. 149, p. 4-15.
Hoffman, P. F., 1991, Did the breakout of Laurentia turn Gondwanaland inside-out: Science, v. 252, no. 5011, p. 1409-1412.
Holland, H. D., 2006, The oxygenation of the atmosphere and oceans: Philosophical Transactions of the Royal Society B: Biological Sciences, v. 361, no. 1470, p. 903-915.
Hunt, P. A., and Roddick, J. C., 1988, A compilation of K-Ar ages: Report 18; Radiogenic Age and Isotopic Studies: Report 2: Geological Survey of Canada.
Jackson, G., Iannelli, T., Knight, R., and Lebel, D., 1985, Neohelikian Bylot Supergroup of Borden Rift Basin, northwestern Baffin Island, District of Franklin: Current research, part A. Geological Survey of Canada, Paper, p. 639-649.

James, D. E., and Fouch, M. J., 2002, Formation and evolution of Archaean cratons: insights from southern Africa: Geological Society, London, Special Publications, v. 199, no. 1, p. 1-26.
Jones, C. H., Mahan, K. H., Butcher, L. A., Levandowski, W. B., and Farmer, G. L., 2015, Continental uplift through crustal hydration: Geology, v. 43, no. 4, p. 355-358.
Jordan, T. H., 1978, Composition and development of the continental tectosphere: Nature, v. 274, no. 5671, p. 544-548.
-, 1981, Continents as a chemical boundary layer: Philosophical Transactions of the Royal Society of London A: Mathematical, Physical and Engineering Sciences, v. 301, no. 1461, p. 359-373.
Kah, L. C., Sherman, A. G., Narbonne, G. M., Knoll, A. H., and Kaufman, A. J., 1999, δ13C stratigraphy of the Proterozoic Bylot Supergroup, Baffin Island, Canada: implications for regional lithostratigraphic correlations: Canadian Journal of Earth Sciences, v. 36, no. 3, p. 313-332.
Karlstrom, K. E., Harlan, S. S., Williams, M. L., McLelland, J., Geissman, J. W., and Åhäll, K.-I., 1999, Refining Rodinia: Geologic Evidence for the Australia–Western US connection in the Proterozoic: GSA TODAY, v. 9, no. 10.
Karlstrom, K. E., and Timmons, J. M., 2012, Many unconformities make one Great Unconformity: Spec. Pap., Geol. Soc. Am, v. 489, p. 73-79.
Kelly, R. K., Kelemen, P. B., and Jull, M., 2003, Buoyancy of the continental upper mantle: Geochemistry, Geophysics, Geosystems, v. 4, no. 2.
Kerr, J. W., 1979, Structural framework of Lancaster aulacogen, Arctic Canada: Geological Survey of Canada.
Knoll, A. H., 2003, The geological consequences of evolution: Geobiology, v. 1, no. 1, p. 3-14.
Kohn, B. P., Gleadow, A. J., Brown, R. W., Gallagher, K., Lorencak, M., and Noble, W. P., 2005, Visualizing thermotectonic and denudation histories using apatite fission track thermochronology: Reviews in mineralogy and geochemistry, v. 58, no. 1, p. 527-565.
Korenaga, J., 2013, Initiation and evolution of plate tectonics on Earth: theories and observations: Annual Review of Earth and Planetary Sciences, v. 41, p. 117-151.
Krabbendam, M., Prave, T., and Cheer, D., 2008, A fluvial origin for the Neoproterozoic Morar Group, NW Scotland; implications for Torridon–Morar Group correlation and the Grenville Orogen foreland basin: Journal of the Geological Society, v. 165, no. 1, p. 379-394.
Kretz, R., 1994, Petrology of veined gneisses of the Otter complex, southern Grenville Province: Canadian Journal of Earth Sciences, v. 31, no. 5, p. 835-851.
Krogh, T., Davis, G., Ermanovics, I., and Harris, N., U-Pb isotopic ages of zircons from the Berens Block and English River gneiss belt, *in* Proceedings Proc. 1976 Geotraverse Conf., University of Toronto1976.
Lee, C.-T. A., Luffi, P., and Chin, E. J., 2011, Building and destroying continental mantle: Annual Review of Earth and Planetary Sciences, v. 39, p. 59-90.
Lenardic, A., and Moresi, L. N., 1999, Some thoughts on the stability of cratonic lithosphere: Effects of buoyancy and viscosity: J. Geophys. Res., v. 104, no. B6, p. 12747-12758.

Levandowski, W., Boyd, O. S., Briggs, R. W., and Gold, R. D., 2015, A random - walk algorithm for modeling lithospheric density and the role of body forces in the evolution of the Midcontinent Rift: Geochemistry, Geophysics, Geosystems, v. 16, no. 12, p. 4084-4107.
Li, Z.-X., Bogdanova, S., Collins, A., Davidson, A., De Waele, B., Ernst, R., Fitzsimons, I., Fuck, R., Gladkochub, D., and Jacobs, J., 2008, Assembly, configuration, and break-up history of Rodinia: a synthesis: Precambrian research, v. 160, no. 1, p. 179-210.
Long, D. G., and Turner, E. C., 2012, Tectonic, sedimentary and metallogenic re-evaluation of basal strata in the Mesoproterozoic Bylot basins, Nunavut, Canada: Are unconformity-type uranium concentrations a realistic expectation?: Precambrian Research, v. 214, p. 192-209.
Lorencak, M., 2003, Low temperature thermochronology of the Canadian and Fennoscandian Shields: Integration of apatite fission track and (U-Th)/He methods: University of Melbourne, School of Earth Sciences.
Lorencak, M., Kohn, B., Osadetz, K., and Gleadow, A., 2004, Combined apatite fission track and (U–Th)/He thermochronometry in a slowly cooled terrane: results from a 3440-m-deep drill hole in the southern Canadian Shield: Earth and Planetary Science Letters, v. 227, no. 1, p. 87-104.
Lovera, O. M., Richter, F. M., and Harrison, T. M., 1989, The 40Ar/39Ar Thermochronometry for Slowly Cooled Samples Having a Distribution of Diffusion Domain Sizes: Journal of Geophysical Research, v. 94, no. no. B12, p. 17917-17935.
Lovera, O. M., Richter, F. M., and Harrison, T. M., 1991, Diffusion Domains Determined by 39Ar Released During Step Heating: Journal of Geophysical Research, v. 96, no. no. B2, p. 2057-2069.
Martin, H., 1986, Effect of steeper Archean geothermal gradient on geochemistry of subduction-zone magmas: Geology, v. 14, no. 9, p. 753-756.
McDougall, I., and Harrison, T. M., 1999, Geochronology and Thermochronology by the 40Ar/39Ar Method, Oxford University Press, USA.
McGregor, E., Nielsen, S., Stephenson, R., Petersen, K., and MacDonald, D., 2013, Long-term exhumation of a Palaeoproterozoic orogen and the role of pre-existing heterogeneous thermal crustal properties: a fission-track study of SE Baffin Island: Journal of the Geological Society, v. 170, no. 6, p. 877-891.
McKenna, M. C., 1972, Possible Biological Consequences of Plate Tectonics: BioScience, v. 22, no. 9, p. 519-525.
Meert, J. G., 2012, What's in a name? The Columbia (Paleopangaea/Nuna) supercontinent: Gondwana Research, v. 21, no. 4, p. 987-993.
Menzies, M. A., and Xu, Y., 1998, Geodynamics of the North China craton: Mantle dynamics and plate interactions in East Asia, p. 155-165.
Mitrovica, J. X., Beaumont, C., and Jarvis, G. T., 1989, Tilting of continental interiors by the dynamical effects of subduction: Tectonics, v. 8, no. 5, p. 1079-1094.
Mosher, S., Levine, J., and Carlson, W., 2008, Mesoproterozoic plate tectonics: A collisional model for the Grenville-aged orogenic belt in the Llano uplift, central Texas: Geology, v. 36, no. 1, p. 55-58.

Musacchio, G., White, D., Asudeh, I., and Thomson, C., 2004, Lithospheric structure and composition of the Archean western Superior Province from seismic refraction/wide‐angle reflection and gravity modeling: Journal of Geophysical Research: Solid Earth, v. 109, no. B3.

Naeser, C. W., and Crowley, K. D., 1990, Fission-track dating of apatite from deep borehole ATK-1 at Atikokan, Ontario: International Atomic Energy Agency.

Nelson, K. (1991) A unified view of craton evolution motivated by recent deep seismic reflection and refraction results. Geophysical Journal International 105, 25-35.

Nicholson, S. W., and Shirey, S. B., 1990, Midcontinent rift volcanism in the Lake Superior region: Sr, Nd, and Pb isotopic evidence for a mantle plume origin: Journal of Geophysical Research: Solid Earth, v. 95, no. B7, p. 10851-10868.

Nitescu, B., Cruden, A., and Bailey, R., 2006, Crustal structure and implications for the tectonic evolution of the Archean Western Superior craton from forward and inverse gravity modeling: Tectonics, v. 25, no. 1.

Ola, O., Frederiksen, A., Bollmann, T., van der Lee, S., Darbyshire, F., Wolin, E., Revenaugh, J., Stein, C., Stein, S., and Wysession, M., 2016, Anisotropic zonation in the lithosphere of Central North America: Influence of a strong cratonic lithosphere on the Mid-Continent Rift: Tectonophysics, v. 683, p. 367-381.

Pearson, D. G., Carlson, R. W., Shirey, S. B., Boyd, F. R., and Nixon, P. H., 1995a, Stabilization of Archean lithospheric mantle: A Re-Os isotope study of peridotite xenoliths from the Kaapvaal craton: Earth Planet. Sci. Lett., v. 134, p. 341-357.

Pearson, D. G., Shirey, S. B., Carlson, R. W., Boyd, F. R., Pokhilenko, N. P., and Shimizu, N., 1995b, Re-Os, Sm-Nd, and Rb-Sr isotope evidence for thick Archaean lithospheric mantle beneath the Siberian craton modified by multistage metasomatism: Geochimica et Cosmochimica Acta, v. 59, no. 5, p. 959-977.

Percival, J., Sanborn-Barrie, M., Skulski, T., Stott, G., Helmstaedt, H., and White, D., 2006, Tectonic evolution of the western Superior Province from NATMAP and Lithoprobe studies: Canadian Journal of Earth Sciences, v. 43, no. 7, p. 1085-1117.

Percival, J., Skulski, T., Sanborn-Barrie, M., Stott, G., Leclair, A., Corkery, M., and Boily, M., 2012, Geology and tectonic evolution of the Superior Province, Canada: Tectonic Styles in Canada: The Lithoprobe Perspective. Geol Assoc Canada Spec Paper, v. 49, p. 321-378.

Perry, H. K. C., Eaton, D. W. S., and Forte, A. M., 2002, LITH5.0: a revised crustal model for Canada based on Lithoprobe results: Geophys. Jour. Int., v. 150, p. 285-294.

Pollack, H. N., 1986, Cratonization and thermal evolution of the mantle: Earth and Planetary Science Letters, v. 80, no. 1, p. 175-182.

Rainbird, R., Cawood, P., and Gehrels, G., 2012, The great Grenvillian sedimentation episode: Record of supercontinent Rodinia's assembly, Tectonics of Sedimentary Basins: Recent Advances, Blackwell Publishing Ltd, p. 583-601.

Rainbird, R., Stern, R., Rayner, N., and Jefferson, C., 2007, Age, provenance, and regional correlation of the Athabasca Group, Saskatchewan and Alberta, constrained by igneous and detrital zircon geochronology: Bulletin - Geological Survey of Canada, v. 588, p. 193.

Rainbird, R. H., Heaman, L. M., and Young, G., 1992, Sampling Laurentia: Detrital zircon geochronology offers evidence for an extensive Neoproterozoic river system originating from the Grenville orogen: Geology, v. 20, no. 4, p. 351-354.
Rainbird, R. H., McNicoll, V., Theriault, R., Heaman, L., Abbott, J., Long, D., and Thorkelson, D., 1997, Pan-continental river system draining Grenville Orogen recorded by U-Pb and Sm-Nd geochronology of Neoproterozoic quartzarenites and mudrocks, northwestern Canada: The Journal of Geology, v. 105, no. 1, p. 1-17.
Rayner, N., Stern, R., and Bickford, M., 2005, Tectonic implications of new SHRIMP and TIMS U Pb geochronology of rocks from the Sask Craton, Peter Lake Domain, and Hearne margin, Trans-Hudson Orogen, Saskatchewan: Canadian Journal of Earth Sciences, v. 42, no. 4, p. 635-657.
Rogers, J. J., and Santosh, M., 2002, Configuration of Columbia, a Mesoproterozoic supercontinent: Gondwana Research, v. 5, no. 1, p. 5-22.
Rudnick, R. L., 1995, Making continental crust: Nature, v. 378, no. 6557, p. 571-578.
Rudnick, R. L., and Nyblade, A. A., 1999, The thickness and heat production of Archean lithosphere: constraints from xenolith thermobarometry and surface heat flow: Mantle petrology: Field observations and high pressure experimentation: A tribute to Francis R.(Joe) Boyd, v. 6, p. 3-12.
Schmandt, B., Lin, F. C., and Karlstrom, K. E., 2015, Distinct crustal isostasy trends east and west of the Rocky Mountain Front: Geophysical Research Letters.
Schneider, D., Cope, N., and Holm, D., 2013, Thermochronology of the Mont Laurier terrane, southern Canadian Grenville Province, and its bearing on defining orogenic architecture: Precambrian Research, v. 226, p. 43-58.
Schneider, D. A., Heizler, M. T., Bickford, M. E., Wortman, G. L., Condie, K. C., and Perilli, S., 2007, Timing constraints of orogeny to cratonization: Thermochronology of the Paleoproterozoic Trans-Hudson orogen, Manitoba and Saskatchewan, Canada: Precambrian Research, v. 153, p. 65-95.
Schulz, K. J., and Cannon, W. F., 2007, The Penokean orogeny in the Lake Superior region: Precambrian Research, v. 157, no. 1, p. 4-25.
Scott, D.J. (1999) U–Pb geochronology of the eastern Hall Peninsula, southern Baffin Island, Canada: a northern link between the Archean of West Greenland and the Paleoproterozoic Torngat Orogen of northern Labrador. Precambrian Research 93, 5-26.
Scully, K. R., Canil, D., and Schulze, D. J., 2004, The lithospheric mantle of the Archean Superior Province as imaged by garnet xenocryst geochemistry: Chemical Geology, v. 207, no. 3, p. 189-221.
Sengor, A., Burke, K., and Dewey, J. F., 1978, Rifts at high angles to orogenic belts; tests for their origin and the Upper Rhine Graben as an example: American Journal of Science, v. 278, no. 1, p. 24-40.
Shen, W., Ritzwoller, M. H., and Schulte‐Pelkum, V., 2013, Crustal and uppermost mantle structure in the central US encompassing the Midcontinent Rift: Journal of Geophysical Research: Solid Earth, v. 118, no. 8, p. 4325-4344.
Skipton, D., Schneider, D., McFarlane, C., St-Onge, M. and Jackson, S. (2016) Multi-stage zircon and monazite growth revealed by depth profiling and in situ U-Pb

geochronology: resolving the Paleoproterozoic tectonics of the Trans-Hudson Orogen on southeastern Baffin Island, Canada. Precambrian Research.
Skipton, D., Schneider, D.A., Kellet, D.A. and Joyce, N.L. (2016, submitted, in review) Deciphering the Paleoproterozoic cooling history of the northeastern Trans-Hudson Orogen, Baffin Island (Canada), using 40Ar/39Ar step-heating and UV laserprobe thermochronology. Lithos.
Smit, K. V., Pearson, D. G., Stachel, T., and Seller, M., 2014, Peridotites from Attawapiskat, Canada: Mesoproterozoic Reworking of Palaeoarchaean Lithospheric Mantle beneath the Northern Superior Superterrane: Journal of Petrology, v. 55, no. 9, p. 1829-1863.
Stein, C. A., Kley, J., Stein, S., Hindle, D., and Keller, G. R., 2015, North America's Midcontinent Rift: When rift met LIP: Geosphere, v. 11, no. 5, p. 1607-1616.
Suckro, S. K., Gohl, K., Funck, T., Heyde, I., Ehrhardt, A., Schreckenberger, B., Gerlings, J., Damm, V., and Jokat, W., 2012, The crustal structure of southern Baffin Bay: implications from a seismic refraction experiment: Geophysical Journal International, v. 190, no. 1, p. 37-58.
Tappe, S., Smart, K. A., Pearson, D. G., Steenfelt, A., and Simonetti, A., 2011, Craton formation in Late Archean subduction zones revealed by first Greenland eclogites: Geology, v. 39, no. 12, p. 1103-1106.
Taylor, S. R., and McLennan, S. M., 1995, The geochemical evolution of the continental crust: Reviews of Geophysics, v. 33, no. 2, p. 241-265.
Thurner, S., Margolis, R., Levander, A., and Niu, F., 2015, PdS receiver function evidence for crustal scale thrusting, relic subduction, and mafic underplating in the Trans-Hudson Orogen and Yavapai province: Earth and Planetary Science Letters, v. 426, p. 13-22.
Thybo, H., and Artemieva, I. M., 2013, Moho and magmatic underplating in continental lithosphere: Tectonophysics, v. 609, p. 605-619.
Timmons, J. M., Karlstrom, K. E., Dehler, C. M., Geissman, J. W., and Heizler, M. T., 2001, Proterozoic multistage (ca. 1.1 and 0.8 Ga) extension recorded in the Grand Canyon Supergroup and establishment of northwest- and north-trending tectonic grains in the southwestern United States: Geological Society of America Bulletin, v. 113, no. 2, p. 163-181.
Tréhu, A., Meyer, R., Hajnal, Z., Karl, J., Mereu, R., Sexton, J., Shay, J., Chan, W. K., Epili, D., and Jefferson, T., 1991, Imaging the Midcontinent Rift beneath Lake Superior using large aperture seismic data: Geophysical Research Letters, v. 18, no. 4, p. 625-628.
Turner, E. C., Long, D. G., Rainbird, R. H., Petrus, J. A., and Rayner, N. M., 2016, Late Mesoproterozoic rifting in Arctic Canada during Rodinia assembly: impactogens, trans‐continental far‐field stress and zinc mineralisation: Terra Nova, v. 28, no. 3, p. 188-194.
Van Lankvelt, A., Schneider, D., Biczok, J., McFarlane, C., and Hattori, K., 2016, Decoding Zircon Geochronology of Igneous and Alteration Events Based on Chemical and Microstructural Features: a Study from the Western Superior Province, Canada: Journal of Petrology, p. egw041.
Van Schmus, W., and Hinze, W., 1985, The midcontinent rift system: Annual Review of Earth and Planetary Sciences, v. 13, no. 1, p. 345-383.

Weeraratne, D. S., Forsyth, D. W., Fischer, K. M., and Nyblade, A. A., 2003, Evidence for an upper mantle plume beneath the Tanzanian craton from Rayleigh wave tomography: Journal of Geophysical Research: Solid Earth (1978–2012), v. 108, no. B9.

White, D., Musacchio, G., Helmstaedt, H., Harrap, R., Thurston, P., Van der Velden, A., and Hall, K., 2003, Images of a lower-crustal oceanic slab: Direct evidence for tectonic accretion in the Archean western Superior province: Geology, v. 31, no. 11, p. 997-1000.

Whitmeyer, S. J., and Karlstrom, K. E., 2007, Tectonic model for the Proterozoic growth of North America: Geosphere, v. 3, no. 4, p. 220-259.

Williams, M., Dumond, G., Mahan, K., Regan, S., and Holland, M., 2014, Garnet-forming reactions in felsic orthogneiss: Implications for densification and strengthening of the lower continental crust: Earth and Planetary Science Letters, v. 405, p. 207-219.

Wyman, D. A., and Kerrich, R., 2002, Formation of Archean continental lithospheric roots: the role of mantle plumes: Geology, v. 30, no. 6, p. 543-546.

Zartman, R. E., Kempton, P. D., Paces, J. B., Downes, H., Williams, I. S., Dobosi, G., and Futa, K., 2012, Lower-crustal xenoliths from Jurassic kimberlite diatremes, upper Michigan (USA): Evidence for Proterozoic orogenesis and plume magmatism in the lower crust of the southern Superior Province: Journal of Petrology, p. egs079.

Zeitler, P. K., 1987, Argon diffusion in partially outgassed alkali feldspars: Insights from 40Ar/39Ar analysis: Chemical Geology: Isotope Geoscience section, v. 65, no. 2, p. 167-181.

Zhang, H., Lee, S., Wolin, E., Bollmann, T. A., Revenaugh, J., Wiens, D. A., Frederiksen, A. W., Darbyshire, F. A., Aleqabi, G. I., and Wysession, M. E., 2016, Distinct crustal structure of the North American Midcontinent Rift from P wave receiver functions: Journal of Geophysical Research: Solid Earth, v. 121, no. 11, p. 8136-8153.

Appendix A: Sample characterization and constraining geochronologic data

Samples are presented from Canadian Shield terranes with bracketing thermochronology data. Data from nearby samples are given when information about the sample from this study is lacking additional thermal constraints. See **Table S1** for samples dated in this paper and **Table S2** for U-Th/He data for western Superior province.

Table S1: North American craton $^{40}Ar/^{39}Ar$ samples

Sample	Longitude (DD)	Latitude (DD)	Rock type
Superior Province, ON			
70	-90.659	52.945	pegmatite leucogranite/trondhjemite
WN-1	-95.841	50.250	granite/granodiorite, Winnipeg River subprovince - Lac du Bonnet Batholith
Grenville Province, QC			
OL-13	-76.509	45.779	syenogranite
Athabasca			
BF02-76B	-105.198	59.424	cross-cutting pegmatite, Chipman domain
BF02-108B	-105.284	59.322	granitic segregation, Chipman domain
BF02-123A	-105.312	59.328	granitic vein
02M133A	-105.412	59.42	mafic granulite
Saskatchewan			
SK-KM-01	-103.196	54.085	K-feldspar granitoid foliate core
SK-KM-02	-104.905	54.814	K-feldspar granitoid foliate core
SK-KM-03	-104.897	57.841	pegmatite granite
Baffin Island, Hall Peninsula			
S112A	-65.537	63.937	Bt Hbl Monzogranite
S092C1	-65.829	63.294	Bt Ms Sil Kfs pelite
S020	-65.929	63.324	Bt tonalite gneiss
Mid-Continent U.S.A.			
95-11	-90.692	44.373	Neillsville Granite
95-13	-90.726	44.393	Hatfield Gneiss
IL-ST-3	-89.867	42.433	Illinois UPH3 basement granite core

96-WIS-11	-88.109	45.392	Athelstane Gneiss
WRB-3	-88.783	44.805	granite, Wolf River Batholith
EC-8	-87.507	45.880	granite, East-Central Minnesota Batholith
EC-13	-87.586	45.691	granite, East-Central Minnesota Batholith
EC-25	-87.767	45.604	granite, East-Central Minnesota Batholith

Table S2: W. Superior Province, Ontario apatite (U-Th)/He data

Table S2: Apatite U-Th/He data for craton samples

Sample	long/lat DD	Corrected Date (Ma)	Analytic Unc. (Ma)	4He (mol)	U (ppm)	Th (ppm)	Sm (ppm)	eU (ppm)	Rs (μm)	Raw Date (Ma)	±	Ft
#70	-90.66/52.95	524.36	11.37	3.564E-13	30.6	63.5	217.8	45.5	61.97	408.07	7.92	0.77
	CRH Corr. Age: 396.1 ± 8.5 Ma (1σ analytic unc)			2.668E-13								

Sample*	long/lat DD	Corrected Date (Ma)	Full Unc. (Ma)	Analytic Unc. (Ma)	4He (nmol/g)	U (ppm)	Th (ppm)	Sm (ppm)	eU (sph) ppm	Rs (μm)	Raw Date (Ma)	±	Ft
01-OE-108_a01	-90.21/51.4	601.57	45.84	13.11	32.118	6.63	27.67	19.83	13.1	62.12	435.07	13.11	0.723
01-OE-108_a02	-90.21/51.4	571.84	49.83	20.38	25.615	6.28	22.76	16.19	11.6	53.51	392.65	20.38	0.687
01-OE-108_a03	-90.21/51.5	419.80	44.10	13.03	24.170	9.46	28.57	15.21	16.2	45.97	269.43	13.03	0.642
01-OE-108_a04	-90.21/51.6	493.84	68.19	23.24	20.243	6.46	22.53	14.33	11.8	44.12	309.05	23.24	0.626
01-OE-108_a05	-90.21/51.7	560.76	84.37	16.97	33.403	8.78	36.40	18.04	17.3	43.44	345.67	16.97	0.616
	Mean age (Ma	529.56	60.49	17.81									

**all single grain data from R. Flowers (pers. comm.)*

Appendix: Craton samples and constraining data

Western Superior Province, Ontario

Sample No. 70 is from the Archean North Caribou Terrane of the western Superior Province in Ontario Canada and is part of one of the oldest Archean cratonic cores in North America. The ca. 2.7 Ga merger of micro-continent blocks during the Uchi orogeny occurred from lateral plate-tectonic-like accretionary stacking of various proto-continents and oceanic fragments during multiple well-documented events (Percival et al., 2006; Percival et al., 2012; White et al., 2003). The craton stabilized by about 2.5 Ga after orogenesis terminated by 2.6 Ga. However, major reactivation occurred at ~1.9 Ga, and during failed rifting of the mid-continent in peripheral terranes near Lake Superior at ~1.1 Ga (Percival and Easton, 2007). This sample and others in the same area were dated

and described in Van Lankvelt et al. (2016) and is denoted sample #72 in their paper. Most of the rocks in this region record high-temperature 2.6-3.1 Ga magmatic activity and hydrothermal alteration (Van Lankvelt et al., 2016). Sample #70 rock is a tonalite-trondjhemite granite (TTG) and nearby sample #71 has zircon and titanite U-Pb age of 2858 ± 5 Ma and 2854 ± 7 Ma, respectively with Ti-in-zircon thermometry indicating zircon crystallization temperatures of 752 ± 37°C. Approximately 50-100 km to the east/southeast of sample #70, localized carbonatite dikes yield K-Ar biotite ages of 1014 ± 40 Ma and 1070 ± 40 Ma (Gittins et al., 1967; Wanless et al., 1967). The dikes in this part of Ontario are the southeastern extension of the ~1.27 Ga Mackenzie dike swarm originating to the northwest at the Coppermine mantle plume LIP locus in the Slave Province (Hou, 2012).

Apatite fission-track ages from this region of Ontario are ca. 350-450 Ma (Kohn et al., 2005; Lorencak, 2003) and at Atikokan, Ontario (borehole ATK-1) to the southwest, near the Minnesota border, apatite fission-track dates range from 515 ± 72 to 376 ± 46 Ma from depths of 4 m to 993 m, respectively (Naeser and Crowley, 1990). Sample #70 was dated via (U-Th-Sm)/He analysis for this study using the continuous heating method (Idleman and Zeitler, 2014; McDannell et al., 2015), which produced an alpha-corrected single grain cooling age of 531.53 ± 31.89 Ma (2σ); uncorrected age: 408.07 ± 7.9 Ma (1σ), eU = 45.5 ppm, spherical equivalent radius, Rs = 62 μm). The CRH corrected age is ~396 ± 9 Ma; see Chapter 2.

Sample WN-1 is a granodiorite from the Winnipeg River sub-province of the Superior craton taken from core at the deep borehole site at the Whiteshell Nuclear Research laboratory outside Winnipeg, Manitoba from the Lac du Bonnet Batholith that was emplaced 2665 ± 20 to 2568 ± 23 Ma (Everitt et al., 1996; Krogh et al., 1976). This sample was from 30.5 m depth and dated previously via $^{40}Ar/^{39}Ar$ of biotite, yielding a late Kenoran orogeny age of 2291 ± 27 Ma (Hunt and Roddick, 1988). This sample was then dated via $^{40}Ar/^{39}Ar$ of K-feldspar in 1990 by C. Roddick (pers. comm. with P. Zeitler) and was never published. The age spectrum presented here is from that laboratory experiment. AFT data from a borehole at the underground research lab where sample WN-1 was obtained shows ages of ca. 370-250 Ma, decreasing with depth. The sample URL-6-2 at nearly the same depth/elevation as WN-1 has an AFT age of 373 ± 29 Ma (Feinstein et al., 2009). Osadetz et al. (2002) also show AFT ages of ~300-400 Ma for SE Manitoba. Apatite fission-track (AFT) thermochronology of Ontario and W. Manitoba show ages of ca. 350-500 Ma (Kohn et al., 2005). These data suggest these rocks have been cooler than ca. 110°C throughout the Phanerozoic. Further to the east where there are geologic constraints in the form of Ordovician sediments overlying crystalline basement near the Sudbury Igneous Complex, combined AFT and AHe thermal history models suggest erosional cooling phases at main stages of the Appalachian Orogeny with episodic burial reheating and ensuing unroofing (Feinstein et al., 2009; Lorencak, 2003; Lorencak et al., 2004).

Grenville Province, Quebec

The Grenville Province represents the remains of a deeply eroded collisional mountain range that formed primarily between 1.35 to 1.0 Ga (McLelland et al., 1996), bordering the E. Superior Province. **Sample OL13** is a syeno-granite from the Otter Lake region of Quebec, approximately 75-100 km northwest of Ottawa. This area underwent upper-amphibolite facies metamorphism at temperatures and pressures of 700 ± 50°C and 6.5-7.5 kbar (Kretz, 1994) during the Elzivirian and Ottawan phases of the Grenville orogeny. Titanite from this sample was dated via U-Pb of different petrologic phase of the same sample giving concordant ages of 1025 ± 11 Ma, 1023 ± 7.8 Ma, 1029.7 ± 5.7 Ma for hornblende and hornblende-pyroxene granites (D. Schneider, pers. comm.). This sample is now used as the titanite U-Pb standard at the Canadian Geologic Survey where samples at the same outcrop as OL-13 gave a SHRIMP concordia age of 1017.1 ± 3.6 Ma and a TIMS U-Pb concordia age of 1014.8 ± 2.0 Ma (Sample OLT1) and a SHRIMP age of 1021.8 ± 2.4 Ma and TIMS age of 1018.1 ± 1.7 Ma for Sample TCB (Kennedy et al., 2010). The same sample as OL13, renamed NC9-7, yields a biotite $^{40}Ar/^{39}Ar$ plateau age of 885.2 ± 4.3 Ma (total gas age: 875.6 ± 13.8 Ma) and a nearby sample NC9-8 (<10 km away) has a hornblende $^{40}Ar/^{39}Ar$ plateau age of 959.2 ± 6.9 Ma (total gas age of: 979.9 ± 41.8) (Cope, 2012; Schneider et al., 2013).

Nearby low-temperature zircon and apatite (U-Th)/He data from granitic orthogneisses of a basement transect along the Ottawa embayment and Mont Tremblant rift flank in Quebec are quite scattered, but ages are generally between ca. 300-600 Ma and 150-300 Ma, respectively, while $^{40}Ar/^{39}Ar$ analysis of biotite from Mont Tremblant yielded ages

between 928 ± 4 Ma and 977 ± 4 Ma (Hardie, 2016). Grenvillian-shed sediments of the rift flank give detrital zircon ages of 176 ± 14 to 579 ± 46 Ma with a large range in eU values (Hardie, 2016).

East Lake Athabasca region

The Snowbird Tectonic Zone is a shear/collisional boundary between the Rae-Hearne cratons of the Western Churchill Province, active during the Trans-Hudson orogeny at ca. 1.9 Ga during assembly of Laurentia (Baldwin et al., 2003; Berman et al., 2007; Flowers et al., 2008; Hoffman, 1988; Mahan and Williams, 2005). Northern Saskatchewan contains one of the few areas of the North American craton where Paleoproterozoic sediments are preserved in the form of the ca 1.7-1.65 Ga Lake Athabasca sequence (Rayner et al., 2003). Samples **BF02-76B** (pegmatite), **BF02-108B** (granite), **BF02-123A** (granitic vein) and **02M133A** (mafic granulite gneiss) come from the Chipman Domain in the East Athabasca mylonite triangle and high and low-temperature data are published in (Flowers et al., 2008; Flowers et al., 2006a; Flowers et al., 2006b). Rocks in the Chipman Domain have U-Pb zircon, titanite, apatite, and rutile ages of ca. 1895, 1885, 1820-1860, and 1860 Ma, spanning temperatures of ~400-800+ °C. Biotite and muscovite $^{40}Ar/^{39}Ar$ ages are ca. 1760 Ma, with zircon and apatite He ages mainly spanning 1730-1580 and 950-550 Ma, respectively (Flowers et al., 2006b). Sediments from the Athabasca basin yield depositional ages of ca. 1650 Ma and place these rocks near the surface around that time.

Central Saskatchewan

Three granitoid cores of Precambrian basement, **SK-KM-01, SK-KM-02, and SK-KM-03** were obtained from the Regina core library in Saskatchewan. Sample **SK-KM-01** is from a kimberlite exploration borehole collared ~66 km south of the Precambrian Shield margin, near Cumberland Lake to a depth of 154.5 m (507 ft). This borehole was drilled in Phanerozoic sedimentary rocks and penetrated the Phanerozoic-Precambrian unconformity (in the Sask craton) at a depth of ~150 m. It is a K-feldspar bearing granitoid foliate, likely ca. 1850 Ma in age, taken ~4 m beneath the unconformity. Effects of unconformity-associated weathering and alteration persist to at least ca. 154 m depth and the sampled rock appears to have avoided major effects of alteration and was taken at the end of the available core. Both samples SK-KM-01 and SK-KM-02 (near the Glennie Domain boundary; ca. 1.85-1.89 Ga) were cored through Phanerozoic cover in the Reindeer-Sask Boundary Zone. Sample **SK-KM-02** was taken from a borehole drilled as a kimberlite test over a magnetic anomaly to a depth of 194 m (637 ft). Sample **SK-KM-03** was drilled in the Hearne Province in a reconnaissance study of the eastern Athabasca Basin between Cree Lake and Wollaston Lake, the geology here is 66 m of overburden and Athabasca Group sediments from 66 to 447.3 m to a basal conglomerate unconformity. The basement was then drilled from 447.3 to 581 m (EOH) and the sample was taken from a pegmatite at 525-528.3 m depth. The upper basement is believed to be Archean from the presence of amphibolite with some mild alteration in localized zones. About 1 km from sample SK-KM-03, borehole pegmatite sample CB95-065 yields U-Pb zircon and monazite crystallization ages of 1811 ± 1 Ma and 1805 ± 1 Ma, respectively

(Annesley et al., 1999). Osadetz et al. (2002) apatite fission-track ages for south-central Saskatchewan bedrock are ~200-300 Ma.

Hall Peninsula, Baffin Island

Samples **S092C** (pelite), **S112A** (monzogranite), and **S020** (tonalite gneiss) are all from the southeastern margin of the Hall Peninsula rocks bear a THO overprint and are ca. 1.8-1.7 Ga. The Hall Peninsula is an exposed portion of the mid-crust along the northeast extension of the ca. 1920-1800 Ma Trans-Hudson orogen. U-Pb TIMS dating of zircon along the eastern Archean gneiss domain of the peninsula yield ages of ca. 2850 Ma with ca. 1830-1850 Ma metamorphic overgrowths and younger titanite ages near ~1740-1750 Ma (Scott, 1999). Peak mid-amphibolite-facies conditions existed on the eastern peninsula at ~720-740°C and 6.25-7.25 kbar with timing of metamorphism of ca. 1860-1820 Ma constrained by U-Pb monazite geochronology (Skipton et al., 2016b). Multiple phases of growth occurred between 1861-1833 Ma and 1800-1874 Ma revealed through depth profiling of zircon grains with monazite ages between ca. 1800-1750 Ma forming through metamorphic reactions interpreted to be from end-stage collision with the Superior craton, followed by post-orogenic heating for almost 70 Ma after the thermal maximum (Skipton et al., 2016a).

The post-orogenic evolution of the southeastern peninsula has been constrained through $^{40}Ar/^{39}Ar$ analyses of biotite, muscovite, and phlogopite grains of amphibolite to granulite-facies rocks (Skipton et al., 2016, submitted, in review). Reported biotite step-heating ages range from ca. 1790 to 1620 Ma, 1730-1655 Ma for muscovite, and 1720-

1630 Ma for phlogopite, with UV-spot muscovite ages of approximately 1640-1680 Ma with 20-30 Ma age gradients from core to rim. Argon diffusion models suggest post-metamorphic cooling on the order of 1-2°C/Ma and slightly faster cooling up to 2.5°C/Ma at the end of the Paleoproterozoic. These results suggest that mid-crustal rocks on Baffin Island remained elevated at temperatures in excess of 400°C for 150-200 Ma after THO peak metamorphism and that despite high temperatures and crustal thickness analogous to other hot orogens, gravitational stability was maintained (Skipton et al., 2016, submitted, in review).

Apatite fission-track ages from the SE section of Baffin Island range from ca. 200-440 Ma with a 'boomerang' trend in track lengths, indicative of synchronous cooling of rocks from a range of initial temperatures (McGregor et al., 2013). Their results suggest that a simple exhumation scenario is likely with the modern rugged topography being a remnant of Paleoproterozoic orogenesis. Apatite and zircon He ages are highly dispersed across the peninsula, both systems spanning nearly 1 Ga in age (AHe mainly 200-600 Ma; ZHe mainly 600-900 Ma), however thermal history models still predict extended slow cooling over the entire Hall Peninsula, with the majority of cooling setting ages in the Carboniferous-Permian with subsequent exhumation rates of ~10 m/Ma and integrated cooling rates <1°C/Ma over the Phanerozoic (Creason, 2015). This work also proposes that although the Greenland margin and Torngat Mountains to the south experienced rapid cooling during rifting and separation of Greenland, Baffin Island did not.

Mid-Continent, USA

Samples from this region include those from the East-Central Minnesota Batholith (EC-8, EC-13, EC-25), Athelstane Granite (96-WIS-11), Wolf River Batholith (WRB-3), Neillsville Granite (95-11) and Hatfield Gneiss (95-13) of Wisconsin, and granite core sample from the northern Illinois border (ILST-3). The EC-samples are rocks from the North American mid-continent (WI, MI, IL, USA) near Lake Superior and Lake Michigan record a Penokean orogen (1.83-1.87 Ga) high-temperature signature marking oceanic arc collision with the Superior craton at approximately 1880 Ma (Schulz and Cannon, 2007), coincident with the Trans-Hudson orogeny to the northwest. The Penokean and THO denote the rapid assembly of Archean continents that formed the majority of Laurentia in the Mid-Paleoproterozoic (Hoffman, 1989). The Yavapai (ca. 1.7 Ga) and Mazatzal (ca. 1.6 Ga) orogenies continued the southward building of Laurentia and the juvenile Penokean crust was intruded by widespread anorogenic igneous complexes at ca. 1400-1500 Ma, including the Wolf River Batholith in NE Wisconsin yielding a Rb/Sr model age of 1468 ± 34 Ma (Van Schmus et al., 1975a) and a U-Pb zircon ages between 1468 ± 4 to 1484 ± 2 Ma (Dewane and Van Schmus, 2007), with a lower temperature $^{40}Ar/^{39}Ar$ biotite plateau age of 1391.6 ± 12.9 Ma (Holm and Lux, 1998). The Mid-Continent Rift (MCR) was also a major magmatic episode at approximately 1.1-1.0 Ga (Hinze et al., 1997). Muscovite Ar cooling ages and modeling of the MCR region suggest that the upper crust remained stable since 1.6 Ga and intra-crystalline diffusive models of argon distribution suggest residence at ~400°C for nearly 350 Ma or a short, 500°C thermal pulse for a few million years (Schneider et al., 2011). This work supports the flexural swell hypothesis of Peterman and Sims (1988) where

prior to 1.1 rifting, rocks were in an isotopic partial retention zone and rapid MCR volcanic loading caused these rocks to undergo uplift and then preserved younger <1.2 Ga cooling ages, or simply that the younger cooling ages are the result of shallow reheating and resetting due to MCR magmatism (Schneider et al., 2011).

The East-Central Minnesota Batholith (1787-1772 Ma) is made up of a widespread post-orogenic diorite-granodiorite plutonic complex, exposing deep sections of the Penokean crust (Holm et al., 2005). Sample EC-25 has a zircon U-Pb age of 1788 ± 4 Ma and sample EC-8 has a biotite $^{40}Ar/^{39}Ar$ plateau age of 1846 ± 6 Ma, with EC-13 granite being crystallized by ca. 1760 Ma (Holm et al., 2005). To the southeast in the >2.5 Ga Marshfield terrane, sample 95-11 of the Neillsville Granite has a $^{40}Ar/^{39}Ar$ biotite plateau age of 1357 ± 5 Ma (total gas age: 1341 Ma) reported in (Romano et al., 2000) and a zircon recrystallization U-Pb age of 1871 ± 5 Ma (Sims, 1993), while the nearby (~3 km away) Hatfield Gneiss (95-13) has a protolith zircon U-Pb crystallization age of 2815 ± 20 Ma (Maass and Brown, 1987), with the lower temperature Ar system likely similar in age to sample 95-11. The Athelstane Granite (sample 96-WIS-11) has a U-Pb zircon age of ca. 1860 ± 15 Ma (Van Schmus et al., 1975b). Sample ILST-3 was taken from a core at ~4526 m depth of borehole UPH-3 of Hoppe et al. (1983) from Illinois basement of the 1.45-1.5 Ga Eastern-Granite Rhyolite Province and was dated using U-Pb in zircon providing an age of 1463 ± 10 Ma.

APPENDIX B:

$^{40}Ar/^{39}Ar$ thermochronology analytical methods

Instrumentation for $^{40}Ar/^{39}Ar$ dating at Lehigh University includes automated furnace and laser extraction systems connected on-line to a Thermo Argus VI noble-gas mass spectrometer. The furnace line is built around a double-vacuum resistance furnace utilizing Mo crucibles. Furnace temperature is monitored by a W-Re thermocouple and vacuum in the extraction line and furnace is maintained by two turbo-molecular pumps and a 30 l/s ion pump. The laser extraction line is equipped with a Merchantek dual CO_2/UV laser system. Ca and K salts are fused with a CO_2 laser for calculating the mass discrimination factor and mass interferences. The GA-1550 biotite standard is also degassed for neutron flux monitoring to determine irradiation constants. The laser produces a continuous 10.6 μm beam with output power variable up to 35 W and the sample chamber accepts copper trays holding up to 200 samples each and is positioned by a Newport 3-axis motion control system operable under computer control. Gas cleanup for both extraction lines is handled by SAES getters and for larger hydrous samples, a LN_2-cooled cold finger is available. All valves essential for gas handling on both extraction systems can be operated under computer control.

The Argus VI multi-collector mass spectrometer is operated at 4.5 kV accelerating potential and 200 mA trap current. Under these conditions, the background for ^{36}Ar is $1x10^{-14}$ cc STP. Routine Ar analyses are performed in multi-collector mode using Faraday detectors to measure ^{40}Ar, ^{39}Ar, ^{38}Ar and ^{37}Ar. Either a fifth Faraday detector or an ion-counting electron multiplier is used to measure ^{36}Ar. The Faraday detector

sensitivity of the mass spectrometer is ~$5.6x10^{-17}$ moles/fA open to the furnace line. During routine analyses, the five Ar peaks are measured 150 times and baselines measured 90 times using a two second integration period. Our latest measurements of atmospheric argon yielded $^{40}Ar/^{36}Ar$ values of 307.5 ± 0.22% (n=14) corresponding to a mass discrimination of ~1.0%/amu. The mass spectrometer and extraction lines are integrated into a fully automated system under the control of a Windows PC running LabSpec, a LabVIEW program for noble-gas mass spectrometry developed at Lehigh by Bruce Idleman.

Raw data from the mass spectrometer are reduced using ArArCalc (Koppers, 2002). Beam values are regressed to the time of inlet to the mass spectrometer, then corrected for background, line blank, discrimination, decay of ^{37}Ar and ^{39}Ar, and Ca and K-derived nucleogenic interferences. All $^{40}Ar/^{39}Ar$ ages determined at Lehigh are accompanied by a complete assessment of uncertainties, including the propagation of uncertainties in peak-height regressions, blank, discrimination, nucleogenic interferences, flux monitor measurements, J-factor interpolation, and decay constants. In general, the age uncertainty that can be expected for an individual sample will vary because the precision of a $^{40}Ar/^{39}Ar$ age is dependent upon many sample-specific factors (e.g., age, K, radiogenic yield, extent of nucleogenic interferences from Ca and K, and so forth). However, for late-Tertiary and older K-rich samples that are well-behaved, ages are regularly obtained with associated analytical precision of <1%. For example, the typical analytical precision for single-crystal laser fusion analyses of biotite age standard GA-1550 (98 Ma) is ~0.3%.

$^{40}Ar/^{39}Ar$ multi-diffusion domains and thermal history modeling methods

Modeling of K-feldspar diffusion domains was done using the *Domains* code developed by Peter Zeitler from the original core routines of the *autoarr* code of Oscar Lovera at UCLA. The program inverts for domain-size distributions based on misfit minimization between observed and predicted $\log R/R_o$ data. The code selects a R_o reference and associated activation energy (E_a) and predicts a domain distribution that is then fit using the Levenberg-Marquardt method of least squares fitting. To be consistent and rigorous with all samples, the same steps were taken when modeling domain distributions as follows: (1) use of a slab diffusion geometry; (2) modeling was only performed up to 1050-1100°C, just before typical K-feldspar melting temperatures of approximately 1100°C; (3) the number of domains was allowed to be between 3 to 10 and E_a values of 40 to 52 kcal/mol and values between 2 to 8 s^{-1} for $\log D_o/r^2$ were enforced from Lovera et al. (1997), and (4) at least 8 points were used during regression of the Arrhenius data.

Thermal history modeling was done using the *Arvert* code developed at Lehigh University (Zeitler, 2004) for extracting thermal histories from $^{40}Ar/^{39}Ar$ age spectra using the controlled random search (CRS) algorithm (Price, 1977) utilizing adaptations from (Willett, 1997). The newest version of *Arvert* (v. 6.0) can incorporate additional thermochronometric constraints. The inversion algorithm uses a Monte Carlo (MC) approach with an enhanced "learning" component of the CRS algorithm to drive convergence, and uses the observed age spectrum, kinetic data, and diffusion domain distribution as input. The algorithm searches parameter space for misfit minima (thermal histories) that lead to better fits between observed and predicted age spectra and mineral

ages. In our case a mean square weighted deviates (MSWD) misfit is used that accounts for assigned errors on each age spectrum heating step and any additional mineral age errors. Obtaining MSWD values within analytical uncertainty are often rare in these thermal history inversions, simply because the high age precision of individual heating steps during stepwise Ar degassing.

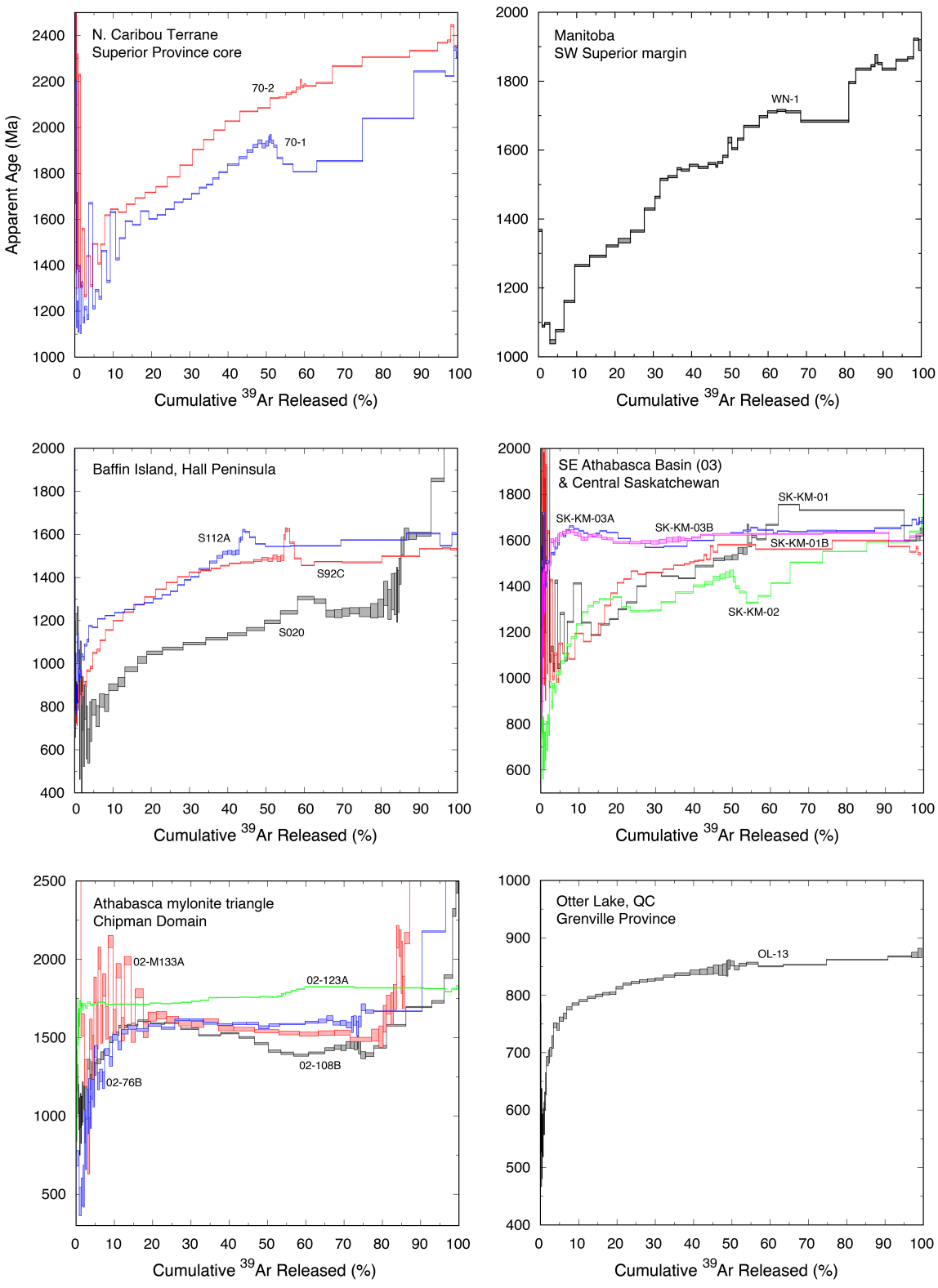
At the model start, a pool of 150 thermal histories is randomly generated that obeys any user-enforced constraints on the thermal history, i.e. maximum/minimum temperature bounds for the inversion, or any implicit constraint on maximum/minimum heating and cooling rates for the model pool. An age spectrum (and mineral cooling age) is determined for each thermal history in the pool and compared to the observed spectrum, with a misfit calculated for the derived thermal history; as new thermal histories are created they are kept or thrown out with respect to the worst fit in the model pool. The CRS method takes a random subset of 15 histories from the main MC pool, plus one more thermal history. The 15 histories are averaged and by projecting the additional history through the averaged bundle (using an amplification factor), a new thermal history is created. This continues until the specified number of model iterations or convergence has been reached for the inversion. An important point to note is that Arvert tries to make *every* model in the MC pool a good fit, while a purely Monte Carlo model explores the problem space trying to find good-fitting histories that adhere to explicit constraints. Plotted output shows the temperature-time (Tt) paths in the upper panel and the modeled age spectrum in the bottom panel. Green lines are the top 15 Tt paths while red lines are the worst 15 paths at the end of the finalized model run (heavy black lines

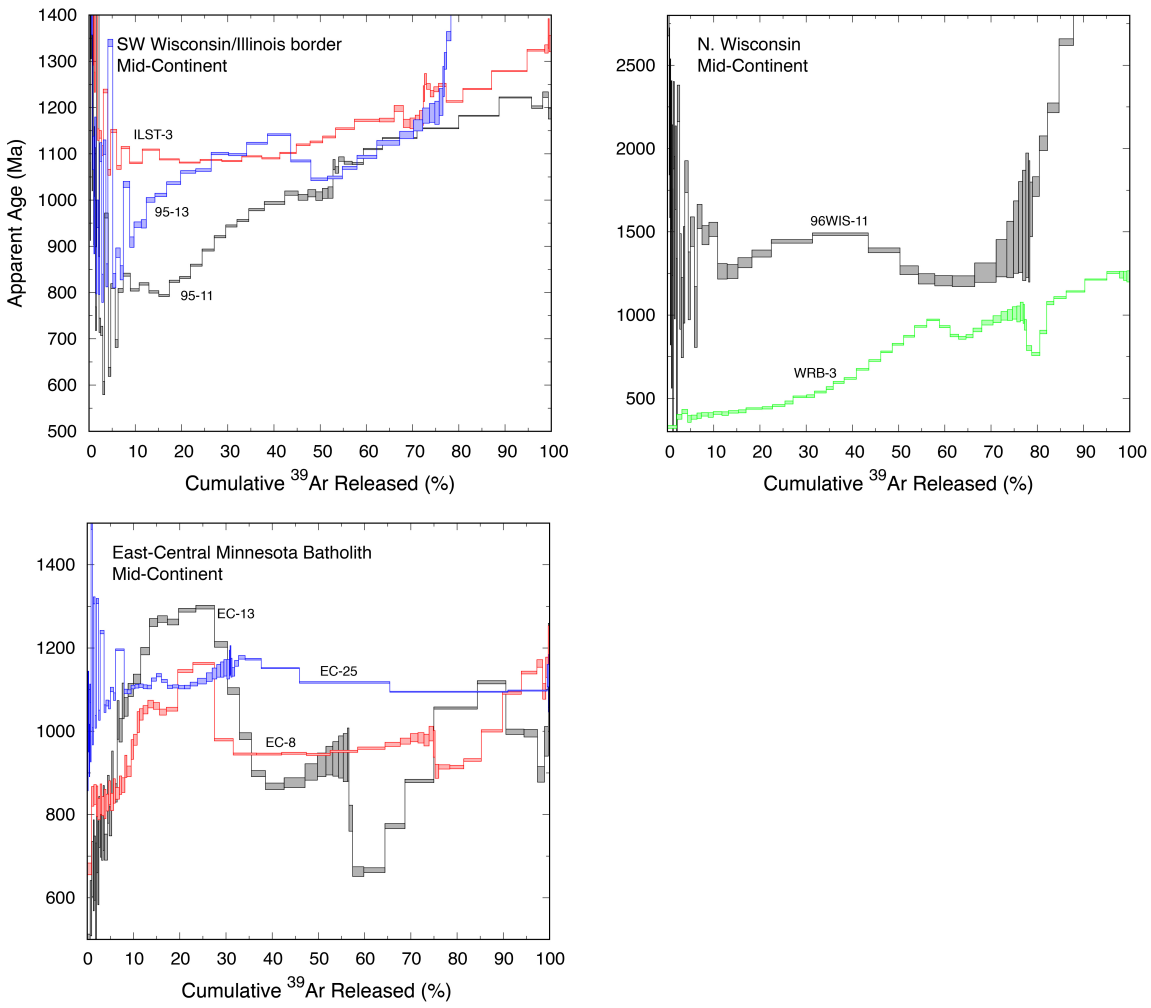
just outline the bundle and are not part of the solution). Gray lines in the background show the MC pool and the light green band denotes the portion of Tt-space that is constrained by the Ar age spectrum, while the light gray band denotes the region constrained by other thermochronologic mineral systems. The lower age spectrum panel shows the observed age spectrum (heavy gray line) with the modeled section highlighted in blue. The green and red lines are the best/worst model spectra corresponding to the best/worst model thermal histories in Tt-space.

APPENDIX C: Age spectra and thermal history models

$^{40}Ar/^{39}Ar$ age spectra (see below)

Note: only samples that could be modeled are shown in the thermal history modeling section.


N. Caribou Terrane
Superior Province core
70-2
70-1
Apparent Age (Ma)
Cumulative 39Ar Released (%)
Manitoba
SW Superior margin
WN-1
Cumulative 39Ar Released (%)
Baffin Island, Hall Peninsula
S112A
S92C
S020
Cumulative 39Ar Released (%)
SE Athabasca Basin (03)
& Central Saskatchewan
SK-KM-01
SK-KM-03A
SK-KM-03B
SK-KM-01B
SK-KM-02
Cumulative 39Ar Released (%)
Athabasca mylonite triangle
Chipman Domain
02-M133A
02-123A
02-108B
02-76B
Cumulative 39Ar Released (%)
Otter Lake, QC
Grenville Province
OL-13
Cumulative 39Ar Released (%)

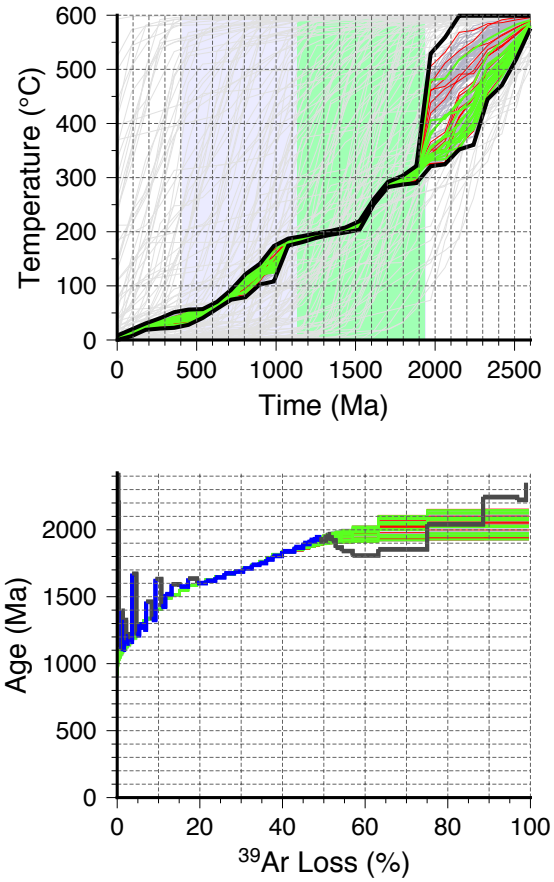


^{40}Ar/^{39}Ar age MDD age spectra for K-feldspar samples from across the Canadian Shield.

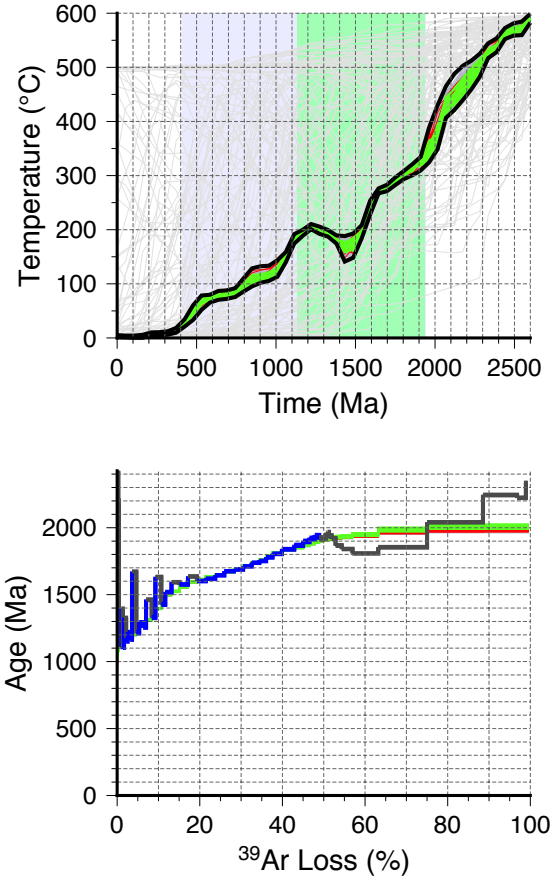
See Appendix A: Table 1 for samples locations.

Arvert inverse thermal history models followed by domains information

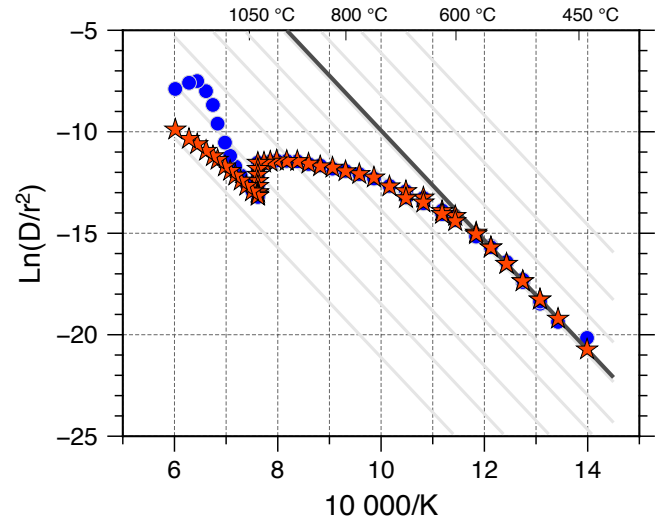
Western Superior Province



Sample 70-1782: Arvert monotonic inverse thermal histories. 15,000 iterations, MC and CRS max cooling rates allowed 2.0/3.0 C/my. Best fit: 28.02; worst fit: 30.19



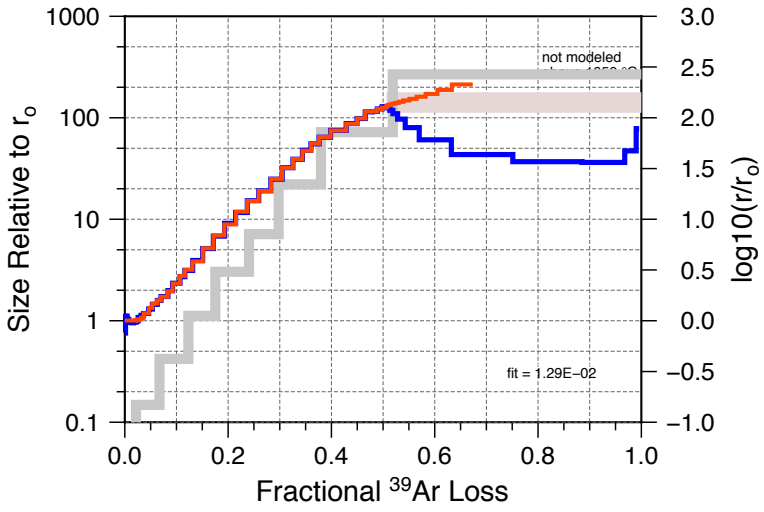
Sample 70-1782: Arvert reheating allowed inverse thermal histories. 10,000 iterations, MC and CRS max reheating rates 1.0/1.0 C/my and cooling rates 3.0/3.0 C/my. Best fit: 18.77; worst fit: 21.09

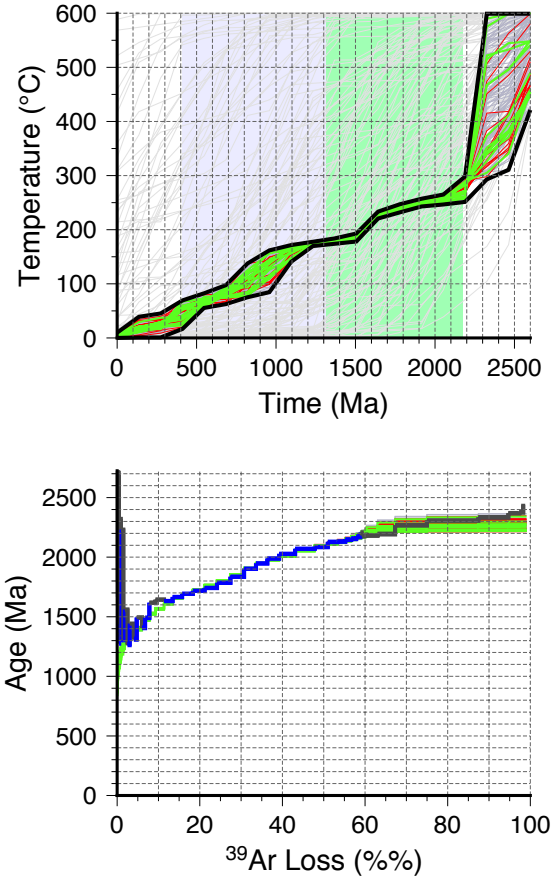


SAMPLE: No70−1782
Using steps 4 to 11:
E = 53.70 ± 1.84 kcal/mol
$Log_{10}(D/r_o^2)$ = 7.427 ± 0.501
Unweighted regression
Infinite−slab geometry

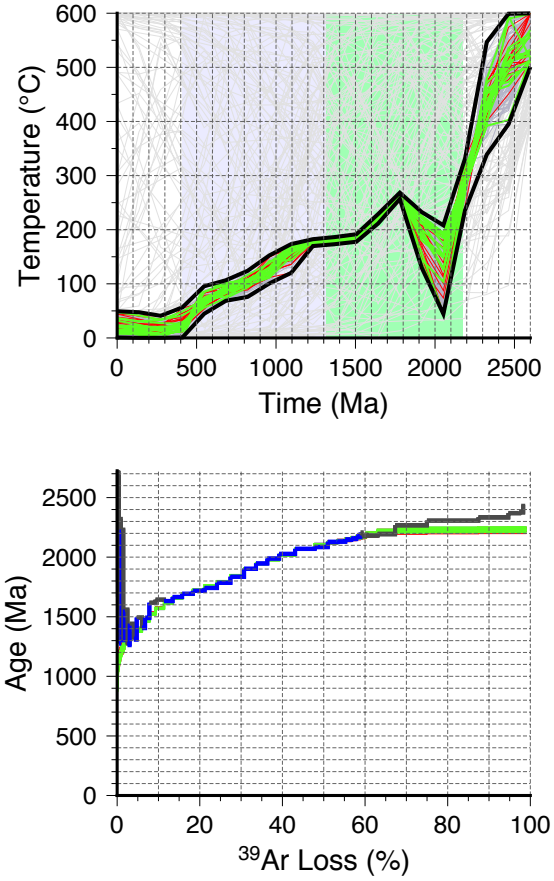
9 domains:

N	Vol.	Vol_T	Rel. Size	Tc10
1	0.022	0.02	0.046	207.
2	0.045	0.07	0.148	227.
3	0.056	0.12	0.421	246.
4	0.052	0.18	1.119	266.
5	0.065	0.24	3.038	287.
6	0.058	0.30	7.134	307.
7	0.082	0.38	22.08	335.
8	0.139	0.52	72.20	368.
9	0.481	1.00	268.1	408.

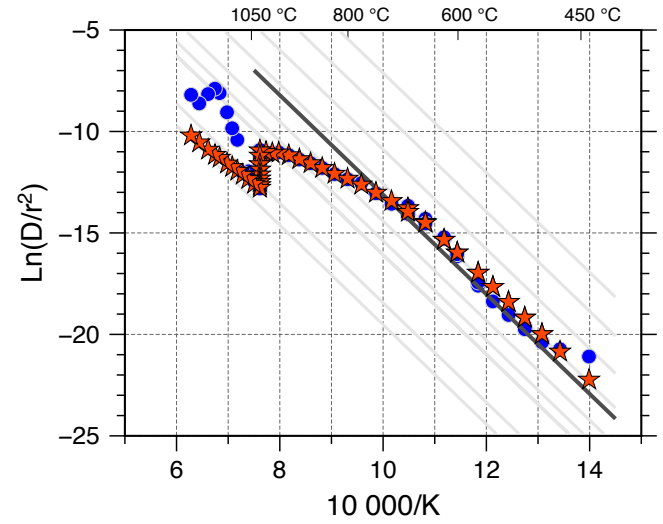




Sample 70-2051 (same sample as above): Arvert monotonic inverse thermal histories. 20,000 iterations, max MC/CRS cooling rates, 1.0/5.0 C/my. Best fit: 68.35; worst fit: 77.91



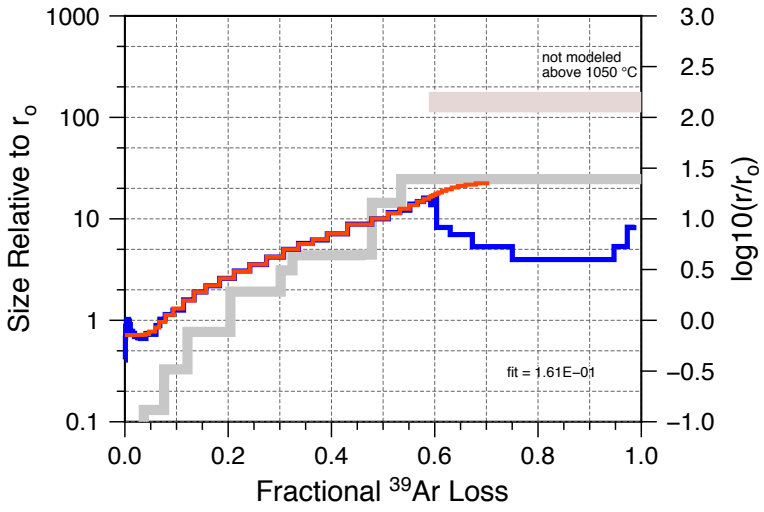
Sample 70-2051: Arvert reheating allowed inverse thermal histories. 35,000 iterations, max MC/CRS reheating rates, 1.0/1.0 and cooling rates, 2.0/5.0 C/my. Best fit: 42.00; worst fit: 53.97

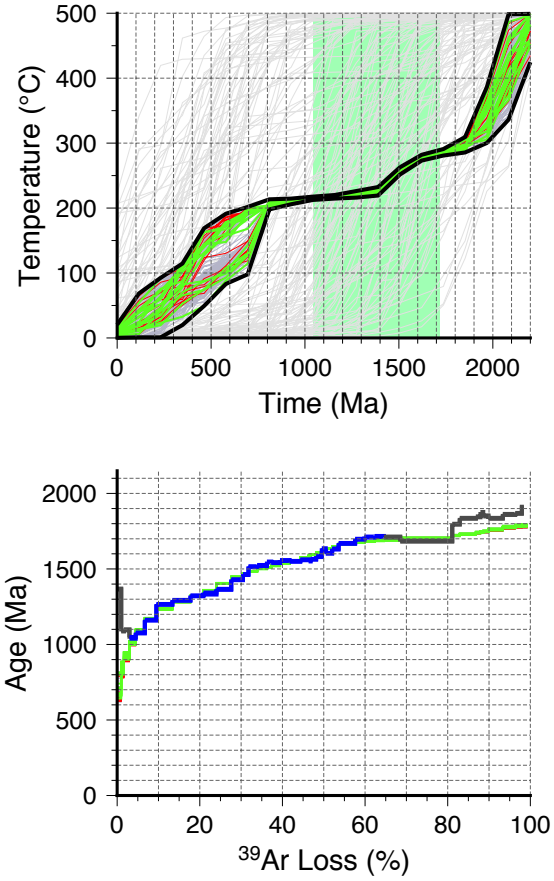


SAMPLE: No70−2051
Using steps 8 to 11:
E = 48.73 ± 2.41 kcal/mol
$Log_{10}(D/r_o^2)$ = 4.961 ± 0.638
Unweighted regression
Infinite−slab geometry

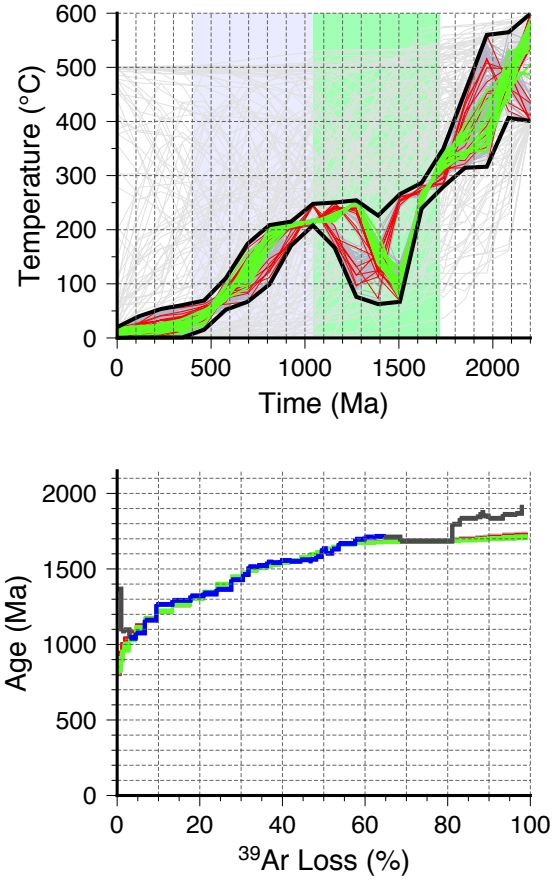
10 domains:

N	Vol.	Vol_T	Rel. Size	Tc10
1	0.037	0.04	0.050	212.
2	0.039	0.08	0.131	230.
3	0.045	0.12	0.328	249.
4	0.083	0.20	0.769	268.
5	0.097	0.30	1.917	289.
6	0.023	0.32	3.108	302.
7	0.131	0.46	4.374	310.
8	0.023	0.48	4.439	311.
9	0.057	0.54	14.38	344.
10	0.465	1.00	24.66	360.

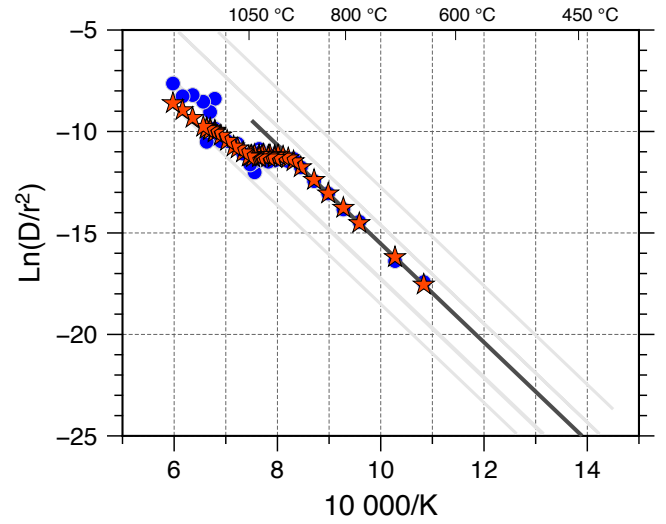




Sample WN-1: Arvert monotonic inverse thermal histories. 31,000 iterations, max MC/CRS cooling rates 2.0/5.0 C/my. Best fit: 56.52; worst fit: 57.32



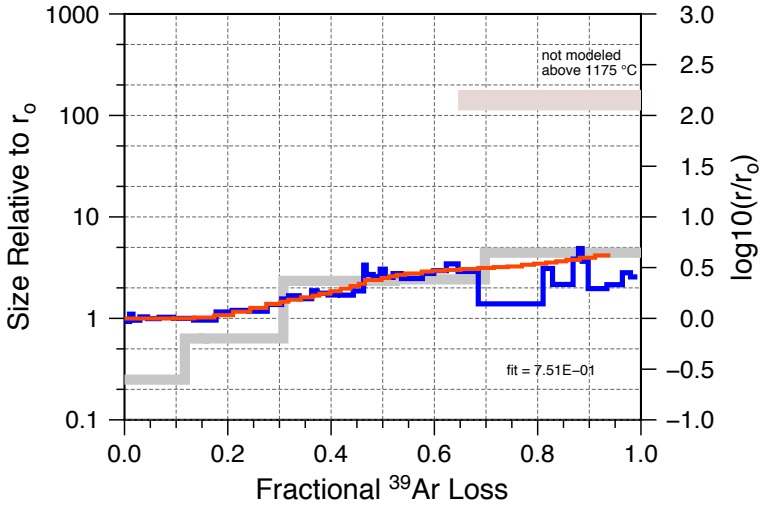
Same WN-1: Arvert reheating allowed inverse thermal histories. 100,000 iterations, max reheating MC/CRS rates, 1.0/1.0 C/my, max cooling rates, 2.0/5.0 C/my. Best fit: 69.44; worst fit: 75.75



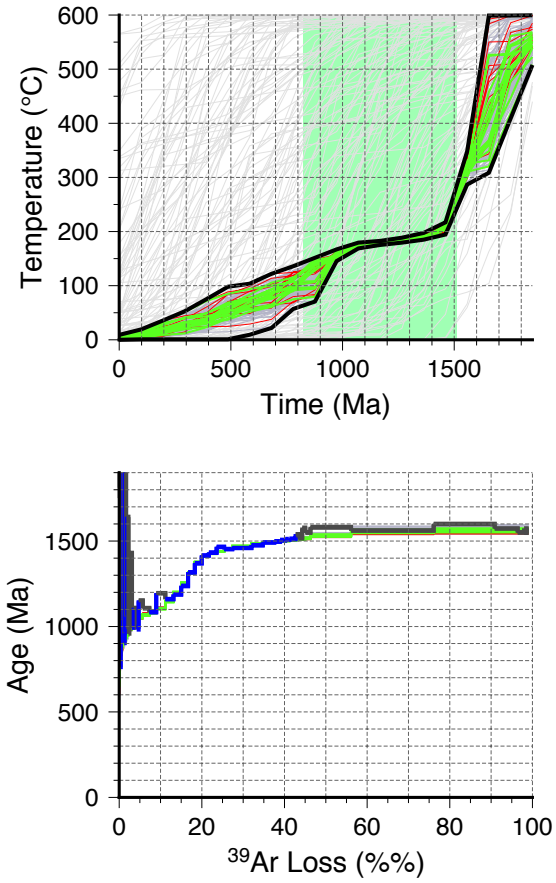
SAMPLE: WN−1
Using steps 1 to 8:
E = 48.26 ± 0.95 kcal/mol
$Log_{10}(D/r_o^2)$ = 3.811 ± 0.193
Unweighted regression
Infinite−slab geometry

6 domains:

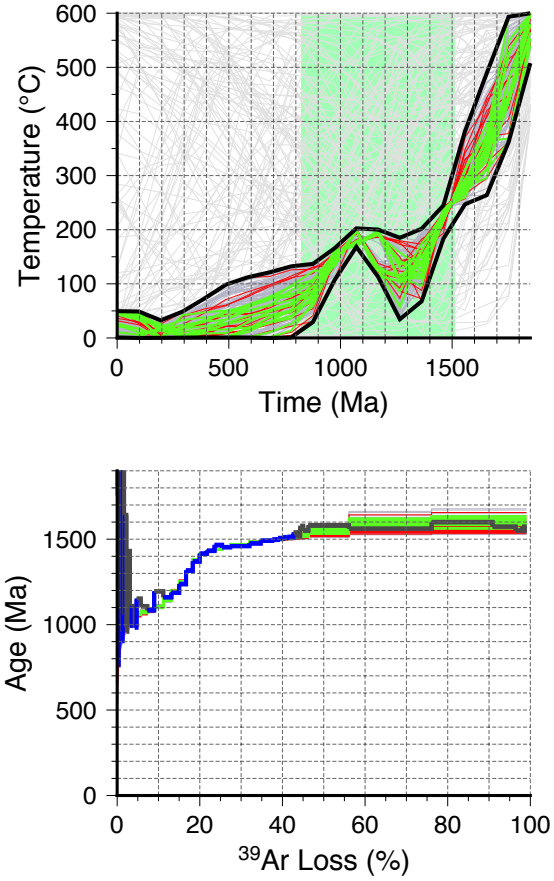
N	Vol.	Vol_T	Rel. Size	Tc10
1	0.117	0.12	0.249	267.
2	0.036	0.15	0.633	289.
3	0.154	0.31	0.634	289.
4	0.216	0.52	2.342	324.
5	0.174	0.70	2.425	325.
6	0.302	1.00	4.436	342.



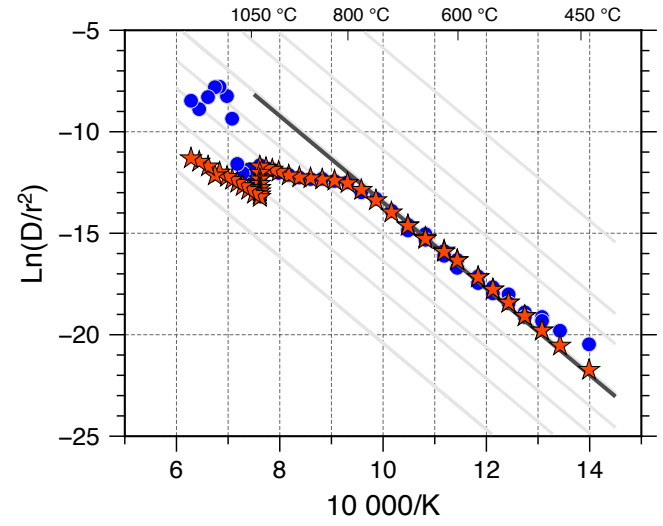
Saskatchewan



Sample SK-KM-01B: Arvert monotonic inverse thermal histories. 10,000 iterations. Max MC/CRS cooling rates 2.0/5.0 C/my. Best fit: 26.01; worst fit: 28.78



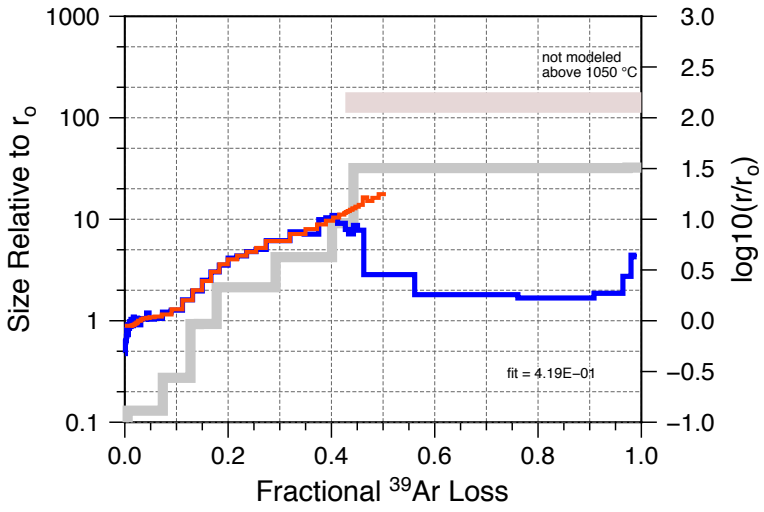
Sample SK-KM-01B: Arvert reheating allowed inverse thermal histories. 20,000 iterations. Max MC/CRS reheating rates, 1.0/1.0 C/my and max cooling rates, 2.0/5.0 C/my. Best fit: 24.18; worst fit: 28.30

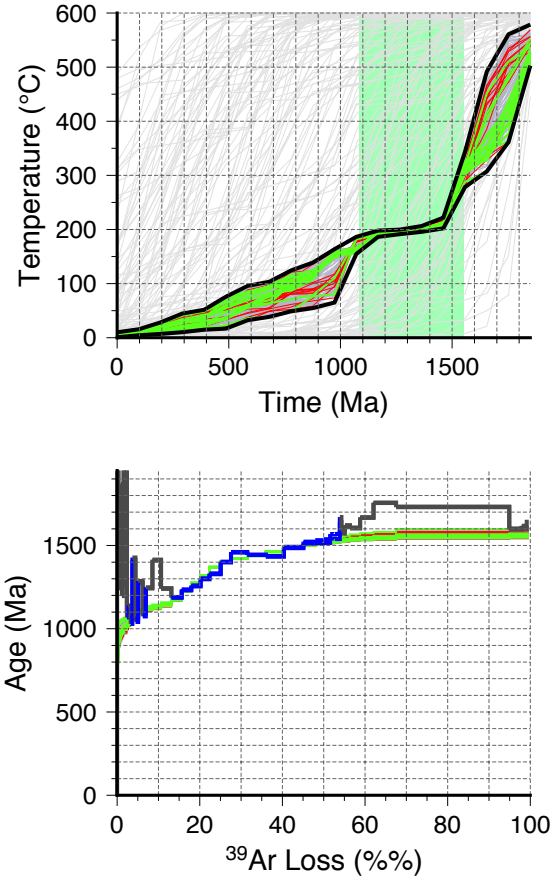


SAMPLE: SK−KM−01B
Using steps 12 to 19:
E = 42.25 ± 2.82 kcal/mol
$Log_{10}(D/r_o^2)$ = 3.386 ± 0.687
Unweighted regression
Infinite−slab geometry

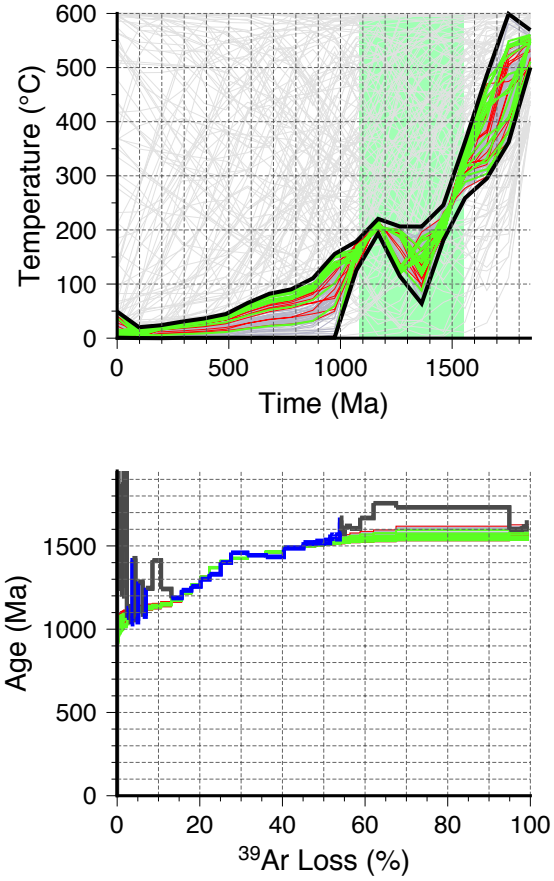
10 domains:

N	Vol.	Vol_T	Rel. Size	Tc10
1	0.005	0.01	0.022	165.
2	0.068	0.07	0.130	198.
3	0.054	0.13	0.274	213.
4	0.016	0.14	0.928	241.
5	0.035	0.18	0.931	241.
6	0.114	0.29	2.138	261.
7	0.109	0.40	4.228	279.
8	0.041	0.44	9.146	301.
9	0.530	0.97	31.93	340.
10	0.027	1.00	32.30	341.

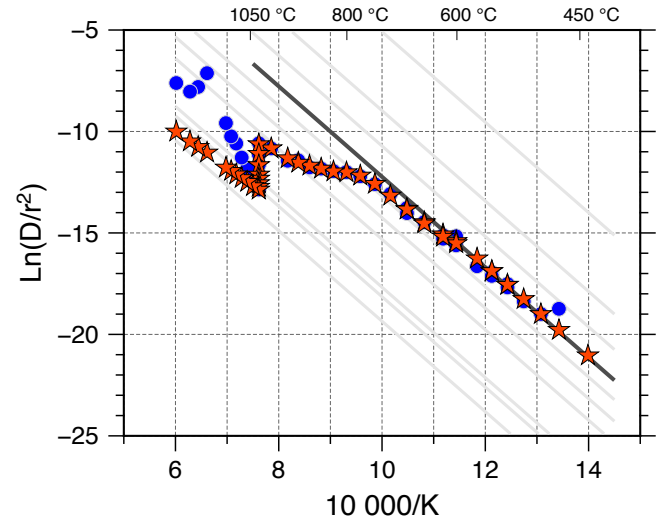




Sample SK-KM-01: Arvert monotonic inverse thermal histories. 10,000 iterations, max MC and CRS cooling rates: 2.0/5.0 C/my. Best fit: 55.68; worst fit 57.65



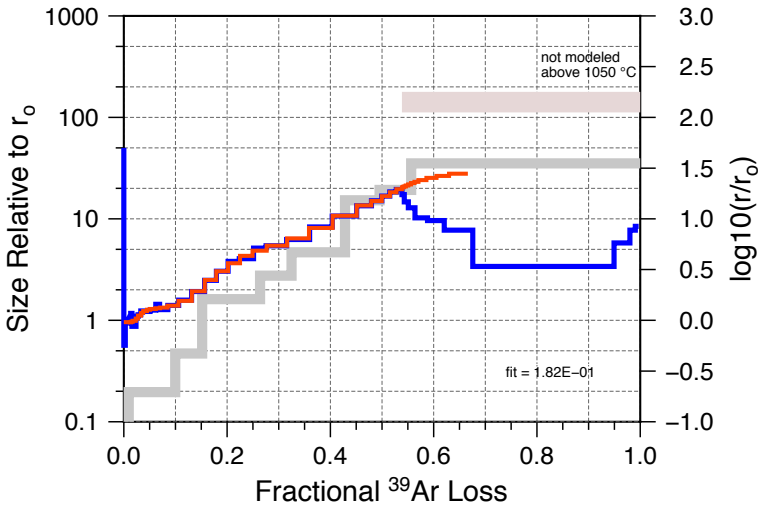
Sample SK-KM-01: Arvert reheating allowed inverse thermal histories. 20,000 iterations, max MC/CRS heating rates: 1.0/1.0 C/my and max cooling rates: 2.0/5.0 C/my. Best fit: 52.13; worst fit: 54.65

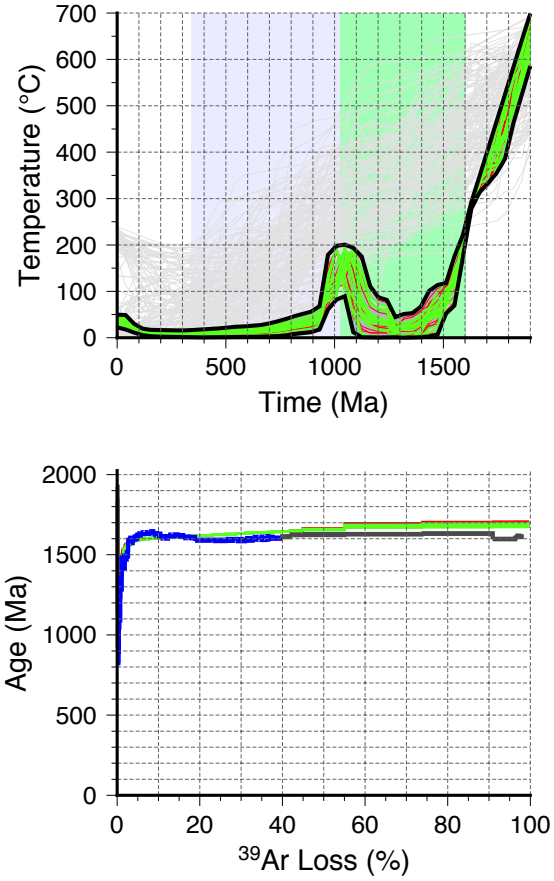


SAMPLE: SK−KM−01
Using steps 3 to 10:
E = 44.26 ± 2.79 kcal/mol
$Log_{10}(D/r_o^2)$ = 4.368 ± 0.750
Unweighted regression
Infinite−slab geometry

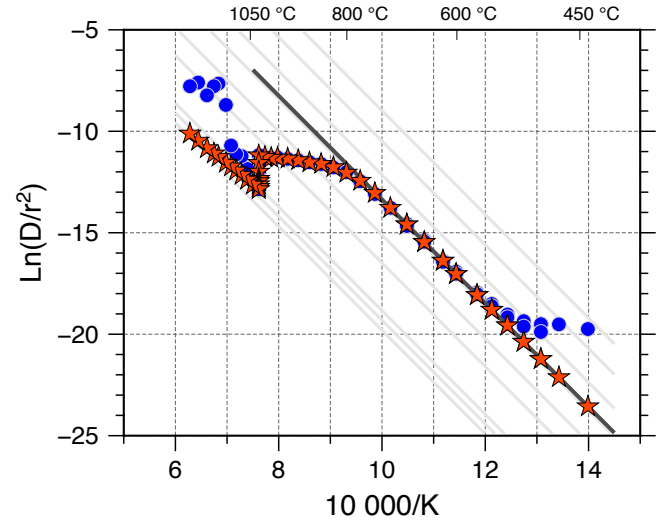
9 domains:

N	Vol.	Vol_T	Rel. Size	Tc10
1	0.009	0.01	0.028	170.
2	0.090	0.10	0.196	205.
3	0.052	0.15	0.470	223.
4	0.112	0.26	1.614	251.
5	0.061	0.32	2.751	263.
6	0.104	0.43	4.679	277.
7	0.067	0.50	15.23	309.
8	0.061	0.56	19.24	316.
9	0.444	1.00	35.24	334.





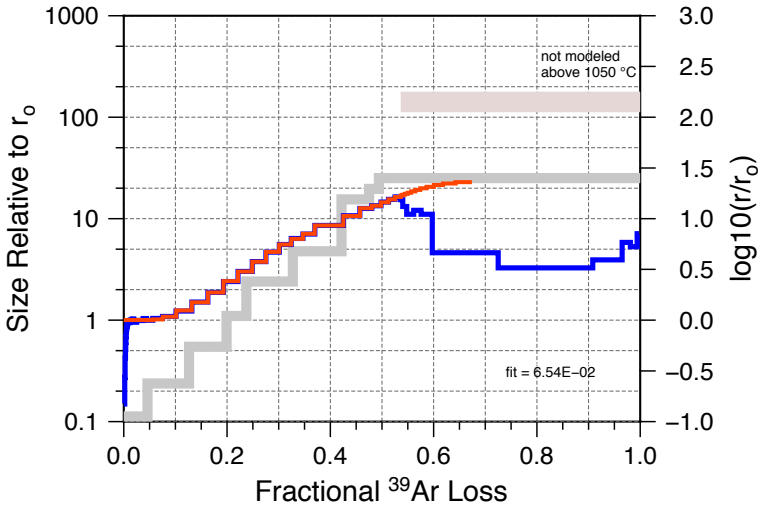
Sample SK-KM-03 (S. Athabasca basin margin): Arvert reheating allowed inverse thermal histories. 10,000 iterations, max MC/CRS heating rates, 2.0/3.0 C/my and max cooling rates 5.0/5.0 C/my. Best fit: 26.94; worst fit 28.25 (note: monotonic model unable to find good histories) – this sample is marginally acceptable for modeling given the intermediate age maximum.



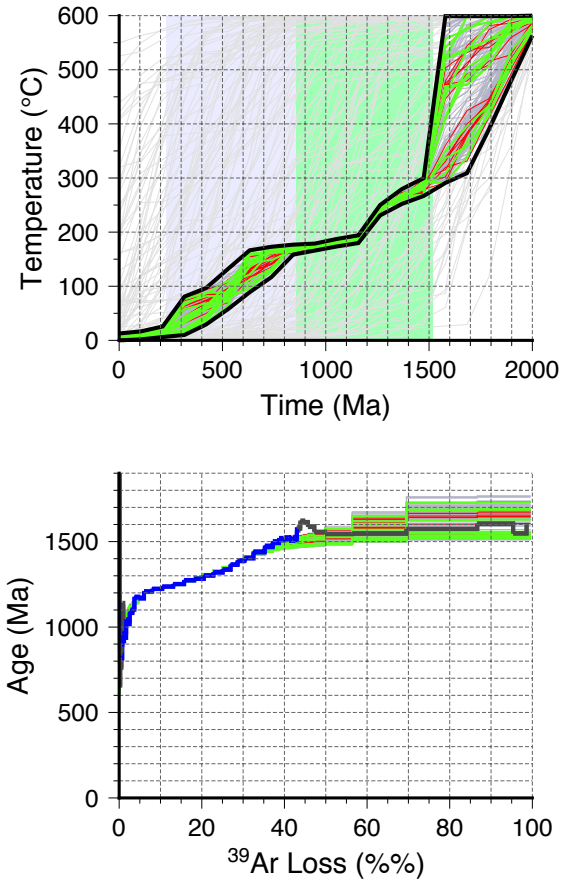
SAMPLE: SKKM03BDo
Using steps 14 to 21:
E = 50.75 ± 0.93 kcal/mol
$Log_{10}(D/r_o^2)$ = 5.296 ± 0.220
Unweighted regression
Infinite–slab geometry

9 domains:

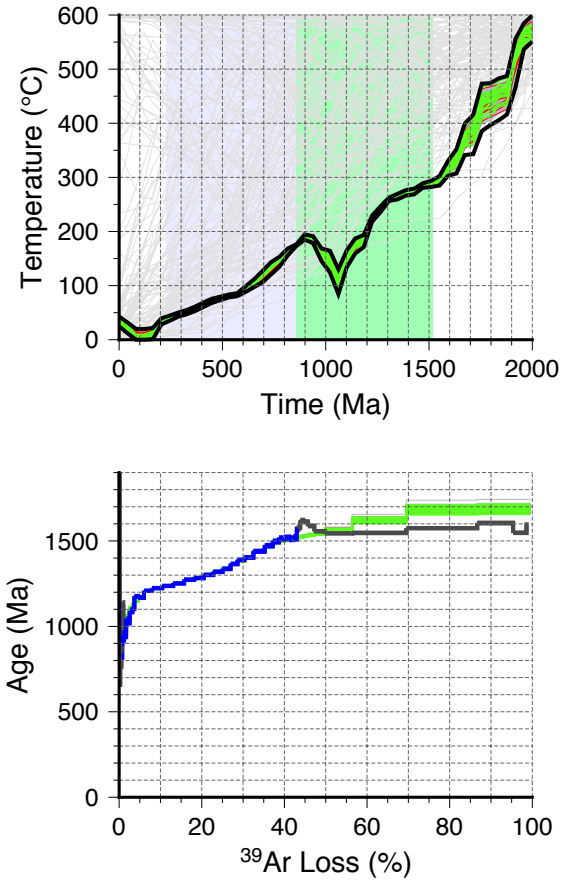
N	Vol.	Vol_T	Rel. Size	Tc10
1	0.046	0.05	0.112	240.
2	0.080	0.13	0.238	255.
3	0.073	0.20	0.547	273.
4	0.038	0.24	1.100	289.
5	0.090	0.33	2.403	308.
6	0.094	0.42	4.775	326.
7	0.053	0.48	15.48	359.
8	0.019	0.49	19.63	366.
9	0.506	1.00	25.12	374.



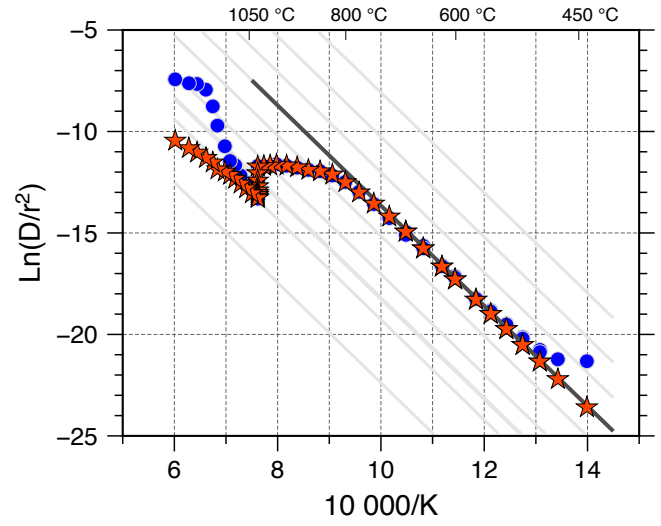
Baffin Island, Hall Peninsula



Sample S112A: Arvert monotonic inverse thermal histories. 10,000 iterations, max MC/CRS cooling rates, 2.0/5.0 C/my. Best fit: 28.76; worst fit: 33.40



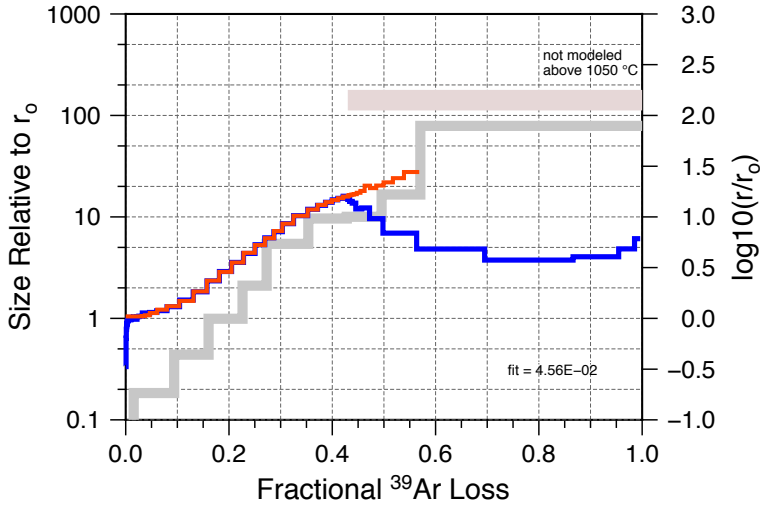
Sample S112A: Arvert reheating allowed inverse thermal histories. 15,000 iterations, max MC/CRS reheating rates, 1.0/1.0 C/my and max cooling rates, 2.0/5.0 C/my. Best fit: 27.53; worst fit: 28.17

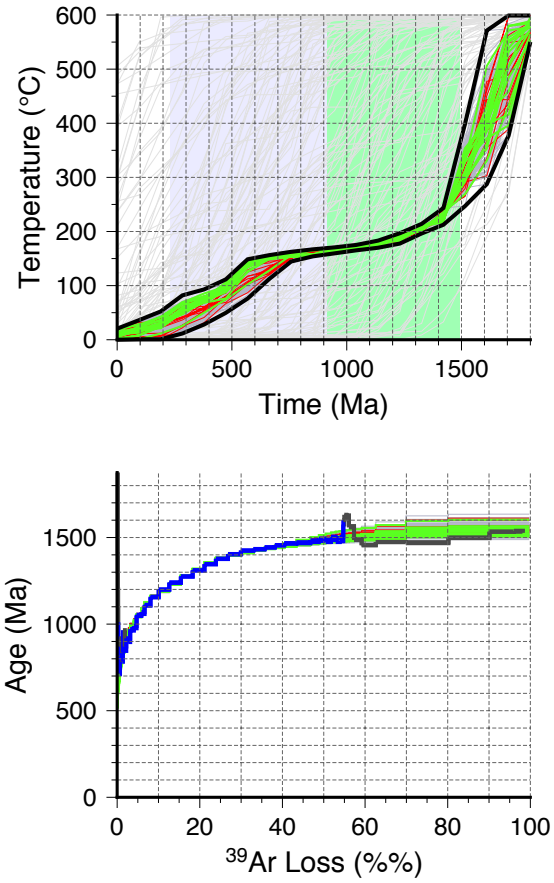


SAMPLE: S112A
Using steps 10 to 17:
E = 49.05 ± 0.86 kcal/mol
$Log_{10}(D/r_o^2)$ = 4.797 ± 0.217
Unweighted regression
Infinite−slab geometry

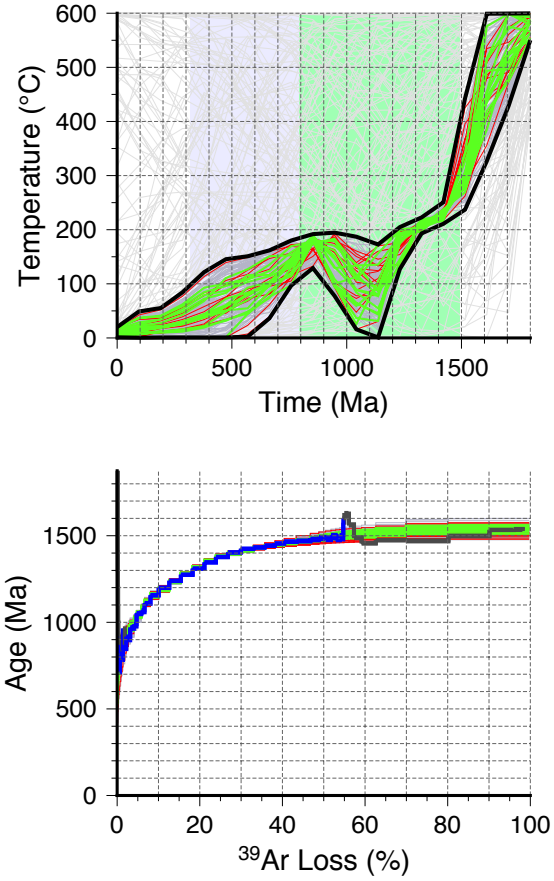
10 domains:

N	Vol.	Vol_T	Rel. Size	Tc10
1	0.015	0.02	0.062	222.
2	0.079	0.09	0.184	244.
3	0.067	0.16	0.439	263.
4	0.066	0.23	0.993	282.
5	0.047	0.27	2.103	300.
6	0.081	0.35	5.422	325.
7	0.074	0.43	9.639	341.
8	0.067	0.50	10.03	343.
9	0.075	0.57	16.61	358.
10	0.430	1.00	78.95	409.

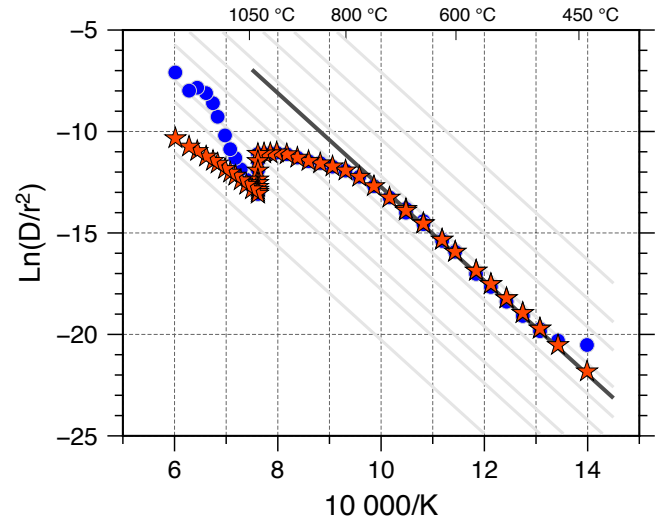




Sample S092C: Arvert monotonic inverse thermal histories. 5,000 iterations, max MC/CRS cooling rates 2.0/5.0 C/my. Best fit: 21.22; worst fit: 28.64



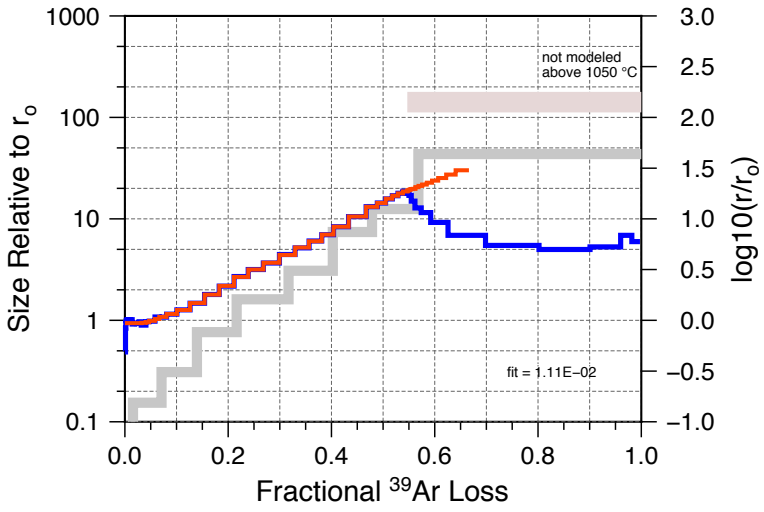
Sample S092C: Arvert reheating allowed inverse thermal histories. 23,000 iterations, max MC/CRS reheating rates, 1.0/1.0 C/my and max cooling rates, 2.0/5.0 C/my. Best fit: 11.92; worst fit: 27.20

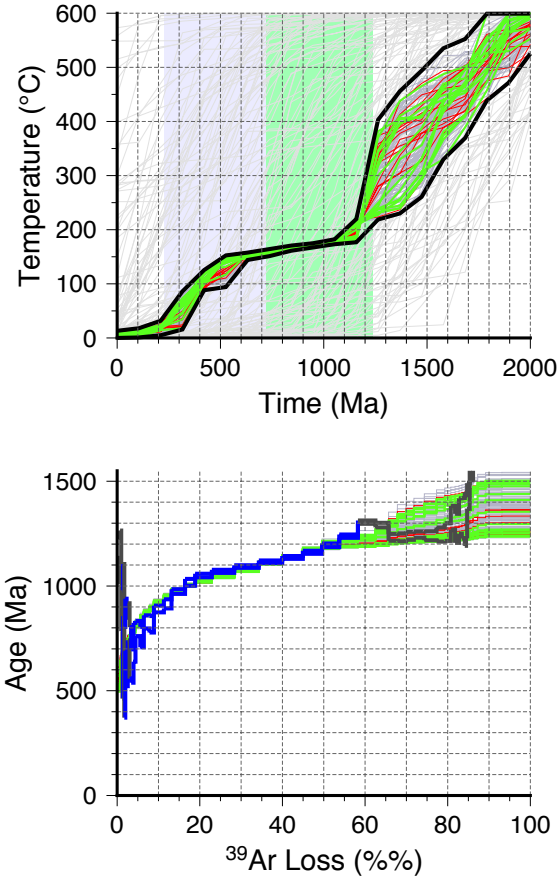


SAMPLE: S092C1
Using steps 4 to 11:
E = 45.92 ± 0.41 kcal/mol
$Log_{10}(D/r_o^2)$ = 4.513 ± 0.112
Unweighted regression
Infinite−slab geometry

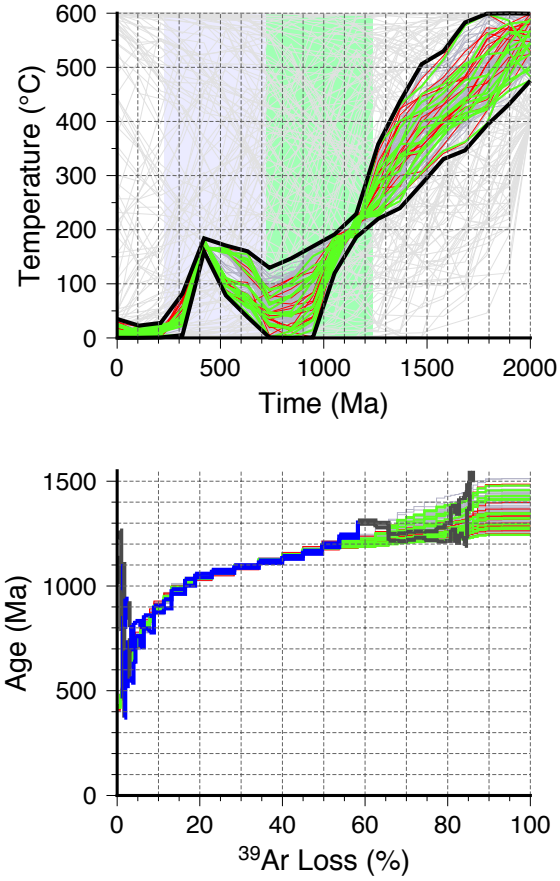
9 domains:

N	Vol.	Vol_T	Rel. Size	Tc10
1	0.016	0.02	0.059	196.
2	0.055	0.07	0.154	215.
3	0.069	0.14	0.309	229.
4	0.077	0.22	0.765	248.
5	0.101	0.32	1.610	266.
6	0.086	0.40	3.077	282.
7	0.076	0.48	7.410	305.
8	0.090	0.57	12.50	320.
9	0.432	1.00	43.52	358.

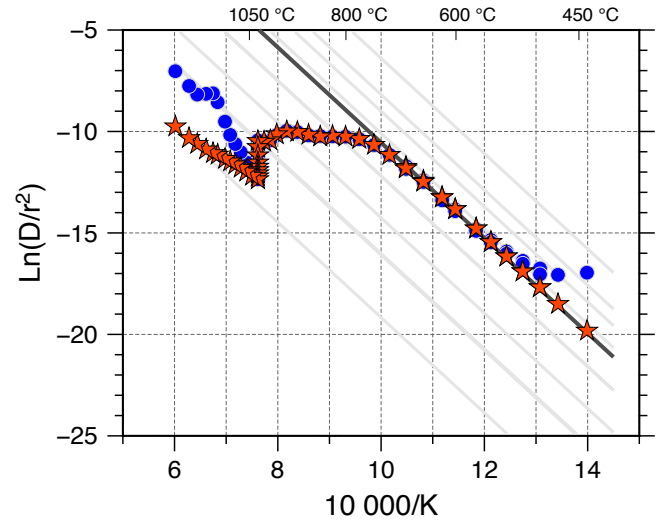




Sample S020: Arvert monotonic inverse thermal history. 20,000 iterations, max MC/CRS cooling rates, 2.0/5.0 C/my. Best fit: 12.23; worst fit: 13.74



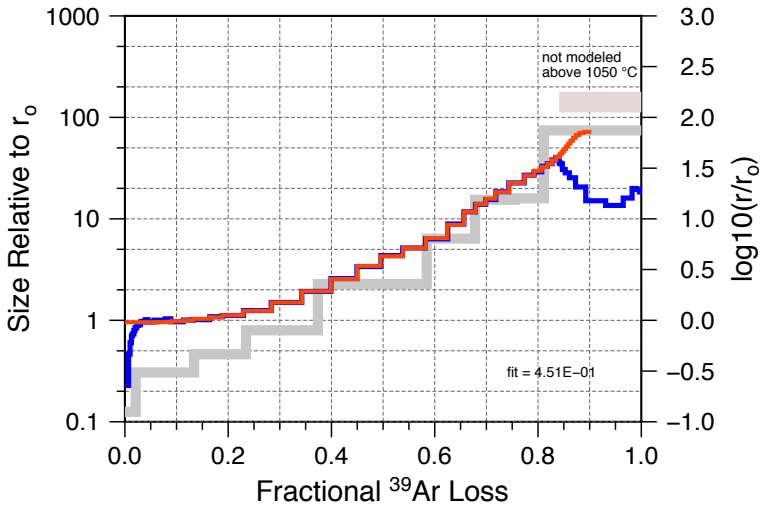
Sample S020: Arvert reheating allowed inverse thermal history. 30,000 iterations, max MC/CRS heating rates 1.0/1.0, max cooling rates, 2.0/5.0 C/my. Best fit: 6.19; worst fit: 7.54



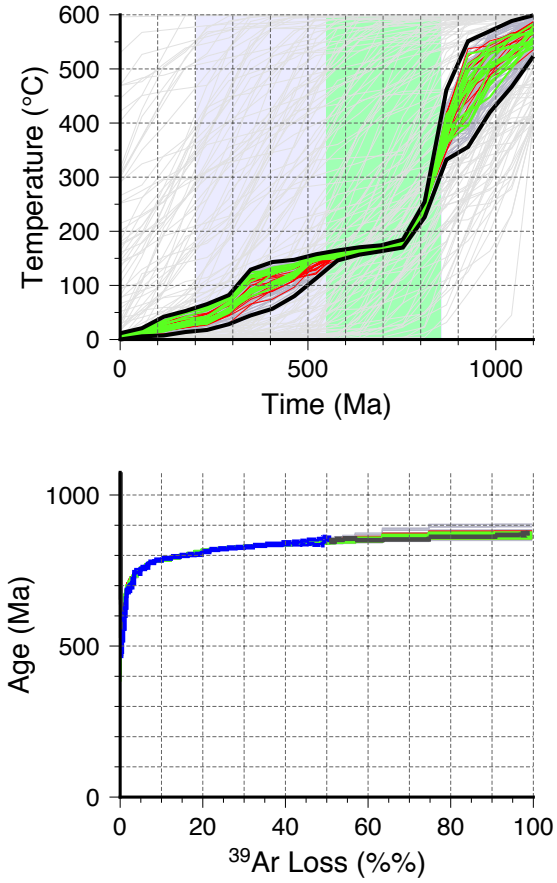
SAMPLE: S020
Using steps 12 to 19:
E = 46.62 ± 0.94 kcal/mol
$Log_{10}(D/r_o^2)$ = 5.613 ± 0.229
Unweighted regression
Infinite−slab geometry

10 domains:

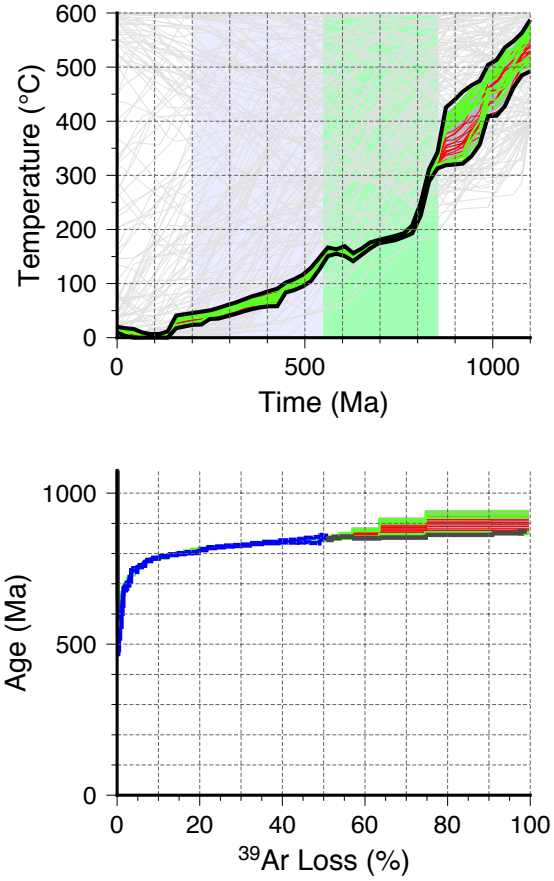
N	Vol.	Vol_T	Rel. Size	Tc10
1	0.021	0.02	0.125	194.
2	0.113	0.13	0.306	211.
3	0.101	0.23	0.462	219.
4	0.139	0.37	0.797	230.
5	0.105	0.48	2.275	252.
6	0.106	0.58	2.277	252.
7	0.093	0.68	6.381	276.
8	0.077	0.75	15.41	299.
9	0.057	0.81	15.96	300.
10	0.189	1.00	74.39	344.



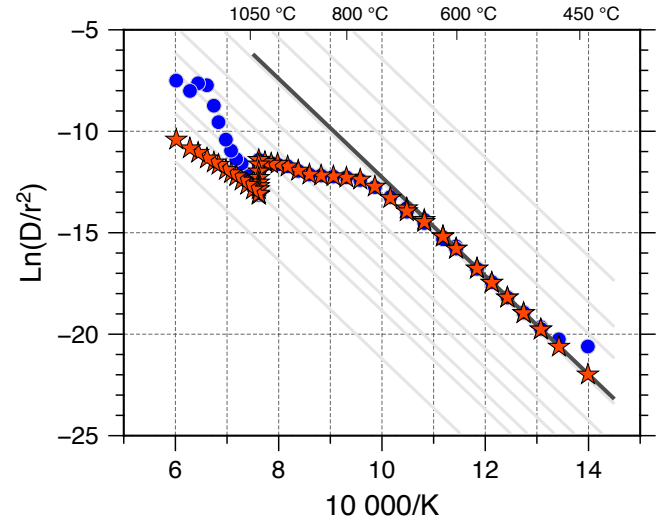
Grenville Province



Sample OL13: Arvert monotonic inverse thermal history. 5,000 iterations, max MC/CRS cooling rates, 2.0/5.0 C/my. Best fit: 2.56; worst fit: 3.69



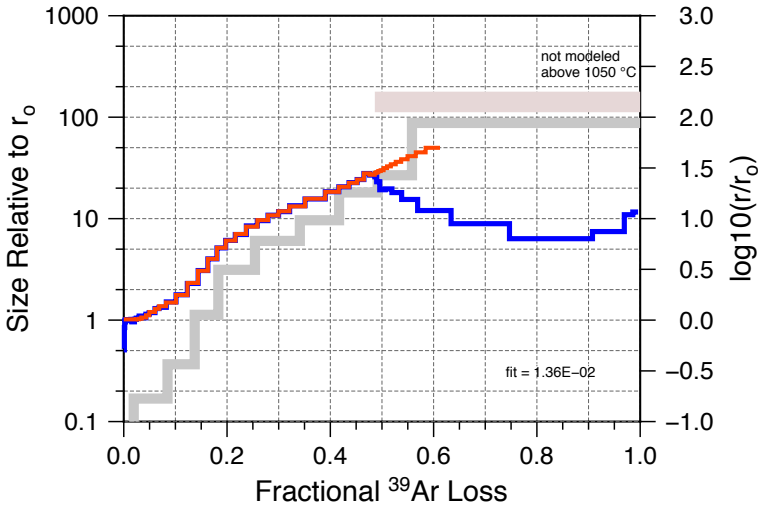
Sample OL13: Arvert reheating allowed inverse thermal history. 10,000 iterations, max MC/CRS reheating rates, 1.0/1.0 and cooling rates, 2.0/5.0 C/my. Best fit: 3.11; worst fit: 3.29



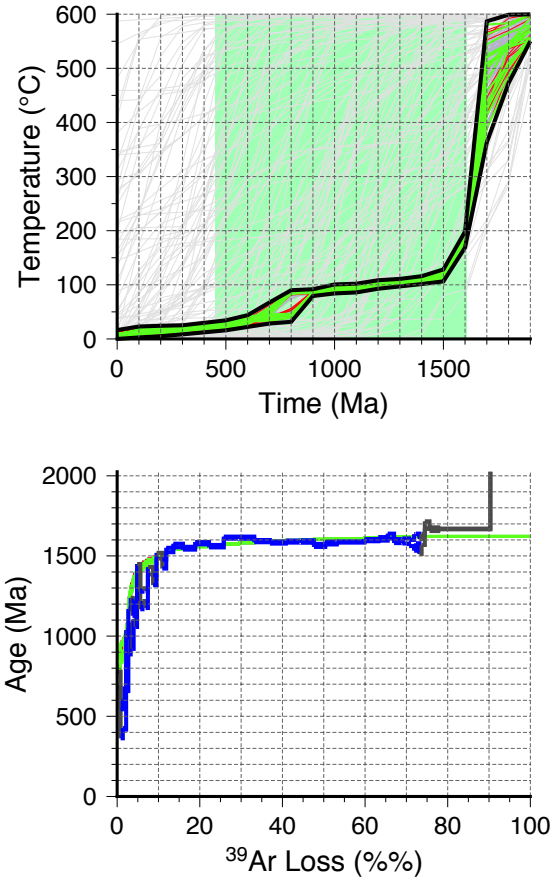
SAMPLE: OL–13
Using steps 4 to 11:
E = 48.24 ± 0.29 kcal/mol
$Log_{10}(D/r_o^2)$ = 5.222 ± 0.080
Unweighted regression
Infinite–slab geometry

10 domains:

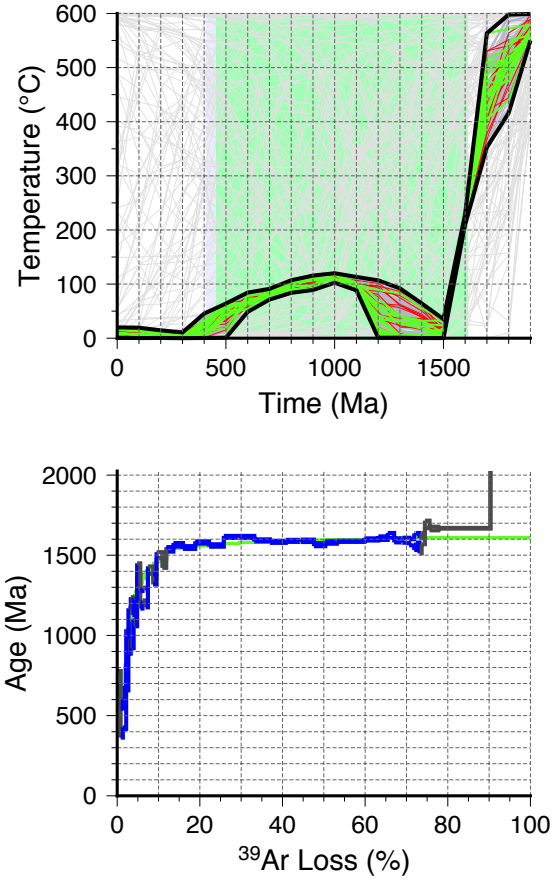
N	Vol.	Vol_T	Rel. Size	Tc10
1	0.019	0.02	0.054	203.
2	0.066	0.08	0.168	224.
3	0.052	0.14	0.367	240.
4	0.046	0.18	1.126	264.
5	0.071	0.25	3.133	288.
6	0.087	0.34	6.040	305.
7	0.076	0.42	9.648	318.
8	0.075	0.49	18.11	336.
9	0.066	0.56	26.82	347.
10	0.442	1.00	87.77	385.



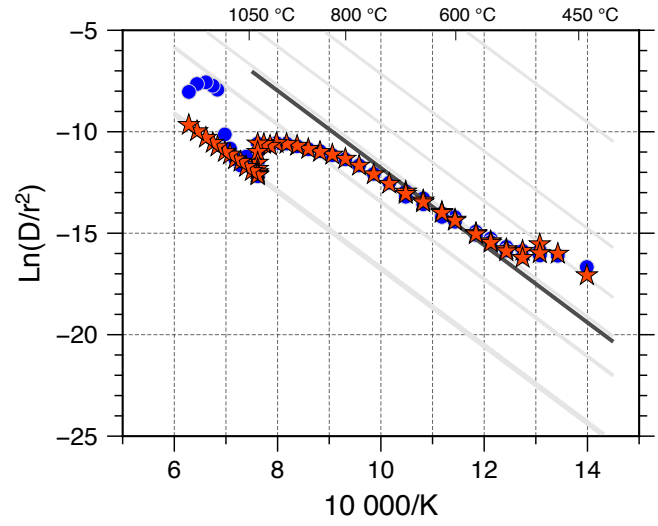
Athabasca



Sample 02-76B: Arvert monotonic inverse thermal history. 5,000 iterations, max MC/CRS cooling rates, 2.0/5.0 C/my. Best fit: 9.05; worst fit: 9.35



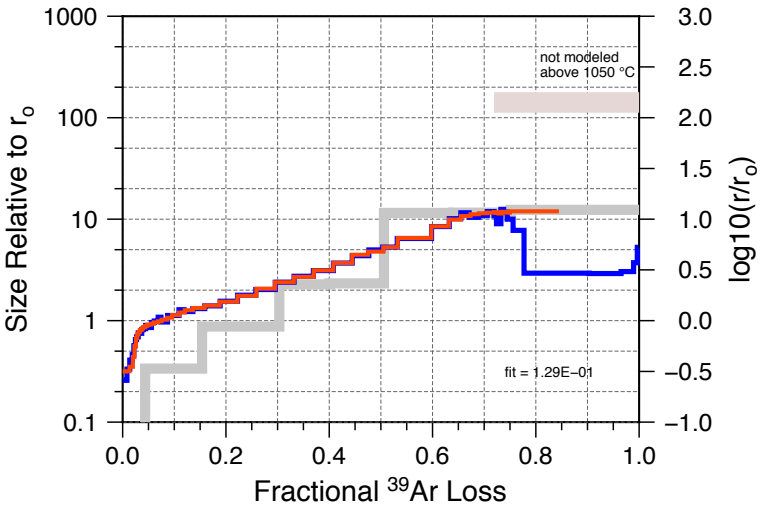
Sample 02-76B: Arvert reheating allowed inverse thermal history. 13,000 iterations, max MC/CRS reheating rates 2.0/2.0 and cooling rates, 5.0/5.0 C/my. Best fit: 4.64; worst fit: 4.74. **For this sample only used 4 steps were used in Domains program Arrhenius regression to obtain a reasonable activation energy.

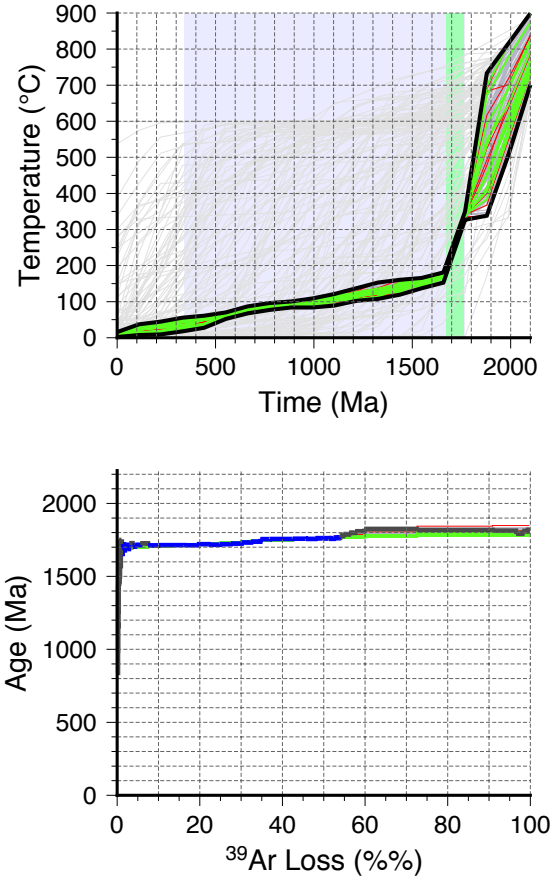


SAMPLE: BF0276B–
Using steps 14 to 17:
E = 37.80 ± 6.05 kcal/mol
$Log_{10}(D/r_o^2)$ = 3.149 ± 1.477
Unweighted regression
Infinite–slab geometry

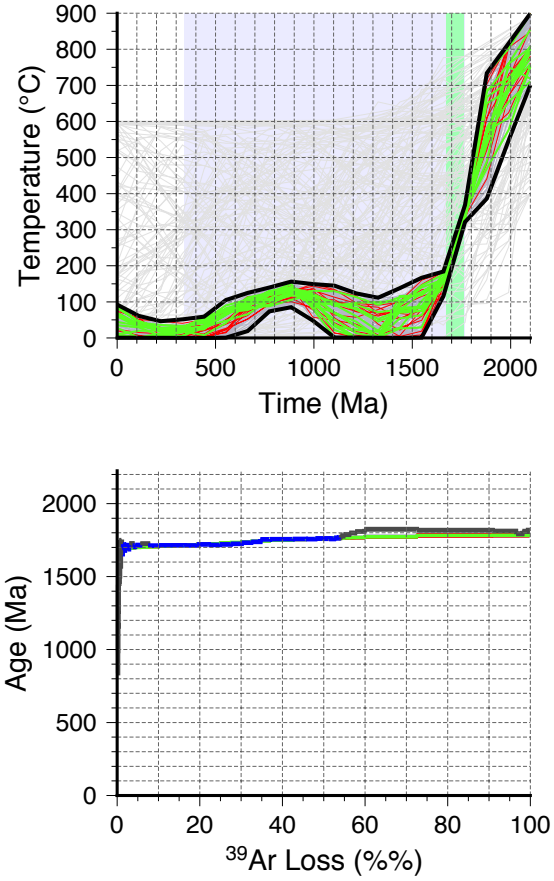
9 domains:

N	Vol.	Vol_T	Rel. Size	Tc10
1	0.016	0.02	0.007	107.
2	0.027	0.04	0.098	149.
3	0.110	0.15	0.336	172.
4	0.150	0.30	0.874	192.
5	0.097	0.40	2.276	214.
6	0.105	0.51	2.332	215.
7	0.134	0.64	11.52	256.
8	0.111	0.75	11.59	256.
9	0.249	1.00	12.37	258.

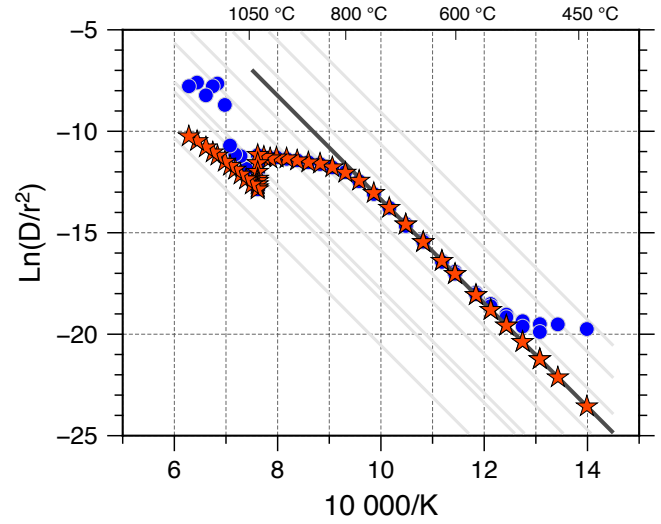




Sample 02-123A: Arvert monotonic inverse thermal history. 5,000 iterations, max MC/CRS cooling rates, 2.0/5.0 C/my. Best fit: 11.43; worst fit: 14.32



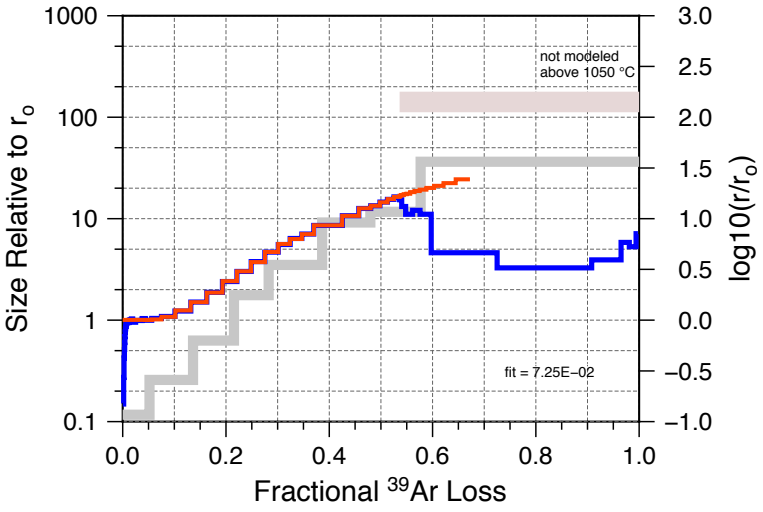
Sample 02-123A: Arvert reheating allowed inverse thermal history. 5,000 iterations, max MC/CRS reheating rates 1.0/1.0 and cooling rates, 2.0/5.0 C/my. Best fit: 10.12; worst fit: 15.46



SAMPLE: BF02−123A
Using steps 14 to 21:
E = 50.75 ± 0.93 kcal/mol
$Log_{10}(D/r_o^2)$ = 5.296 ± 0.220
Unweighted regression
Infinite−slab geometry

8 domains:

N	Vol.	Vol_T	Rel. Size	Tc10
1	0.052	0.05	0.117	240.
2	0.084	0.14	0.258	257.
3	0.079	0.22	0.629	276.
4	0.067	0.28	1.762	300.
5	0.104	0.39	3.505	318.
6	0.093	0.48	9.177	344.
7	0.097	0.58	11.68	351.
8	0.423	1.00	36.37	386.



Appendix References

Annesley, I. R., Madore, C., Krogh, T. E., Kwok, Y., and Kamo, S., 1999, New U-Pb zircon and monazite geochronological results for Archean and Paleoproterozoic basement to the southeastern part of the Athabasca Basin, Saskatchewan: Summary of investigations, v. 2, p. 99-94.92.

Baldwin, J., Bowring, S., and Williams, M., 2003, Petrological and geochronological constraints on high pressure, high temperature metamorphism in the Snowbird tectonic zone, Canada: Journal of Metamorphic Geology, v. 21, no. 1, p. 81-98.

Berman, R., Davis, W., and Pehrsson, S., 2007, Collisional Snowbird tectonic zone resurrected: Growth of Laurentia during the 1.9 Ga accretionary phase of the Hudsonian orogeny: Geology, v. 35, no. 10, p. 911-914.

Cope, N. J., 2012, Thermochronology and geochronology of the Otter Lake region, QC, Central Metasedimentary Belt, Grenville Province [Master of Science: Kent State, 117 p.

Creason, C. G., 2015, Phanerozoic Exhumation History of Hall Peninsula, Baffin Island: Insights from Apatite and Zircon (U-Th-Sm)/He Thermochronology and 3D Thermokinematic Modeling [Master of Science: Dalhousie University, 138 p.

Dewane, T., and Van Schmus, W., 2007, U–Pb geochronology of the Wolf River batholith, north-central Wisconsin: Evidence for successive magmatism between 1484Ma and 1468Ma: Precambrian Research, v. 157, no. 1, p. 215-234.

Everitt, R., McMurry, J., Brown, A., and Davison, C., Geology of the Lac Du Bonnet batholith, inside and out: AECL's underground research laboratory, southeastern Manitoba, *in* Proceedings Field excursion B-5: guidebook. Geological Association of Canada–Mineralogical Association of Canada Joint Annual Meeting1996.

Feinstein, S., Kohn, B., Osadetz, K., Everitt, R., and O'Sullivan, P., 2009, Variable Phanerozoic thermal history in the Southern Canadian Shield: Evidence from an apatite fission track profile at the Underground Research Laboratory (URL), Manitoba: Tectonophysics, v. 475, no. 1, p. 190-199.

Flowers, R., Bowring, S., Mahan, K., Williams, M., and Williams, I., 2008, Stabilization and reactivation of cratonic lithosphere from the lower crustal record in the western Canadian shield: Contributions to Mineralogy and Petrology, v. 156, no. 4, p. 529-549.

Flowers, R., Mahan, K., Bowring, S., Williams, M., Pringle, M., and Hodges, K., 2006a, Multistage exhumation and juxtaposition of lower continental crust in the western Canadian Shield: Linking high‐resolution U‐Pb and 40Ar/39Ar thermochronometry with pressure‐temperature‐deformation paths: Tectonics, v. 25, no. 4.

Flowers, R. M., Bowring, S. A., and Reiners, P. W., 2006b, Low long-term erosion rates and extreme continental stability documented by ancient (U-Th)/He dates: Geology, v. 34, no. 11, p. 925-928.

Gittins, J., Macintyre, R., and York, D., 1967, The ages of carbonatite complexes in eastern Canada: Canadian Journal of Earth Sciences, v. 4, no. 4, p. 651-655.

Hardie, R., 2016, (U-Th)/He thermochronology of the Ottawa Embayment, Eastern Canada: the temperature-time history of an ancient, intracratonic rift basin [Master of Science: University of Ottawa, 119 p.
Hinze, W., Allen, D. J., Braile, L. W., and Mariano, J., 1997, The Midcontinent rift system: A major Proterozoic continental rift: Special Papers - Geological Society of America, p. 7-36.
Hoffman, P. F., 1988, United plates of America, the birth of a craton: early Proterozoic assembly and growth of Laurentia: Ann. Rev. Earth Planet. Sci., v. 16, p. 543-603.
Hoffman, P. F., 1989, Precambrian geology and tectonic history of North America: The Geology of North America, p. 447-512.
Holm, D., and Lux, D., 1998, Depth of emplacement and tilting of the Middle Proterozoic (1470 Ma) Wolf River batholith, Wisconsin: 40Ar/39Ar thermochronologic constraints: Canadian Journal of Earth Sciences, v. 35, no. 10, p. 1143-1151.
Holm, D. K., Van Schmus, W. R., MacNeill, L. C., Boerboom, T. J., Schweitzer, D., and Schneider, D., 2005, U-Pb zircon geochronology of Paleoproterozoic plutons from the northern midcontinent, USA: Evidence for subduction flip and continued convergence after geon 18 Penokean orogenesis: Geological Society of America Bulletin, v. 117, no. 3-4, p. 259-275.
Hoppe, W., Montgomery, C., and Van Schmus, W., 1983, Age and significance of Precambrian basement samples from northern Illinois and adjacent states: Journal of Geophysical Research: Solid Earth, v. 88, no. B9, p. 7276-7286.
Hou, G., 2012, Mechanism for three types of mafic dyke swarms: Geoscience Frontiers, v. 3, no. 2, p. 217-223.
Hunt, P. A., and Roddick, J. C., 1988, A compilation of K-Ar ages: Report 18; Radiogenic Age and Isotopic Studies: Report 2: Geological Survey of Canada.
Idleman, B. D., and Zeitler, P. K., 2014, Rapid characterization of noble-gas kinetics using continuous heating and gas accumulation, 14th International Conference on Thermochronology: Chamonix, France.
Kennedy, A. K., Kamo, S. L., Nasdala, L., and Timms, N. E., 2010, Grenville skarn titanite: potential reference material for SIMS U–Th–Pb analysis: The Canadian Mineralogist, v. 48, no. 6, p. 1423-1443.
Kohn, B. P., Gleadow, A. J., Brown, R. W., Gallagher, K., Lorencak, M., and Noble, W. P., 2005, Visualizing thermotectonic and denudation histories using apatite fission track thermochronology: Reviews in mineralogy and geochemistry, v. 58, no. 1, p. 527-565.
Koppers, A. A., 2002, ArArCALC—software for 40 Ar/39 Ar age calculations: Computers & Geosciences, v. 28, no. 5, p. 605-619.
Kretz, R., 1994, Petrology of veined gneisses of the Otter complex, southern Grenville Province: Canadian Journal of Earth Sciences, v. 31, no. 5, p. 835-851.
Krogh, T., Davis, G., Ermanovics, I., and Harris, N., U-Pb isotopic ages of zircons from the Berens Block and English River gneiss belt, *in* Proceedings Proc. 1976 Geotraverse Conf., University of Toronto1976.

Lorencak, M., 2003, Low temperature thermochronology of the Canadian and Fennoscandian Shields: Integration of apatite fission track and (U-Th)/He methods: University of Melbourne, School of Earth Sciences.

Lorencak, M., Kohn, B., Osadetz, K., and Gleadow, A., 2004, Combined apatite fission track and (U–Th)/He thermochronometry in a slowly cooled terrane: results from a 3440-m-deep drill hole in the southern Canadian Shield: Earth and Planetary Science Letters, v. 227, no. 1, p. 87-104.

Maass, R., and Brown, W. G., Archean gneiss at Lake Arbutus Dam, Jackson County, Wisconsin, *in* Proceedings North-Central Section of the Geological Society of America1987, Volume 5, Geological Society of Amer, p. 189.

Mahan, K., and Williams, M., 2005, Reconstruction of a large deep-crustal terrane: Implications for the Snowbird tectonic zone and early growth of Laurentia: Geology, v. 33, no. 5, p. 385-388.

McDannell, K. T., Idleman, B. D., and Zeitler, P. K., 2015, Characterization of helium diffusion behavior from continuous heating experiments: Sample screening and identification of multiple 4He components, AGU Fall Meeting, Volume V33D-3131: San Francisco, CA, American Geophysical Union.

McGregor, E., Nielsen, S., Stephenson, R., Petersen, K., and MacDonald, D., 2013, Long-term exhumation of a Palaeoproterozoic orogen and the role of pre-existing heterogeneous thermal crustal properties: a fission-track study of SE Baffin Island: Journal of the Geological Society, v. 170, no. 6, p. 877-891.

McLelland, J., Daly, J. S., and McLelland, J. M., 1996, The Grenville orogenic cycle (ca. 1350-1000 Ma): an Adirondack perspective: Tectonophysics, v. 265, no. 1, p. 1-28.

Naeser, C. W., and Crowley, K. D., 1990, Fission-track dating of apatite from deep borehole ATK-1 at Atikokan, Ontario: International Atomic Energy Agency.

Osadetz, K., Kohn, B., Feinstein, S., and O'Sullivan, P., 2002, Thermal history of Canadian Williston basin from apatite fission-track thermochronology—implications for petroleum systems and geodynamic history: Tectonophysics, v. 349, no. 1, p. 221-249.

Percival, J., and Easton, R., 2007, Geology of the Canadian shield in Ontario: an update. Ontario Geological Survey, Open File Report 6196, Geological Survey of Canada, Open File 5511, Ontario Power Generation: Ontario Geological Survey, p. 66.

Percival, J., Sanborn-Barrie, M., Skulski, T., Stott, G., Helmstaedt, H., and White, D., 2006, Tectonic evolution of the western Superior Province from NATMAP and Lithoprobe studies: Canadian Journal of Earth Sciences, v. 43, no. 7, p. 1085-1117.

Percival, J., Skulski, T., Sanborn-Barrie, M., Stott, G., Leclair, A., Corkery, M., and Boily, M., 2012, Geology and tectonic evolution of the Superior Province, Canada: Tectonic Styles in Canada: The Lithoprobe Perspective. Geol Assoc Canada Spec Paper, v. 49, p. 321-378.

Peterman, Z. E., and Sims, P., 1988, The Goodman Swell: A lithospheric flexure caused by crustal loading along the Midcontinent Rift System: Tectonics, v. 7, no. 5, p. 1077-1090.

Price, W. L., 1977, A controlled random search procedure for global optimisation: The Computer Journal, v. 20, no. 4, p. 367-370.
Rayner, N. M., Stern, R. A., and Rainbird, R. H., 2003, SHRIMP U-Pb detrital zircon geochronology of Athabasca Group sandstones, northern Saskatchewan and Alberta: Geological Survey of Canada.
Romano, D., Holm, D. K., and Foland, K., 2000, Determining the extent and nature of Mazatzal-related overprinting of the Penokean orogenic belt in the southern Lake Superior region, north–central USA: Precambrian Research, v. 104, no. 1, p. 25-46.
Schneider, D., Cope, N., and Holm, D., 2013, Thermochronology of the Mont Laurier terrane, southern Canadian Grenville Province, and its bearing on defining orogenic architecture: Precambrian Research, v. 226, p. 43-58.
Schneider, D. A., Camacho, A., Milne, G., and Holm, D. K., Muscovite Ar-Ar laser probe ages and thermal models coupled with lithospheric mechanical modeling, *in* Proceedings Geological Society of America Annual Meeting, Minneapolis, MN, 2011, GSA.
Schulz, K. J., and Cannon, W. F., 2007, The Penokean orogeny in the Lake Superior region: Precambrian Research, v. 157, no. 1, p. 4-25.
Scott, D. J., 1999, U–Pb geochronology of the eastern Hall Peninsula, southern Baffin Island, Canada: a northern link between the Archean of West Greenland and the Paleoproterozoic Torngat Orogen of northern Labrador: Precambrian Research, v. 93, no. 1, p. 5-26.
Sims, P. K., 1993, Petrography and geochemistry of early Proterozoic granitoid rocks in Wisconsin Magmatic terranes of Penokean Orogen, northern Wisconsin, US Government Printing Office, v. 1904.
Skipton, D., Schneider, D., McFarlane, C., St-Onge, M., and Jackson, S., 2016a, Multi-stage zircon and monazite growth revealed by depth profiling and in situ U-Pb geochronology: resolving the Paleoproterozoic tectonics of the Trans-Hudson Orogen on southeastern Baffin Island, Canada: Precambrian Research.
Skipton, D., Schneider, D. A., Kellet, D. A., and Joyce, N. L., 2016, submitted, in review, Deciphering the Paleoproterozoic cooling history of the northeastern Trans-Hudson Orogen, Baffin Island (Canada), using 40Ar/39Ar step-heating and UV laserprobe thermochronology: Lithos.
Skipton, D. R., St-Onge, M. R., Schneider, D. A., and McFarlane, C. R. M., 2016b, Tectonothermal Evolution of the Middle Crust in the Trans-Hudson Orogen, Baffin Island, Canada: Evidence from Petrology and Monazite Geochronology of Sillimanite-bearing Migmatites: Journal of Petrology, v. in press, p. 1-26.
Van Lankvelt, A., Schneider, D., Biczok, J., McFarlane, C., and Hattori, K., 2016, Decoding Zircon Geochronology of Igneous and Alteration Events Based on Chemical and Microstructural Features: a Study from the Western Superior Province, Canada: Journal of Petrology, p. egw041.
Van Schmus, W., Medaris, L., and Banks, P., 1975a, Geology and age of the Wolf River batholith, Wisconsin: Geological Society of America Bulletin, v. 86, no. 7, p. 907-914.

Van Schmus, W., Thurman, E., and Peterman, Z. E., 1975b, Geology and Rb-Sr chronology of middle Precambrian rocks in eastern and central Wisconsin: Geological Society of America Bulletin, v. 86, no. 9, p. 1255-1265.

Wanless, R. K., Stevens, R. D., Lachance, G. R., and Edmonds, C. M., 1967, K-Ar isotopic ages, Report 7; Age determinations and geological studies,: Geological Survey of Canada.

White, D., Musacchio, G., Helmstaedt, H., Harrap, R., Thurston, P., Van der Velden, A., and Hall, K., 2003, Images of a lower-crustal oceanic slab: Direct evidence for tectonic accretion in the Archean western Superior province: Geology, v. 31, no. 11, p. 997-1000.

Willett, S. D., 1997, Inverse modeling of annealing of fission tracks in apatite; 1, A controlled random search method: American Journal of Science, v. 297, no. 10, p. 939-969.

Zeitler, P. K., 2004, Arvert 4.0.1 Inversion of 40Ar/39Ar age spectra, Volume 6.0: Users Manual 2004, updated 2016, Available at http://www.ees.lehigh.edu/geochronology.html.

CONCLUSIONS

The works presented in this dissertation have discussed applying thermochronology to old, slowly cooled settings and some of the problems that are encountered during its implementation. Recent advances in understanding the coupling of atmospheric, lithospheric, and surficial processes, along with innovative developments in geochronology and thermochronology over the past few decades, have allowed better integration of temporal records to reconstruct past tectonic environments, orogenic evolution, and erosional processes. Slowly-cooled terranes present challenges for the interpretation of thermochronologic and geologic records, mainly in the face of the long timescales innately associated with their development, and the detrimental effect of subsequent tectonic activity on primary thermal information. Elucidating upper-crustal histories also presents challenges for the employed analytical techniques themselves, namely in apatite (U-Th)/He thermochronometry, where unexplained age dispersion is common in slowly-cooled settings. The Continuous Ramped Heating (CRH) method presented here is an example of an analytical improvement that with further work has the potential to offer greater understanding of the contributing mechanisms of cooling age dispersion.

The other presented chapters demonstrate that low-temperature thermochronometers contain much valuable information on constraining topographic histories in settings where post-orogenic activity has been minimal. Central Mongolia experienced typical rapid decay following major continental assembly and mountain-building during the Late Paleozoic-Early Mesozoic. The topographic relief of the Hangay Mountains of central

Mongolia were originally comparable to nearby modern, active ranges such as the Chinese Tian Shan. Since the Cretaceous, this region has experienced very slow erosion on the order of 10s of meters per million years. Far-field effects of the India-Asia collision, ongoing uplift of the Mongolian Plateau, local lithosphere-asthenosphere interactions, and recent glaciations have introduced geodynamic complexity in the form of surface uplift and valley-scale incision. However, due to sustained high aridity the regional erosion has remained low. This setting is an important example for highlighting the antiquity and longevity of some of Earth's landscapes, which are generally seen as youthful or undergoing relatively continuous development at most active plate boundaries.

The billion-year timescale common in cratons is fraught with the same challenges as previously mentioned with thermochronometric data interpretation, just on a grander scale. The southern Canadian Shield is a region where long-term stability since the Precambrian has been inferred mainly due to *a lack* of information rather than geologic evidence. The evidence that does exist is commonly sporadic and records a much younger, progression of events over the last ~500 million years. The Athabasca region in the northwest craton is highly constrained from sedimentary and geochronologic data, suggesting a rapid, and prolonged nearly two billion year history of stability – in line with conventional views. Thermal-history data from the southern Canadian Shield indicate that currently exposed rocks were still at temperatures of ~200 °C at 1 Ga. Similar histories are observed in other bordering Baffin Island terranes to the north. Collectively, regardless of monotonic or reheating histories these areas were still at elevated

temperatures at 1 Ga and suggest unroofing was initiated in the Neoproterozoic after a long period of slow cooling. This prior history ties into the later Paleozoic-Mesozoic evidence of mantle-induced dynamic topography and sea-level fluctuations that affected the entire continent and caused widespread, episodic unroofing and burial of the craton to modest levels of ≤ 2 km.

The Mongolian Plateau and the southern Canadian Shield have some broad similarities. Both regions are continental interiors that have been affected by peripheral tectonism, albeit vastly separated in time. Throughout central Asia there is clear evidence that deformation continues to progress northward from India colliding with Asia. The physiographic expressions of this tectonism are separated by over 2500 km, with the locus of tectonic activity at the high-elevation Himalaya and Tibetan Plateau, while the other end-member is the Baikal rift abutting the Siberian craton at approximate sea-level elevation. The Grenville orogeny at ~1 Ga was of similar scale to the modern Himalaya and may have produced similar far-field effects.

Isostatic considerations from a thickened crust may lend support for high-elevation topography in both Mongolia and the ancient craton. Studies over the past 40 years have suggested that mafic magmatic additions to the lower crust are very important for crustal growth and thickening over long timescales. This mechanism can explain the reactivation of the craton and renewal of inferred exhumation after an ~500 m.y. period of mid-crustal holding for southern Canadian Shield rocks. Magmatic underplating due to Mid-Continent mantle plume impingement on the lithosphere could have driven uplift and

unroofing of the craton (see Nelson, 1991 for an overview in cratons). Similar underplating processes have been proposed for central Mongolia (e.g. Chen et al., 2015; Petit et al., 2002; Stosch et al., 1995).

The Earth system is very dynamic and complex, however there are certainly exceptions to this – many locations around the globe are characterized by minimal tectonic activity but impressive topography or landscapes persist, like the Appalachian Mountains or central Mongolia. Regions such as central Mongolia suggest that in the face of minimal external forcing, landscapes can endure for extremely long timescales. Ultimately given enough time a lot can happen geologically, nonetheless we often think of continental margins and interiors as being distinctly separate instead of a continuum. Perhaps the Mongolian interior and cratonic interiors are not so different after all and these areas are just in different stages of their tectonic lifecycle.

References

Chen, M., Niu, F., Liu, Q. and Tromp, J. (2015) Mantle-driven uplift of Hangai Dome: New seismic constraints from adjoint tomography. Geophysical Research Letters 42, 6967-6974.

Nelson, K. (1991) A unified view of craton evolution motivated by recent deep seismic reflection and refraction results. Geophysical Journal International 105, 25-35.

Petit, C., Deverchere, J., Calais, E., San'kov, V. and Fairhead, D. (2002) Deep structure and mechanical behavior of the lithosphere in the Hangai-Hovsgol region, Mongolia: new constraints from gravity modeling. Earth and Planetary Science Letters 197, 133-149.

Stosch, H.G., Ionov, D.A., Puchtel, I.S., Galer, S.J.G. and Sharpouri, A. (1995) Lower crustal xenoliths from Mongolia and their bearing on the nature of the deep crust beneath central Asia. Lithos 36, 227-242.

KALIN T. MCDANNELL

Department of Earth & Environmental Sciences
Lehigh University
Bethlehem, PA 18015

Research Interests

- Understanding crustal dynamics, mainly the interaction between tectonics and climate in mountain systems and their spatial and temporal influence on landscape evolution, (i.e. topographic relief change and exhumation histories) using low-temperature (U-Th)/He thermochronology and thermo-kinematic modeling
- The thermal and geodynamic evolution of continents (i.e. cratons) over long, billion year timescales linking high-temperature U-Pb, medium-temperature $^{40}Ar/^{39}Ar$, and low-temperature (U-Th)/He records
- Integrating detrital sediment records, structural kinematics, geophysical modeling, and geochemical data to understand the co-development of basin and mountain systems
- (U-Th)/He noble gas thermochronology refinement of laboratory dating methodology and technique development

Education

2017 **Lehigh University, Bethlehem, PA** (May 2017)
Ph.D., Earth & Environmental Sciences
Dissertation: Deep-time thermochronology of slowly cooled terranes: Insights from Mongolia and the North American craton – Advisor: Dr. Peter K. Zeitler
Committee: Dr. Anne S. Meltzer, Dr. Kenneth P. Kodama, and Dr. Rebecca M. Flowers (University of Colorado, Boulder)

2011 **West Virginia University, Morgantown, WV**
M.S., Geology
Thesis: Exhumation in the Bendeleben Mountains (Seward Peninsula, Alaska) constrained by (U-Th)/He thermochronology – Advisor: Dr. Jaime Toro
Committee: Dr. J. Steven Kite and Dr. Jonathan C. Lewis

2008 **Indiana University of Pennsylvania, Indiana, PA**
B.S., Geology – Environmental Science (concentration)
Capstone research: Contemporary Shearing on the Tucurrique Fault: Evidence for an Active Pull-Apart Basin at Pejibaye, Costa Rica
Advisor: Dr. Jonathan C. Lewis

Professional Appointments

2011-present	*Research Assistant,* Lehigh University, Earth and Environmental Sciences
2016	*Fellow*, Lehigh University, College of Arts and Sciences
2011-2016	*Teaching Assistant & Lecturer*, Lehigh University, EES
2014	*Professional Intern, Earth Sciences*, Chevron, ETC - Hydrocarbon Charge team I
2013	*Professional Intern, Earth Sciences*, Chevron, ETC - Hydrocarbon Charge team II
2011	*Visiting Lecturer,* West Virginia University, Petrol. & Natural Gas Engineering
2010	*Computational Geologist Intern*, URS Corporation, Department of Energy, NETL
2008-2011	*Teaching Assistant & Lecturer,* West Virginia University, Geology & Geography

Teaching Experience

Visiting Lecturer, 2011
West Virginia University, Dept. of Petroleum and Natural Gas Engineering
Course: GEOL 342 Structural Geology for Petroleum Engineering (1 semester, 21 students)

Lecturer and Teaching Assistant, 2011-2016
Lehigh University, Dept. of Earth and Environmental Sciences
EES 004: The Science of Environmental Issues (TA, 2 semesters, 30 students each)
EES 080: Introduction to the Earth System (lab lecturer, 2 sem., 15-20 students each)
EES 100: Earth Systems Science (TA, 1 semester, 37 students)
EES 022: Exploring Earth (lecturer, 2 semesters total, 2 sections each sem., ~50 students
EES 318: Geographic Analysis in EES (TA, 1 semester, 13 students)
EES 325: Remote Sensing of Terr. and Aquatic Environments (TA, 1 semester, 10 students)

Lecturer and Teaching Assistant, 2008-2011
West Virginia University, Dept. of Geology and Geography
Course: GEOL 341: Structural Geology (TA, 1 semester, 25 students)
Course: GEOL 102: Dynamic Earth (lecturer, 4 semesters, 4 sections/semester, 25 students each)
Course: GEOL 103: Earth Through Time (TA, 1 semester, ~100 students)

Internships

5/2014-7/2014 **Professional Intern, Earth Sciences**
Chevron Corporation, Energy Technology Company
Hydrocarbon Charge Team I - Exploration and New Ventures Unit

- Basin calibration and modeling utilizing Trinity and Petromod
- Source rock quality and characterization
- Source-to-oil Family geochemistry data review and quality control
- Fetch area analysis, transformation ratio mapping, hydrocarbon migration analytics
- Petroleum system and migration sensitivity analysis
- Seismic data cross-referencing against structural models

5/2013-8/2013 **Professional Intern, Earth Sciences**
Chevron Corporation, Energy Technology Company
Hydrocarbon Charge Team II - Exploration & New Ventures Unit
Strategic Research Project – petroleum migration efficiency

- Basin analysis and quantitative mass-balance assessment of hydrocarbon migration efficiency in petroleum systems of varying complexity at the prospect-scale
- >275 wells QCed for geochemical data, stratigraphy, and basin model structural calibration
- P10, P50, P90 for Rock-Eval source thickness, maturity and quality
- Transformation Ratio and fetch area maps, OIP volumes, API, HC type, field information catalogued
- IHS database integration
- Stochastic modeling of hydrocarbon charge and sensitivity analysis

7/2010-12/2010 **Computational Geologist Intern**
URS Corporation, United States Department of Energy - National Energy Technology Lab, Morgantown, WV
Earth and Mineral Sciences Division, Unconventional Oil and Enhanced Oil Recovery - Gas Shale Research Group - Marcellus Shale

- Database development and management of legacy EGSP data
- GIS analysis and data compilation of well data, geology, and coal zones
- Involved in compilation of computed core tomography (CT) scan data
- SEM, confocal scanning, and fluorescence microscopy training

Publications

Submitted or in press

McDannell, K.T., Zeitler, P.K., Idleman, B.D., *in review,* Relict topography of the Hangay Mountains in central Mongolia: Quantifying long-term exhumation and relief change of an old landscape, *Earth and Planetary Science Letters*.

Idleman, B.D., Zeitler, P.K., **McDannell, K.T.**, *submitted*, Characterization of helium release from apatite by continuous ramped heating, *Chemical Geology*.

In preparation

McDannell, K.T., Zeitler, P.K., Idleman, B.D., *in prep for Geochimica et Cosmochimica Acta*, Screening apatites for (U-Th)/He thermochronometry via continuous ramped heating: Helium age components and implications for age dispersion.

McDannell, K.T., Zeitler, P.K., Schneider, D.A., *in prep for Earth and Planetary Science Letters*, Instability of Laurentia during Earth's Middle Age.

Published

McDannell, K.T., J. Toro, J. K. Hourigan, and D. Harris (2014), Thermochronologic constraints on Late Cretaceous to Cenozoic exhumation of the Bendeleben Mountains, Seward Peninsula, Alaska, *Geochemistry Geophysics Geosystems*, 15, 4009–4023, doi:10.1002/2014GC005424.

Conference Proceedings & Presentations

** denotes conference abstract; ^ denotes talk*

^**McDannell, K.T.**, 2017, Instability of the Canadian craton during the Late Proterozoic, Lehigh University, Earth and Environmental Sciences graduate student symposium

*Zeitler, P.K., **McDannell, K.T.**, Harrison, T.M., Schoene, B.S., 2016, Extending the range of U-Pb apatite thermochronology using SIMS analysis, 15th International Conference on Thermochronology, Maresias, Brazil, 18-22 September.

*Muscio, G.P.A., Everett, M.A., Marpung, L.P., **McDannell, K.T.**, Miceli-Romero, A.A., Yurchenko, I., 2016, Insights into migration losses based on stochastic mass balance calculations and full-physics forward basin modeling. AAPG Hedberg Conference "The Future of Basin and Petroleum Systems Modeling," April 3-8, 2016, Santa Barbara, CA.

***McDannell, K.T.**, Idleman, B.D., Zeitler, P.K., 2015, Characterization of helium diffusion behavior from continuous heating experiments: Sample screening and identification of multiple ^{4}He components. AGU Fall Meeting Abstract, V33D-3131, 12/2015.

*Meltzer, A., Ancuta, L., Carlson, R., Caves, J., Chamberlain, C.P., Gosse, J., Idleman, B.D., Ionov, D., **McDannell, K.T.**, Mendelson, T., Mix, H., Munkhuu, U., Russo, R., Sabaj-Perez, M., Sahagian, D., Sjostrom, D., Smith, S, Stachnik, J., Tsagaan, B.,

Wegmann, K.W., Winnick, M., Zeitler, P.K., Prousevitch, A., 2015, Betwixt and Between: Structure and Evolution of Central Mongolia. AGU Fall Meeting Abstract, T22A-05, 12/2015.

***McDannell, K.T.**, Zeitler, P.K., Ancuta, L.A., Idleman, B.D., Boulton, S., Wegmann, K.W., 2014, The Hangay Dome, central Mongolia: A relict Mesozoic landscape, AGU Fall Meeting Abstract T21A4559, 12/2014.

***Wegmann, K.W., Tamra, M., Sabaj Pérez, M., Lopresti, M., Cole, M.B., Gosse, J.C., Smith, S.G., Bayasgalan, G., Ancuta, L.D., **McDannell, K.T.**, Gallen, S.F., 2014, Geomorphic and Fish Genetics Constraints on Late Cenozoic Long Wavelength Topographic Evolution of the Hangay Mountains, Central Mongolia, AGU Fall Meeting Abstract T21A-4560, 12/2014

***McDannell, K.T.**, Zeitler, P.K., Idleman, B.D., Schneider, D., Flowers, R., 2014, Deep-time thermochronology: K-feldspar $^{40}Ar/^{39}Ar$ assessment of post-orogenic cooling within the North American craton – When did the Shield become a shield? 14th International Conference on Thermochronology, September 8-12, 2014.

^**McDannell, K.T.** 2014, *invited talk,* Slow times at Hangay High*:* Landscape evolution in the Hangay Dome, Mongolia, Indiana University of Pennsylvania Geoscience Dept., Geoscience Day April 28.

^**McDannell, K.T.** 2014, Landscape evolution in the Hangay Dome, Mongolia, Lehigh University Earth and Environmental Sciences Graduate Student Symposium, Feb. 21.

^**McDannell, K.T.**, 2014, Chevron ETC Earth Science Thursday Seminar internship research talk (international corporate-wide audience)

***McDannell, K.T.**, Ancuta, L.A., Smith, S.G., Idleman, B.D., Wegmann, K.W., Zeitler, P.K., 2013, Long-term landscape evolution in the Hangay Dome, Mongolia, American Geophysical Union (AGU) Fall Meeting.

*Muscio, G.P., Miceli Romero, A. A., **McDannell, K.T.**, 2013, Evaluating migration efficiency and its key controlling factors, 26th International Meeting on Organic Geochemistry (IMOG), September 2013.

^**McDannell, K.T.**, 2013, Chevron ETC Earth Science Thursday Seminar internship research talk (international corporate-wide audience)

***McDannell, K.T.**, 2013, PECUBE thermal modeling of exhumation in the Hangay Dome, Mongolia. Poster presentation: Lehigh University EES Dept. Graduate Student Symposium

*Meltzer, A., Ancuta, L. D., Carlson, R. W., Caves, J. K., Chamberlain, P., Gosse, J. C., Idleman, B. D., Ionov, D. A., **McDannell, K. T.**, Mendelson, T., Mix, H. T., Munkhuu, U., Proussevitch, A. A., Russo, R. M., Sabaj-Perez, M., Sahagian, D. L., Sjostrom, D. J., Stachnik, J. C., Tsagaan, B., Wegmann, K. W., Winnick, M. J., Zeitler, P. K., 2012, Intracontinental Deformation and Surface Uplift - Geodynamic Evolution of the Hangay Dome, Mongolia Central Asia, AGU Fall Meeting abstract T12A-05, 12/2012

***McDannell, K.T.**, 2012, Exhumation of the Hangay Dome, central Mongolia from apatite (U-Th)/He and $^{4}He/^{3}He$ thermochronology. Lehigh University EES Dept. Graduate Symposium

***McDannell, K.T.**, Toro, J., Hourigan, J.K., 2010, Exhumation in the Bendeleben Mountains, (Seward Peninsula), Alaska constrained by radiogenic helium thermochronometry. 2010 AGU Fall Meeting

*Soeder, D.J., Mroz, T., Crandall, D., **McDannell, K.T.**, 2010, Multi-scale and Integrated Characterization of the Marcellus Shale in the Appalachian Basin: From Microscopes to Mapping, AGU Fall Meeting.

*Harris, D., Toro, J., **McDannell, K.T.**, 2010, Cretaceous Tectonic and Magmatic Evolution of the Bendeleben and Windy Creek Plutons, Seward Peninsula, Alaska. GSA Cordilleran Section Meeting, Session 51: T11

***McDannell, K.T.**, Lewis, J.C., Montero, W.P., 2008, Contemporary Shearing on the Tucurrique Fault: Evidence for an Active Pull-Apart Basin at Pejibaye, Costa Rica, Central American Geology Congress.

Short Courses

- 2016 UCLA SIMS Ion Probe workshop (*invited*)
- 2014 ExxonMobil Integrated Basin Analysis short course (*invited*)
- 2008 NSF funded Integrated School of Earth Sciences (ISES), Colorado College: States, Rates, and Dates, 1 week short course (*invited*)

Professional Affiliations

American Geophysical Union
Geological Society of America
Geochemical Society
American Association of Petroleum Geologists
Sigma Gamma Epsilon - Upsilon Chapter, West Virginia University

Awards

Lehigh University College of Arts and Sciences Fellowship, 2016
20th Annual Lehigh University Earth and Environmental Science Dept., Graduate Student Symposium Best Poster Presentation award, 2/2015
WVU Sigma Gamma Epsilon - Upsilon Chapter - Golden Brick Award, 2010
WVU Geology Dept. Fieldwork Grant, 2009
WVU Schumaker Fund Grant, 2009
Ronald E. McNair Scholar, Indiana University of Pennsylvania, 2007-2008
Indiana University of Pennsylvania Geoscience Day Best Research Award, 2008
Indiana University of Pennsylvania Undergraduate Scholars Forum: Best Scientific Sources Bibliography Award, 2008
U.S. Dept. of Education (SMART) Grant, 2007
IUP Edith Davis Eve Academic Scholarship, 2005-2008;
IUP Natural Science Department Scholarship, 2004-2008

Field Experience

- Central and Northern Mongolia (2 seasons) - geochronologic sampling
- Powder River Basin, Wyoming – clinker deposit locating and sampling
- Seward Peninsula, Alaska – mapping and geochron. sampling
- USGS EDMAP project Bendeleben, AK Quadrangle
- Talamanca Cordillera, Costa Rica – terrace riser and strike-slip fault mapping
- Owens Valley fault zone and Death Valley, California; Guadalupe Mountains, New Mexico
- Devil's Kitchen, WY, Sheep Mountain, WY, and Henderson Mountain, MT – geologic mapping
- Appalachian Mountains (Allegheny Plateau/Valley and Ridge): Indiana County, PA; Altoona, PA; C&O Canal, MD; Lehigh Gap-Delaware Water Gap, PA; Otter Creek, WV; Catskills, NY

Mentorship & Outreach

***Mentoring*:** assisted students in performing fieldwork in Mongolia as part of the NSF project "Intracontinental Deformation and Surface Uplift: Geodynamic Evolution of the Hangay Dome, Mongolia, Central Asia" (2011-2017).

- Informally assisted undergraduate and M.S. students in the Lehigh noble gas laboratory with sample preparation, lab protocols, instrumentation/analyses, data reduction, and modeling.

Curriculum development: worked closely with Lehigh Earth & Environmental Science faculty in refining introductory-level EES 080 and EES 022 laboratory curriculum and classroom implementation.

***K-12 student outreach*:** involved in outreach in the form of classroom and school-wide presentations about "Earth Materials," "Rocks and Minerals," and "Geoscience Careers" aimed at middle school students from Broughal Middle School in Bethlehem, PA and St. Patrick's School, Newry, PA.

Department Service

- Graduate student representative at Lehigh EES dept. faculty meetings (2016-2017)
- Lehigh University Earth and Environmental Science Graduate Student Symposium coordinator and master of ceremonies (2013-2014)
    - Invited alumnus keynote speaker; Organized student presentation style (poster/talks) and created abstract program booklet; Organized correspondence between graduate student representatives and faculty; Planned catering menu, venue reservations, RSVP, and daily schedule/organization of events; designed and ordered individual gifts for all attendees

- Lehigh University EES graduate student symposium committee member (2011-2015)
- IUP Geoscience Club vice president and president 2007-2008

Other Memberships

Sierra Club
The Wilderness Society
National Marrow Donor Program (NMDP) 2004-present
- anonymous bone marrow/stem cell donor, 2007

Languages

English – native; Spanish - conversational (6 years of study)